Alma Mater Studiorum – Università di Bologna

DOTTORATO DI RICERCA IN

Chimica

Ciclo XVII

Settore Concorsuale di afferenza: 03/A2 – Modelli e metodologie per le scienze chimiche

Settore Scientifico disciplinare: CHIM/02 – Chimica Fisica

Structure, Dynamics and Reactivity in the Organic Solid State: Anthracene Derivatives and Charge Transfer Crystals

Presentata da: Tommaso Salzillo

Coordinatore Dottorato

Prof. Aldo Roda

Relatore

Prof. Aldo Brillante

Co-Relatori

Prof. Elisabetta Venuti

Prof. Raffaele Guido Della Valle

Esame finale anno 2015

Dr. Tommaso Salzillo, Curriculum: Chimica Fisica, Relatore: Prof. Aldo Brillante; Co-relatori: Prof. Elisabetta Venuti, Prof. Raffaele Guido Della Valle.

Thesis title: **"**Structure, Dynamics and Reactivity in the Organic Solid State: Anthracene Derivatives and Charge Transfer Crystals.**"**

The work performed by Dr Salzillo during the first and second year of his PhD was mainly focused on crystal- to-crystal photochemical reactions of some anthracene derivatives, with the aim of exploring the large variety of cases that can be encountered when photochemistry meets the solid state.

Dr. Salzillo first treated the remarkable transformation of dinitro-antracene to anthraquinone, where the stunning acrobatics of the entire single crystals under irradiation mark a significant relationship between molecular (chemical) changes and unit cell (physical) changes. Subsequently, the classical example of the photodimerization reaction of 9-cyano-anthracene was revisited with a novel approach. This reaction represents a typical case of violation of the topochemical principle, whose paradigm implies the molecular preformation of the product in the unit cell of the reactant as the strict prerequisite to the positive outcome of the dimerization. The perfect structural fit which leads to a complete topochemical reaction was instead found in the photo-dimerization of 9-methylanthracene. The last photoreaction to be studied was the intriguing issue of 9-anthracene-carboxylic acid, as a case of a reversible dimerization in which crystal mechanical motions are indeed observed, but are not sufficient to validate the successful outcome of the reaction.

In the last year of his PhD work, Dr. Salzillo has been studying the phenomenon of polymorphism in small-molecule organic semiconductors (9-diphenylanthracene) and charge transfer (CT) crystals. CT crystals represent a new emerging class of organic semiconductors, that is quickly gaining interest because of its potential for improved optoelectronic functionalities in devices. However, there is still very little understanding and control over the solid state structure and properties of the donor-acceptor co-crystals. Indeed, the scientific challenge of polymorphism is even more intellectually stimulating for a two component crystal. Preliminary studies have been performed on this topic, by working on the prototype semiconductor perylene combined with tetracyanoquinodimethane and its fluorinated forms, which represent the donor and acceptor, respectively.

During his PhD studies, Dr. Salzillo has spent a three month period at the University of Strasbourg (hosted by Prof. L. De Cola), as well as three more months at the Department of Physics, University of Bath (hosted by Prof. Enrico Da Como). At the latter Institution Dr. Salzillo started to work on CT crystals, and he showed an unprecedented enthusiasm and a very mature approach in conducting this research, contributing to the consolidation of the links between Bath and Bologna. Such links, in fact, are expected to get tighter in the future, also on the basis of a common research proposal submitted within the EU program HORIZON 2020.

Over the entire time of his PhD studentship, Dr. Salzillo has shown a definite attitude to research, with a marked disposition to work in a group and in collaboration with other colleagues and researchers. He has consolidated his knowledge in solid state physical chemistry and has become familiar with several complementary techniques, fundamental in the experimental study of materials science. He has proven to be a very reliable, organized person with excellent laboratory practice. He has acquired skills in many spectroscopic methods quickly, and has been planning experiments. He has also been very good at supervising undergraduate student work.

His main scientific achievements during this three year period are documented by six papers in peer review journals, three contributions in Conferences and topical meetings, with two oral communications, and two seminars given at foreign Institutions. He attended three international schools. Two more papers are going to be submitted and more are planned on the basis of the research started in the last three years.

In view of the results here presented, and as supervisor of his thesis, I judge as excellent the work done by Dr Tommaso Salzillo during his PhD.

Index

Index

Structure, Dynamics and Reactivity in the Organic Solid State: Anthracene Derivatives and Charge Transfer Crystals

1. Introduction

1.1 Elementary Excitations in Molecular Crystals

Organic molecules when organized in a crystal lattice keep their molecular identity forming the class of materials called molecular crystals, where strong intramolecular interactions prevail on the weaker intramolecular ones. The subtle inter-play between these interactions affect structure, dynamics and reactivity, giving rise to the wide variety of properties encountered in these systems.

The physico-chemical properties in a crystal environment are strongly dependent on the mutual positions of the molecules and, in this sense, they are defined *collective properties*. Consequently, under excitation, the energy does not remain localized in a single lattice site, but spreads from site to site as a wave which propagates throughout the crystal as a *collective excitation*. The complex equations of motions of the crystals are solved by diagonalizing the Hamiltonian in a harmonic approximation, if the displacements of the molecules from their equilibrium positions are small. The solutions represent the *collective oscillations* of the individual normal modes, each related to a motion of a free oscillator with a definite frequency and phase. According to quantum theory, these waves carry momentum and thus can also be described in terms of particles. These particles, or quasi-particles, are called *elementary excitations*. Depending on the nature of the excitation, there is a large variety of quasi-particles: phonons, excitons, plasmons and polaritons, among others. In terms of them, spectroscopic properties related to IR, Raman and electronic processes are explained. An experimental description and a theoretical treatment of these phenomena can be found in various textbooks. [1-3]

1.2 Excitons in Molecular Crystals

Upon light absorption, an electronic excitation spreads throughout the crystal. Due to the intermolecular electrostatic interactions, an extended delocalized wave-like excitation is established and travels from one molecule to its neighbor, coherent in space and time. This

wave is called *exciton*. The resulting neutral crystal state is called an *exciton state* and the early description of Frenkel [4] still holds when electrons or holes are localized. In this sense, the exciton theory describes localized charges but delocalized excitations. Related phenomena are absorption and fluorescence spectra of molecular crystals. Moreover, excitons may also interact with electrodes, defects, impurities to reach an ionized state that produces an electric current. Again, the relative positions and the interactions between molecules in the lattice are the driving factors for exciton hopping and electron-hole separation/recombination. In these cases, related phenomena are, among others, photoconductivity, electroluminescence, photovoltaic effects and charge storage and release [5]. Therefore, the exciton theory stands on the basis of the development of the emerging field of molecular electronics with its applications to organic optoelectronic devices [6-12].

By applying exciton theory to molecular crystals, Davydov showed that each molecular energy level splits in as many components as the number of molecules in the unit cell [1-2], as a consequence of the resonance interaction between translationally inequivalent molecular sites. In terms of Group Theory, the split states belong to different irreducible representations of the space group and show different polarization properties dictated by the symmetry rules. Polarized absorption spectra are then the appropriate experiment to assign spectral transitions in molecular crystals with reference to the molecular properties of the free molecule. The low lattice energy of molecular crystals is the consequence of the weak binding among the molecules which constitute distinct chemical species. According to this picture, many properties of molecular crystals can be treated starting from a free molecule and applying a small perturbation given by the weakly interacting molecular surrounding. Absorption spectra of molecular crystals to low lying excited states can be explained in these relatively simple terms. There are, instead, properties essentially related to the collective nature of the crystalline solid with no counterpart in a free molecules. An example of collective properties is the photoconductivity in a molecular crystal.

1.3 Charge Transfer Crystals

Among molecular crystals there is a class of compounds where the crystal is formed by pairs or stacks of alternating donor (D) and acceptor (A) molecules in a definite stoichiometric ratio, the most common one being 1:1. This class of compounds is referred to as weak DA complex crystals or, more often, weak charge-transfer (CT) crystals. These materials can be

studied in order to gain information into processes where absorption of light generates the separation and the transfer of charge from one molecule to another. This and the reverse phenomenon of electron-hole recombination with light emission are fundamental processes in molecular electronics based on devices where the semiconductor active layer is an organic material with the potential for improved optoelectronic functionality.

1.4 Excitons in CT Complexes

CT excitons in mixed stacks have peculiar properties that make them different from excitons in molecular crystals like naphthalene and anthracene [13-15]. These peculiarities are strongly related to the specific molecular and crystal structure of the CT solid. The ground state of a CT crystal, unlike radical salts such as, for instance, TTF-TCNQ, has a weak, if any, polar character. The charge transfer of a fraction of an electron gives rise to a stable CT ground state with a characteristic CT absorption band. The excited state is very polar and corresponds to an almost complete transfer of an electron from the highest filled donor orbital (HOMO) to the lowest unfilled acceptor orbital (LUMO). The polar character can be verified experimentally by measuring the Stark shift of the CT transition when an electric field is applied parallel to the D–A stack direction [16]. With the electron and hole on separate molecules, strong coupling to the lattice is expected and this interaction leads to broad and structureless absorption CT bands as a consequence of the involvement of several lattice phonons.

A second consequence of the strong exciton-phonon coupling is the relaxation of the nuclei in a new equilibrium position with a reorientation of the molecules in a more relaxed state with lower energy. In other words, the large intermolecular electronic delocalization observed in these systems, due to the strong electrostatic interactions, results in an intense CT absorption band lying at lower energy than the localized molecular excitations. Excitons no longer undergo to a phenomenological behavior typical of Frenkel excitons in one component crystals, but rather to a polarity flipping process [13]. Due to the CT excitons polarity along the one-dimensional D–A mixed stack, a donor (acceptor) molecule may lose (gain) its electron on either side, that is, two CT exciton states can be formed for a given $\boldsymbol{k}$ vector. In a centro-symmetric crystal, the CT exciton state at $\boldsymbol{k}$=0 will have parity and only transitons to the odd parity state will be allowed from the ground state. This symmetry is broken in the presence of an electric field and odd and even parity states will mix and both will be observed [16].

1.5 Structure and Dynamics in Molecular Crystals: Polymorphism and Lattice Phonons

The understanding of molecular structure, phonon dynamics and crystal packing, and the relationships among them, is a key issue in the design of the peculiar properties of molecular crystals in materials science, particularly for their application in organic electronics. One of the most often encountered problem related to the structure is the occurrence of polymorphism, *i.e.*, the possibility for the same chemical compound to exhibit two or more crystalline modifications [17-18]. Since their early applications, X-ray diffraction (XRD) methods were recognized as the technique of choice for the identification of the crystal structure of a compound. In the past years, however, much effort has been put in pursuing both experimental and computational techniques for identifying and predicting new crystal phases, with the aim of determining their relative thermodynamic stability [19] and kinetics. The experimental techniques available nowadays include, besides XRD, thermal analyses and a variety of spectroscopic methods, and it is quite clear that a single one cannot provide exhaustive information about the complex solid state diagrams and crystallization kinetics that many substances display. It is then clear that the study of polymorphism must use data from different sources, requiring a multidisciplinary approach.

Polymorphism is an issue of great importance in crystallography because of its key role in pharmaceuticals and materials science. In fact, a large variety of chemical and physical properties such as solubility and charge mobility, relevant to the field of application of the compound, may dramatically change on going from one crystalline modification to the other. In particular, conformational polymorphism is most likely to occur in molecular electronics [20]. The ideal organic semiconductor is, in fact, constituted by large and flexible molecules with extended π-conjugation and whose geometry may slightly change in the lattice, giving rise to different packings, that is, different crystal structures. Polymorphism in organic electronics may produce serious problems to an efficient carrier migration. In fact, mobilities depend on the crystal structure [21,22] and to match the ideal device with the most suitable polymorph becomes a challenge that requires a structural control during the preparation of the semiconductor active layer. An additional drawback is that there are several experimental evidences of phase mixing [21,23], *i.e.*, the simultaneous coexistence of different crystal structures in the same specimen, down to dimensions of the order of the micrometer. The

boundaries between domains with different structures will then act as a source of intrinsic disorder with detrimental effects on charge transport and other key properties. For these reasons, polymorphism in organic electronic is an issue and the assessment of the phase purity is of paramount importance to optimize the device performance. Chemical purity and phase homogeneity (i.e. *physical purity*) are then both required for an optimal and reproducible operation of a working device, ensuring that the efficiency parameters of the semiconductor layer are effectively due to the intrinsic properties of the material.

The method applied in this thesis to tackle this problem, widely illustrated in the recent years, is to use confocal Raman spectroscopy and sample mapping in the region of lattice phonons [24 and *refs therein*], as illustrated in Figure 1.1.

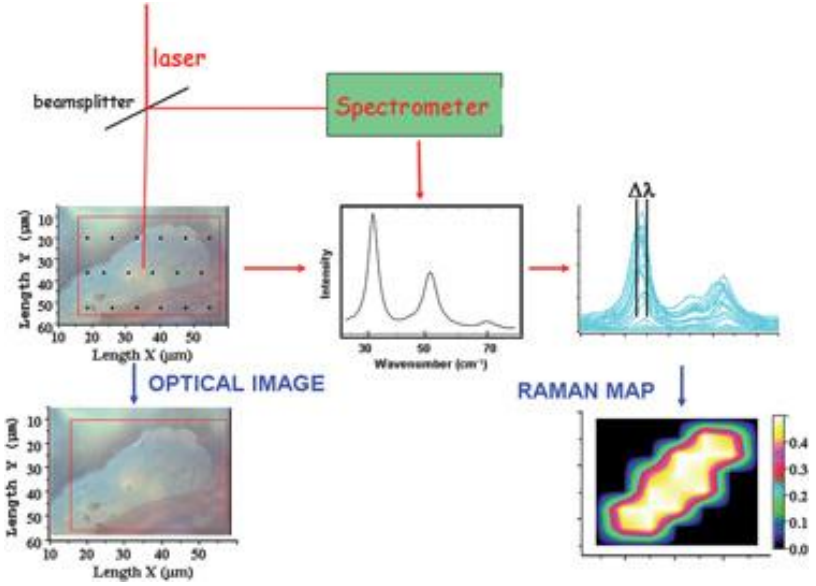

Figure 1.1 A sketch of the experiment.

These modes are collective translational or rotational motions of the molecules in the unit cell and represent the dynamical deformations of the crystal called lattice vibrations or lattice phonons, whose frequencies, involving Raman shifts in the range 10–150 cm^{-1}, probe the intermolecular interactions and are hence very sensitive to even slightly different molecular packings. Because each crystal structure has its own dynamics, in organic molecular crystals lattice phonons are the fingerprints of the individual crystal structure. This method has proved to be fast, non destructive and *in situ*, both for crystal structure recognition and phase mixing in domains at the micrometer scale and can be extended from bulk crystals to thin films on technologically substrates and to working electronic devices [25,26].

In conclusion, the unique relationship between the lattice phonon spectrum (*lattice dynamics*) and its corresponding XRD pattern (*lattice structure*) makes Raman spectroscopy a powerful tool to obtain information on distinct crystal phases. Unlike XRD, the spectroscopic technique can monitor crystal structures in the time scale of a few seconds, also scanning them for physical impurities. The problem of polymorphism in the preparation and characterization of functional molecular materials should then benefit from this technique as a sound method capable to control both crystal structure and molecular recognition in single crystals, thin films and electronic devices.

1.6 Photochemical Reactions in the Solid State

Crystal-to-crystal reactions represent an important category of cooperative phenomena occurring under conditions dictated by the intrinsic degree of order in the crystal lattice. The energetic cost needed to evolve to products requires a large structural reconstruction of the lattice of the reactant, which is often reached with the help of high temperature or high pressure. When the chemical and physical transformations are driven by photons, molecular displacements follow light absorption, which promotes chemical changes according to the relative positions and orientations of the molecules in the crystal. The energy transfer and the chemical reaction itself are then favored by the ordered structure of the crystal, and the lattice becomes the actual cage where the photoreaction takes place [27]. Its counterpart in solution is the perfect fit of dimerized molecules in a confined environment [28].

Systematic studies of photoreactions date back to early work on cinnamic acid derivatives, when a topochemical principle was introduced [29], that is, the reaction product is *preformed* in the packing of the reactant lattice so that only small reorientational motions are required to promote the photoreaction. A survey of the early experiments on the subject can be found in the literature [30].

An important aspect of photoreactions in the solid state is the transformation of the photon energy in new forms, capable of driving the chemical and the physical changes. The most spectacular one is the mechanical motion obtained in response to absorption of light, which manifests as a movement at the supramolecular level (molecular machines) [31-33] or of the entire crystal (photomechanical actuators) [34-39].

It is of great importance to understand the mechanism underlying the crystal-to-crystal transformation, a process complicated by the need to consider all changes occurring in the molecular environment during the course of the reaction. It is self-evident that molecular changes ultimately produce modifications of the crystal lattice and, depending upon the system studied, the extent of the delay of the structural change may considerably vary. While molecular changes under light are produced by a complex mechanism of energetics and dynamics along the potential surface, the structural modifications are strictly mediated by the lattice phonons which couple to the electronic excitation. Structure and dynamics of the crystal lattice are then equally involved and this should be taken into account when designing an experiment aimed to reveal the evolution of the photorection in the solid state.

Among the various techniques that can be employed to study the crystal-to-crystal photoreactions, and their evolution in time, we chose confocal Raman microscopy. The spectroscopic approach has the advantage to efficiently follow in real time both the structural molecular change and the unit cell transformation occurring on going from the reactant to the product. It will be shown that molecular (*chemical*) transformation in most cases follows a faster kinetics with respect to the unit cell (*physical*) modification, the more so when a non-topochemical mechanism underlies the photoreaction.

1.7 Aim of the thesis

The thesis is focused on some fundamental aspects of molecular crystals: structure, dynamics and reactivity. The common ground of these topics is necessarily related to the concept of excitons, phonons and the coupling between them, which has been briefly introduced in the previous sections.

1.7a Structure

The structural aspects here treated are mostly related to the problem of polymorphism, pseudo-polymorphism and co-crystals, as described in chapters 3, 4 and, partially, 5. The sample systems studied are some anthracene derivatives, namely 9,10-diphenyl-anthracene (DPA) and 9-anthracene-carboxylic acid (9ACA). DPA is a polyciclic aromatic molecule that shows both high hole and electron mobilities in the solid state linked to an intense photoluminescence. It seems, therefore, a good candidate of ambipolar organic semiconductor. However, DPA is also an exemplary case of a material whose polymorphism becomes a key factor to achieve reproducible intrinsic electronic mobilities in organics.

Indeed, different crystal packings lead to different transport properties, making the control of the crystal phase a crucial point for device performance. In this thesis we have investigated the experimental conditions to drive the crystal growth towards a specific polymorph in its pure form, as well as how to avoid phase mixing, which would lead to destructive effects of the device performance. Two out of three polymorphs of DPA have been characterized by XRD and Raman spectroscopy and their relative stability has been checked by using energy minimization methods [40]. A third polymorph, grown as microribbons, has been predicted on the basis of its different lattice phonon spectrum.

The problem of 9ACA is a different one. The two crystal forms of the monomer have been investigated with the intent to clarify a relationship between crystal packing and reactivity (photodimerization) in the solid state. In fact, as stated in section 1.6, the initial disposition of the reactant molecules may determine the outcome of the photoproduct. We first started by characterizing the single crystals of the photodimer obtained in solution of different solvents and, much surprisingly, encountered a rich variety of pseudo-polymorphs, whose XRD analysis showed a diversity in the packing of solvent molecules in the unit cell of the dimer. We have then moved our focus towards the study of how each solvent would drive a specific structure of the dimer, to eventually discuss the crystal engineering of this system.

The last subject reported in this thesis on the structural aspects in the organic solid state, is related to CT mixed crystals. CT crystals are binary systems grown with stoichiometry ratios of charge-donor (D) and charge-acceptor molecules (A). As a result of the electronic coupling between the HOMO and LUMO levels of donor and acceptor, many of these compounds exhibit interesting electrical properties, with a behavior which can vary from insulator to semiconductor to metal. The donor and acceptor system of choice was formed by perylene and tetracyano-quinodimethane (TCNQ) and its fluorinated forms. Different methods to grow the single crystals were experimented, resulting in a variety of stoichiometric ratios between D and A. We have tried to rationalize the crystal growth parameters, in order to drive a specific stoichiometry, especially searching the experimental conditions which would lead to the 1:1 ratio. We also tried to play with the temperature of growth to make hypotheses on how the packing of perylene in its two polymorphic forms would eventually affect the insertion of fluorinated TCNQ molecules into the unit cell of the mixed crystals. As experimental methods of investigation, X-ray scattering, Raman and IR spectroscopy have been chosen. Lastly, the degree of ionicity changing the acceptor from the neutral TCNQ to its

fully fluorinated form was calculated using both X-ray diffraction and IR spectroscopy. The goal was to select the most suitable system for ambipolar semiconducting behavior searching for the optimal solid state organization (polymorphism) to reach the best electrical properties.

1.7b Dynamics

In simple terms, the dynamics of a lattice is governed by phonons and, under electronic excitation, by their coupling to excitons. The first phenomenological model of lattice dynamics calculations was proposed in 1912 by Born and von Karman [41], who developed a formal treatment of the quantum theory of crystalline solids [42] and the concept of phonon was introduced. Lattice phonons are the collective excitations produced in the crystal by its deformation following translational and librational motions of the molecules in the unit cell, under optical excitation. Vibrations in solids are experimentally best studied by infrared and Raman spectroscopy. A survey of the spectra of solids with comparison to molecular vibrations can be exhaustively found in the book of Turrel [3], where also the theory of the symmetry of normal modes and their selection rules can be found. The best experimental tool to study optical phonons is Raman spectroscopy in the wavenumber region below 150 cm^{-1}. As shortly outlined in previous sections, the analysis of lattice phonons is strictly related to the corresponding crystal structure. As long as the crystal structure reproduces the equilibrium positions of the molecular nuclei, lattice phonons represent its dynamics. Consequently, a strict relationship is established, since each crystal structure has its own phonon spectrum. We shall also show, in the next section, that optical phonons, when coupled to excitons, are one of the driving factors governing solid state reactivity. Since lattice phonons probe crystal packing and intermolecular interactions, phonon Raman spectroscopy will prove to be a most powerful method to study both polymorphism and crystal-to-crystal photoreactions. In this thesis we have applied this technique by combining spectroscopy and microscopy, that is, by making use of confocality, thus providing insights on the phenomenological aspects of the dynamics of crystal domains at the μm scale.

1.7c Reactivity

The interest for solid state reactions is an evergreen and its application to organic crystals dates back to the early work of the group of Schmidt [29,43], who emphasized how a collective propagation of the excited reactant molecules into the product had necessarily to follow the rule governing ordered systems, that is, a topochemical principle or the capability

of the reactant molecules to be in the correct registry to yield the product with a minimum of orientational reconstruction. During the last few years a revival on the subject has been found in the literature, mostly due to the increasing interest in mechanically responsive single crystals and their potential to transform thermal or light energy into work, specifically seeking for systems behaving like photomechanical actuators [39].

In this thesis we focused our attention on two crystal-to-crystal photoreactions, both related to the rich and widely studied class of anthracene derivatives. After the exemplary case of the light driven transformation of dinitro-antracene (DNA) to anthraquinone (AQ) [44], we will discuss the photodimerization reaction of 9-cyano-anthracene (9CNA) and 9-methyl-anthracene (9MA). While the latter case refers to a perfect structural fit which leads to a topochemical reaction [29], the former compounds represents the classic example of a reaction which is triggered by defects, *i.e.*, a non topochemical one [45]. The novel approach of this work is the study of crystal to crystal photoreactions, and their evolution in time, by using the Raman spectroscopy as a probe of the modifications observed both in the molecular environment and in the unit cell during the course of the reaction. While the analysis of the lattice modes allowed for the study of the physical changes (lattice dynamics), the chemical transformation can be monitored by measuring the intramolecular Raman-active modes of both reactant and product, on the very same spot at the same time. Besides, working in confocal microscopy, with a Raman signal at a spatial resolution below 1 μm, permits to follow the evolution of the photoreaction *in situ* and to compare crystal and molecular spectral changes during the reaction with the microscopic optical images of the sample [44].

One of the major findings of this study is that molecular and lattice transformations do not proceed at the same rate. The molecular transformation precedes the structural crystal change and the delay in time depends on the system studied as well as on sample history. Former guest molecules (early content of photoproduct) eventually become the host molecules and, at the same time, former host molecules (molecules of the starting reactant material) take the place of guests. This is a key point when explaining the evolution mechanism of the reaction in the solid state. The observed time mismatch between chemical and lattice transformation can be used for a modeling of the system and is rationalized by the different behaviors in the kinetic law of molecular and lattice transformation [40]. In the case of 9CNA the formation of the dimer crystal structure always takes place with some delay with respect to the onset of the chemical reaction, a behavior also found for the topochemical

photodimerization of 9MA and previously observed in another crystal-to-crystal photoreaction [44]. The kinetic analysis of the spectroscopic data confirms the hypothesis of an autocatalytic mechanism for the process.

1.8 Organization of the thesis

The thesis is organized as follows. In the second chapter the experimental techniques are described. The photoinduced reactions in single crystals are illustrated in chapter 3. We first show a detailed experimental and computational study of the photoinduced transformation of DNA in AQ. The following cases treated are two phodimerization reactions of 9-substituted anthracene derivatives representing two typical examples of non topochemical (9CNA) and topochemical (9MA) dimerizations. The intriguing case of the pseudo-polymorphs of the photodimers of 9-anthracene-carboxylic acid is also treated here. The polymorphism of the organic semiconductor 9,10 diphenyl-anthracene (DPA) is the content of chapter 4. Chapter 5 is dedicated to CT mixed crystals formed by perylene (D) and tetracyano-quinodimethane (A) and its fluorinated forms. In chapter 6 a survey of the activity performed during a short stay at the University of Strasbourg is given, whereas the Conclusions can be found in chapter 7.

References

[1] A.S. Davydov *"Theory of molecular excitons"* McGraw Hill, New York (1962).

[2] D.P. Craig, S.H. Walmsley "*Excitons in molecular crystals, theory and applications*" W.A. Benjamin, New York (1968).

[3] G. Turrel, "*Infrared and Raman Spectra of Crystals*" Academic Press London (1972).

[4] J. Frenkel Phys. Rev. 37, 17 (1931).

[5] M. Pope, C.E. Swenberg "*Electronic Processes in Organic Crystals and Polymers*" Oxford University Press (1999).

[6] F. Garnier, A. Yassar, R. Hajlaoui, G. Horowitz, F. Deloffre, B. Servet, S. Ries, P. Alnot, J. Am. Chem. Soc. 115, 8716 (1993).

[7] C. D. Dimitrakopoulos, P. R. L. Malenfant, Adv. Mater. 14, 99 (2002).

[8] M. Mas-Torrent, C. Rovira, Chem. Soc. Rev. 37, 827 (2008).

[9] J.E. Anthony, A. Facchetti, M. Heeney, S.R. Marder, X. Zhan, Adv. Mater. 22, 3876 (2010).

[10] G. Schweicher, Y. Olivier, V. Lemaur, Y. H. Geerts, Israel Journal of Chemistry 54, 595 (2014).

[11] A. Yassar, Polymer Science 56, 4 (2014).

[12] N.A. Minder, S. Lu, S. Fratini, S. Ciuchi, A. Facchetti, A.F. Morpurgo, Adv. Mater. 26, 1254 (2014).

[13] D. Haarer, M.R. Philpott, H. Morawitz, J. Chem. Phys. 63, 5238 (1975).

[14] M.R. Philpott, A. Brillante, Mol. Cryst. Liq. Cryst. 50, 163 (1975).

[15] A. Brillante, M.R.Philpott, J. Chem. Phys. 72, 4019 (1980).

[16] D. Haarer, Chem. Phys. Lett. 31, 192 (1975).

[17] J. Bernstein "*Polymorphism in Molecular Crystals*" Oxford University Press, Oxford (2002).

[18] W.C. McCrone "*Polymorphism in Physics and Chemistry of the Organic Solid State*" vol. 2, ed. D. Fox, M. M. Labes and A. Weissberger, Wiley Interscience, New York pp. 725–767 (1965).

[19] A. Gavezzotti, Acc. Chem. Res. 27, 309 (1994).

[20] M. Mas-Torrent, C. Rovira, Chem. Rev. 111, 4883 (2011).

[21] A. Brillante, I. Bilotti, R.G. Della Valle, E. Venuti, S. Milita, C. Dionigi, F. Borgatti, A. N. Lazar, F. Biscarini, M. Mas-Torrent, N. Oxtoby, N. Crivillers, J. Veciana, C. Rovira, M. Leufgen, G. Schmidt, L. W. Molenkamp, CrystEngComm. 10, 1899 (2008).

[22] R. Pfattner, M. Mas-Torrent, I. Bilotti, A. Brillante, S. Milita, F. Liscio, F. Biscarini, T. Marszalek, J. Ulański, A. Nosal, M. Gazicki-Lipman, M. Leufgen, G.Schmidt, L. W. Molenkamp, V. Laukhin, J. Veciana, C. Rovira, Adv. Mater. 22, 4198 (2010).

[23] A. Brillante, I. Bilotti, R. G. Della Valle, E. Venuti, M. Masino, A. Girlando, Adv. Mater. 17, 2549 (2005).

[24] A. Brillante, I. Bilotti, R.G. Della Valle, E. Venuti, A. Girlando, CrystEngComm. 10, 937 (2008).

[25] A. Brillante, I. Bilotti, C. Albonetti, J-F. Moulin, P. Stoliar, F. Biscarini, D.M. de Leeuw, Adv. Funct. Mater. 17, 3119 (2007).

[26] M. Ando, T. B. Kehoe, M. Yoneya, H. Ishii, M. Kawasaki, C.M. Duffy, T. Minakata, R.T. Phillips, H. Sirringhaus, Adv. Mater. (2014).

[27] D.P. Craig, J. Proc. R. Soc. New South Wales 61, 115 (1982).

[28] M. Yoshizawa, Y. Takeyama, T. Okano M. Fujita, J. Am. Chem. Soc. 125, 3243 (2003).

[29] M.D. Cohen, G. M. J. Schmidt, J. Chem. Soc. 1964 (1996).

[30] V. Ramamurthy, K. Venkatesan, Chem. Rev. 87, 433 (1987).

[31] V. Balzani, A. Credi, F.M. Raymo, J.F. Stoddart, Angew. Chem. Int. Ed. 39, 3348 (2000).

[32] V. Balzani, A. Credi, M. Venturi, "*Molecular Devices and Machines: A Journey into the Nano World*" Wiley-VCH Weinheim (2003).

[33] M. Von Delius, D.A. Leigh, Chem. Soc. Rev. 40, 3656 (2011).

[34] M. Irie, S. Kobatake, M. Horichi, Science 291, 1769 (2001).

[35] M. Garcia-Garibay, Angew. Chem., Int. Ed. 46, 8945 (2007).

[36] M. Morimoto, M. Irie, J. Am. Chem. Soc. 132, 14172 (2010).

[37] H. Koshima, K. Takechi, H. Uchimoto, M. Shiro, D. Hashizume, Chem. Comm 2011, 47, 11423 (2011).

[38] C. Weder, J. Mater. Chem. 21, 8235 (2011) and refs therein.

[39] N.K. Nath, M. K. Panda, S.C. Sahoo, P. Naumov, Cryst.Eng.Comm. 16, 1850 (2014).

[40] T. Salzillo, S. Zaccheroni, R.G. Della Valle, E. Venuti, A. Brillante, J. Phys. Chem. C 118, 9628 (2014)

[41] M. Born, T. von Karman, "*Dynamical Theory of Crystal Lattices*" Clarendon Press. Oxford (1912).

[42] M. Born, K. Huang, "*Dynamical Theory of Crystal Lattices*" Oxford University Press, New York, (1954).

[43] E. Heller, G.M.J. Schmidt, Israel J. Chem. 9, 499 (1971).

[44] T. Salzillo, I, Bilotti, R.G. Della Valle, E. Venuti, A. Brillante, J. Am. Chem. Soc. 134, 17671 (2012).

[45] D.P. Craig, P. Sarti-Fantoni, Chem. Commun. 742 (1966).

2. Instruments, experimental setup and crystal growth

2.1 Instruments

In this chapter we describe the experimental setup of the instruments used, the setup for the irradiation in the solid state and in solution and the methods for crystal growth.

The instrumentation used for the the spectroscopic measurements was: a confocal micro-Raman spectrometer Horiba Jobin Yvon T64000, a fluorescence spectrometer Edimburgh FLS920, and an FT-IR microscope Bruker Hyperion 1000.

2.1.1 The Raman spectrometer

Raman spectra were recorded with the Horiba Jobin Yvon T64000 triple spectrometer (Figure 2.1) equipped with three monochromators in double subtractive configuration. This configuration is optimized for the acquisition of Raman spectra very close to the laser line, down to a $\Delta v \approx 5$ cm^{-1}, enabling the detection of the optical phonon region.

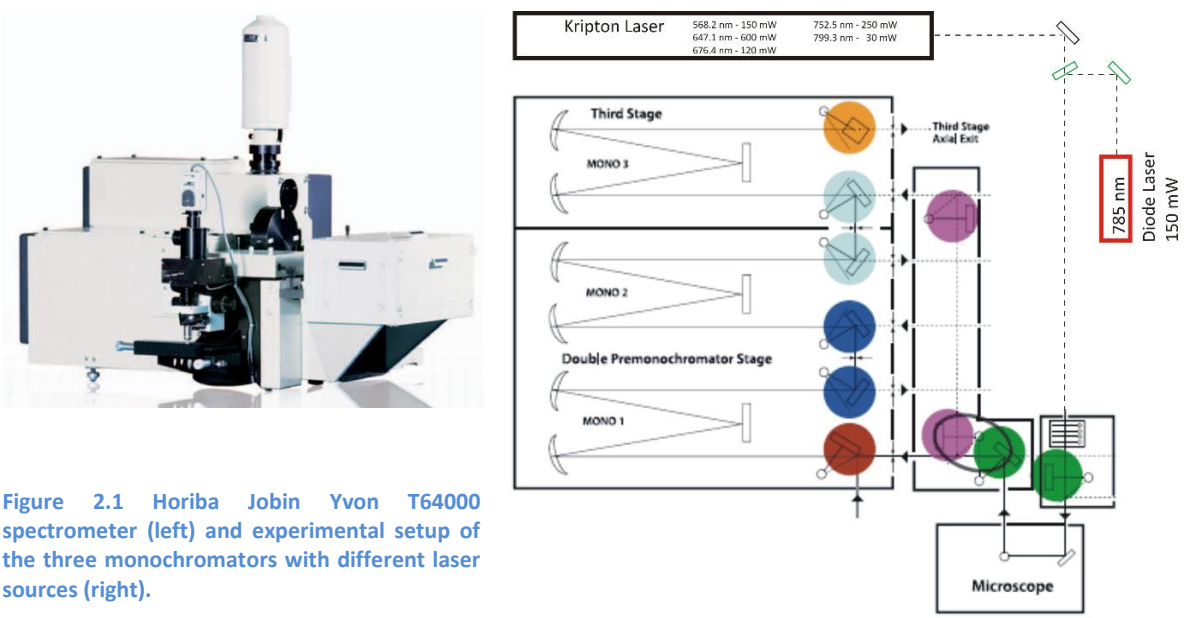

Figure 2.1 Horiba Jobin Yvon T64000 spectrometer (left) and experimental setup of the three monochromators with different laser sources (right).

The spectrometer was coupled to an Olympus BX40 microscope equipped with 100x, 50x, 20x and 10x objectives which allowed for a spatial resolution below 1 micron and a theoretical field depth ranging from about 7 to 450 µm. The spectral acquisition was done with a liquid nitrogen cooled charge-coupled device (CCD) detector, with a spectral response

in the range 500-900 nm. The excitation was from a multiline (647.1 nm, 676.4 nm, 752.5 nm and 792-799 nm) tunable Kr^+ gas laser, using mainly the laser line at 647.1 nm with a nominal power of 1 Watt. The power was reduced by neutral density filters to avoid sample damage. Besides to the gas laser, a diode laser equipped with an external cavity and tuned at 780 nm with a nominal power of 150 mW was used.

2.1.2 Fluorescence spectrometer

Fluorescence spectra of the solid samples were recorded with a FLSP920 Spectrometer by Edinburgh Instruments (Figure 2.2), equipped with a 450 Xe lamp, single emission and excitation monochromators. A Peltier cooled Hamamatsu R928P photomultiplier was used as detector. The spectral range of the instrument goes from 185 to 800 nm (detector cooled to -20 °C) and is extended to 1700 nm (detector cooled with liquid nitrogen).

With this equipment it is also possible to analyze time-resolved emissions (determination of lifetimes) recorded over the whole spectral range (UV-vis-NIR) of the instrument, by using pulsed laser sources (EPLED) or lamps for long phosphorescence.

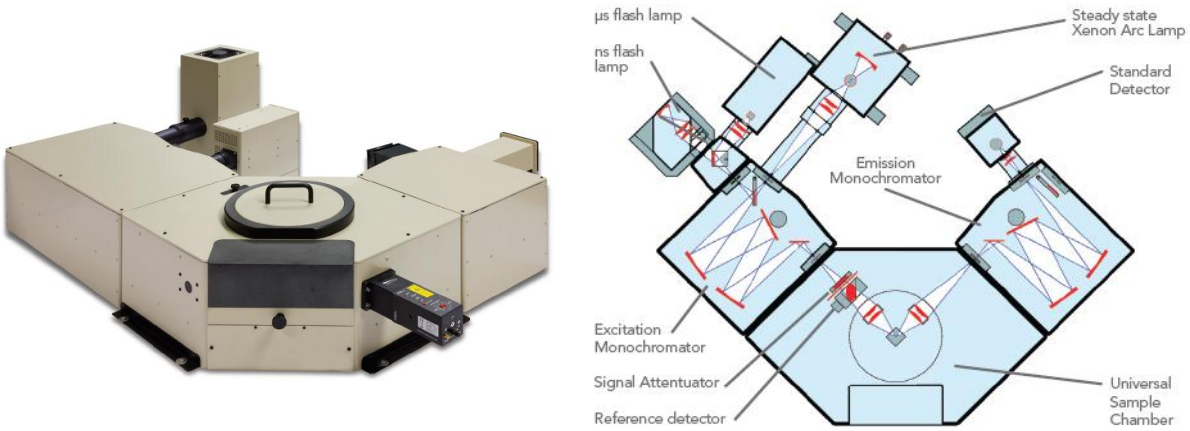

Figure 2.2 The fluorescence spectrometer (left) with its optical scheme (right).

2.1.3 FT-IR microscope

Infrared spectra of the CT crystals were recorded with a Bruker FTIR spectrometer coupled to an IR microscope Hyperion 1000. The spectrometer is equipped with a liquid nitrogen cooled Mercury Cadmium Telluride (MCT) detector. The instrument setup allows for reflection and transmission measurements and polarized spectra. The optical scheme of the spectrometer is shown in Figure 2.3.

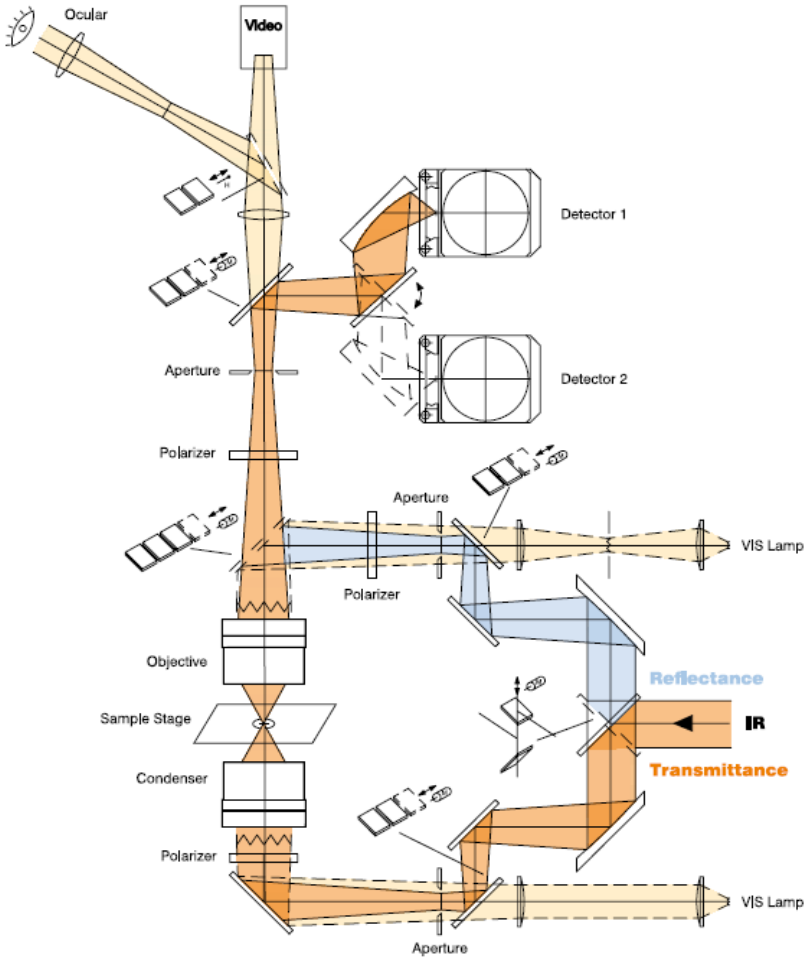

Figure 2.3 Optical layout of the FTIR micro-spectrometer.

2.2 Experimental setup of irradiation for the photochemical reactions

The absorption spectra of anthracene derivatives show the typical vibronic structure of aromatic molecules related to the electronic transitions $\pi^* \leftarrow \pi$ and $\pi^* \leftarrow n$. For this reason, sources with emissions in the UV-Visible range have been used for the irradiation of the crystals.

The irradiation in solution was done with an air cooled 250 Watt Xenon lamp (XBO) in vertical configuration (Figure 2.4) and under nitrogen flux to avoid oxidation of the samples [1]. The irradiation of the samples in the solid state was done with a water cooled Xenon lamp in horizontal configuration (Figure 2.5) and with a nominal power of 75 Watt. In both setups the broad-band Xenon emission was selected with a glass filter (UG11) to obtain a specific wavelength range between 250 and 400 nm. A pyrex glass was chosen to exclude the radiation below 300 nm. Indeed, anthracene derivatives usually show a reversible reaction by excitation

below 300 nm or by heat. A water filter was introduced in the optical path to prevent heating of the crystals.

Figure 2.4 Optical configuration for the irradiation in solution.

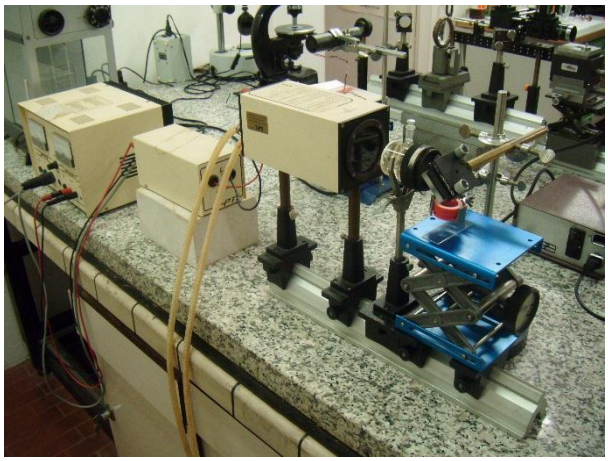

Figure 2.5 Optical configuration for the irradiation of single crystals with the Xenon lamp.

The irradiation of single crystals was also performed by using a monochromatic source from a diode laser tuned to 405 nm with a nominal power of 25 mW. Using laser excitation allowed us to select a specific area of the sample for irradiating with a focused or defocused beam. Variable optical density filters were used to attenuate the laser power and the beam was focused on the sample with a home-made microscope (Figure 2.6). A suitable setup was assembled for irradiation of the crystals at high pressure (Figure 2.7) in a diamond anvil cell (DAC).

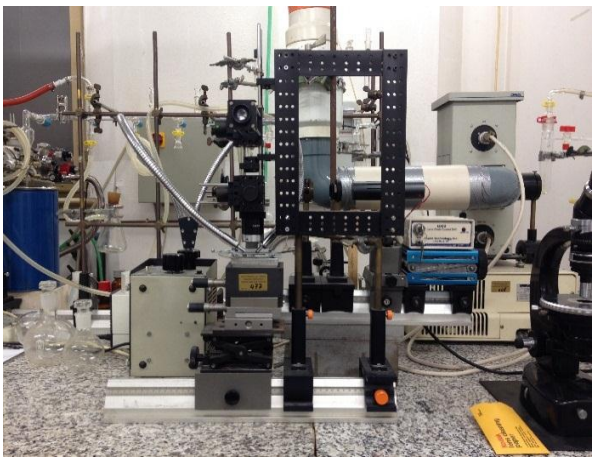

Figure 2.6 Optical configuration for the irradiation of the crystals with the diode laser.

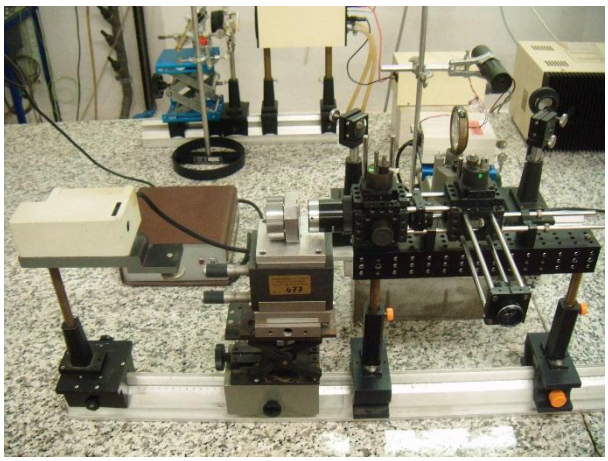

Figure 2.7 Optical configuration for the irradiation of the crystals in a DAC.

2.3 Single-crystal growth of molecular organic materials

A relevant part of the work of this thesis concerns with the application of growth techniques for organic single crystals. In fact, obtaining suitable, pure samples of organic materials is highly important for the determination of the intrinsic physical properties of organic semiconductors and of the reaction behavior in solid state photoreactions. The issue becomes even more important when the goal is the formation of mixed crystals of controlled stoichiometry, such as those described in Chapter 5.

The low melting temperatures, the high vapor pressures and the good solubility of the organic compounds in several organic solvents make these materials suitable candidates both for solution and gas phase growth methods. High quality crystals can be often obtained in different ways. The final choice is, of course, dependent on the nature of the individual molecule and on the specific interactions in the condensed matter of each system. In a general approach to the problem, solution growth methods are selected for materials with very low decomposition and melting temperatures in atmospheric conditions, whereas crystals of materials with high vapor pressures but unstable at high temperatures in oxygen can be grown from the gas phase at low pressures of inert gases [2].

As already mentioned, special efforts have been devoted to obtain binary crystalline systems with interesting properties for applications in organic electronics. These systems are formed by a pair of acceptor-donor charge transfer compounds and may show a wide range of different physical properties showing semiconducting, conducting, and even superconducting or reacting behaviors. The crystal growth methods for such mixed materials are, of course, similar to those for the pure compounds. However, their phase diagrams, polymorphism, stoichiometry and melting properties are still not well understood and, consequently, the outcome of the growth might be, in many cases, unknown. For this reason, the definition of a growth protocol is an important step to assure the reproducibility of the whole process.

In this chapter, solution, gas-phase, and melt-growth methods for organic pure and mixed single crystals employed in this work are described and discussed.

2.3.1 Method of Solvent Evaporation

Many organic compounds are well soluble in organic solvents over a wide range of temperatures and pressures, and therefore the solvent evaporation method [2] is often used to obtain single crystals suitable for XRD structure analysis.

When the saturated solution of a poorly volatile organic material in an organic solvent (commonly used solvents are dichloromethane, chloroform, ethanol and methanol) is left to evaporate, the system reaches slowly super-saturation conditions, in which crystal nucleation starts spontaneously and, where the process is slow (Figure 2.10a), the initially formed seeds can ripen into larger crystals. The main variables of the growth are the different solubility of the compound and the different volatility of the solvent. To obtain crystalline films of organic compounds with good solubility, the drop casting method can be used, in which a drop of solution is cast and let to dry on a solid substrate such as glass or silicon wafer (Si/SiO_2). As some solvents have high volatility, their evaporation rate can be controlled by covering the sample with a holed cap when the formation of large single crystals is needed.

2.3.2 Method of Solution Slow Cooling

The solubility of organic compounds may increase considerably as a function of temperature and this can be exploited to reach saturation conditions [2], with more dissolved materials, at high temperature. By subsequently decreasing the temperature, the solubility also decreases slowly (Figure 2.10b in paragraph 2.3.5). Deposition of new material tends to occur in the seeds already present at the bottom of the container, which grow to form large single crystals. Ostwald ripening [3,4] can be achieved by moving slightly and repeatedly the temperature above and below the saturation point. Smaller crystals would then dissolve and their material can redeposit onto the larger crystals which therefore keep growing.

2.3.3 Method of the Floating-drop (FD)

When placing a drop of a solvent on the surface of another liquid (liquid substrate), immiscible with the former, two different behaviors can be observed: 1) the drop spreads over the substrate covering its surface or 2) the drop takes the shape of a lens on the surface [5]. The different behaviors are thermodynamically described by the spreading coefficient *S,* defined as $S = \gamma_1 - \gamma_2 - \gamma_{12}$. Here γ_1, γ_2 and γ_{12} are the surface tensions of the liquid substrate, of the solvent and of the substrate/solvent interface, respectively. For $S < 0$ the drop forms

the lens on the substrate surface; the case with S > 0 corresponds instead to the optimal spreading of the solvent on the entire substrate surface.

The first treatment of the physics of layers of solvent on water surfaces is by Langmuir [6], and it was found that the thickness of the lens, for $S < 0$, assumes a limiting value at equilibrium which is function of the physical properties of the two liquid phases:

$$t_\infty^2 = -2S\rho_1/g\rho_2(\rho_1 - \rho_2)$$

Here ρ_1 and ρ_2 are the densities of the liquid substrate and solvent, respectively, and g is the gravity acceleration. A sketch of the system described by Langmuir is shown in Figure 2.8.

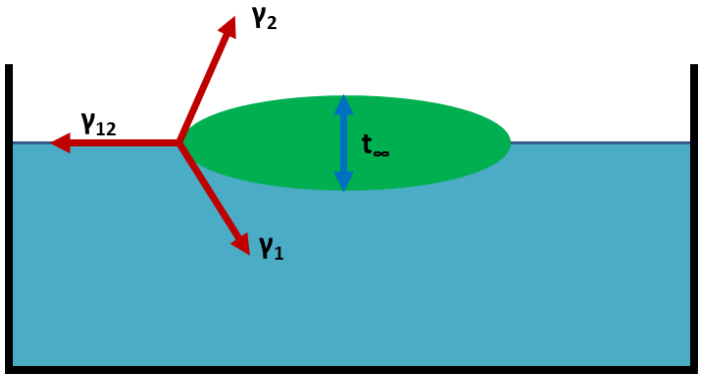

Figure 2.8 Lens floating on the liquid surface described by Langmuir [6].

In the FD method a drop of the solution containing the material to crystallize is placed on the substrate surface and is left to dry slowly. At the beginning of the process, if the concentration of the material in the solvent is low, the system can be described as formed by the substrate and the pure solvent, and the geometry of the lens can be estimated. To grow good quality flat face crystals is necessary to have a flat interface between the two liquids, and this implies minimizing t_∞, condition which is achieved, given water as a liquid substrate, with a solvent of very low surface tension γ_2 and density ρ_2 much lower than the water density.

During the evaporation of the solvent the concentration of the material dissolved increases and the lens geometry may change, either because of the increase of the solution density, or of the possible decrease of the surface tension γ_2 of the solution and, consequently, of the interfacial tension at the solution/water interface.

The first effect is not found to play a relevant role, while in most cases the lens diameter remains constant during the evaporation while the thickness decreases progressively, thus showing that the second effect is at work.

Water, used in the course of our experiments, is usually a good substrate, since after the complete evaporation of the solvent, the crystals of the organic material can be recovered floating on the surface, due to the high surface tension of the liquid substrate. However, the low density of water prevents the use of several common solvents. Clearly, the control of the nucleation and of the thickness of the crystals is given by the suitable combination of substrate and solvent.

2.3.4 1D and semi-2D Organic Nanostructures Method of Growth

In this method, described in details in a number of recent papers [7-9] and illustrated in Figure 2.9, nanostructures can be prepared by injecting under vigorous stirring a small volume of the solution of the organic compound (a) into a poor solubility medium like water, so to gain quick super-saturation of the organic compound in the new environment (b) [7]. To interpret the result of this crystallization process, it has been suggested that in the first step the nucleation proceeds *via* the formation of stable nuclei, together with some tiny meta-stable aggregates (c). Directional interactions such as dipole-dipole interactions will act as the driving force for the process of crystal growth, which results in an isotropic molecular stacking. Under stirring, the meta-stable aggregates would dissolve and transform to yield crystallites which grow preferentially along the orientation of the directional interactions.

The mixture is finally left undisturbed for the time needed to allow the crystal growth and at this stage the size of the crystals increases. Thus the crystals become more stable, while the solubility in the solvent limits the rates of growth and dissolution (d).

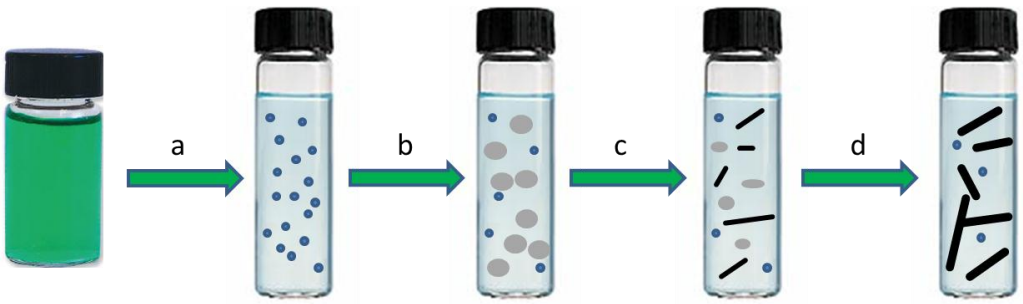

Figure 2.9 Schematic proposed mechanism [7] for 1D and semi 2D nanostructure crystal growth method.

2.3.5 Liquid-liquid diffusion method

The organic compound will dissolve well in certain solvents (“good” solvents) but not in others (“poor” solvents or anti-solvents). This method [2] exploits the different solubility of the material in two solvents, which must be co-miscible and have different densities. The compound is dissolved in the “good” solvent to form a saturated solution and then is placed in a schlenk tube. The “poor” solvent is let flow slowly on top of the saturated solution if less dense of it, or collected at the bottom of the container when the opposite applies, in such a way that two distinct layers are formed as shown in Figure 2.10c. With time the poor solvent diffuses into the solution, yielding an interface mixture in which the solubility of the compound is lower than that in the pure “good” solvent. As a result, crystal formation takes place in the boundary liquid-liquid region.

Care must be taken to achieve the stratification of the two solvents one on the top of the other, to allow for the formation of a clear and distinct interface, in such a way that the mixing of the two liquids occurs only by diffusion. By controlling the temperature of the system, saturation conditions can be changed, and the crystal growth influenced.

A solvent system commonly used for layering consists of a combination of dichloromethane and ethanol. Other successful combinations employ chloroform or dichloromethane together with diethyl ether or a hydrocarbon.

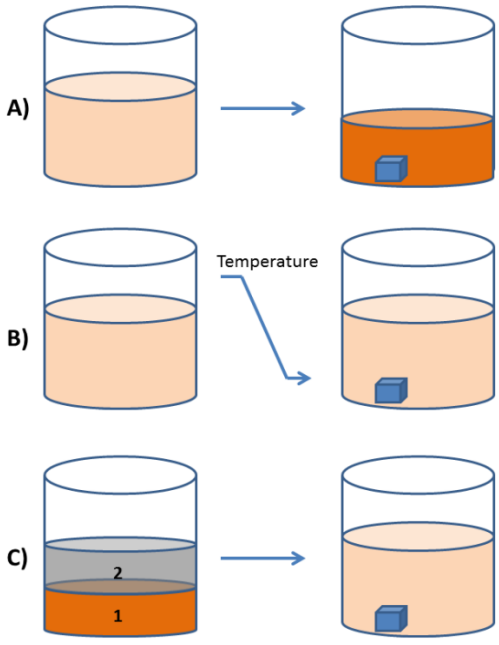

Figure 2.10 Solution-based methods for the growth of organic single crystals [2].

2.3.6 Melt growth method

Crystal growth techniques from the melt are used most frequently for inorganic compounds, characterized by high stability at high temperature and very low vapor pressures. However, also crystals of organic compounds such as anthracene, naphthalene, pyrene and diphenylanthracene can be grown in this way, because these compounds are pretty stable up to the melting point even though they may decompose or react under long term treatment. Large and high quality single crystal can be obtained for several materials, suitable for physical and optical properties studies. It is often necessary to work in controlled atmosphere conditions to avoid oxidation processes or evaporation of the material due to its high vapor pressure [2].

2.3.7 Vacuum sublimation method

Sublimation processes employ the solid-gas equilibrium, and therefore must take place at low pressures and relatively high temperatures. At high temperatures of the sublimation chamber, the crystal growth at the cold end may result into too fast a process, yielding twinned or statically disordered crystals. Good quality crystals by this method can be obtained playing on the *p*,*T* conditions, that is, decreasing the temperature of the process by decreasing the pressure of the system. There are numerous variations of the technique, which employ either static or dynamic vacuum environments. In the case of static conditions, a small amount of sample is placed under vacuum in a Pyrex tube (Figure 2.11) and the material is heated up from the bottom. The crystal grows on a water cooled cold end at the top of the pyrex tube.

This setup produces good quality crystals in hours or possibly weeks, depending on the volatility of the sample and the quality of the vacuum. Vacuum sublimation is also ideal for compounds with low vapor pressure or which are very air sensitive, as the tubes can be loaded in dry boxes, or when the low solubility of the material prevents the crystal growth by any solution method.

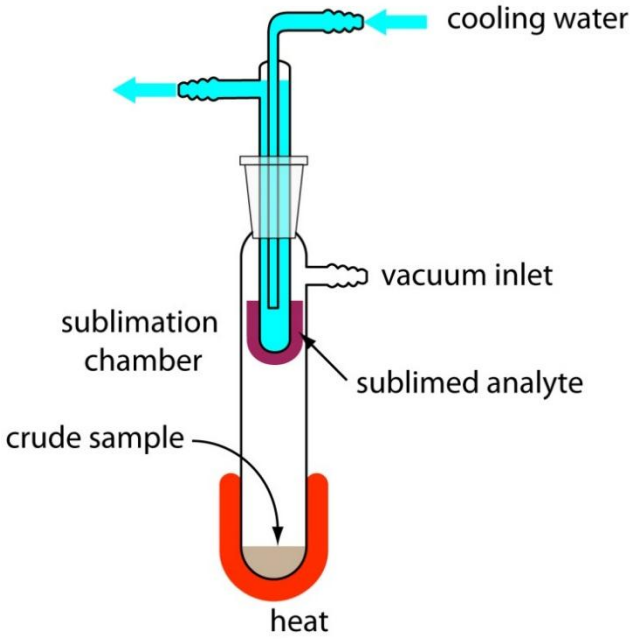

Figure 2.11 Sublimation experimental setup.

2.3.8 Physical vapor transport (PVT) method

PVT is a crystal growth technique [10] which belongs to the gas-phase methods and therefore works with physical principles which are the same as those of the vacuum sublimation method. A scheme of the experimental setup is shown in Figure 2.12.

Crystal growth from vapor phase can be divided in chemical vapor transport (CVT), which is common for the growth of inorganic compound using a chemical transport agent like iodine, and physical vapor transport (PVT) which is instead used for organic materials. In general, this method uses an ampoule sealed under vacuum, at the two ends of which different temperatures are applied, so that the compound inside moves under the resulting temperature gradient [10].

The ampoule is filled with the polycrystalline material, sealed after being evacuated in inert atmosphere, typically nitrogen or argon, and then horizontally placed in a two temperature zones furnace. The ampoule end with the material lies in the high temperature zone, whereas the other end of the ampoule, where the crystals are going to grow, is maintained at a lower temperature. The source material sublimes at the hot end and the temperature gradient causes super-saturation, resulting in the deposition of the vaporized compound at the cold end. The method is suitable for the preparation of high purity crystals,

since a purification process takes place during the growth, and it is very effective for the preparation of mixed single crystals, obtained starting from mixed source materials. As a result of the different conditions of super-saturation of the various compounds, mixed crystals of different stoichiometry may be deposited along the direction of the temperature gradient.

The vapor phase in the ampoule moves by buoyant convection motion, driven by the applied horizontal temperature gradient. Convection in horizontal cavities, as reported in Ref. [10], has been studied by Simpkins and Chen [11], who estimated the magnitude of this phenomenon using the two-dimensional Handley cell model. In such a tube with a horizontal *T* gradient the Handley equation yields a velocity profile described by a cubic function of the depth. Applying hot temperature on the left end, the motion will take place from left to right on the upper part of the ampoule and reverses in the lower part. Simpkins and Chen gave the expression of the maximum velocity μ':

$$\mu' \propto \frac{R}{L}$$

Where L is the aspect ratio, length for gradient/tube diameter (≈ 6) [11], and R is the Rayleigh number defined as:

$$R = \frac{g\ \beta\ \Delta T\ d^3}{\nu\ k}$$

where g is the gravitational constant, β is the thermal expansion coefficient [12], k the thermal diffusivity [12], d is the tube diameter and ΔT is the maximum temperature difference. The maximum velocity, using the principal carrier gases such as Argon (R = 51800), Helium (R = 1120) and Nitrogen (R = 64660), which we used for our experiments, are 14, 1.6 and 12 cm/s, respectively, *i.e.*, are substantially larger than the velocity given by forced convection flow in ampoules with gas inlet. The circulation flow for a closed system is therefore shown in the Figure 2.12, entirely determined by buoyant convection. It is important to say that the above described model is a the result of a simplified system where are not considered several factor like local temperature gradients and three dimensional aspects which are well described by Rosemberger and coworkers [13]. From an experimental point of view, large high quality crystals are obtained when the maximum gradient ΔT is small (around 25°C) and the high

temperature is only slightly higher than the sublimation temperature of the compound at the pressure of the experiment.

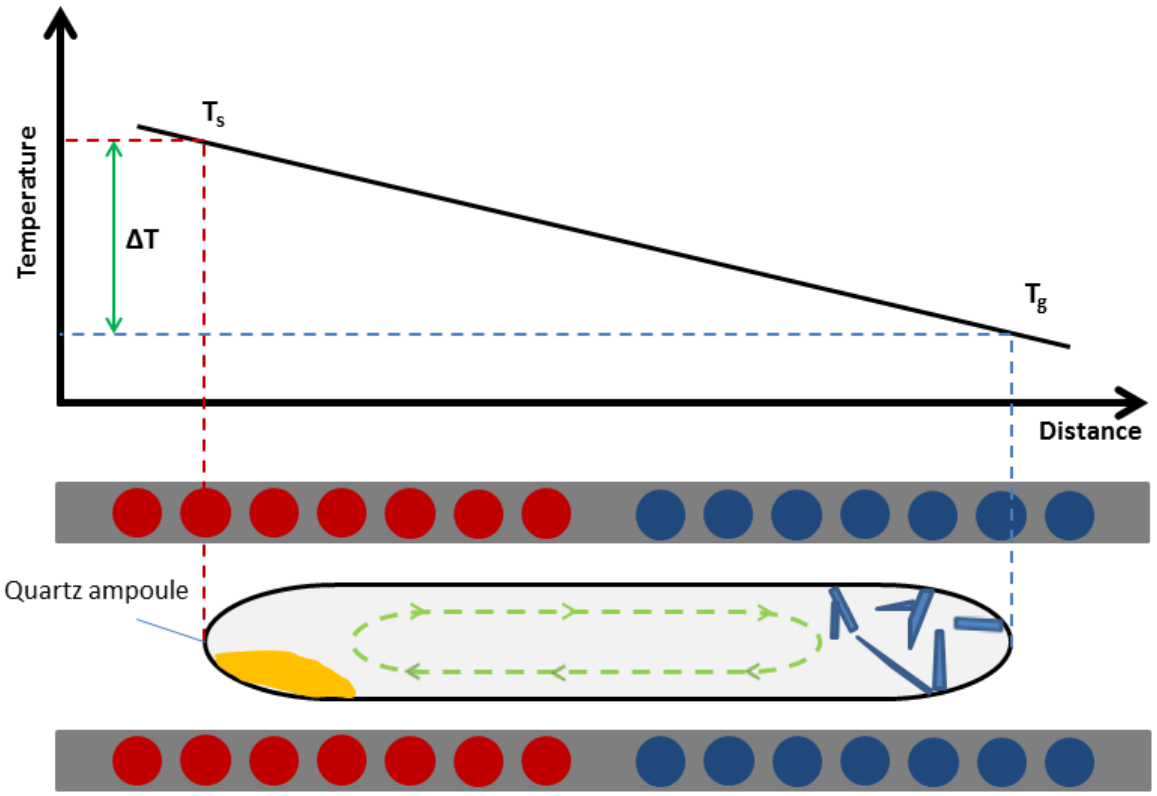

Figure 2.12 Scheme of the ampoule in the two zone temperatures furnace and circulation pattern of the compounds in the gas phase.

References

[1] A.Mallakin, D. G. Dixon, B. M. Greenberg. Chemosphere 40, 1435 (2000).

[2] H. Jiang, and C. Kloc, MRS Bulletin 38, 1, 28 (2013).

[3] W. Ostwald. *Lehrbuch der Allgemeinen Chemie 2*, part 1, Leipzig, Germany.

[4] W. Ostwald, Zeitschrift für physikalische Chemie 22, 289 (1897).

[5] M. Campione, R. Ruggerone, S. Tavazzi and M. Moret, J. Mater. Chem. 15, 2437 (2005).

[6] I. Langmuir, J. Chem. Phys. 1, 756 (1933).

[7] X. Zhang, X. Zhang, B. Wang, C. Zhang, J. C. Chang, C. S. Lee, and S. T. Lee, J. Phys. Chem. C 112, 42, 16264 (2008).

[8] X. Zhang, G. Yuan, Q. Li, B. Wang, X. Zhang, R. Zhang, J. C. Chang, C. S. Lee, and S. T. Lee Chem. Mater. 20, 22, 6945 (2008).

[9] X. Zhang, X. Zhang, K. Zou, C. S. Lee, and S. T. Lee, J. Am. Chem. Soc. 129, 12, 3527 (2007).

[10] R. A. Laudise, C. Kloc, P. G. Simpkins, T. Siegrist, Journal of Crystal Growth 187, 449 (1998).

[11] P. G. Simpkins, K. S. Chen, Journal of Fluid Mechanics 166, 21 (1986).

[12] C. Kloc, P.G. Simpkins, T. Siegrist, R. A. Laudise, Journal of Crystal Growth 182, 416 (1997).

[13] F. Rosemberger, J. Ouzzani, I Viohl, N, Buchan, Journal of Crystal Growth 171, 270 (1997).

3. Solid state photoreactions

Materials capable to change their shape under the external stimulus of light, open the new exciting field of mechanically responsive single crystals, with potential applications in a number of active devices where energy interconversion occurs at molecular level. The search of photoreactions in the solid state, capable to exploit at best the amount of potential energy developed during the progress of the reaction, becomes a challenge of crystal engineering when designing a solid state reaction in which the change of the chemical identity of the reactant must also involve the adjustment of the structure of the lattice. A topochemical perspective of the crystal packing usually helps the selection of suitable reactant candidates to drive their transformation in the solid state.

This chapter of the thesis describes a selection of crystal to crystal photoreactions with the purpose to show the large variety of cases that can be encountered when photochemistry meets the solid state.

The first example, section 3.1, deals with the remarkable transformation of dinitro-antracene (DNO_2A) to anthraquinone (AQ), where the stunning acrobatics of the entire single crystals mark a significant relationship between molecular (chemical) changes and unit cell (physical) change.

Section 3.2 shows the classical example of the photodimerization reaction of 9-cyano-anthracene (9CNA), the typical case of violation of the topochemical principle, whose paradigm implies the molecular preformation of the product in the unit cell of the reactant as strict prerequisite for the positive outcome of the dimerization.

In section 3.3, the dimerization of 9-methylanthracene (9MA) is indeed the classical case of a perfect structural fit which leads to a complete topochemical reaction.

The last section, 3.4, discusses the intriguing issue of 9-anthracene-carboxylic acid (9ACA) as a different case of a reversible photodimerization where crystal mechanical motions are not sufficient to validate the successful outcome of the reaction.

For our investigation, we have used the novel approach of following the reaction by means of lattice phonon Raman microscopy, a technique which easily probes inter-molecular modes, *i.e.*, collective translational or rotational motions of the molecules in the unit cell, to directly follow the solid state transformation of the unit cell of the reactant in that of the product.

3.1 Photoreaction of 9,10-dinitroanthracene to anthraquinone.

The first subject of this chapter is the crystal-to-crystal photochemical reaction of 9,10-dinitroanthracene (DNO_2A) to anthraquinone (AQ) + 2NO. The reaction, has been observed since long time in solution [1] and its mechanism has been more recently revisited [2]. In the solid state this reaction reveals intriguing aspects, since its path requires a striking modification of the crystal lattice, starting from the triclinic structure of DNO_2A, with one molecule per unit cell (Z = 1), to yield the monoclinic structure of AQ with Z = 2. This involves a considerable change of the chemical environment, which implies the use of sensitive probes of intermolecular interactions. We have then used the approach of following the reaction by means of lattice phonon Raman microscopy [3], a technique which directly probes even slightly differences of molecular packing, becoming the ideal tool to monitor changes in the unit cell structure. The additional feature of working in confocal microscopy, has allowed us to follow the evolution of the photoreaction *in situ*, with a Raman signal at a spatial resolution below 1 μm, in order to compare crystal and molecular spectral changes with the optical images of the sample. While the analysis of the lattice modes allowed for the study of the physical changes (lattice dynamics), the chemical transformation was monitored by measuring the intra-molecular Raman-active modes of both, reactant and product, on the very same spot at the same time.

The experiments show that, once triggered, the reaction rapidly proceeds up to a complete transformation to the product. The change in crystal morphology strongly depends on the different conditions of irradiation and on the sample history. In any case, at the macroscopic level, we have detected an impressive relationship between incident light and mechanical strain, which manifests as striking bending and unfolding of the specimens under irradiation. In order to clarify the mechanism underlying the relationship between incident photons and molecular constraints, we have extended the study to high pressure, up to 2 GPa. It was found that above 1 GPa the photoreaction becomes inhibited.

Lastly, lattice dynamics calculations based on standard intermolecular potential models have been employed to simulate the reaction steps transforming the initial unit cell of DNO_2 into the final AQ lattice.

3.1.2 Experimental details.

Single crystals of DNO_2A from Aldrich were grown by sublimation, obtaining in most cases needles elongated along the *a* axis.

Raman spectra were obtained by placing the sample on the optical stage of a microscope (Olympus BX40) interfaced to a Jobin Yvon T64000 Raman spectrometer, with 50x or 100x objectives, which allowed us to obtain a spatial resolution just below 1 μm and a *theoretical* field depth from about 7 to 25 μm. Raman spectra were recorded by excitation from a krypton laser (647.1 nm), an energy sufficient low to avoid background fluorescence from the sample and its possible photochemical side products. The laser power was adjusted in every experiment to prevent crystal damage. The actual power focused on the sample was always less than 1 mW. For more details on the spectroscopic characterization see ref. [3].

Two different procedures were followed to irradiate the crystal, *i.e.*, broadband and laser excitation. For the former, a 75 W Xe lamp was used and the spectral range 250-400 nm was selected with a glass filter. Laser excitation was produced by a 25 mW diode laser tuned at 405 nm.

High pressure measurements were performed with a sapphire windows cell for pressure up to 1 GPa, and a diamond anvil cell above 1 GPa. A 4:1 methanol-ethanol solution was used as hydrostatic medium and the ruby luminescence method was used for pressure calibration [4].

3.1.3 Results.

3.1.3.1 Lattice phonon Raman spectra.

In order to follow the photoreaction we first collected, as a reference, the data of pure reactant and product. The lattice phonon Raman spectra at ambient (*p*,*T*) of DNO_2A and AQ of the actual samples used in the experiments are reported in Figure 3.1. Both agree with data from literature [5,6].

The crystal structure of DNO_2A is triclinic $P\bar{1}$ (C_i^1) with one molecule per unit cell [7]. Since Z=1, only three ***k***=0 optical lattice phonons are expected and are of A_g symmetry, *i.e.*, Raman-active [8]. They all show up in Figure 3.1. The crystal structure of AQ is monoclinic $P2_{1/a}$ (C^5_{2h}) with two molecules per unit cell [9]. Since Z=2, nine ***k***=0 optical lattice phonons are allowed and six of them ($3A_g+3B_g$) are Raman-active. Five out of six [6] are shown in Figure 3.1.

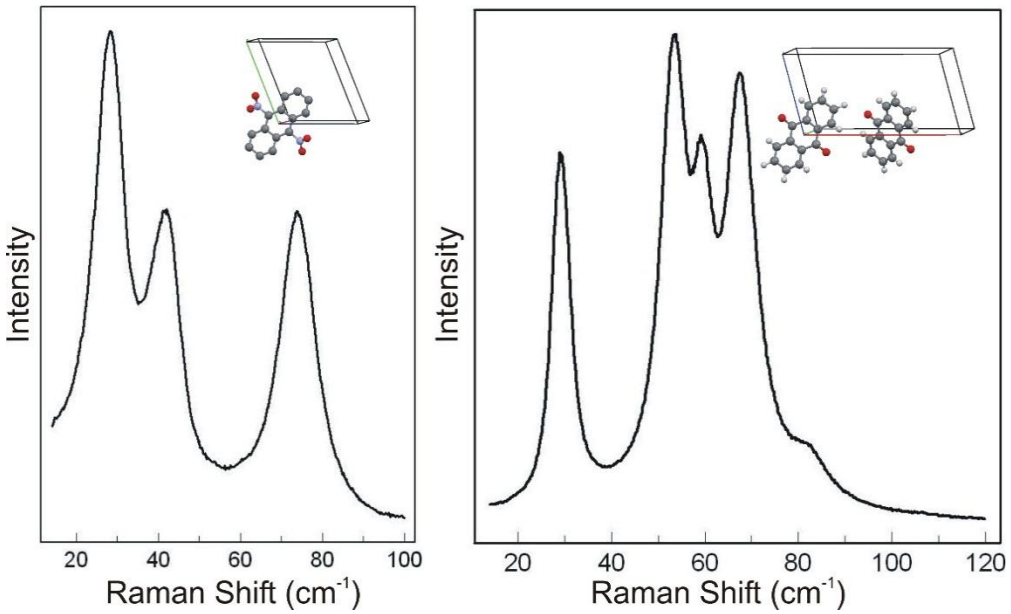

Figure 3.1 Lattice phonon Raman spectra of DNO_2A (left) and AQ (right). In the inset the corresponding molecules in the unit cell are reported.

3.1.3.2 The crystal to crystal photoreaction.

Although studied in solution, no reports can be found in the literature of this reaction in the solid state. Once the reaction is performed by photo-excitation of the crystal, the initial step, following light absorption, is the localization of the exciton in active sites, usually physical traps, which act as nucleation centers for the propagation throughout the entire crystal. In this sense a solid state photoreactions can be classified as cooperative. Selectivity and localization are then the dominant factors of the process [10].

A collective propagation of the excited reactant molecules into the product must necessarily follow the rule governing ordered systems, that is, a topochemical principle or the capability of the molecules to be in the correct registry to yield the product with a minimum of orientational reconstruction. Crystal packing, in other words, owns already the capability of determining the chemical change produced by the incoming light.

Our study is described with reference to three experimental setups: (i) broadband excitation from a UV lamp focused on the crystal; (ii) excitation from a diode laser (λ = 405 nm), with and without focusing; (iii) laser excitation in high pressure cells (0-2 GPa). A number of samples have been treated. The main results are illustrated in the following sections.

3.1.3.3 Broadband excitation

Single crystals of DNO_2A have been irradiated by a Xe lamp (luminous emittance 350 lx) with excitation in the range 250-400 nm selected by a glass filter. A water filter was placed

in the optical path to prevent sample heating. Lattice phonon Raman spectra have been recorded as a function of time to follow the photoreaction. The UV light was focused on one end only of the crystal, in order to compare reacted and un-reacted regions on the same specimen. Figure 3.2 shows the Raman spectra collected at regular time intervals together with the picture of the sample with the indication of the area tested. As a reference, the phonon spectrum of pure AQ, the photoproduct, is reported at the top of the spectra. After only two minutes, a marked color difference was observed between the two ends of the samples. Correspondingly, Raman profiles of the illuminated region (left side of the figure) show the fast growth of AQ lattice phonons which initially overlap the phonon bands of the starting DNO_2A crystal and eventually fully replace them. The right side of the figure shows instead the unchanged spectrum of the DNO_2A in the region of the sample not subjected to irradiation. The reaction quickly proceeds up to its completion after only 4 minutes. The phonon spectrum of the photoproduct shows a large noise and broader bands with respect to those of a pure pristine single crystal AQ (red trace in Figure 3.2). This can be accounted for by the inhomogeneuos broadening induced by local disorder of the irradiated regions.

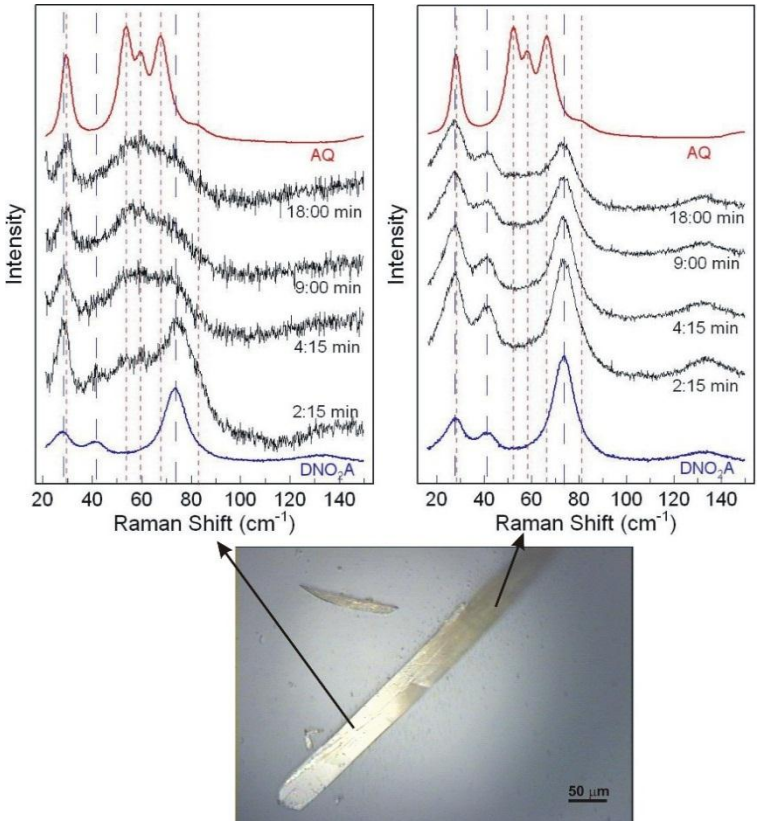

Figure 3.2 Lattice phonon Raman spectra of an irradiated (left) and non irradiated (right) region of a DNO_2A single crystal whose picture is reported at the bottom. In the upper part of the figures the spectrum of the single crystal of AQ is reported in red as reference.

3.1.3.4 Laser excitation

A focused beam from a diode laser tuned at 405 nm (radiative flux 340 W/cm^2), unfailingly produced an immediate and explosive breaking of the crystal. The experiments were then performed with a series of variable optical density filters to attenuate the incoming light up to three order of magnitude, which also resulted in scaling up the time required to get the completion of the reaction in the order of hours. Results are reported in Figure 3.3. Although slower, the modification of the lattice occurs with a gradual change of the whole phonon spectrum from the lattice modes of pure crystalline DNO_2A to those of pure AQ. The optimal control of the reaction can also be deduced by the lack of background fluorescence, whose presence would certainly have been an indication of the formation of side photoproducts acting as impurity traps. The pictures of the crystal at the right side of the figure show that in any case, although less dramatically, the crystal, initially long a few hundreds of μm, breaks up in a number of fragments at the end of the reaction (t = 530 min). The large mechanical strain, which starts in the middle point of crystal where the laser beam was focused, produces this destructive process. The post analysis of the Raman spectra of these fragments indicates that they belong to pure AQ (upper spectrum of the Figure), an evidence that the reaction had indeed reached its full completion. Unlike the spectra of Figure 3.2, all phonon bands are now well resolved with an excellent signal to noise ratio.

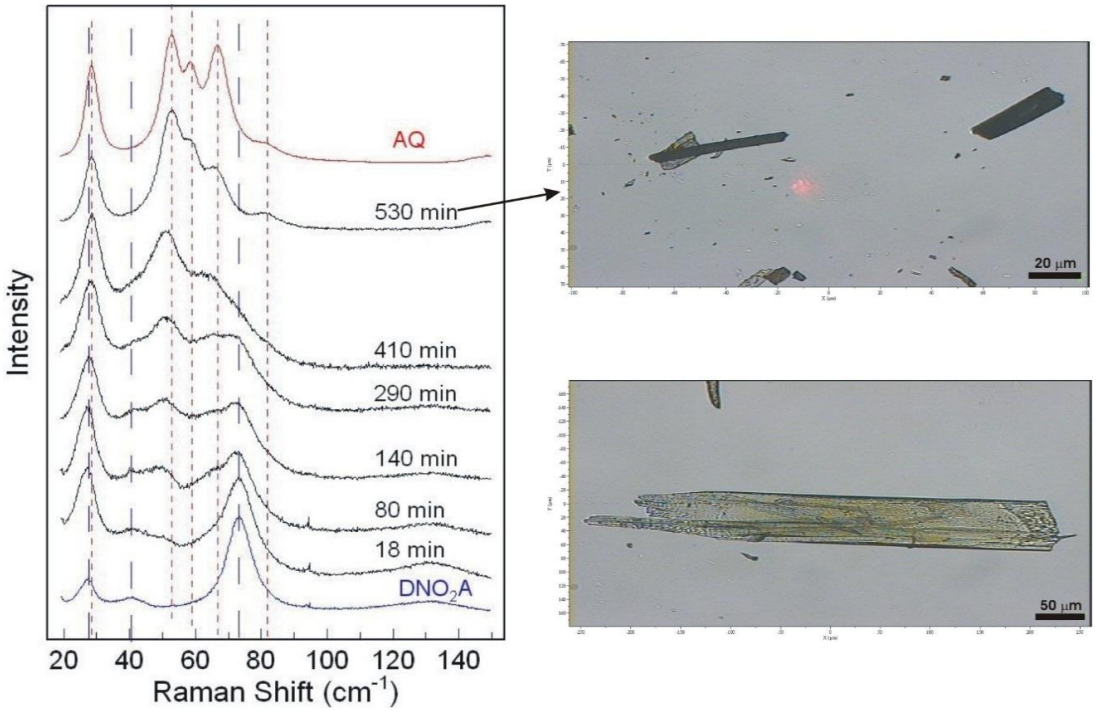

Figure 3.3 Lattice phonon Raman spectra of a DNO_2A single crystal as a function of time after irradiaton from a focused laser at 405 nm. In the right side, the pictures of the crystal before (lower picture) and after (upper picture) the photoreaction are shown.

To avoid the fragmentation of the crystal we defocused the laser beam on the crystal surface to get a more uniform irradiation (radiative flux $3x10^{-2}$ W/cm^2), an expedient also used to control the interfacial strain in the photodimerization of 9-anthracene-carboxylic acid [11]. Under these conditions, the mechanical deformation of the crystal during the progress of the reaction is homogeneously distributed over the entire size of the crystal, avoiding its destructive fragmentation. In other words, the macroscopic boundaries of the crystal, edges and surface, act to soften the strain produced by photons. However, the most intriguing and spectacular results obtained under these experimental conditions are shown in Figure 3.4.

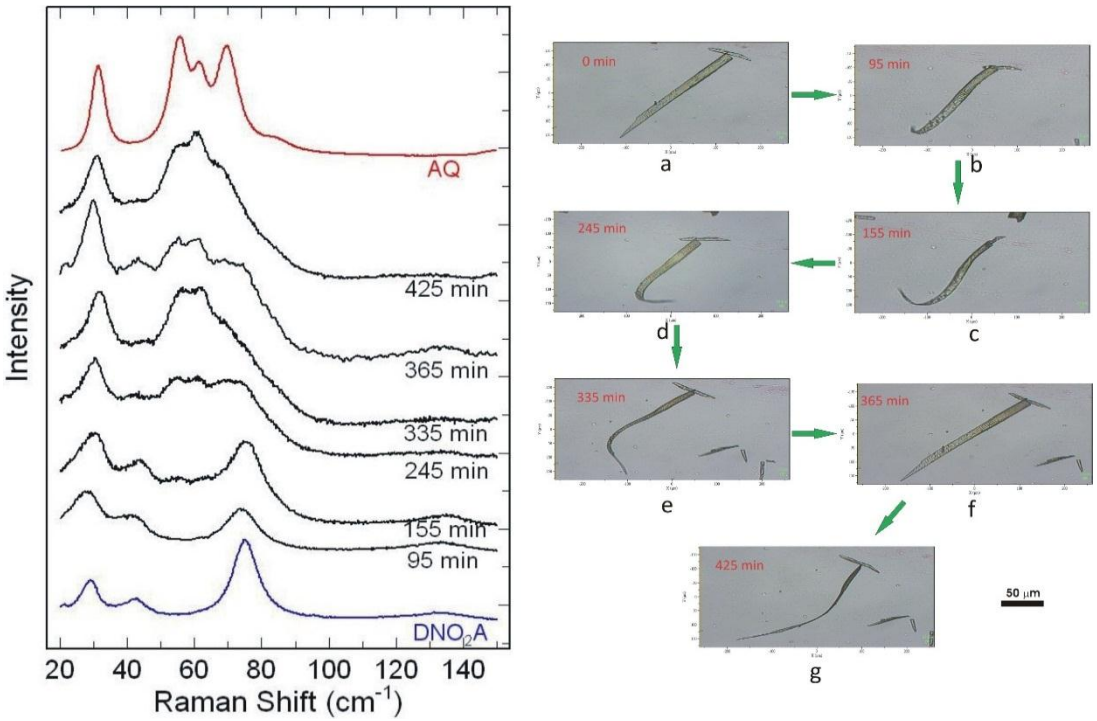

Figure 3.4 Left: lattice phonon Raman spectra of a DNO_2A single crystal as a function of time under uniform irradiaton from a defocused laser beam. Right: snapshots, at the corresponding times, of the irradiated crystal during the course of the reaction.

Here the photoreaction reaches its completion pretty much in the same time scale as that of the previous experiment, where, though strongly attenuated, the laser beam was focused on the crystal. However, in this case the crystal avoids breaking into smaller fragments, but undergoes, under irradiation, a striking series of mechanical movements, which manifest as bending, twisting and unfolding, as shown in the right side of the figure. The well shaped single crystal (a) initially bends, especially at one of its end (b-c), then rotates by 180° along its long axis to reach, after unfolding (d) and further twisting (e), its initial shape (f). At this stage, the transformation is not yet complete, as indicated by the spectral profiles after 365 minutes, where residual phonon bands of DNO_2A lattice are persisting. The final

step, up to the complete formation of AQ, requires a new and fast deformation of the crystal (g) which eventually leads to pure AQ, whose lattice phonon bands undergo some inhomogeneous broadening, as shown by the congested region around 60 cm^{-1}. The different spectral distribution of phonon bands with respect to that of the reference crystal can be accounted for an anisotropic effect determined by a reorientation of the crystal after irradiation. Similar trends have been observed for other crystals of approximately the same shape and size. A more detailed series of snapshots of the spectacular behavior of this reaction is documented in Figure 3.5.

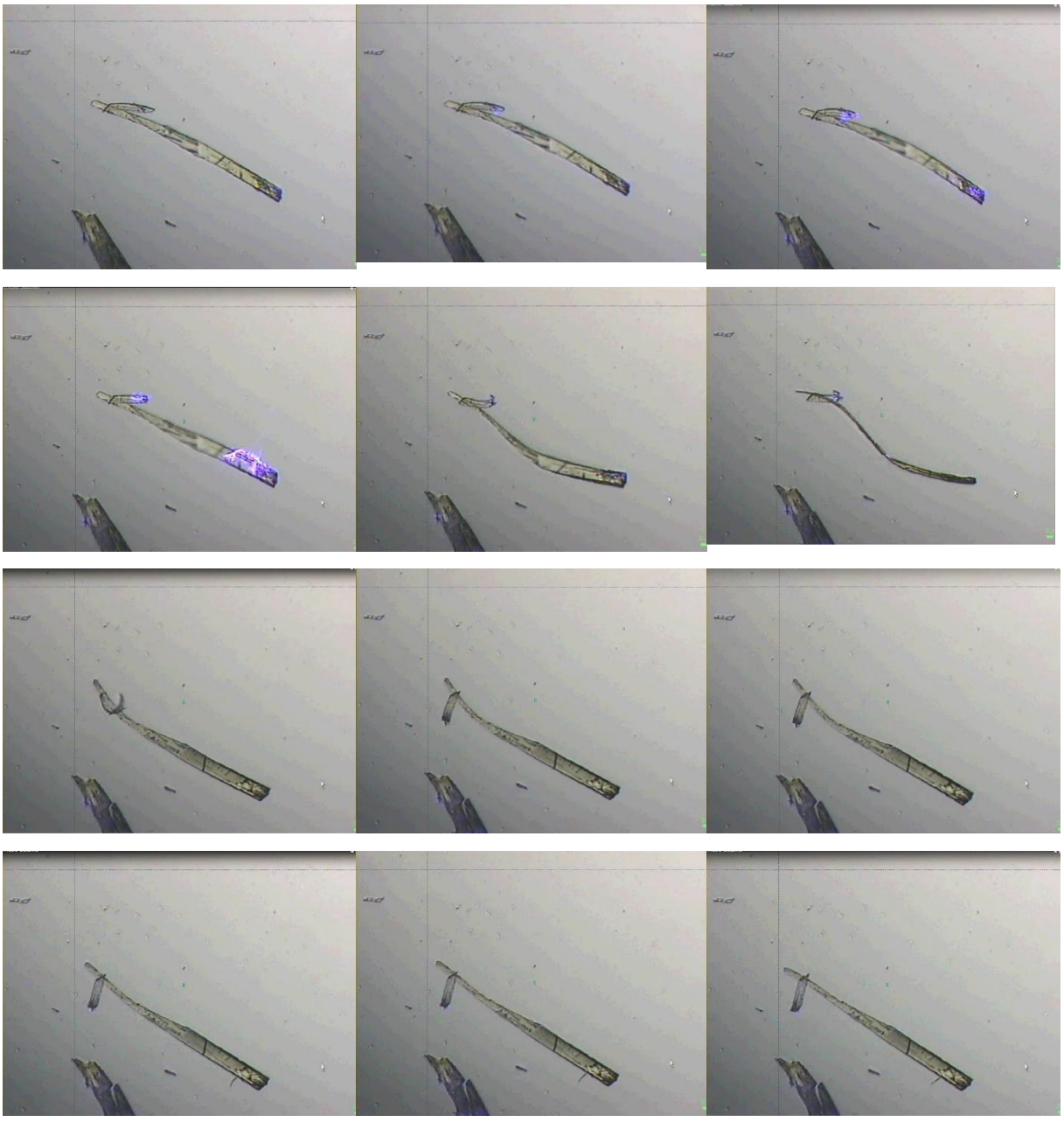

Figure 3.5 Snapshots of photochemical motions.

3.1.3.5 The timing of the reaction and its molecular and lattice kinetics.

During the course of the photoreaction, the extensive study of the Raman phonon spectra (changes of the lattice) has been complemented by the simultaneous detection of the intra-molecular modes (molecular modifications), in order to compare the molecular transformation of DNO_2A to AQ with the changes of the crystal lattice (from triclinic to monoclinic) at the same irradiation times. This investigation is crucial for the determination of the reaction mechanism following photon absorption. Figure 3.6 shows these data.

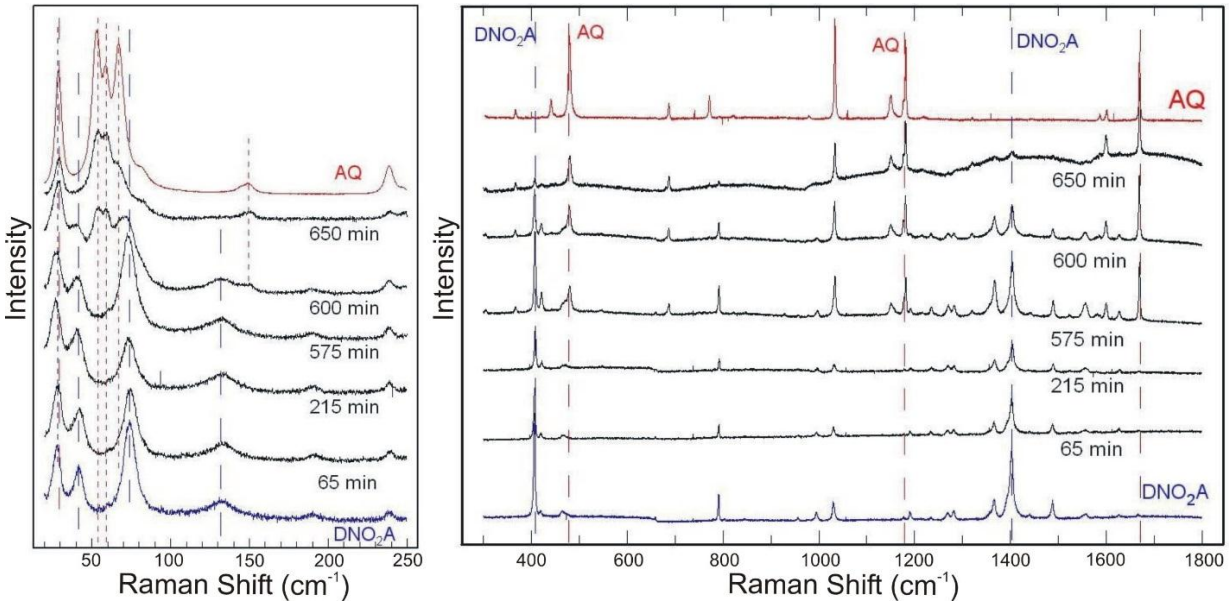

Figure 3.6 Lattice phonon Raman spectra (left) and internal vibration spectra in the region 300 -1800 cm^{-1} (right) at different times of irradiation of a single crystal of DNO_2A.

Quite interestingly, at reaction times for which the lattice phonon spectra are still those of DNO_2A, the internal vibrations of molecular AQ are already well visible, with intensities comparable to those of DNO_2A as can be seen in Figure 3.6, where AQ bands have been marked by vertical lines. This can be verified, for instance, by comparing the relative intensities of the bands at 1403 cm^{-1} and 1675 cm^{-1}, corresponding to intra-molecular modes for DNO_2A and AQ, respectively, that have been analyzed at time 575 min, where the lattice is still that of the pure triclinic DNO_2A crystal. Taking into account the *ab-initio* value of the Raman intensities calculated for the isolated molecules (from the calculations of section 2.5), we can estimate that about 40% of DNO_2A had already reacted at this time and therefore a surprisingly large amount of AQ molecules is still present. In other words, it is as though the photoproduct AQ occupies substitutional sites of the triclinic lattice of DNO_2A, *i.e.*, the molecular transformation by far *precedes* the transformation of the crystal lattice, an important finding that will be discussed in section 2.4.

3.1.3.6 The photochemical reaction at high pressure

Pressure is a most efficient tool of perturbation of intermolecular interactions, though leaving basically unchanged the molecular environment. Since large mechanical strain is undoubtedly involved in the crystal to crystal transformation of DNO_2A to AQ, we have investigated the reaction as a function of pressure, to get further hints on a reaction mechanism where incoming light and molecular constraints play a crucial role on the route to the photoproduct.

High pressure experiments were performed in in a gasketed diamond anvil cell (DAC) [12] with the procedure described in section 3.1.2. Several measurements have been performed over a wide pressure range and under different irradiation conditions. We limit the description of the experiment to few typical cases, one of which is illustrated in Figure 3.7. Here the crystal was subjected to a constant pressure of 0.7 GPa and then irradiated by the diode laser at 405 nm in the DAC. Changes of both phonon spectra and crystal morphology were simultaneously detected at constant time intervals.

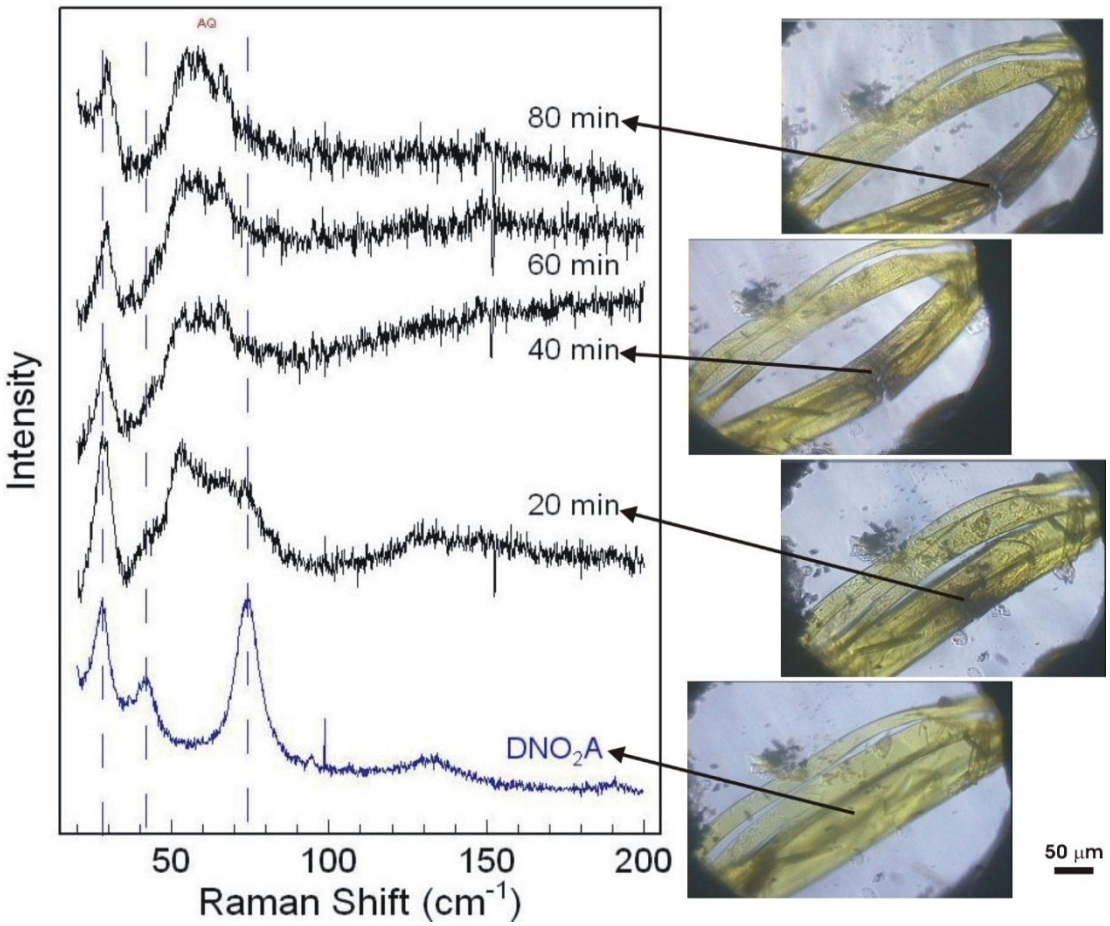

Figure 3.7 Lattice phonon Raman spectra at p = 0.7 GPa (left) and corresponding changes in crystal morphology at constant time intervals (right).

After 80 minutes the reaction reached its full completion in the irradiated region and the observed phonon bands are uniquely attributed to AQ lattice vibrations. It is of some interest to follow the changes of the shape of the crystal during the reaction. Although the crystal is subjected to the strong mechanical strain induced by the incoming light, it is nevertheless constrained in the gasket area, which produces a sort of physical barrier in limiting the sample movement. The crystal bends and splits in two forming a kind of ring in correspondence of the point where the laser was focused. By further increasing the pressure up to about 1 GPa a similar process to that described in Figure 3.7 occurs. Eventually, above 1 GPa, and irrespective of prolonged irradiation, no transformation to AQ occurs, as shown in the spectra of Figure 3.8. We have further verified that the photoreaction is really inhibited above 1.0 GPa by using different crystals loaded in the DAC up to pressures of about 2.0 GPa. Furthermore, the very same DNO_2A crystal which went unreacted at 1.4 GPa completely transforms to AQ after 20 minutes of irradiation once the pressure was released to 0.4 GPa (Figure 3.9). The complete absence of molecular modes of AQ (Figure 3.2,3.10) confirms that the reaction has not started also at the molecular level. The image of the crystal, correspondingly, shows no major changes: although undergoing a longitudinal fracture under pressure and light, it never bends or splits. It seems as though the release of the mechanical energy, revealed by the crystal movements, is indeed the driving force required for the advancement of the photoreaction.

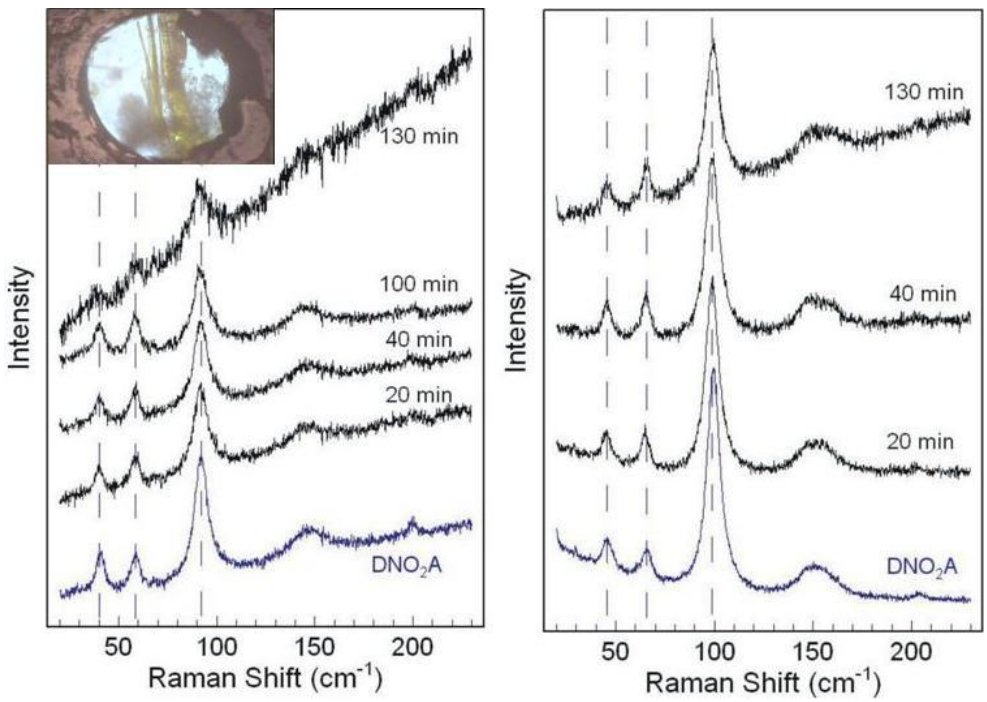

Figure 3.8 Lattice phonon Raman spectra of a crystal irradiated at 1.0 GPa (left) and at 1.4 GPa (right). In the inset a picture of the irradiated crystal at 1.0 GPa is shown.

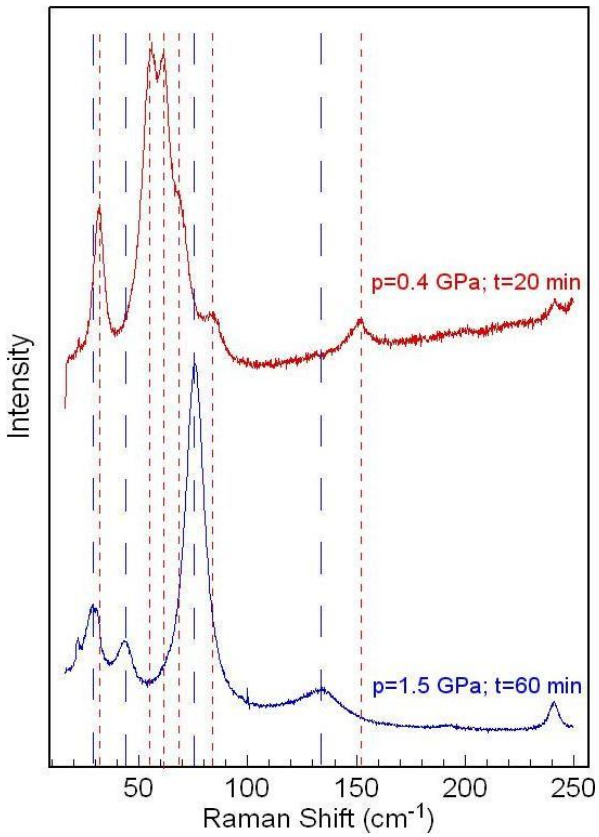

Figure 3.9 Lattice phonon Raman spectra of irradiated crystals above and below the reactive threshold of 1 GPa of pressure. The upper trace shows the pure AQ phonon spectrum once the crystal is irradiated below 1.0 GPa.

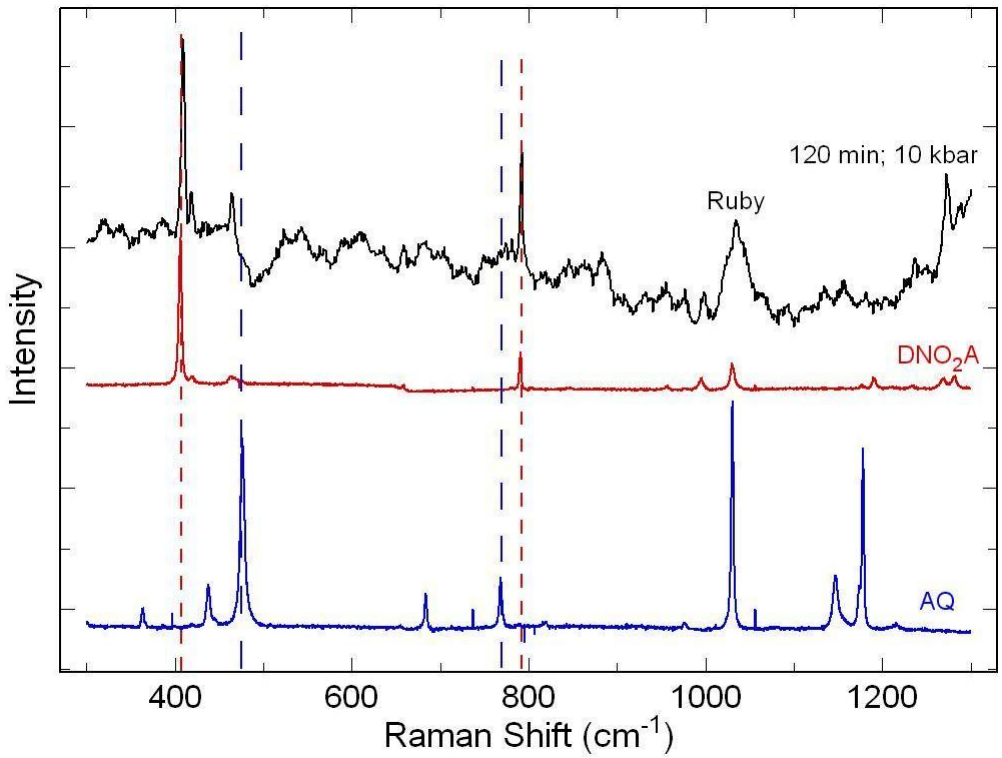

Figure 3.10 Upper trace: Raman spectra of intra-molecular modes of a DNO_2A. A crystal irradiated at 1.0 GPa. Comparison with reference spectra (lower traces) show that no molecular AQ is present, even after 120 minutes.

An additional factor which can explain the inhibition of the reaction at high pressure is that the release of NO cannot take place if the external pressure is too high. However, as discussed later, we anticipate that a photochemical reaction inhibited at high pressure is an indication of a defect-based non-topochemical mechanism, as shown by some experiments a few decades old [13,14]. A topochemical mechanism instead would naturally be favored at the reduced intermolecular separations at high pressures. The larger the pressure, the faster the photoreaction. However, we have to notice that topochemical and non-topochemical mechanism have historically been introduced to describe how much compatible or not were the mutual molecular orientations, finalized to produce the photodimerization reaction [15-17]. In the present study, in analogy to what occurs at molecular level, we can think of a *topochemical* route as the one being compatible at a crystal structure level, *i.e.*, crystal axes and angles compatible with a cell doubling or halving determined by symmetry. This would be better described as a *topophysical principle*, whose description based on a cell doubling mechanism is delayed to section 2.4 and is theoretically simulated in section 2.5.

3.1.4 The progress of the reaction

In a most general description of a reaction in a solid one can think of the formation of the active sites as the first step of the physical and chemical transformation. The nucleation is instead the slowest step, as it requires the activation energy necessary to trigger the reaction. When a crystal-to-crystal transformation is activated, the propagation to the product follows a collective process given by its ordered structure. In the present case, the activation energy, initially given by light absorption, soon involves a large mechanical strain which fuels further lattice deformations to eventually produce the structural change required for the formation of the new crystal lattice of the photoproduct. To make some plausible hypotheses of the reaction mechanism, it is worthwhile to undergo a finer tuning of the steps at the basis of the process:

1) Triggering of the reaction and formation of the active sites (nucleation centers)
2) The chemical reaction in the unit cell (the reaction cage)
3) Collective propagation of the nucleation centers over the entire volume of the crystal
4) Final progress up to the complete formation of crystalline AQ

Step 1. *Triggering the reaction*

The trigger of the reaction occurs through a well known mechanism of photochemical reactions in organic crystals [10]. Following light absorption, a delocalized exciton (*ideal crystal*) forms, which eventually localizes (*real crystal*) into chemical or physical traps of the crystal. These traps are sites of local disorder that become the *active sites*, that is, the nucleation centers which start the photoreaction. The transformation, in these local sites, of molecules of DNO_2A to AQ, provides further disorder, increasing the number of active sites capable of driving the reaction. The reaction starts and as long as DNO_2A molecules continue to transform to AQ, the latter, being in a foreign lattice, creates further trapping sites which favor the course of the reaction, following an auto-catalytic mechanism.

Step 2. *The chemical reaction in a cage: the cage is the unit cell*

Once the reaction has been triggered, the ordered structure of the crystal is the dominating factor for its propagation. By looking at the crystal parameters of DNO_2A and AQ (Table 2.1, section 2.5), it is tempting to think of a simple reaction mechanism mostly based on a cell doubling, in a direction that could be the axes *b* or *c*, or a more complicated combination of them. This would result in an appropriate *topophysical* disposition able to justify how the reaction easily reaches its completion, starting from the triclinic cell (Z = 1) of DNO_2A to get the monoclinic cell (Z = 2) of AQ of about a double volume. The triclinic unit cell of DNO_2A can thus be considered as the *chemical cage* where the photoreaction begins [10]. However, as previously shown, this reaction is inhibited at high pressure. One could then infer that, although the two structures are definitely compatible with a crystal to crystal modification, the role played by defects should be somehow predominant in governing the proceeding of the reaction. This effect could be underestimated by merely looking at the unit cell parameters of the two crystal structures.

The reaction path leading to the cell doubling will be computationally modeled in section 2.5.

Step 3. *The propagation of the reaction: from the cage to the entire crystal*

The information of the crystal structure obtained through the Raman phonon spectra give interesting clues on the progress of the reaction after its beginning. The key point is that the molecular transformation *precedes* the transformation of the crystal lattice, as clearly

indicated by Figure 3.6. AQ guest molecules, which at the beginning of the reaction occupy substitutional sites in the DNO_2A lattice, *i.e*., maintain positions and orientations of the host molecules, soon reach a concentration sufficiently high to make hardly sustainable the existence of a stable triclinic unit cell. This is possibly the reason why, at this very moment, the energy stored in the system is released and gives rise to strong mechanical deformations which manifest as bending and unfolding of the whole crystal, as illustrated in Figures 3.4 and 3.5. We believe that this is the step (Figure 3.4, picture c) when the triclinic lattice of DNO_2A begins to transform into to the monoclinic lattice of AQ, whose lattice phonons soon become predominant in the Raman profiles. Therefore, the mechanical movement induced by light absorption, as shown in the pictures from 3.4c to 3.4f, provides the energetic cost of the crystal to crystal transformation.

Step 4. *The complete formation of crystalline AQ*

At the final stage the AQ molecules, formerly guest molecules in the triclinic DNO_2A lattice, become themselves host molecules in a monoclinic lattice where unreacted DNO_2A molecules are now guests. This implies that, although the new crystal lattice is formed, the reaction is not complete until all reactant molecules are transformed to AQ in the AQ lattice. This would allow us to advance an hypothesis on why in Figure 4, picture *g*, the crystal, which after having recovered its initial shape at time 365 min, undergoes further distortion by shrinking and bending in a fashion similar to the process previously exhibited in pictures *a* to *f*. Indeed, the completion of the photoreaction still requires that a sizable amount of DNO_2A molecules to react and a corresponding stoichiometric amount of NO molecules to leave the crystal, which therefore shrinks to keep its cohesion. At this stage only, the reaction completely ends.

We must remark once again the importance of the relationship between the intra-molecular vibrational spectra and the intermolecular lattice phonon spectra. This relationship is of paramount importance in probing, at the same time, both the photochemical transformation of the molecules and the change of the crystal lattice.

3.1.5 Modeling the reaction

Now we aim to describe the transformation of DNO_2A to AQ in the solid-state by emulating the experimental process, that is by first chemically transforming DNO_2A into AQ without changes to the lattice, and then by continuously deforming the crystal lattice into the

final AQ structure, without further chemical changes and along the path with the lowest energy barrier. We must, in effect, identify the transition state, which is the minimum energy saddle point between reactants and products. To implement this program we need a model for the molecules and then a model for their interactions in the crystal.

For the molecular model we have chosen the minimum energy geometries of isolated DNO_2A and AQ molecules, determined *ab-initio* with the program GAUSSIAN03 [18], using the B3LYP/6-31G* combination of density functional and basis set. The model is adequate, since the equilibrium geometries so obtained closely match the experimental molecular geometries in the crystals [7,9], with the only noticeable difference of a small deviation (below 5°) in the C-C-N-O torsion angles in DNO_2A.

Intermolecular interactions were modeled by an atom-atom potential with electrostatic and Buckingham terms, $V_{ij}(r)=q_iq_j/r+A_{ij}\exp(-B_{ij}\,r)-C_{ij}/r^6$. The atomic charges q_i are the "ESP" charges [18] fitted to the electrostatic potential evaluated in the just mentioned *ab-initio* calculations on the isolated molecules. The parameters A_{ij}, B_{ij} and C_{ij} for H, C, N and O atoms are from a potential model [19] specifically designed to be internally consistent and transferable. Crystal structures were determined by seeking minimum energy lattice configurations using the program WMIN [20], with molecules maintained rigid in their *ab-initio* geometries. Several experimental and hypothetical initial lattice structures have been considered, as discussed below. The stability, or lack of stability, of the optimized structures was assessed by computing the phonon frequencies which, as a necessary and sufficient condition for local stability [21], must be real and ≥ 0 (non-negative force constants).

As a first validation of the molecular and potential models, starting from the experimental structures [7,9] of DNO_2A (triclinic, space group $P\bar{1}$, with Z=1) and AQ (monoclinic, space group $P2_1/a$, with Z=2), we have determined the equilibrium configurations by minimizing the potential energy with respect to all independent structural parameters allowed by the space group symmetry. The resulting structures, hereafter labeled as D_1 and A_2, are shown in Figure 3.11, while their lattice parameters are listed in Table 3.1. The excellent agreement between calculated and experimental parameters confirms that the models are realistic. Also excellent is the agreement between the computed binding energy of the lattice and its closest experimental equivalent, namely the sublimation enthalpy, available only for AQ [22].

Table 3.1: Experimental and computed lattice parameters [7,9] and binding energies [22].

	Z	Space group	Structure	*a*	*b*	*c*	α	β	γ	V	E
				(Å)	(Å)	(Å)	(deg)	(deg)	(deg)	(Å^3)	kcal/mol
DNO_2A	1	$P\bar{1}$	Expt.[7]	3.950	8.680	8.760	106.77	98.98	98.02	278.59	
			Calc. D_1	3.713	8.824	8.825	105.69	98.09	98.13	270.67	−36.38
AQ	1	$P\bar{1}$	Calc. A_1	4.157	8.258	7.778	107.74	85.60	106.30	244.08	−27.99
	2	$P\bar{1}$	Calc. A_1'	16.407	4.157	8.138	77.08	101.47	70.83	488.15	−27.99
	2	C2/m	Calc. T_2	15.314	3.963	9.163	90.00	98.90	90.00	489.63	−26.88
	2	$P2_1/a$	Expt.[9,22]	15.780	3.942	7.868	90.00	102.69	90.00	480.21	−27.2±4.8
			Calc. A_2	16.010	3.929	7.805	90.00	102.71	90.00	478.75	−29.09

As discussed in previous sections, the photochemical molecular transformation of DNO_2A to AQ precedes the transformation of the lattice. To model this behavior, starting from the known structure of DNO_2A, we have converted all DNO_2A molecules into AQ molecules and then minimized the lattice energy. We have thus reached a *virtual* triclinic AQ structure with Z=1 (labeled A_1), which represents a local energy minimum, since all computed force constants are non-negative. This hypothetical structure, although *mechanically* stable, is predicted to be *thermodynamically* unstable, since it is less bound than the Z=2 monoclinic structure A_2 (see energies in Table 3.1). Immediate conversion of A_1 into A_2 is hindered by the energy barrier that separates the two structures. To estimate this barrier, we have searched all possible reaction paths between A_1 and A_2. The procedure used to identify the transition state is shortly described below and is extremely artificial. Nevertheless, we will immediately see that the resulting reaction path, illustrated in Figure 3.11, describes a quite obvious and easily understandable process.

The transition state, labeled T_2, is a Z=2 non-primitive monoclinic structure with space group C2/m. The two molecules are equivalent by translation and parallel to *ac* plane. The structure, optimized with respect to all structural parameters allowed by the monoclinic lattice, sits on an energy saddle, since some of its phonons have negative force constants. When first perturbed by slightly rotating the two molecules, either in the same or in opposite directions, the state T_2 in fact falls to either one of the two different minima A_2 or A_1'. It may also be noticed, as shown in Figure 3.11, that A_1 is just a cell halving of A_1', and, in fact, A_1' and A_1 have exactly the same energy (i.e. they are just two equivalent description of the same structure).

We can now fully describe the transformation, illustrated in the figure, from D_1 (the Z=1 DNO_2A lattice) to A_2 (the Z=2 AQ lattice). We first photo-chemically transform D_1 into A_1

(AQ in the Z=1 DNO_2A lattice), which is immediately doubled into A_1'. We then progressively deform the Z=2 triclinic lattice A_1' into a monoclinic lattice, while simultaneously rotating the two molecules until they lye parallel to the ac plane. The T_2 saddle structure is thus reached, after paying an activation energy of 1.11 kcal/mol. We then rotate the two molecules in opposite directions, finally reaching the monoclinic A_2 lattice and recovering 2.21 kcal/mol, with a net, though small, gain.

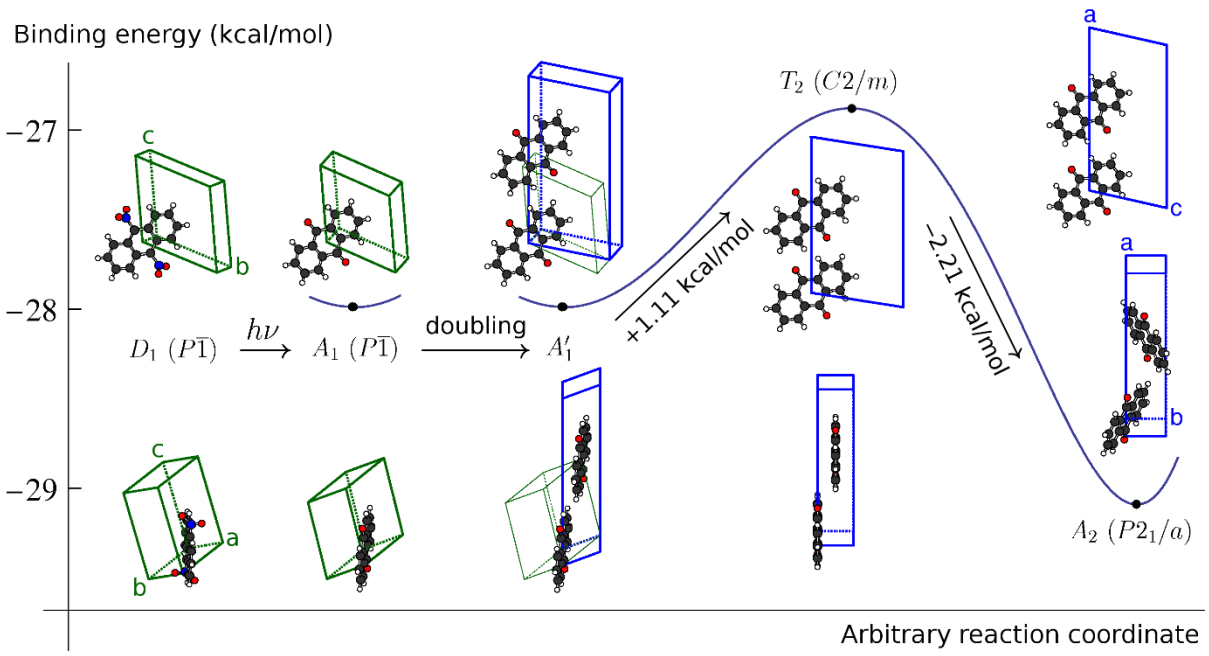

Figure 3.11 Reaction path from DNO_2A to AQ. D_1 is the Z=1 DNO_2A structure which, when photochemically transformed to AQ, becomes the Z = 1 metastable structure A_1. A_1 is mathematically equivalent (through a cell doubling) to A_1', which may be transformed into the transition state T_2. Finally, T_2 spontaneously converts to A_2 (the Z = 2 AQ structure). Axonometric views of the various computed structures along the path are shown close to their energies. AQ and DNO_2A molecules maintain their ab-initio geometries (with D_{2h} and C_{2h} symmetry, respectively) and reside on inversion sites. Graphics by MolScript [23].

In conclusion, the photo-induced reaction of dinitro-anthracene to antraquinone fits the general picture of molecular materials that change shape and dimensions by means of the transformation of photon energy into mechanical work [24]. However, what we aim to emphasize here, is the mechanism underlying the crystal to crystal transformation, a process complicated by the need to consider all changes occurring in the molecular environment during the course of the reaction. It is self evident that molecular changes ultimately produce modifications of the crystal lattice. Raman spectroscopy has revealed to be the ideal tool to conveniently follow this process. While the analysis of the lattice modes allowed for the study of the physical changes, the chemical transformation was monitored by measuring the intra-molecular Raman-active modes of both, reactant and product. The structural reconstruction

required to drive the photoreaction explains the different evolution of crystal morphology under irradiation. We have shown that a completely destructive process is observed when irradiation is produced by an intense focused laser beam, whereas a uniform distribution of the exciting radiation with a lower intensity permits a more controlled structural change. In the latter case the crystal initially keeps its shape, propagating the mechanical strain to edges and surfaces rather than undergoing cracks or breaking in small fragments.

One of the major outcome of this study is that molecular and lattice transformations do not proceed at the same rate. The molecular transformation precedes the structural crystal change, which implies a key role played by host and guest molecules, that interchange in the substitutional sites of the unit cell. The observed time mismatch between chemical and lattice transformation allows for a clear way of modeling the crucial step of the cell doubling. In fact, once the AQ molecules are formed inside the DNO_2A lattice, the system relaxes to a readily accessible mechanically stable structure still with Z=1. From here, a local minimum, the thermodynamically stable structure with Z=2 can be attained with a small energy expense which leads the system through a plausible transition state.

To clarify the mechanisms underlying the relationship between incoming light and molecular constraints we have extended the study to high pressure up to 2 GPa. It was found that after 1 GPa the photoreactions becomes inhibited, a finding which fits a possible scenario of a crystal to crystal *photophysical* process triggered by defects [10,17].

As a last point we again underline the role played by the mechanical strain induced by light. A large structural reconstruction, as that involved in the doubling of the triclinic unit cell of DNO_2A to yield the monoclinic structure of AQ, cannot occur without striking crystal deformations accompanying the photoreaction. Light energy initially produces the chemical transformation of the molecular units in the lattice. This change induces the mechanical deformations which eventually become the driving factor of the structural change. At high pressure (> 1 GPa) where crystal movements meet with molecular constraints, the photoreaction lacks its driving force and cannot reach its completion.

3.2 The Photodimerization reaction of 9-cyanoanthacene

The crystal-to-crystal photodimerizations of anthracene and 9-substituted anthracenes have been considered for a long time as model systems for bimolecular solid state reactions. The dimer is formed through an excited state [4+4] cycloaddition, where the reaction centers are a pair of carbon-carbon double bonds located on two distinct molecules lying adjacent in the crystal lattice. It has been recognized [25-28] that in these systems the dimerization mechanism involves as a first step the formation of an excimer intermediate, or physical dimer, generated by electronic excitation of the monomer, from which the chemical dimer can be obtained via a non-radiative decay path [29]. In agreement with the so-called topochemical postulate [15], the possibility for the reaction to follow its course is determined by a number of parameters, the values of which depend on the monomer crystal packing. Distances between the potentially reactive atoms of the two adjacent molecules must be below a threshold value, while relative orientations of the anthracene skeletons and lateral shifts between the orbitals of the reactive atoms must be favorable to the formation of the new molecular geometry [30]. Thus, only when all these parameters are within the boundaries identified by the topochemical principle [30], can the photodimerization occur and the dimer crystal obtained, with a structure which was already present (or pre-formed) in the lattice of the monomer precursor.

The solid-state reaction of 9-cyanoanthracene (9CNA) [31,32] is the earliest case in which the dimerization occurs quite rapidly under irradiation, but the topochemical principle cannot be *a-priori* applied. In fact, 9CNA molecules are arranged in the lattice in such a way to give a head-to-head or *cis* dimer as a product, but the formation of this is not thermodynamically favoured due to the steric hindrance arising from having both substituents on the same side. What is observed instead is the formation of the thermodynamically stable *trans* dimer (head-to-tail configuration) [31-34]. Such a result is explained by assuming that the reaction is first triggered in defective sites of the crystal, and in particular along partial (221) dislocations where the crystal planes are shifted in such a way that pairs of molecules end up lying in a head-to-tail arrangement, as schematically shown in Figure 3.12.

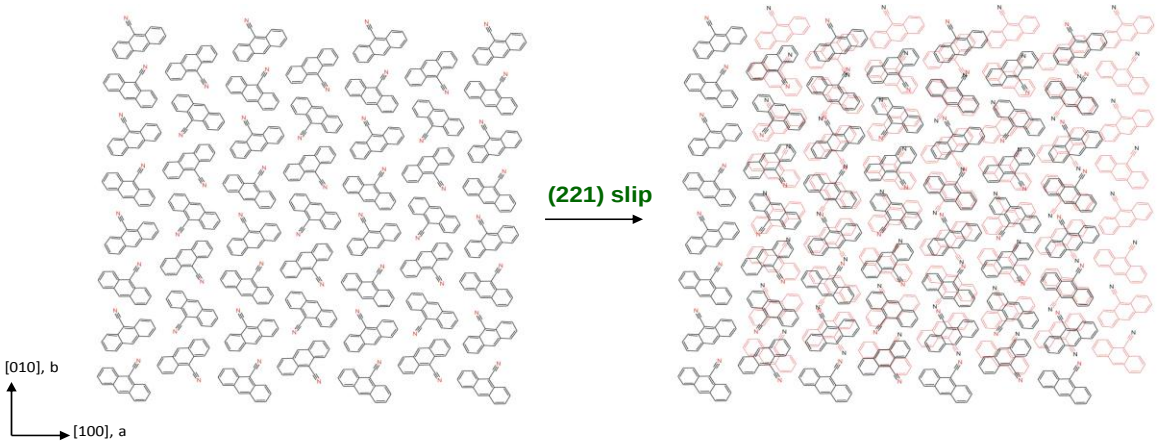

Figure 3.12 Simulation of a defective zone by (221) slip plane.

The pairs of molecules in a head-to-tail arrangement can therefore easily form the trans excimer and hence the chemical dimer via its non-radiative decay [32]. Once the transformation is triggered in the original defect, the reaction site itself is the origin of more defects, so that the process can spread auto-catalytically to the entire crystal due to the progressive loss of order.

In this thesis work we wanted to revisit the classic 9CNA photodimerization by employing the confocal Raman microscopy technique, already used to follow the unimolecular reaction of dinitro-anthracene [35] previously described. As in the case of dinitro-anthracene, Raman spectra were collected both in the energy range of intramolecular vibrations and at low wavenumbers (10-150 cm^{-1}), where the bands characteristic of the lattice vibrations can be detected. In the former energy interval we have been able to follow the reaction from a molecular point of view, detecting the bands typical of the reactant and of the product as a function of the irradiation time. Intermolecular interactions were instead probed in the region at low wavenumbers, where the Raman spectrum displays dramatic changes when the molecular packing changes or the order and the spatial correlation in an existing structure are disrupted. Therefore, the Raman technique allowed us to monitor directly and simultaneously both the formation of a new chemical species and the associated structural changes. This represents an advantage with respect to other spectroscopic methods used to investigate solid state reactions, such as electronic absorption, emission and vibrational spectroscopy of molecular normal modes. Besides, by exploiting the confocality of the micro-Raman technique, the entire process was followed on single crystals, precisely identifying portions of the sample subjected to irradiation.

One of the interesting results found for the reaction of the dinitro-anthracene crystal was, also in this case, the delay between the chemical and the physical modifications, easily observable on the time scale of the experiment. Thus, it felt important to understand if this kind of behavior was altogether general, starting from a system that is in some respect prototypical, such as the 9CNA dimerization reaction.

3.2.1 Experimental

Single crystals of 9CNA were grown by slow evaporation of an ethanol solution of the commercial product from Aldrich. Light yellow needles a few mm long were obtained, elongated along the short *a* crystallographic axis.

The trans 9-cyanoanthracene dimer (9CNAD) was also photochemically synthesized in ethanol solution (Figure 3.13) to obtain nicely shaped single crystals to use as a spectroscopic reference of the product of the solid state photoreaction.

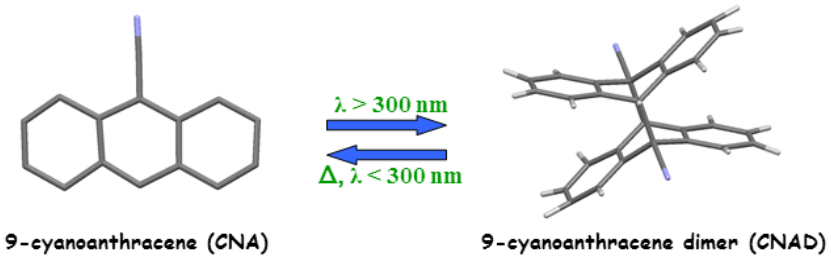

Figure 3.13 Dimerization reaction scheme.

Following the procedure described in the literature [36,37], a stirred solution of 9CNA in ethanol was irradiated in a pyrex flask under nitrogen atmosphere with a 250 W Xe lamp. As the pyrex glass light transmission is very low at wavelengths below 300 nm, with a maximum above 340 nm, the reverse reaction from dimer to monomer was prevented under these conditions. White needle crystals of 9CNAD, insoluble in ethanol, were separated by filtration after about 4 h of irradiation, repeatedly washed with ethanol and dried. Mass and NMR spectra, reported in Figures 3.14 and 3.15, respectively, were recorded to make sure that the synthesized dimer was chemically pure of the monomer and the only species obtained was the head-to-tail configuration. In the mass spectra the molecular peaks of monomer and dimer are observed, while in the H^1 NMR spectrum the formation of dimer is clearly present as confirmed by the detection of the aliphatic hydrogens in the range 4.8-5.0 ppm. The ^{13}C NMR spectrum confirms the presence of the dimer structure.

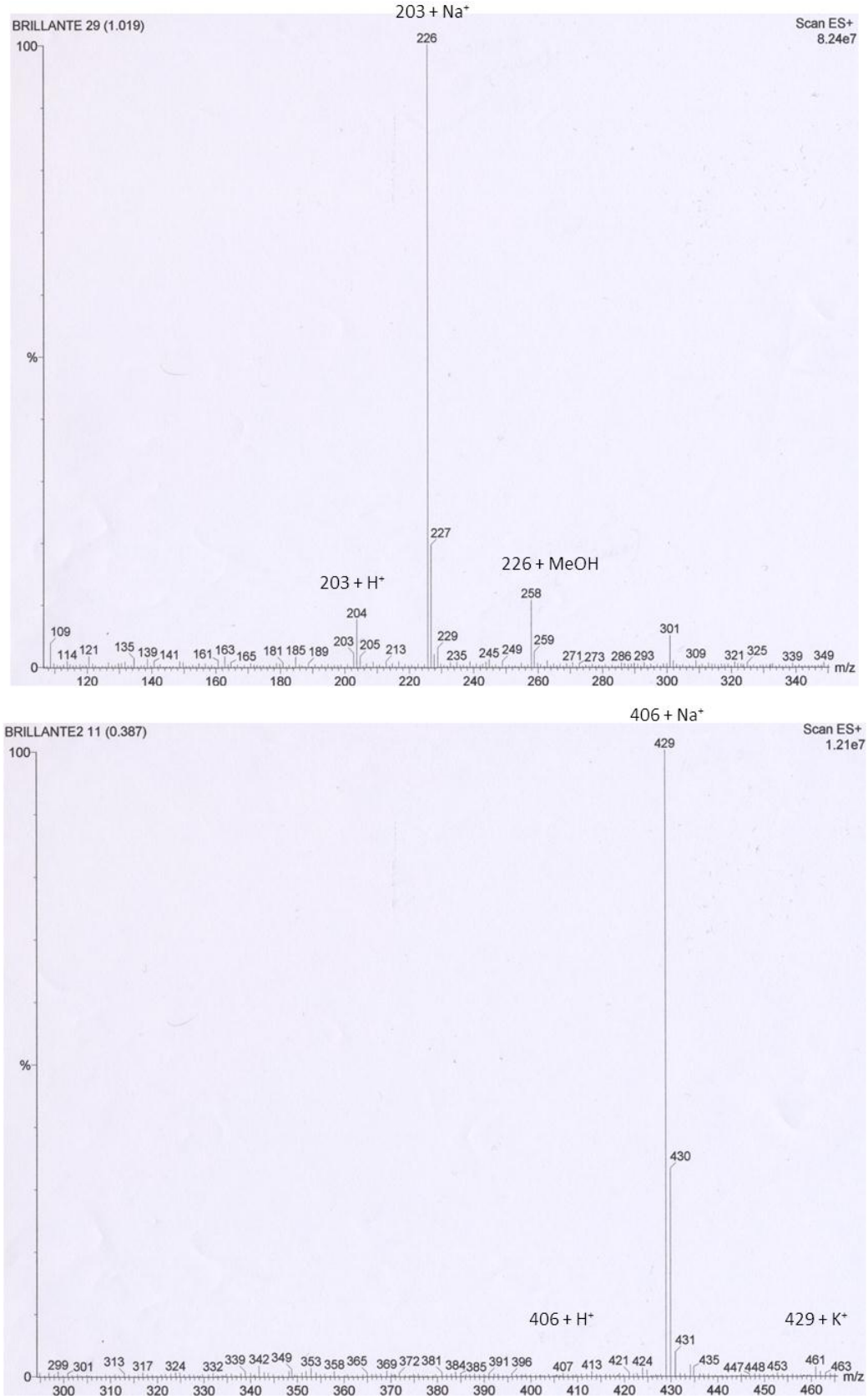

Figure 3.14 Mass spectra of monomer (top) and dimer (bottom) of 9CNA

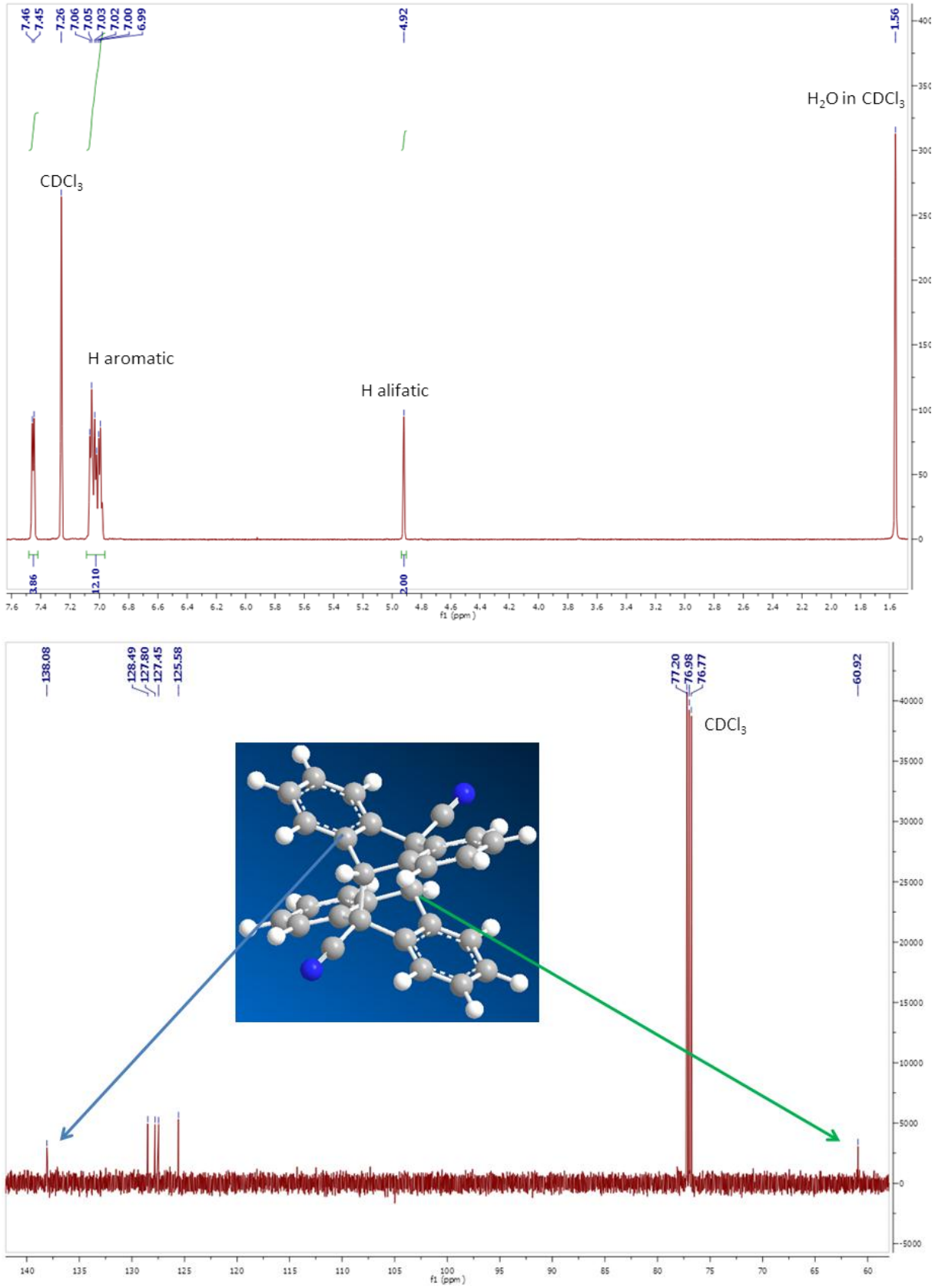

Figure 3.15 NMR spectra ^{1}H (top) and ^{13}C (bottom) of 9CNA dimer.

To irradiate the 9CNA crystals two distinct sources were employed: the UV excitation of a 75 W Xe lamp (radiative flux 5×10^{-5} W/cm^2), in the range 300-400 nm, and the beam of diode laser tuned at 405 nm. The focused laser source had a radiative flux of 340 W/cm^2, which decreased to 0.03 W/cm^2 when out of focus.

Raman spectra were recorded with the Raman micro-spectrometer as described in chapter 2. The Raman excitation source was a krypton laser at 647.1 nm and, when needed, the impinging power was reduced with suitable filters to prevent crystal damage.

Fluorescence spectra of the solid samples were recorded with a FLSP920 Spectrometer by Edinburgh Instruments, also described in chapter 2.

3.2.2 Results and Discussion

3.2.2.1 Lattice phonon Raman spectra of the reference crystals

The lattice phonon spectra of pure 9CNA and 9CNAD crystals, which are needed as reference spectra of reactant and product, respectively, are reported in Figure 3.16. The orthorhombic structure of 9CNA crystal belongs to the space group $P2_1P2_1P2_1$ (D_2^4), with Z=4 and unit cell parameters *a* = 17.15 Å *b* = 15.11 Å, *c* = 3.93 Å [38]. The four molecules lie on generic positions (site symmetry C_1) and are exchanged by the group symmetry operations. The number and the symmetry of the Raman active lattice modes (***k***=0) in this orthorhombic structure can be determined by the factor group analysis. Of the 24 lattice modes, 21 are Raman active, with symmetries $6A_1 + 5B_1 + 5B_2 + 5B_3$.

The structure of the most stable polymorph of 9CNAD is triclinic and belongs to the space group $P\bar{1}$ with Z=4 [39], with unit cell parameters *a* = 10.217 Å, *b* = 10,235 Å, *c* = 11.594 Å, α = 95,20°, β = 90.37 and γ =120.13°. Two molecules lie on inversion sites at (0,0,0) and (0,1/2,1/2) (site symmetry C_i) while two more lie on generic sites (site symmetry C_1) and are exchanged by inversion. Therefore, the unit cell contains 3 asymmetric units: one dimer molecule and two half dimer molecules. Of the 24 lattice phonon normal modes, 12 are of gerade symmetry A_g and are Raman active.

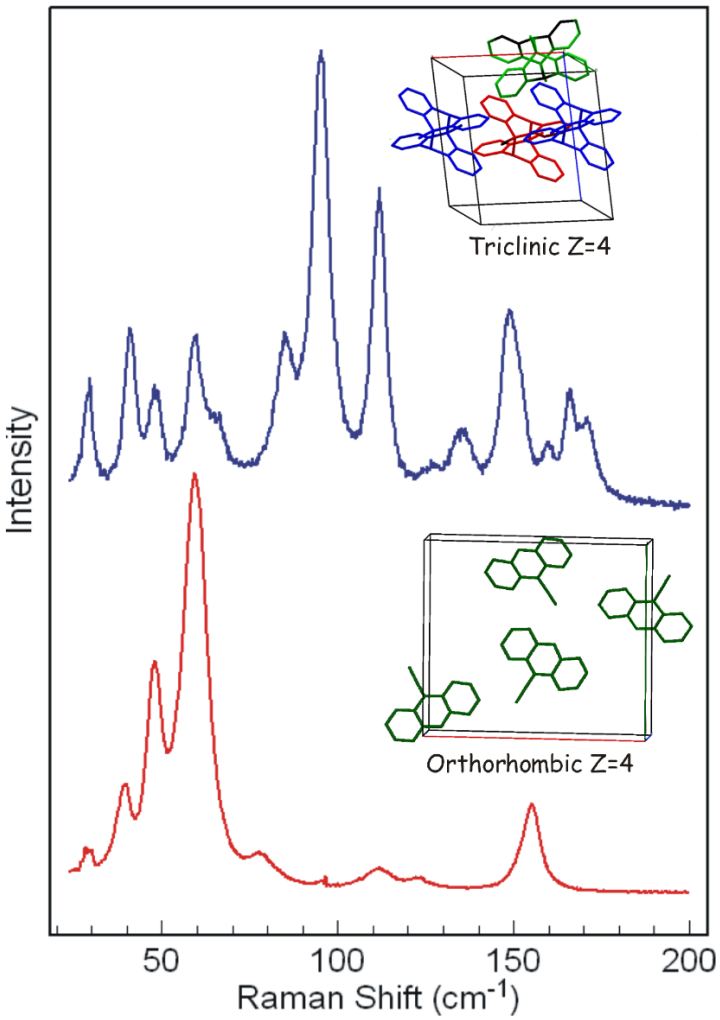

Figure 3.16 Lattice phonon Raman spectra and unit cells of 9CNA (bottom) and 9CNAD (top) crystals.

By observing the two spectra of figure 6, one could infer that lattice phonon bands of either crystal, suitable for following the progress of the reaction, could be easily identified especially in the range 80-130 cm^{-1}. However, the simple features of the 9CNA spectrum of Figure 3.16 are quite deceptive. By recording the spectra of a sample of 9CNA with various orientations of the crystal planes with respect to the incoming beam, as shown in Figure 3.17, we could probe the high anisotropy of this system, arising from the high symmetry of the lattice and its large number of vibrational modes. Different orientations also produce very different spectral features, and it is clear that, unlike what anticipated, there are many accidentally coincident bands observed in 9CNA and 9CNAD. Thus, the task of disentangling the spectra of the two species in the course of the reaction is far from being easy, especially considering that (*vide infra*) the irradiated sample will transform into a polycrystalline system, will move and get re-oriented.

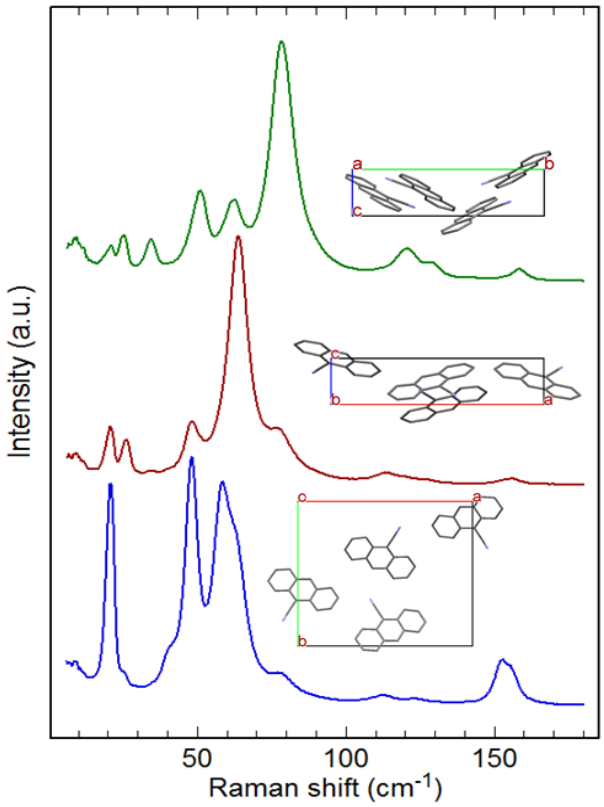

Figure 3.17 Effect of crystal anisotropy on the lattice phonon Raman spectra of 9CNA crystal recorded in different orientation and for various crystal faces.

To measure polarized Raman spectra, the orientation of the crystal faces and axes in a reference frame must be known. In the case of 9CNA, a reasonable guess of the *c* crystallographic axis could be made even without the aid of the X-rays, as this the shortest axis and is very likely the direction of fastest growth and coincides with the long axis of the needle crystals. Once the *c* axis was identified, the 9CNA needle crystals could be rotated around it, thus presenting to the observer (and to the exciting light) either the *ac* or the *bc* face. Finally, by placing the needle perpendicular to the measuring stage, the *ab* face could be exposed.

To clarify the following discussion on polarized spectra of 9CNA crystal, in equation 1 the symmetry of the polarizability matrix tensor of the unit cell group D_2 is given.

$$\begin{pmatrix} A & B_1 & B_3 \\ B_1 & A & B_2 \\ B_3 & B_2 & A \end{pmatrix} \equiv \begin{pmatrix} \alpha_{aa} & \alpha_{ab} & \alpha_{ac} \\ \alpha_{ab} & \alpha_{bb} & \alpha_{bc} \\ \alpha_{ac} & \alpha_{bc} & \alpha_{cc} \end{pmatrix}$$

Figure 3.18 shows the polarized spectra of a 9CNA needle single crystal in which the alignment of the *c* crystallographic axis with respect to the laser beam polarization direction is known. In particular, the spectra a) and b) of Figure 3.18 show the Raman scattering from crystal faces containing the *c* axis (either *ac* or *bc* face), whereas the spectra in c) concern the scattering from the *ab* face.

By keeping excitation and detection both parallel to each other and to the *c* axis (par-par configuration), all the modes of A_1 symmetry which owe their intensities (or part of it) to the *cc* component of the polarizability tensor could be detected. Top spectra (par-par) 3.18a) and 3.18b) must show the same bands, either as pure lattice vibrations (five) or coupled with molecular vibrations. Variable relative intensities of the bands may occur, due to slight crystal misalignments. By aligning the crystal with the *c* axis along the direction of light propagation, we were looking at face *ab* as in spectra 3.18c). In the (par-par) spectrum of Figure 3.18c excitation and analyzed scattering are polarized parallel to each other. The observed modes are still those of A_1 symmetry, but now the *aa* or *bb* tensor polarization components (or a combination of both) are probed, so that the detected bands can display significant intensities variability. As for the non totally symmetric vibrations, symmetry selection rules tell us B_1 modes can be detected on the *ab* face, B_2 in *bc* and B_3 in *ac*.

The spectra of Figure 3.18a and 3.18b labelled as (par-perp) were collected with the Raman scattering polarized perpendicular to both excitation light and *c* axis for the *ac* and *bc* faces. This was be attained by rotating both the crystal and the excitation polarization by 90°, while keeping the position of the analyzer fixed. These spectra should allow us to disentangle and assign B_2 and B_3 modes, probing tensor polarizability components *ac* and *bc*. Analogously, the bottom spectra of Figure 3.18c, also labelled par-perp, give information only on B_1 modes.

The careful analysis of the spectra of Figure 3.18 and many others has indeed allowed us to identify with certainty at least 19 of the expected 21 lattice phonon bands, safely discriminating A_1 and B modes and obtaining the information needed to the interpretation of spectra with overlap of monomer and dimer bands.

As a last remark, we should point out that the analysis of the polarized 9CNAD Raman spectra would not provide more information on this system. In the case of 9CNAD we are dealing with the spectrum of a centrosymmetric triclinic crystal lattice, for which all the total symmetric A_g modes are always Raman allowed, regardless of the orientation of the crystal and of the polarization of exciting and scattered light. However, different crystal orientations probe different elements of the polarizability tensors, and also 9CNAD Raman spectra were found to change dramatically from sample to sample, a phenomenon which was especially evident when comparing the reference spectra with those of the photoproducts of the solid state reaction.

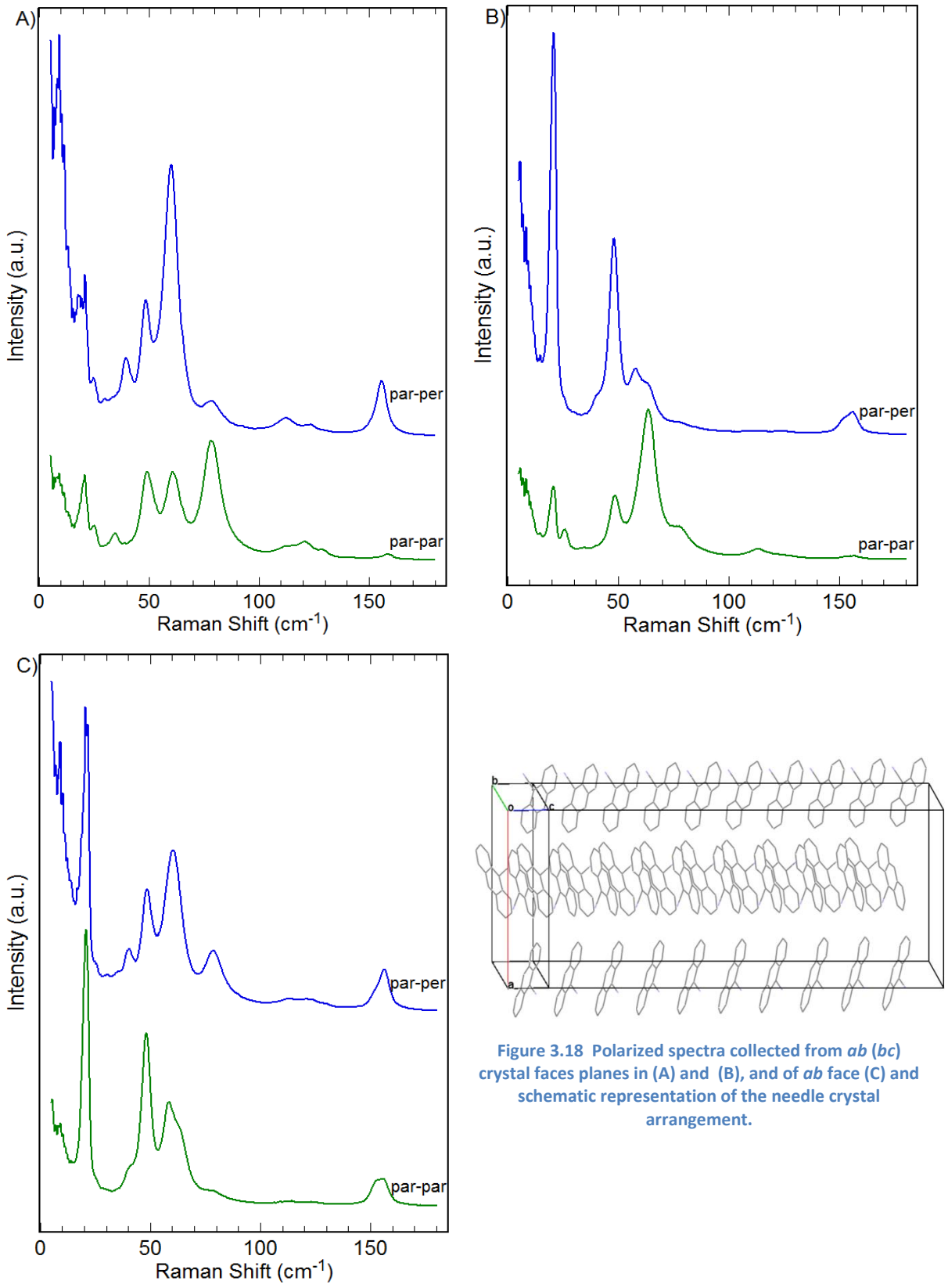

Figure 3.18 Polarized spectra collected from *ab* (*bc*) crystal faces planes in (A) and (B), and of *ab* face (C) and schematic representation of the needle crystal arrangement.

3.2.2.2 Raman spectra of irradiated samples

The broadband UV excitation of the 75 W Xe lamp was used to irradiate the 9CNA crystal of Figure 3.19. From the image it clearly appears that the sample is composed of a large crystal having the shape of a needle with a micro-crystal lying on top of it.

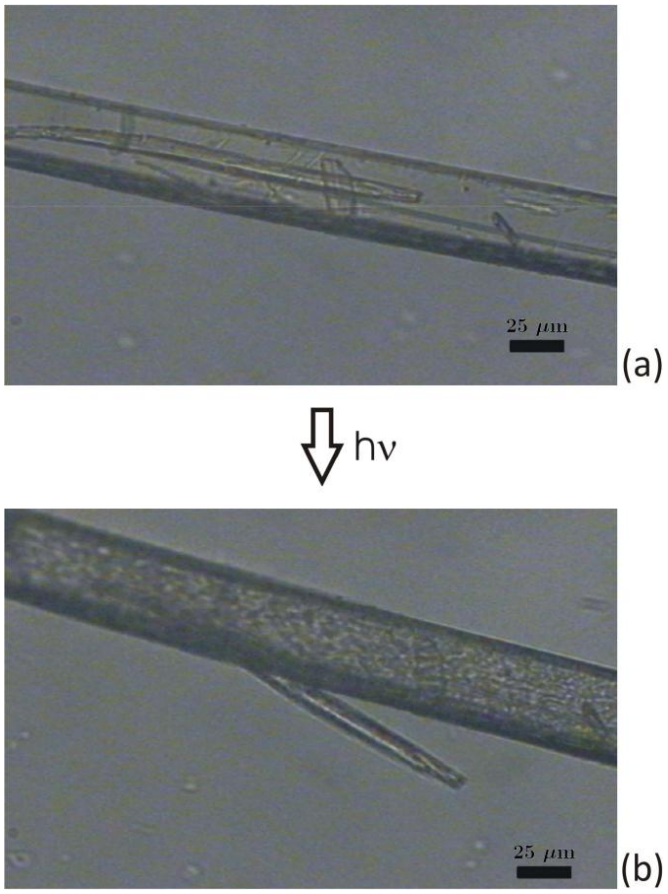

Figure 3.19 9CNA crystal before (a) and after (b) UV irradiation with a Xe lamp.

The Raman spectra of the sample are reported in Figure 3.20 as a function of the irradiation time, together with the reference spectrum of the 9CNAD dimer obtained from the photochemical reaction in solution. As can be seen from the spectra of Figure 3.20b, in the sample under investigation the vibrational bands of the 9CNAD molecule appear after 30 min of irradiation and within a time span of 240 min no further spectral modifications could be observed.

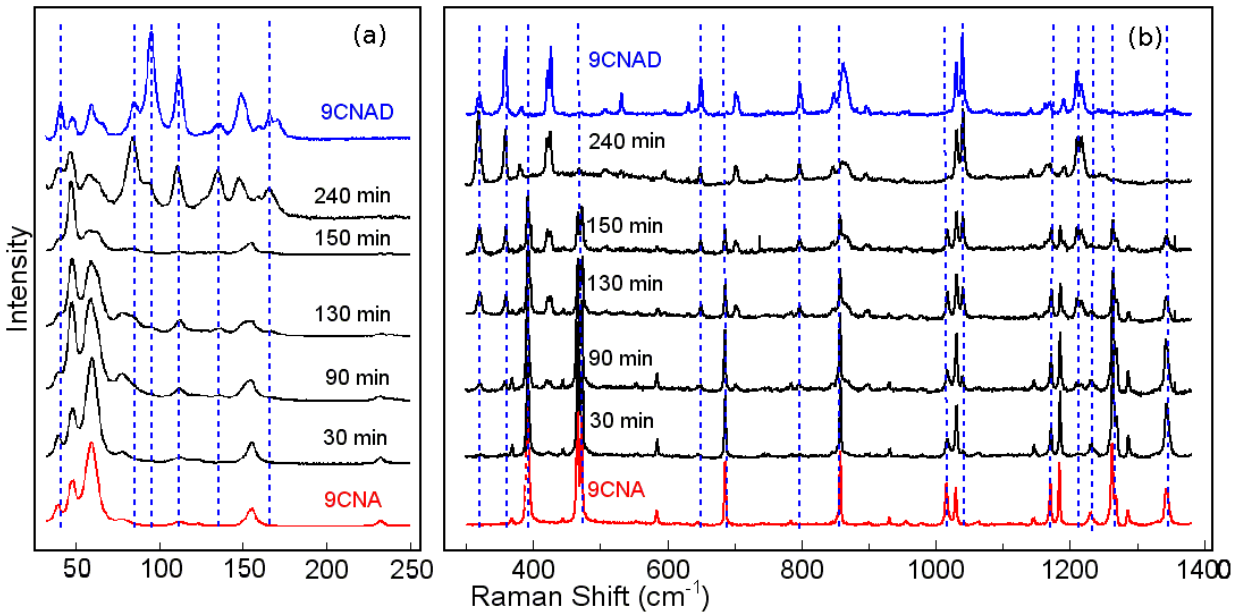

Figure 3.20 Raman spectra of a single crystal of 9CNA as a function of the irradiation time with a broadband excitation: (a) lattice phonon modes, (b) molecular vibrations in the region 350-1400 cm^{-1}. The dashed lines identify the vibrational modes which best show the progress of the dimerization.

The change of the Raman spectrum with time was accompanied by a blue-shift (from green-yellow to blue) of the fluorescence emission, detectable even by the naked eye while the sample was irradiated. Indeed, the measurement of the fluorescence in the course of the reaction (Figure 3.21) showed that new bands at ≈ 411 and 440 nm appeared as shoulders of the strong maximum at ≈ 490 nm, which characterizes the emission spectrum of 9CNA and is assigned to the trans excimer [13]. The new bands are instead assigned to the exciton emission of residual 9CNA molecules trapped within dimeric regions while the reaction proceeds. An example of the behavior of the emission with irradiation time is reported in Figure 3.21c. Interestingly, a progression of bands at ≈ 411, 440 and 460 nm also characterizes the emission spectrum of 9CNAD crystal obtained in solution. These bands probably mark the presence of unreacted monomer impurities, which cannot be removed even after recrystallization and which cannot even be detected by NMR as having too low a concentration.

a)

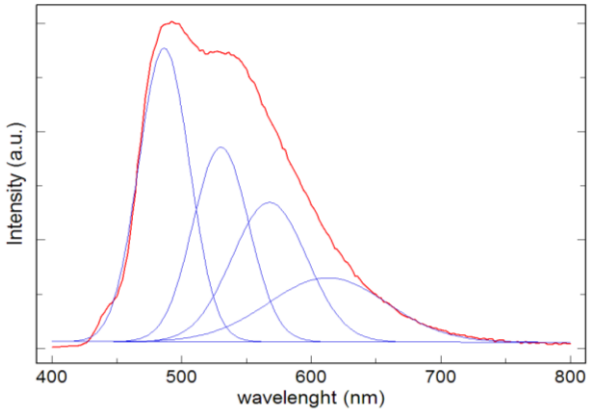

b)

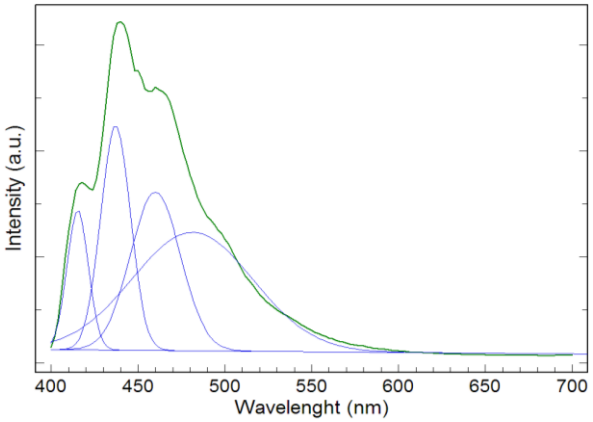

c)

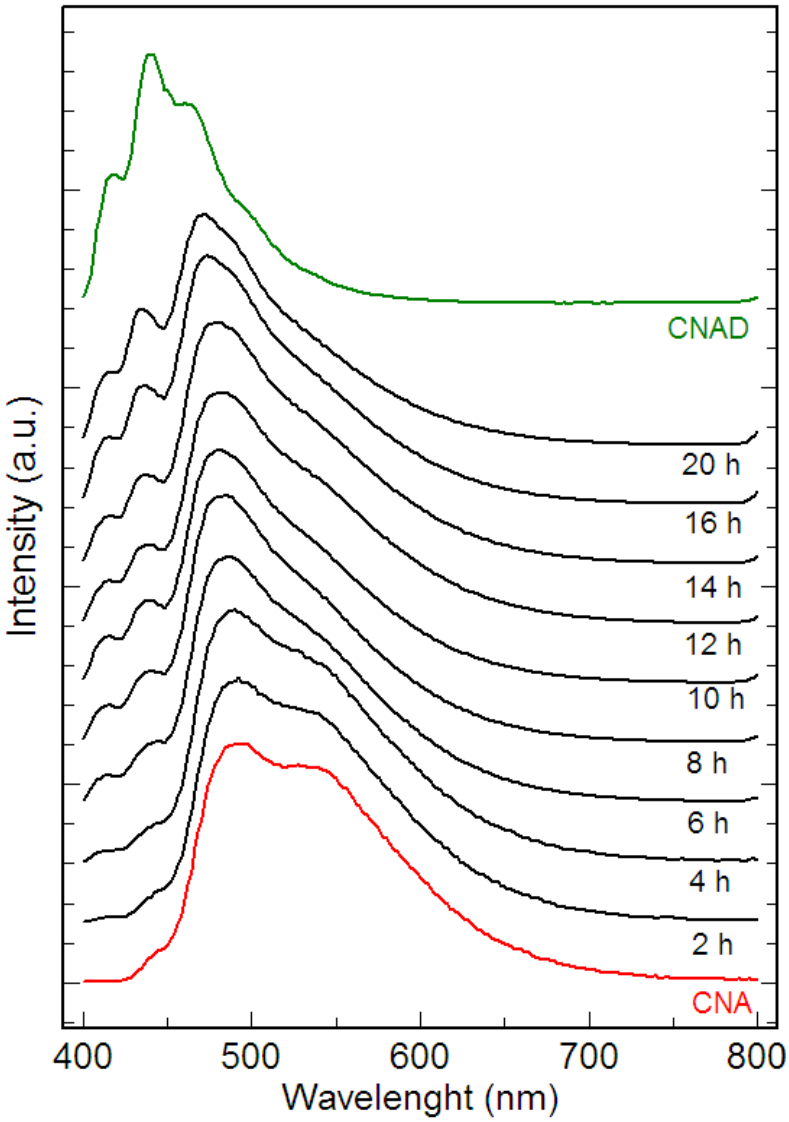

Figure 3.21 a) and b): fluorescence spectra of pure 9CNA and 9CNAD, respectively; c) set of fluorescence spectra recorded as a function of the irradiation time.

Experiments of irradiation were performed on many single crystals which showed a similar behavior as that whose Raman spectra appeared in Figure 3.20. However, it was observed the timing of the reaction depended on the size, shape and history of the starting crystal. This appears to be a common feature in crystal-to-crystal-photoreactions.

Figure 3.22 shows the bands which allowed us to follow better the progress of the *chemical reaction* with time.

The energy interval typical of C-H bending vibrations is reported in Figure 3.22a, for instance, and we can observe how the ratio between the intensities of the bands at 1040 cm^{-1} and 1018 cm^{-1}, belonging to 9CNAD and 9CNA, respectively, monitors the increasing concentration of the product and the disappearing of the reactant over a narrow wavenumber range. This intensity ratio is therefore an ideal probe to collect quantitative information on the reaction yield.

In the range 1350-1650 cm^{-1}, given in Figure 3.22b, the vibrations typical of the aromatic anthracene systems can be found [40,41], with maxima for 9CNA at 1412, 1485, 1562 and 1628 cm^{-1}, which correspond to C-C and/or ring deformation modes, all of A_1 symmetry in the 9-substituted anthracene molecule. The weakening of the intensity of these bands represents a good probe of the progress of the reaction, as it probes the loss of aromaticity arising from reaction at the carbon atoms in position 9 and 10 of the anthracene central ring.

The two series of spectra in Figure 3.20 (a and b) provide the piece of information we were looking for: a detectable concentration of dimer molecules is already present after 30 min of irradiation, but the lattice phonon spectra at this time are not changed yet. Lattice phonon bands of the dimer appear only after 90 min of irradiation. We can therefore infer that a significant concentration of dimer product must form in the parent phase, before a new crystal phase finally grows, thus following a path already detected by Raman microscopy in the dinitro-anthracene photoreaction [35].

The dashed lines in the spectra of Figure 3.20a identify the lattice dimer peaks the intensity of which is visibly increasing with time. While it is straightforward to follow the behaviour of the 9CNAD phonon bands with time, it is remarkably more difficult to use Raman bands for the disappearance of the monomer, especially below 80 cm^{-1}. This is due to the large spectral overlap between reactant and product, as can be seen by comparing the spectra of the crystals of the pure compounds, where many accidental degeneracies can be singled out. After 240 min the complete crowded spectrum of the dimer is clearly present, showing

that the system has undergone a crystal-to-crystal transformation. No further spectral changes were detectable at longer irradiation times and the Raman signal remained unchanged after keeping the sample for days at ambient *p,T* conditions. Different intensity distributions among the modes are observed when comparing the spectra of the photo-product with that the 9CNAD reference crystal. This is not surprising, in the light of the large differences among the 9CNAD spectra collected at different crystal orientations, as mentioned above. The spectrum of the photoproduct is likely the result of various crystal orientations and polarization effects, as we expect that many randomly oriented micro-domains are formed upon irradiation in the sample of Figure 3.19. In fact, similar large differences in peak intensities have been observed for all the irradiated specimens.

Noticeably, we observed that in the course of the reaction, and precisely when the dimer lattice phonons were just detectable, the position of the micro-crystal of Figure 3.19a changed with respect to the larger needle, so that at the end of the process (Figure 3.19b), after a macroscopic jump, it was seen stemming from the needle itself. The photomechanical response which accompanies several solid state photoreactions is widely studied as a potentially exploitable way of converting the absorbed light into mechanical work [35,42-47]. The mechanical work originates from of the release of the strain accumulated in the parent lattice while the reaction is progressing. As possible sources of strain, we can identify both the formation of the product molecules in the parent lattice (the guest-host mechanism) and the nucleation of the new phase (the dimer crystal) in the old one. In many cases, and especially when the reaction is fast, the uncontrolled energy release can lead to the shattering of the crystal [48], and we will also see this in dimerization reaction of 9-methyl-anthracene, though in small enough specimens with a large surface-to-volume ratio the excess energy may be dissipated through the surface.

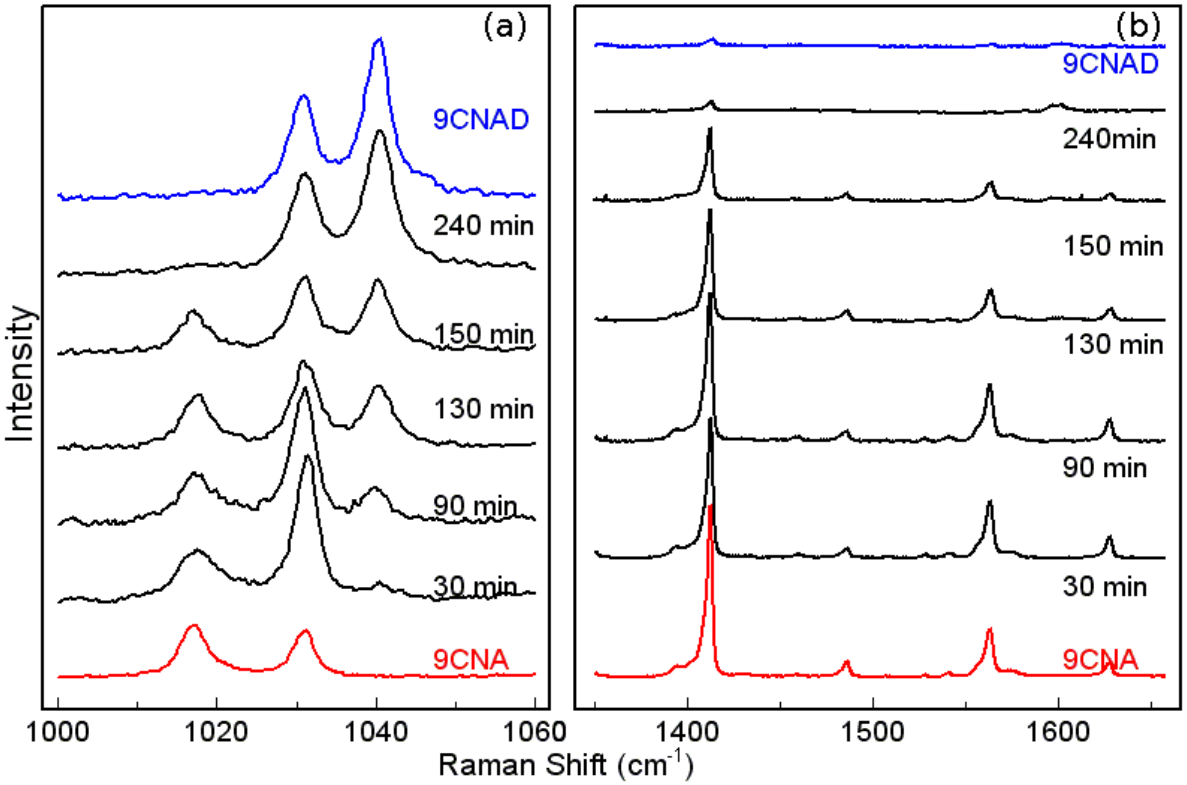

Figure 3.22 Selected bands of the Raman spectra which show the molecular transformation from 9CNA to 9CNAD; (a) wavenumber intervals 1000-1060 cm^{-1}, (b) wavenumber intervals 1350-1650 cm^{-1}.

3.2.2.3 Laser irradiation of the 9CNA crystal

Either the focused (radiative flux 340 W/cm^2) or the unfocused (radiative flux 0.03 W/cm^2) beam of a 25 mW diode laser tuned at 405 nm were also used to irradiate needles only a few micro-meters long. When the laser is unfocused, the impinging radiation is evenly spread over the entire crystal, while the radiative flux is reduced. This has the effect of slowing down the reaction, but to produce it simultaneously over a larger area, and the strain arising either at the interfaces of reacted and unreacted portions of the sample or from thermal gradients can be avoided [49]. This should prevent the localization of the photoreaction and the fragmentation of the crystal under irradiation. Indeed, the many crystals probed with the unfocused laser all reacted on time scales comparable to those recorded when employing the Xe lamp, despite the greater radiative flux of the 405 nm source. In view of the broader energy spectrum of the lamp excitation, this result is not unexpected, but it is difficult to quantify due to the variable dimensions of the various samples. Interestingly, the reaction spread quickly to the entire body of the crystals. Sometimes, macroscopic changes could be observed, such as the motion of the sample or even the nucleation of the dimer in the shape of thin whiskers on the surface and on the edges of the disrupted monomer crystal. Such a variety of

incontrollable behaviours is clearly the consequence of the fact that the different samples display different concentrations and distributions of the defects triggering the reaction in the crystals.

By employing a focused laser beam the reaction was both started and then completed in a shorter time but appeared to remain localized onto the irradiated area and the growth of dimer crystals from the surface of the monomer was always observed (see Figure 3.23).

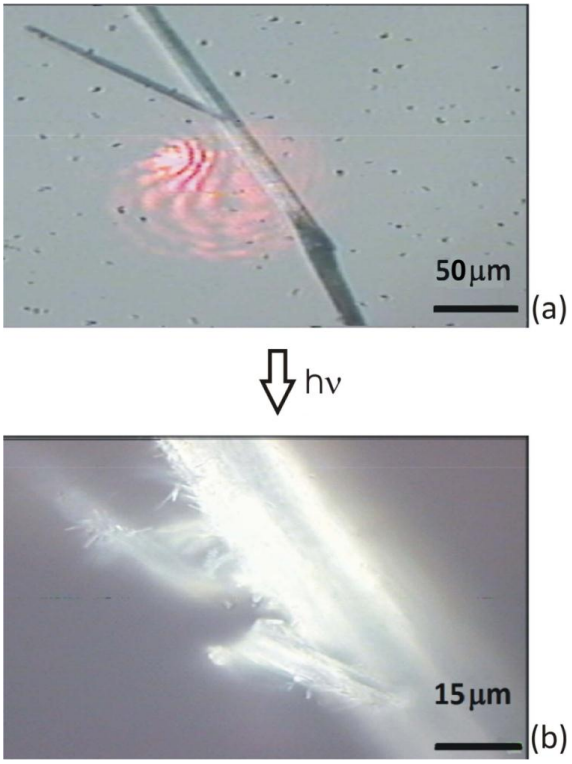

Figure 3.23 9CNA crystal before (a) and after (b) irradiation with the 405 nm line of a diode laser.

3.2.2.4 Kinetics analysis based on the intensities of the Raman bands

As just pointed out, the initial concentration of defects in 9CNA crystals determines the initial concentration of the pre-formed trans-dimers and hence of the trans-excimers which can decay non-radiatively to form 9CNAD. The Raman experiments are a direct probe of the local molecular response for the photoreaction via the time dependence of the band intensities of reactant and product. Performing a kinetic analysis over the different Raman energy ranges allows for the investigation of the observed delay between the dimerization bi-molecular event and the lattice transformation, quantitatively rather than by visually analyzing the single spectra. Simultaneously, the applicability of the various kinetic models can be tested on both processes.

In choosing the sample to irradiate for the kinetic analysis, care was taken to select a single needle crystal slightly bent at one end (and therefore certainly defective), as can be seen from the microscope image of Figure 3.24. The defective area could be entirely irradiated with a slightly unfocused laser and we assumed that here the photoreaction could be started quickly.

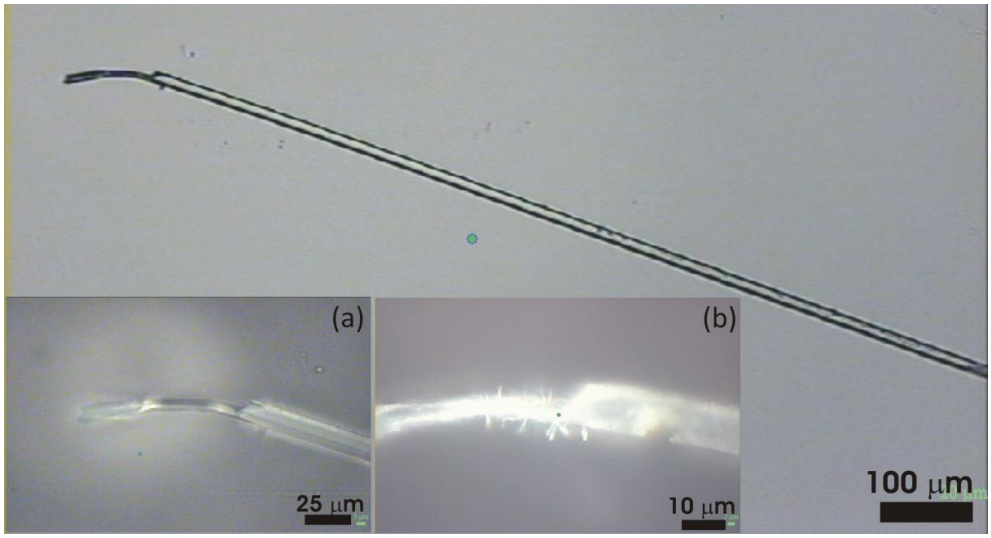

Figure 3.24 9CNA crystal selected for the kinetic study; inset: before (a) and after (b) UV irradiation with a 405 nm line of a diode laser.

The spectra used for the analysis (Figure 3.25) were collected in the very same area, which at the end of the irradiation displayed the growth of whiskers from the crystal surface. The Raman inspection of the growth confirmed this was formed by 9CNAD.

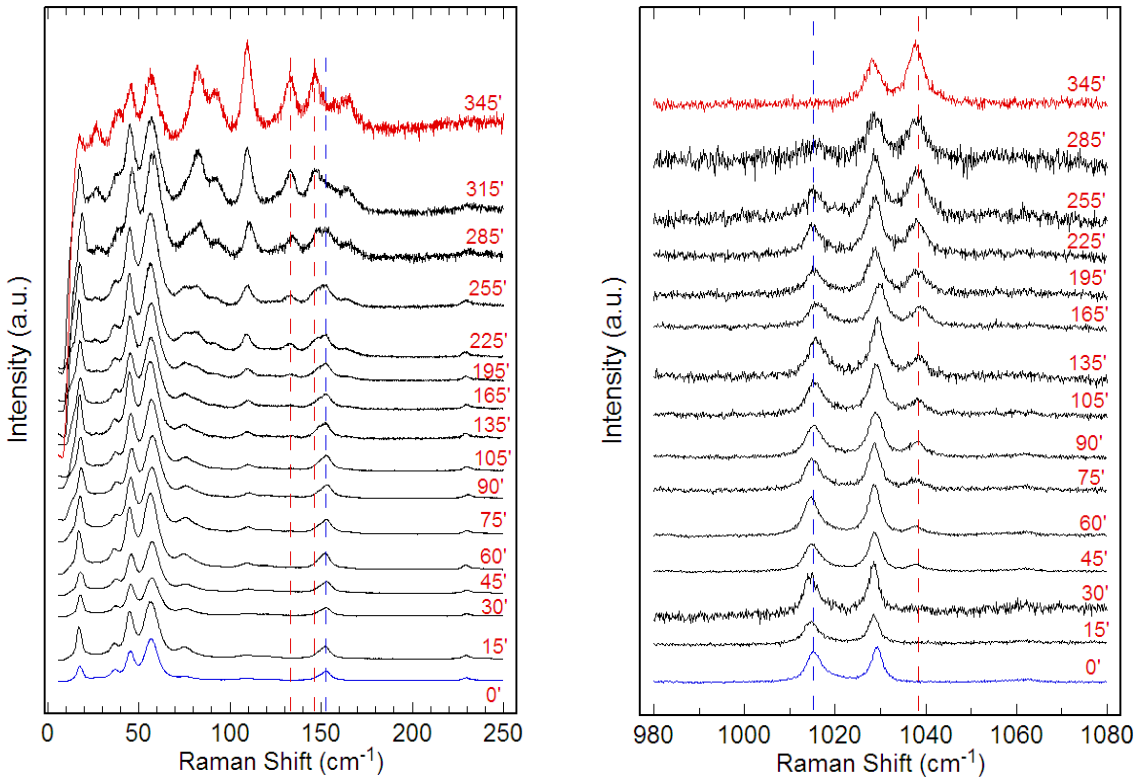

Figure 3.25 Raman spectra used for the kinetic study: on the left phonon region; on the right intramolecular modes region.

Using the micro-Raman data to analyze the kinetics offers several advantages: the technique allows for the direct investigation of the area of the crystal which is irradiated with a micrometric precision, and also allows for the close inspection of the effects in its surroundings. On the other hand, the spectra may become progressively noisier with the advancing of the reaction, while all the bands become broader. This phenomenon, which is due to the progressive loss of order in the reacting lattice while a new lattice is formed, is not surprising, but undesirable. Besides, macroscopic movements of the 9CNA crystals under irradiation, which have been recorded for a large number of specimens and normally occur when the Raman spectrum of the lattice is also changing, require the adjustment of the microscope focus, thus modifying slightly the measurement conditions. For all these reasons, intensity measurements become less reliable at long reaction times and the estimate of the reaction extent is possible only if bands of 9CNA and 9CNAD with increasing and decreasing intensities, respectively, can be safely identified over the necessary time spans. This is relatively easy for the molecular vibrations (see for instance the 1000-1060 cm^{-1} interval in Figure 3.25), but it may pose a problem in the overcrowded lattice phonon region. Here the large overlap between the spectra of the two crystals limits the number of bands which can

be used in the analysis and requires anyway global analysis methods for the determination of the band amplitudes.

3.2.2.4.1 The kinetic equation

The rather overwhelming literature on the kinetics of solid-state reactions has been reviewed in several papers [50-52]. Following the literature on the photochemical reactions of anthracene and the spectroscopic evidence, we can assume that 9CNA dimerization proceeds via i) the absorption of a photon followed by creation of an exciton (A^*), ii) the exciton migration to a defect trap, iii) the formation of excimer (AD^*) at the defect site, and iv) the final non-radiative decay of the physical excimer onto the chemical dimer (A_2). These sequence of steps can be summarized in the following scheme (in which, for the reasons given in the following, no kinetic constant are explicitly).

$$\boldsymbol{2A \xrightarrow{h\nu} A_2}$$

$$A \xrightarrow{h\nu} A^* \qquad \textbf{i}$$

$$A^* + D \longrightarrow (AD^*) \longrightarrow A_2 \qquad \textbf{ii, iii}$$

$$A_2 + A \longrightarrow A_2 + D \qquad \textbf{iv}$$

Chemical reaction and formation of the product crystal phase, as we can probe them, do not start simultaneously. The formation of the product in the host lattice and the subsequent growth of the new crystal phase both increase the concentration of the defects which trigger and then propagate the reaction, with an autocatalytic effect.

Since steps we can identify as the reaction itself and the catalytic are certainly interrelated [53], the actual reaction scheme must be quite complex and is best described with kinetic constant which express it in terms of lumped species [50]. If we use a pseudo-unimolecular step for the original non-catalyzed reaction and then add an autocatalytic effect, the kinetic equation proposed by Finkey and Watzky (FW) [54], which directly accounts for

autocatalysis, represents a particularly natural choice for analyzing our data. The FW equation, rewritten in terms of the conversion fraction α (the fraction of transformed reactant, increasing from 0 to 1) as a function of time t is

$$\alpha = 1 - \frac{k_1 + k_2'}{k_2' + k_1 e^{(k_1 + k_2')t}} \qquad (2)$$

Here k_1 is the rate constant of the original non-catalyzed reaction and k_2' the constant for the autocatalytic process. Indeed equation (2) is adopted for processes where the product of the reaction increases the rate of that reaction and has been used to describe nucleation processes with nucleation branching [53], nucleation and growth [54], autoinhibition in solids [55] and the autocatalysis photodimerization of β-9-anthracenecarboxylic acid [56].

It has been shown [52,57] that the behavior of FW equation is numerically indistinguishable from that of the classical Johnson-Mehl-Avrami-Erofeyev-Kolgomorov (JMAEK) equation [58-64], that has often been used for treating both phase transitions and solid state reactions. Although the two equations give totally equivalent fits to experimental kinetic data, the FW equation appears preferable, since it is widely accepted that the two parameters of the JMAEK equation do not provide a real physical insight of the process under investigation [52]. The classical Prout-Thomkins (PT) autocatalytic equation [51,57,65], also often used, is just a limiting case of the FW equation (when $k_2 >> k_1$). Since the FW equation is so flexible, separate fits with the JMAEK and PT equations, and other similar kinetic equations, are unnecessary.

The conversion fractions α to be fed in equation were obtained from the intensities of selected bands of reactant and product at different reaction times. Bands in the interval 1000-1300 cm^{-1} were taken for the intramolecular vibrations, while among the lattice phonons the choice had to be limited to the interval 100-150 cm^{-1}, with bands at 133, 146, 151 and 156 cm^{-1} (shown in Figure 3.26), two each for reactant and product.

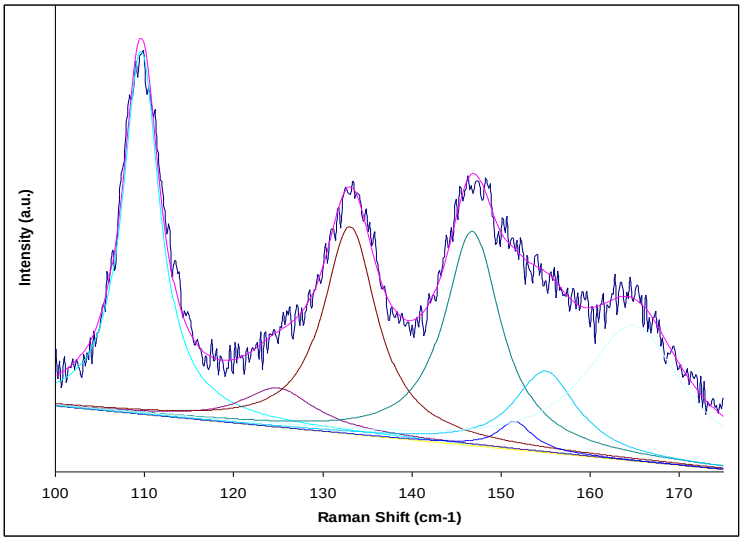

Figure 3.26 Deconvolution of the bands used for the kinetic study in the phonon region.

The observed intensities at each time were fitted as linear combination of the intensities of product and reactant with linear coefficients α and 1−α, respectively. Band intensities of the pure compounds, overall intensity of each spectrum, and the fraction α, were the adjustable parameters.

Figure 3.27 shows the fractions α reaction time, as obtained from the intensity analysis of either the intramolecular vibrations or of the lattice phonons, together with the corresponding FW fitted curves. In both cases, the fits yielded R^2 values ≥ 0.99.

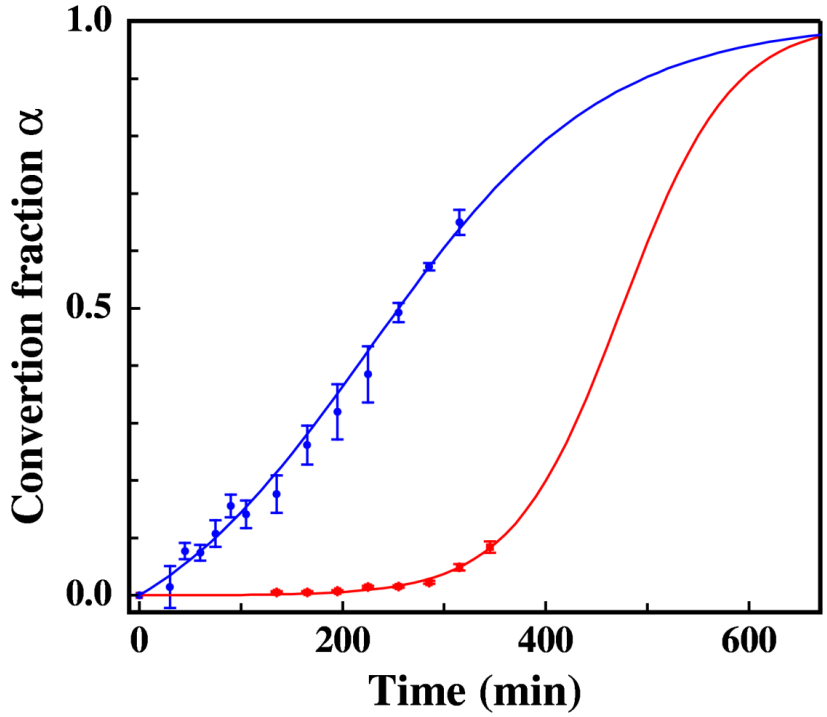

Figure 3.27 Conversion fraction α as a function of time as obtained from the band intensities of micro-Raman spectra. Blue and red points: α values from the global fit to the measured intensities of intramolecular modes and lattice phonons, respectively. The half width of the error bars indicates the 3σ standard deviation. Lines: fitted curves according to the FW equation.

In the case of the intramolecular vibrations, the range of α values covers about the 65% of conversion for the sample chosen and the autocatalytic model works well, with fitted constants $k_1=(1.04\pm0.05)\times10^{-3}$ min^{-1} and $k_2'=(7.7\pm0.2)\times10^{-3}$ min^{-1}. As the two rates have comparable values, we may conclude that the initial concentration of defects, which may act as "reaction intermediates" in the dimer formation, rules the early stage of the reaction.

The kinetic analysis based on the lattice phonon intensities provides information on the rearrangement of the crystal lattice of the reactant into the crystal lattice of the product. The investigated interval covers a range of transformation more limited than that of the chemical reaction, partly due to the experimental problems reported above, but also due to longer delay of the transformation itself. Nonetheless, some interesting conclusions can still be drawn. The FW kinetic laws still applies, with fitted constants $k_1 = (2.8\pm0.3)\times10^{-6}$ min^{-1} and $k_2' = (1.85\pm0.04)\times10^{-2}$ min^{-1}.

Since $k_2' >> k_1$, this is actually the limiting case in which the classic PT autocatalytic rate law applies. The non catalytic constant k_1 is orders of magnitude smaller than the autocatalytic constants k_2' of both the chemical and physical processes, which have comparable values.

From a physical point of view, this implies that the initial concentration of nucleation "seeds" of crystalline 9CNAD is very low and grows slowly with time. From a purely mathematical point of view, it means that the curve describing the lattice transformation is shifted forward on the time axis with respect to that of the chemical reaction by a delay which corresponds to the induction period of the process. As a result, we find that ≈ 30% of the monomer molecules have already reacted when finally the bands of the new lattice can be observed in the Raman spectrum. The time elapsed between the onset of the chemical reaction and the re-organization of the lattice is the time needed for the product concentration to cross a saturation limit and determine the new phase segregation. The autocatalytic effect, via an increasing concentration of (chemically and physically) reacting centers, drives the transformation.

As far as the expected reaction yield is concerned, it has been demonstrated [66,67] that photodimerizations in one dimensional stacks cannot proceed to a complete monomer to dimer conversion, due to formation of isolated monomers which remain unreacted. Photodimerization driven by defects has also been theoretically considered [66], and it has been suggested that a sizable population of isolated monomers should remain also in this

case. Due to this theoretical prediction and to the observation of exciton emission attributable to unreacted 9CNA, we cannot assert that the 9CNA to 9CNAD reaction proceeds to completion. For this reason, we have repeated the fits with equation scaled to yield an adjustable final conversion factor α_∞. Although the data are not inconsistent with values of α_∞ just below 1, no statistical improvement of the fits was found with respect to the unmodified equation (α_∞=1).

In conclusion, the Raman, fluorescence and optical observations described in this thesis, together with the kinetic analysis of the Raman intensities yield a coherent picture of the 9CNA solid state dimerization. In the classic literature on solid state photochemistry (Ref. [15,25-29] and references therein), reactions in which a phase separation occurs were classified as heterogeneous, as opposed to those in which there is not such separation. The distinction might not be rigid, as in some cases the system can remain homogeneous up to a certain degree of chemical conversion and then switch to heterogeneous. Very recently [68], photoinduced denitrogenation solid state reactions in triazolines were studied as test models and the nature of the physical changes accompanying the reactions were reviewed, also in the light of a previous analysis on the same subject [48]. Following an initial stage of solid solution with the reactant, which can be identified as a homogeneous system, the product can i) transform into an amorphous phase, ii) form a metastable phase in the lattice of the reactant, iii) undergo a structural reconstruction into a new lattice or, finally and more rarely, iv) show a single-crystal-to-single-crystal transformation.

Indeed, the growth of the new crystal phase of the product portrays the photodimerization of a single 9CNA crystal as a typical case of phase reconstruction. By employing the micro-Raman technique, a single measurement clearly allows for the identification both of the stage in which the reacted molecules are hosted in the parent lattice, with the dimer forming a solid solution with the monomer, and the onset of the structural reconstruction. The spectroscopic data show that no amorphous phase is formed during the irradiation, as a lattice phonon pattern is retained in the irradiated spot at all reaction times. The dimer crystal structure is detected to appear only when a sizable portion of monomer molecules have reacted, without the single crystal showing at this stage macroscopic changes as shattering or fragmentation. However, as the spectroscopic technique reveals that the lattice is finally changing, the accumulated lattice strain can be released and the relaxation process induces quick movements or jumps.

The kinetics analysis here performed of the chemical reaction and of the phase transformation supports the early hypothesis of an autocatalytic mechanism [45,48-50]. Certainly, the complexity of solid state reaction mechanisms precludes the possibility of identifying the elementary autocatalytic steps [50]. Nonetheless, the picture of an advancing front of reacted molecules, starting from a defect and propagating in its surroundings, conveys the idea of an autocatalytic process in our chemical intuition. In fact, it has been proposed [69-71] that in defect induced reactions, new defects are created by the separation of the product phase. However, even before a phase separation occurs, the formation of any new dimer molecule generates new defect sites [66], which are the source from where the reaction can spread further.

3.3 9-methyl anthracene photodimerization reaction.

9-methyl anthracene (9MA) is another anthracene derivative that undergoes a [4+4] photodimerization by irradiation with a wavelength λ > 300 nm [16,72-77] both in solution and in the solid state. The reverse process can be induced by heating or by UV light with λ below 300 nm (Figure 3.28) [78-80], but the crystalline photodimer is stable at ambient conditions and the reaction can be classified as effectively irreversible.

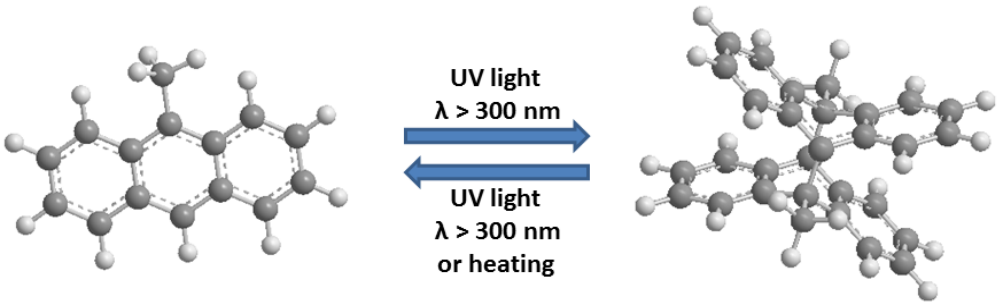

Figure 3.28 Photodimerization scheme of 9MA

In the literature, a number of 9-substituted anthracenes have been investigated and most of them follow the topochemical principle, with the noticeable exception of 9-cyano anthracene, treated in the previous section. 9MA follows this general rule, thus only the *trans* dimer is expected in the solid state, as observed in previous experiments [77,81] and in the present work.

The structure of the monomer 9MA and of the dimer 9MAD have been published by Bart et al. [82] and Cox et al. [83] and have been more recently re-determined by Turowska-Tyrk et al. [75]. 9MA and 9MAD crystallize in the same monoclinic structure, space group $P2_1/c$, with 4 molecules (Z=4) and 2 molecules (Z=2) per unit cell, respectively. The cell parameters are reported in Table 3.2.

Table 3.2 Cell paramaters of both 9MA and 9MAD structures [75].

	9-methyl anthracene (9MA)	9-methyl anthracene dimer (9MAD)
Chemical Formula	$C_{15}H_{12}$	$C_{30}H_{24}$
Molecular weight	192.25 g/mol	384.49 g/mol
Crystal system	monoclinic	monoclinic
Space group	$P2_1/c$	$P2_1/c$
A	8.8859(13) Å	9.7650(13) Å
B	14.594(2) Å	13.6035(19) Å
C	8.0395(11) Å	8.1177(10) Å
A	90°	90°
B	96.505(14)°	113.308(15)°
Γ	90°	90°
V	1035.86 $Å^3$	990.338 $Å^3$
Z	4	2

A comparison between the two structures (Figure 3.29) provides useful hints for the understanding of the mechanism of the photodimerization reaction. First of all, the monomer in the packing is organized in pairs of molecules related by the crystal inversion centre, with distances between adjacent ones below the threshold of 4 Å. In this almost perfect fit for a *trans* dimerization, a reaction quickly progressing with a high yield is expected. Secondly, the structures of both monomer and dimer belong to the same space group $P2_1/c$, with differences in cell parameters in the 1% to 10% range.

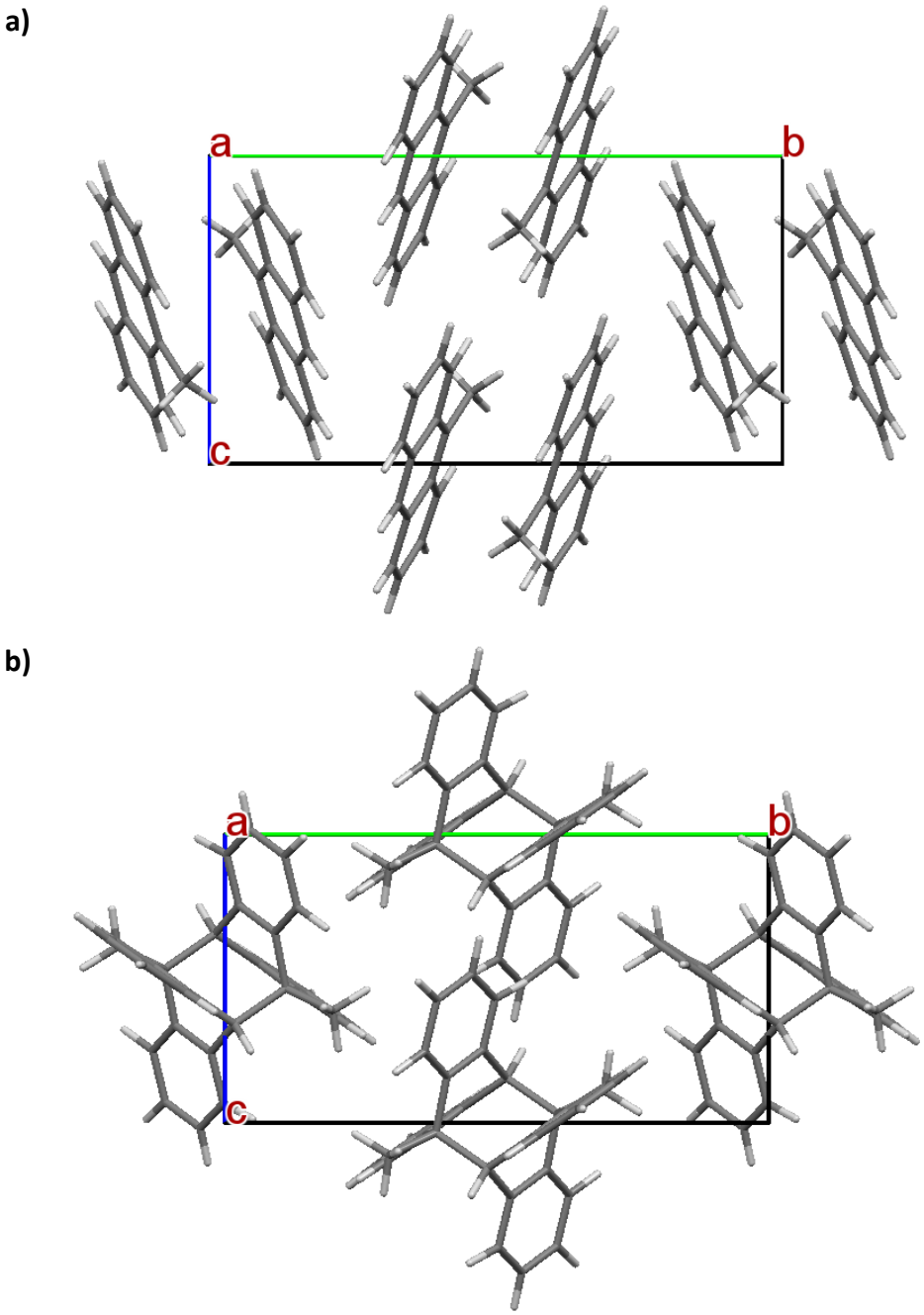

Figure 3.29 Crystal structure of a) 9MA monomer and b) 9MAD [75]. View is along the *a* axis

Such a limited variation accounts for the reasonable volume contraction of 4.4% observed in going from the monomer to the dimer. Lastly, the molecular orientations in both structures are well compatible with the established reaction mechanism, which predicts the bending of the anthracene rings at positions 9 and 10 under irradiation, to facilitate the photodimerization. In other words, reactant molecules appear to be in an ideal structural preformation to give the *trans* topochemical dimer, with a reaction yield which can be estimated to be close to 100%. The crystal-to-crystal transformation would still require slight structural rearrangements, and these would explain the mechanical motions that accompany this as well as the other solid state reactions described in the previous paragraphs of this chapter.

The structural match between reactant and product in the present case gives the chance of having a 100% conversion. This makes of 9MA an ideal model system to illustrate how heterogeneous reaction kinetics, together with a suitable crystal shape, can be used to design elements of new potential photomechanical materials [77].

3.3.1 Lattice phonon Raman spectra of the reference crystals.

9MA was purchased from Sigma Aldrich and the single crystals were grown from an acetone solution by slow evaporation at room temperature. 9MAD was synthesized by irradiating a nearly saturated solution of 9MA in ethanol with a XBO lamp for 4 hours, using a bandpass filter to select the 300-400 nm wavelength range. Colorless rhombohedral crystals of 9MAD, as shown in Figure 3.30b, were obtained by precipitation from the ethanol solution. Both 9MA and 9MAD crystals were characterized by Raman spectroscopy in the lattice phonon (Figure 3.30a) as well as in the internal vibrations (Figure 3.30c) regions. The latter spectra were found to differ especially around 1400 cm^{-1}, where some typical modes of the anthracene backbone obviously disappear after dimerization, as reported above 9CNAD. More different spectral features characterize the range 300-600 cm^{-1} and above 120 cm^{-1} (Figure 3.30a).

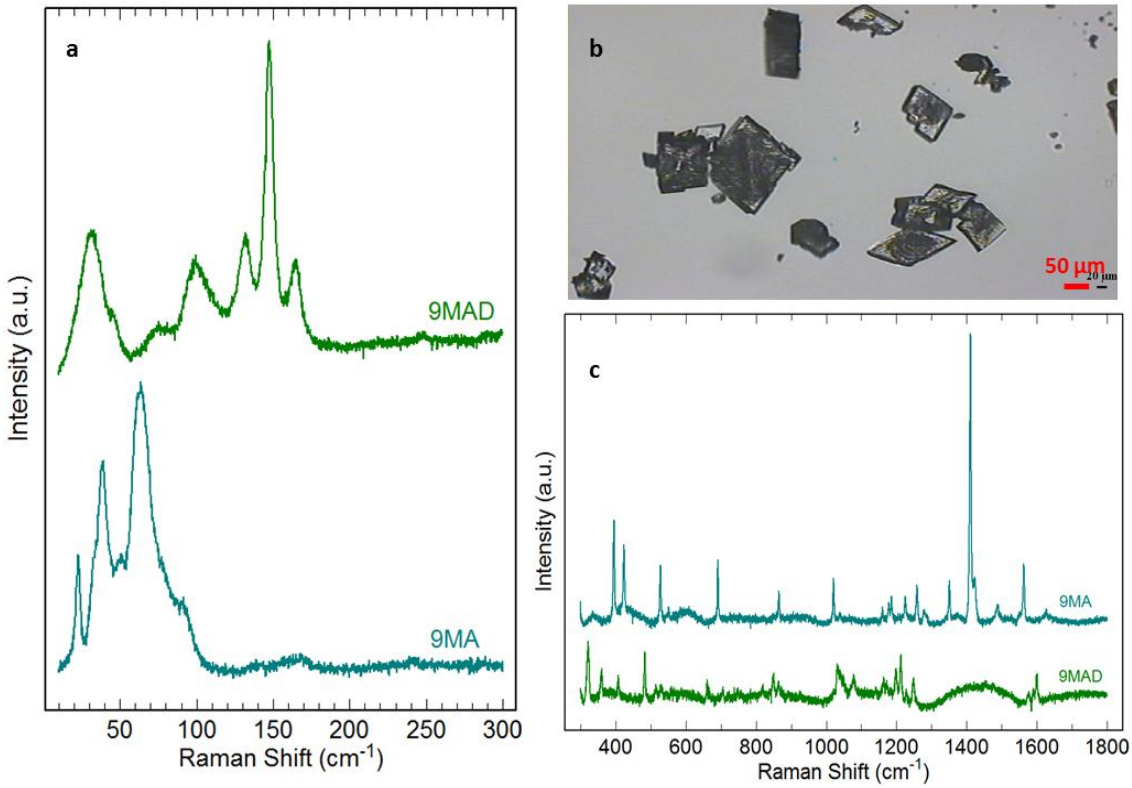

Figure 3.30 a) Raman spectra down to the lattice phonon region of 9MA and 9MAD; b) crystal shape of the 9MAD crystals obtained from the irradiated in solution; c) Comparison of intra-molecular modes of reactant, 9MA, and product, 9MAD.

Polarized phonon spectra of 9MA and 9MAD are shown in Figure 3.31. An accurate analysis of mode assignment was beyond the aim of the present work, where the main purpose was to understand qualitatively the anisotropic effects due to reorientations of the samples during the reaction. It was also important to check the profiles of the spectra of the crystal powder against those of single crystals in different polarization conditions. Therefore, we limit the discussion to recall that a mutual exclusion rule is expected for the A_g (parallel-parallel, or par-par configuration) and B_g modes (parallel-perpendicular, or par-perp configuration) of a centrosymmetric monoclinic crystal. All the bands of gerade symmetry must be instead visible in a powder-like sample, where all possible orientations are present and therefore the complete A_g+B_g spectrum should appear. This is perfectly reproduced in the spectra of 9MA (left side of the figure) as in a textbook example. The bands in the region above 110 cm^{-1} belong to internal modes, which are expected show as closely spaced A_g+B_g doublets. Lattice dynamics calculations, not reported here, confirm this finding.

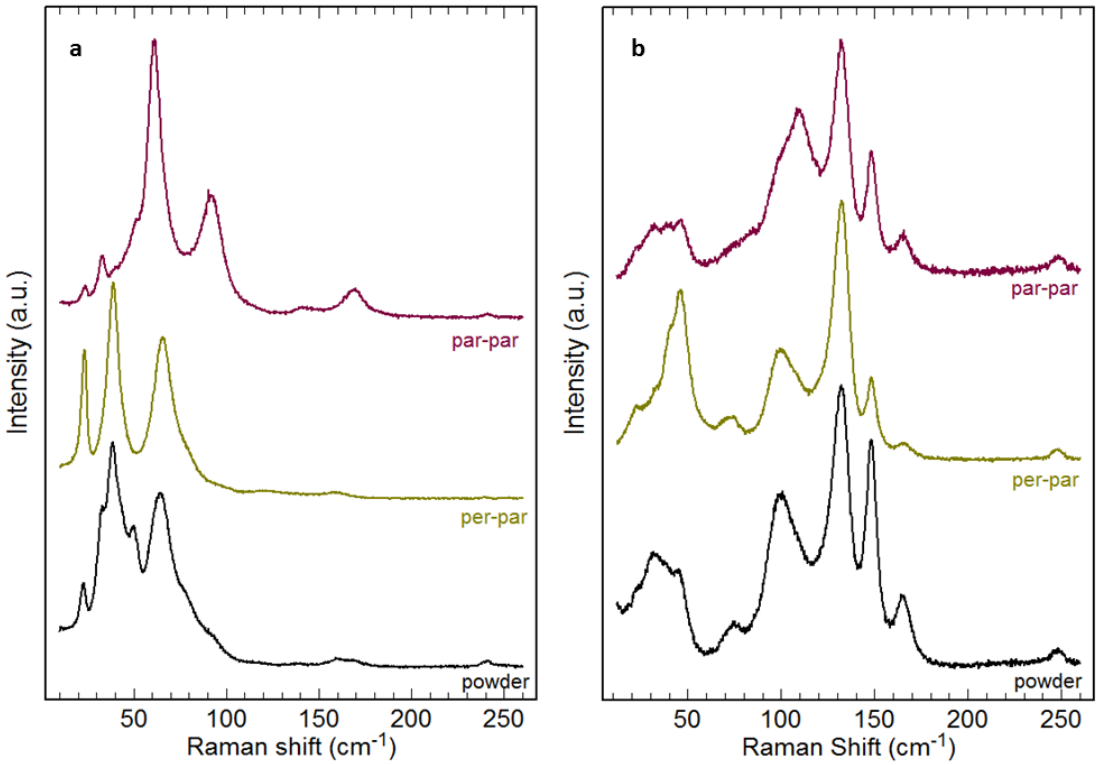

Figure 3.31 Polarized lattice phonon spectra of a) 9MA and b) 9MAD.

The same considerations hold for the polarized spectra of the dimer shown in Figure 3.31b, which also follow the selection rule of mutual A_g/B_g exclusion in the corresponding monoclinic system. Here the frequency range boundary between inter- and intra-molecular modes is even more evident: the three most intense bands above 120 cm^{-1} are easily assigned as intramolecular. For these modes, doublets with different polarizations are expected, but just one band for both of them shows up in either configuration, not being resolved at room temperature. Their unusually high intensity can be explained by the more flexible nature of the dimer molecule, whose low frequency internal modes should therefore be larger than those of the monomer, both in number and activity, carrying a stronger coupling with the lattice phonons. Again, what observed above is confirmed by lattice dynamics calculations.

3.3.2 Raman spectra of the irradiated samples.

The photodimerization of 9MA crystals was first studied using high-resolution solid state ^{13}C NMR by Takegoshi et al. [83], who showed that only the trans photodimer was formed. The same study reports that both *cis* and *trans* dimers are produced in solution, although the *cis* dimer is thermodynamically unstable and a thermal reverse reaction occurs [16,84]. Later, Turowska-Tyrk [75] and coworkers monitored the structural changes in a crystal

of 9MA during the photodimerization by means of X-ray diffraction, recording only a 28% degree of monomer-dimer conversion, because of crystal disintegration. They justified the disintegration process as due to the dimer crystal packing, which resulted in an increase of the unit cell volume at the beginning of the reaction, followed by a subsequent contraction. It is worth mentioning, however, that the irradiation power they used was of 24 mW/mm^2, that is four order of magnitude larger than that used in the present work, and this can reasonably explain the outcome of their experiment. In a time resolved X-ray diffraction study by Mabied and coworkers [76], the complete transformation of the reactant was reported for powder samples and, obviously, using these rather than macroscopic single crystals prevented the system disintegration.

A very recent study [77] reports on how crystal morphology and reaction dynamics can affect the photomechanical deformations of single microcrystals. By changing preparation conditions, Bardeen and coworkers obtained differently shaped crystals, microneedles or microribbons, which bent or twisted, respectively, under irradiation. For both shapes, the maximum deformation occurred at roughly the midpoint of the reaction, after which the crystals recovered their original shape. This behavior was qualitatively explained as the result of the motion driven by the strain between spatially distinct reactant and product domains, also called heterometry [77]. However, the Authors found no explanation for a sizable amount of unreacted monomer still found in their system at the end of the process.

Different techniques have been used to study 9MA photodimerization but not all of them are equally effective to follow the dynamics of the reaction. The crystal size is also of relevant importance, because of the constraints produced in large crystals under transformation, which lead to disintegration and prevent following the reaction by x-ray single crystal technique. In this thesis we report the study of 9MA photodimerization by means of Raman spectroscopy both in the lattice phonon and in the intramolecular vibrational regions, where we have detected the structural modifications and the chemical transformation, respectively.

Figure 3.32 shows the morphology of a crystal of monomer before and after irradiation with a diode laser of 20 mW of power, tuned at 405 nm and focused on a specific region of the sample. The starting power impinging onto the sample was $3x10^{-3}$ mW/mm^2, but was attenuated with an optical filter by a factor of two. Nonetheless, after 5 minutes of irradiation the crystal had already split in two bits. The Raman spectra were collected (Figure 3.33) and

the transformation resulted so fast that both inter- and intramolecular spectra did not show any residual peak of the monomer, suggesting that the reaction had reached its completion. It is worth mentioning that the reaction was not confined to the surface of the crystal but had been propagating in its depth, as confirmed by the spectra recorded by varying the microscope objective from 50x to 10x.

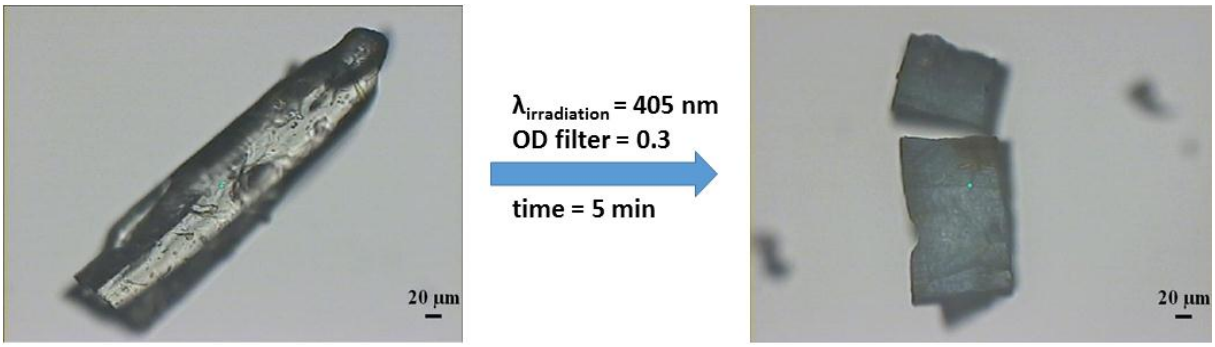

Figure 3.32 Crystal morphology of the crystal before (left) and after (right) 5 minutes of irradiation.

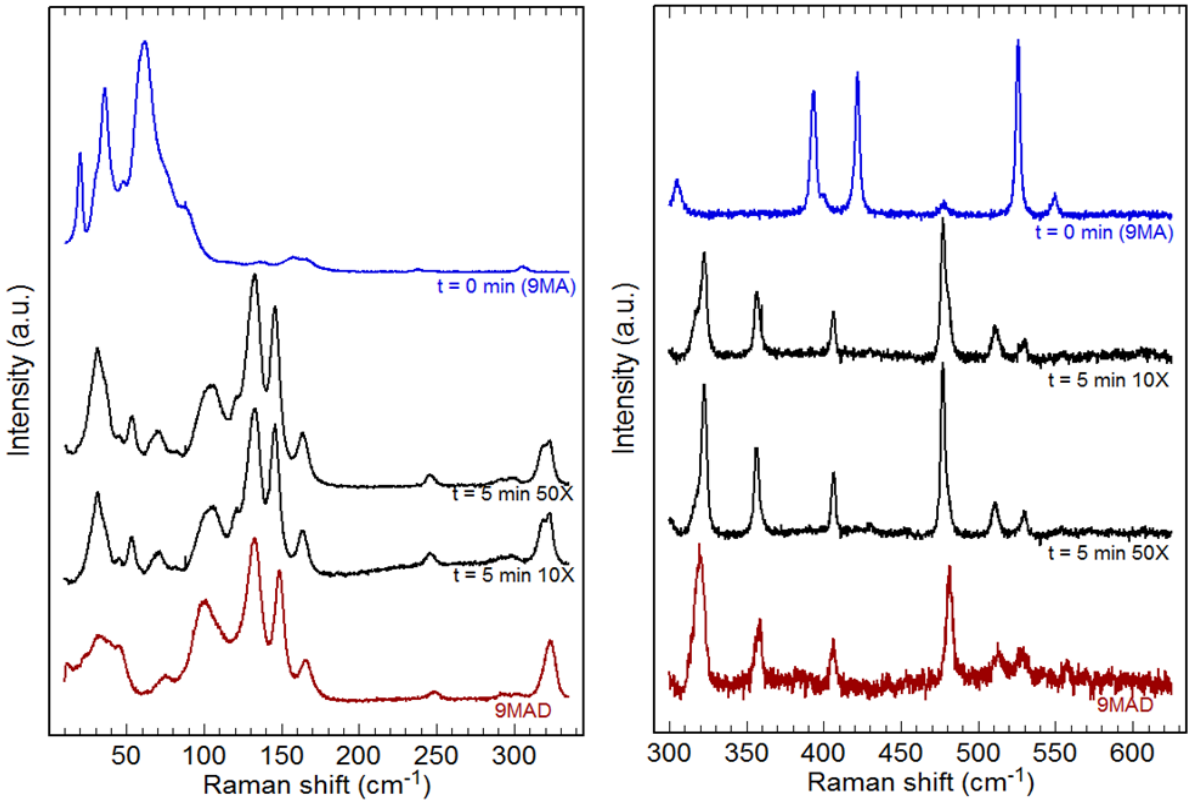

Figure 3.33 Raman spectra in the lattice phonon region (left) and in the 300-600 cm^{-1} intra-molecular region (right) for the irradiation process of the crystal shown in Figure 3.32.

A new crystal, shown in Figure 3.35, was also irradiated, attenuating the power by a factor of two order of magnitude. Even with such a lower irradiation power the crystal broke again in two parts after 25 minutes. The Raman spectra of the largest segment at this stage of the reaction are shown in Figure 3.34.

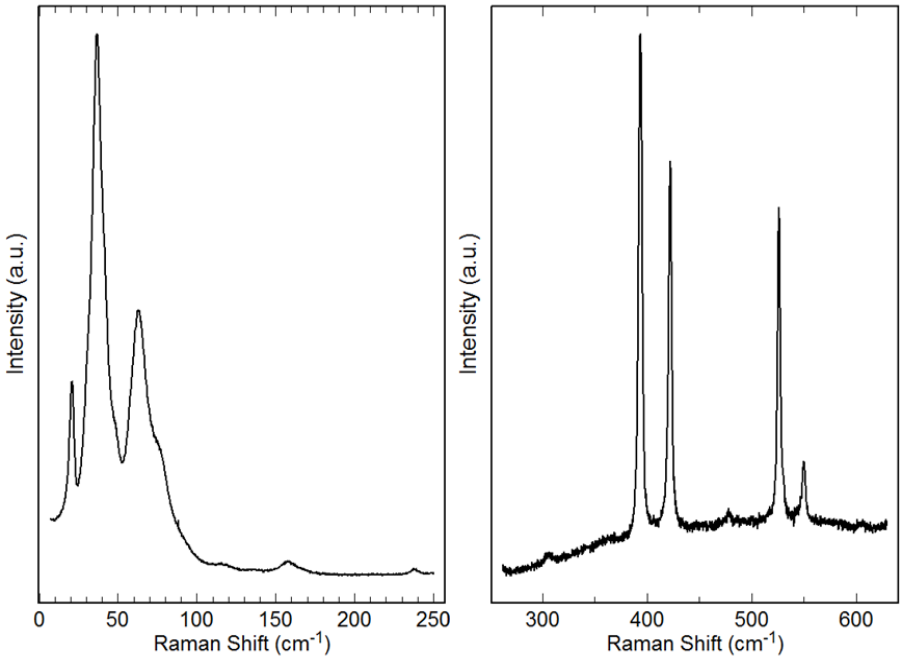

Figure 3.34 Raman spectra in the lattice phonon region (left) and in the 300-600 cm^{-1} intra-molecular region (right) at time 25 minutes.

By looking at the figure, it is interesting to notice that, in these conditions and at this reaction time, we have picked up the onset of the molecular transformation at its very beginning, whereas the lattice has not yet changed. In fact, the small band above 300 cm^{-1} is the only modification observed in the Raman spectra, and it probes the initial appearance of dimer molecules in the unchanged monomer lattice.

The largest fragment was irradiated for further 10 minutes and the spectra of figure 8 indicate that this additional irradiation time was sufficient to reach the completion of the photodimerization. Also shown in the figure is a linear scan of the spectral profiles, which was recorded starting from the point where the laser beam was focused up to the not irradiated end. The purpose of this experiment was to identify the possible propagation of the front of dimer molecules into the non irradiated regions of the crystal, by producing a set of spectra of both phonons (Figure 3.35 left side) and internal vibrations in the range 150-600 cm^{-1} (Figure 3.35 left and right sides). Both spectral regions show that the reaction is indeed confined to the irradiated zone of the sample, without any propagation to the rest of the

crystal. Reacted and unreacted zones can also be distinguished from each other by the different degree of grey shade on the crystal surface.

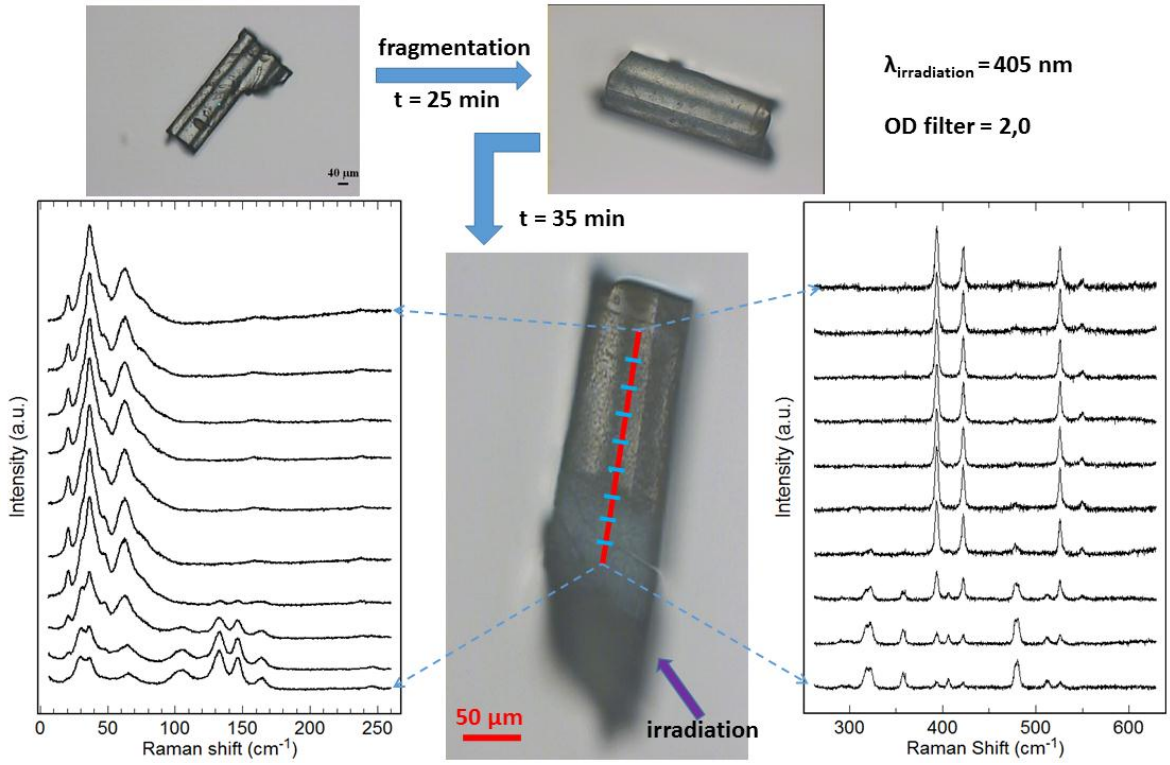

Figure 3.35 Crystal shape of the 9MA before and after irradiation and linear map of the lattice phonon (left) and intramolecular (right) spectral range.

Finally, to better understand the progress of the reaction, a fresh monomer crystal was irradiated with an attenuation of the laser beam by a factor of 1000, *i.e.*, an effective power onto the crystal of $3x10^{-6}$ mW/mm^2. The pictures of the crystal before and after 21 minutes of irradiation, together with the corresponding Raman spectra, are shown in Figure 3.36. The spectra definitely confirm that after 21 minutes some dimer bands start to appear (see the internal vibration bands marked with vertical red lines in the figure) whereas the lattice phonon spectra are still entirely those of the monomer lattice. The crystal, despite being transformed, maintains its shape without breaking.

It is now definitely clear that the molecular transformation precedes that of the crystal and the dimer molecules are hosted in the monomer lattice in the early stages of the reaction. In the specific case of 9MA-9MAD, this agrees with the idea of the almost perfect geometrical fit of reactant and product systems, which we were able to infer on the basis of the structural data of Figure 3.29. This is also in agreement with the results obtained for other solid state photoreactions reported in literature [35,85] and illustrated in the previous sections of this chapter.

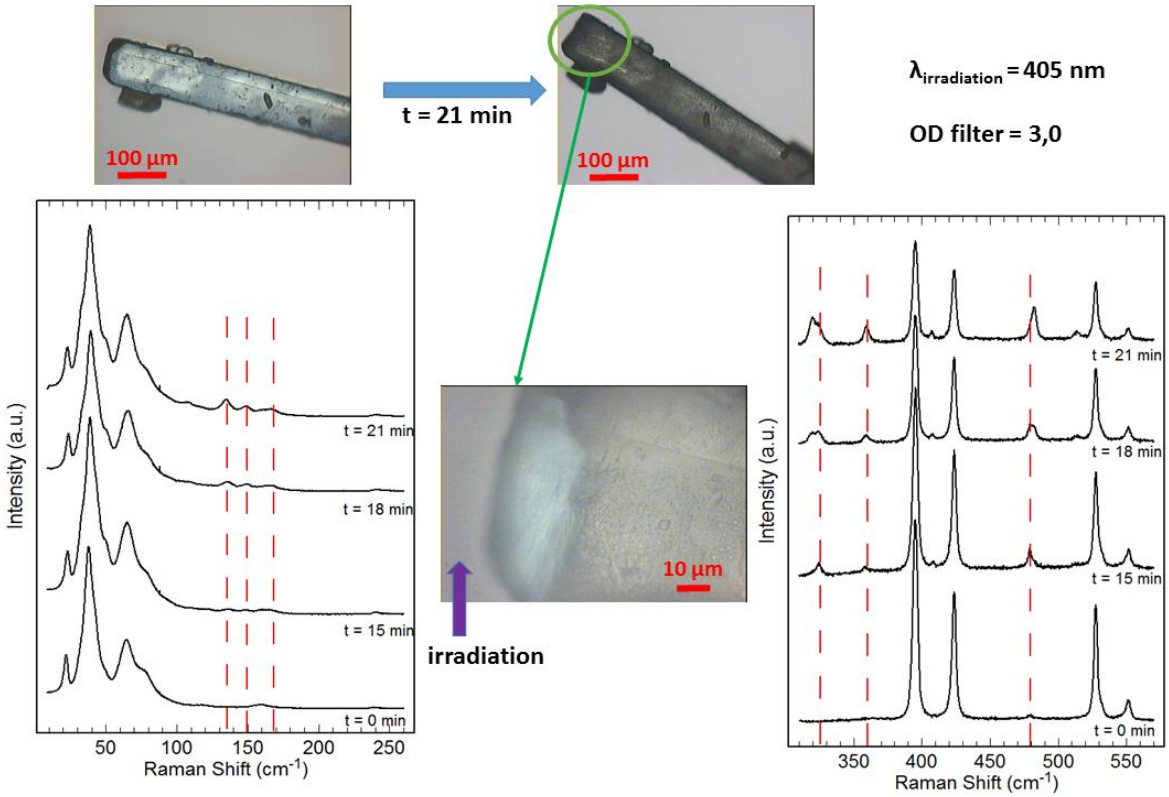

Figure 3.36 Crystal morphologies before and after irradiation by a diode laser tuned at 405 nm with an optical filter OD = 3.0. Raman spectra in the phonon (left) and in the intramolecular (right) regions. In the middle a close up of the actual irradiated zone of the crystal is shown. The vertical lines mark internal modes of the dimer molecule.

In conclusion, we performed a Raman study of 9MA during its [4+4] photodimerization reaction. By using microscopy and confocality we were able to investigate at the same time and in the very same spot the reaction dynamics for both its molecular and its lattice transformations. This [4+4] cyclo-addiction is a typical example of a crystal-to-crystal photodimerization which follows perfectly the topochemical principle [26]. The study was carried out using the setup described in chapter 2 and irradiating the sample by a diode laser tuned at 405 nm and modulating its power of irradiation to slow down the reaction in its initial stage. In this way the fragmentation of the single crystal could also be avoided.

It is worth comparing these last results obtained what obtained for the photoreactions of DNO_2A (paragraph 3.1) and 9CNA (paragraph 3.2). As already observed with the crystal-to-crystal reaction of DNO_2A to AQ and with the dimerization of 9CNA, the chemical transformation (molecular changes) precedes the crystal lattice transformation (physical changes).

The mechanical response to the light, which is clearly depending on the shape and the length scale of the crystal, has been attributed to the interfacial strain generated at the interface between different domains of the dimer embedded in the monomer matrix [77].

The actual value of the reaction yield for the solid state dimerization of 9MA is still matter of debate. The expectation would be for a yield close to 100%, because of the perfect fit between reactant to product molecules. In their work, Mabied and coworkers [76] reported that the reaction in a polycrystalline powder had gone to completion. However, their analysis was based on the disappearing of the monomer signals in the IR spectra, which can monitor the reaction progress from the molecular point of view only, and give no information on the corresponding changes of the unit cell. Bardeen and coworkers [77], working on microribbons and microneedles, observed a 10-20% of unreacted monomer. As mentioned above, the Authors could not provide a clear reason for this behavior as, unlike 9ACA and 9CNA, monomers are already paired in their lattice, and statistically none of them should be left out as the reaction goes on. Lattice distortions and formation of local defects in the course of the reaction were claimed as possible explanations [77].

In the present experiments we did not observe any residual monomer bands (see Figures 3.33 and 3.35) in the Raman spectra, and this is a neat indication of a complete reaction, within the detection limits of the spectroscopic method. Moreover, the topochemical nature of the process makes this transformation dramatically faster than those previously studied [35,85], with the photoproduct that can be obtained within minutes. We believe that reaction rate and reaction yield are two non separable factors in solid state reactions, which both drive the outcome of the reaction. It may well be of course that a role, for the purpose, is played by defects, kind and size of the sample and its history: intrinsic defects of the sample can destroy the perfect order of the molecules, *prior* of the formation of reactive sites, changing the kinetics of the reaction and forming an amount of un-reacted monomer.

3.4 The Reversible Photodimerization reaction of 9-anthracene-carboxylic acid

In the search of model systems for solid state photodimerizations of substituted anthracene compounds it was unavoidable to deal with the case of 9-anthracenecarboxylic acid (9ACA) (Figure 3.37), as an example of reversible reaction.

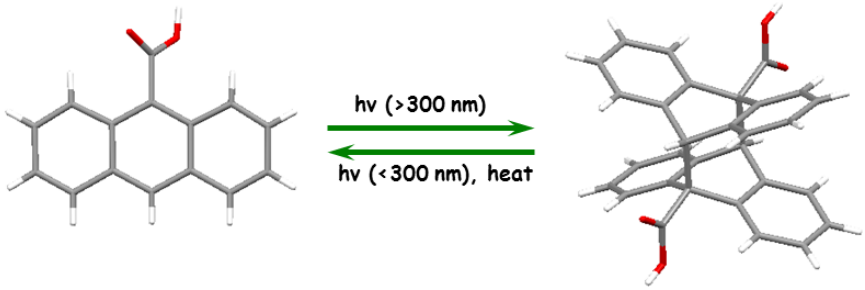

Figure 3.37 9-Anthracene-carboxylic acid structure and reactivity scheme.

In both the known polymorphs of 9ACA [16,49,86,87] the anthracene backbones of the molecules are aligned in stacks in which the geometrical requirements for the [4+4] dimerization, following the topochemical principle, are fully satisfied. Besides, the system displays excimer fluorescence, that is the proof of the formation of the intermediate state, whose existence is the first necessary step of the reaction. However, the molecules in the 9ACA crystal stacks are arranged to yield the sterically hindered head-to-head (cis) photodimer, and already in 1971 Schmidt and Heller [16] stated that 9ACA was highly photostable in the solid state. Since then there have been a number of reports [49,87,88] which contradict the early findings. In the light of the results of these reports, 9ACA does dimerize in its crystal state, but the reaction is reversible within a timespan which depends on sample size and history, temperature and exposition to ambient light. The photoreaction takes place relatively quickly in solution [89], where it yields a mixture of both head-to-tail and head-to-head dimers, with the former prevailing by a ratio of 5:1, but Ito [88] found that the head-to-head form was actually more stable in the solid state than in solution. Most recently Bardeen and coworkers [11,47,49,90] have described a reversible twisting of microribbons of 9ACA resulting from its light irradiation. The analysis of the experimental data suggested that crystal motion is generated by the interfacial strain between unreacted monomer and photoreacted dimer regions within the crystal, as in the case of 9CNA reported in chapter 3.2.

Photoactivated motions in reversible systems have been considered particularly appealing in the search of micro and nano photoresponsive objects [11,47,49,90], and this is

one of the reasons why research on systems like 9ACA and similar compounds has been revisited.

Interestingly, however, X-ray characterization of neither photodimer, head-to-tail- or head-to-head have ever been reported in the literature, being in fact the crystal motion under irradiation the sole hint of the structural modification. In the case of the head-to-head dimer in the solid state reaction, one can assume that this is due to the short lifetime of the species and that by the time the system could be probed by X-rays, it has already reverted to the monomeric state. It is all the same quite surprising that even after 77.8 h of irradiation, crystal samples still display the X-ray structure of the monomer, just with an increased disorder [87].

In the light of the somehow controversial and incomplete information available on 9ACA solid state behavior under irradiation, our work on this system focused on the detection of the structural change linked to the chemical transformation. In other words: after recognizing that NMR and spectroscopic results detect the (labile) existence of the dimer under irradiation, we wondered whether the elusive crystal-to-crystal step could be observed by lattice phonon Raman spectroscopy. The presence of two stable 9ACA polymorphs and their possible different reactivity also needed be investigated.

3.4.1 Experimental

The overall instrumental set up and the irradiation conditions were the same as for 9CNA and have already been described in detail in Section 3.2.1 of this Chapter.

Well formed, single crystals of 9ACA, suitable for irradiation, were grown by slow evaporation either from ethyl acetate or p-xylene solutions of the commercial product from Aldrich, following the procedure described in Ref [11]. In the former case it is possible to obtain the monoclinic $P2_1/n$ polymorph [11,86], also present in the pristine material and named hereafter α-9ACA. In the latter case the triclinic $P\bar{1}$ structure (β-9ACA) is instead grown. Light yellow needles a few mm long were obtained in both cases. We also prepared 9ACA microribbons as those studied in Ref. [11]. The microribbons were obtained at the interface between 9ACA dissolved in ethyl acetate and milliQ purified water, following the method and the concentration conditions of Ref. [49]. When the ethyl acetate evaporated, the 9ACA microribbons floating on the water surface were carefully recovered after letting also the water evaporate slowly in the dark over a period of two weeks.

Following Ito and Wolff [88,89], we assumed that both head-to-head and head-to-tail photodimers, although in different proportions, could be synthesized and then separated by precipitation in solutions of various solvents, such as ethanol, methanol, ethyl-acetate, methyl-tert-butylether (MTBE), acetone, anisole and methyl-anisole. As in the case of 9CNAD, the aim was to synthesize through a different route the pure product of the reaction, to have a reference Raman spectrum to compare with those obtained during the reaction progression in the solid state. The surprising results of our approach will be described in detail in paragraph 3.5. Here we only report that it did not produce the expected dimer phases.

3.4.2 Results and Discussion

3.4.2.1 Lattice phonon Raman spectra of the reactant crystals

Figure 3.38 shows the lattice phonon Raman spectra of the two known 9ACA polymorphs. The monoclinic $P2_1/n$ structure [86] of α-9ACA has 4 molecules per unit cell (Z = 4) and structural parameters *a* = 3.897 Å, *b* = 9.355 Å, *c* = 28.980 Å and β=90.79°. The molecules lie on generic positions (site symmetry C_1) so they are all symmetry equivalent and exchanged by the group four symmetry operations.

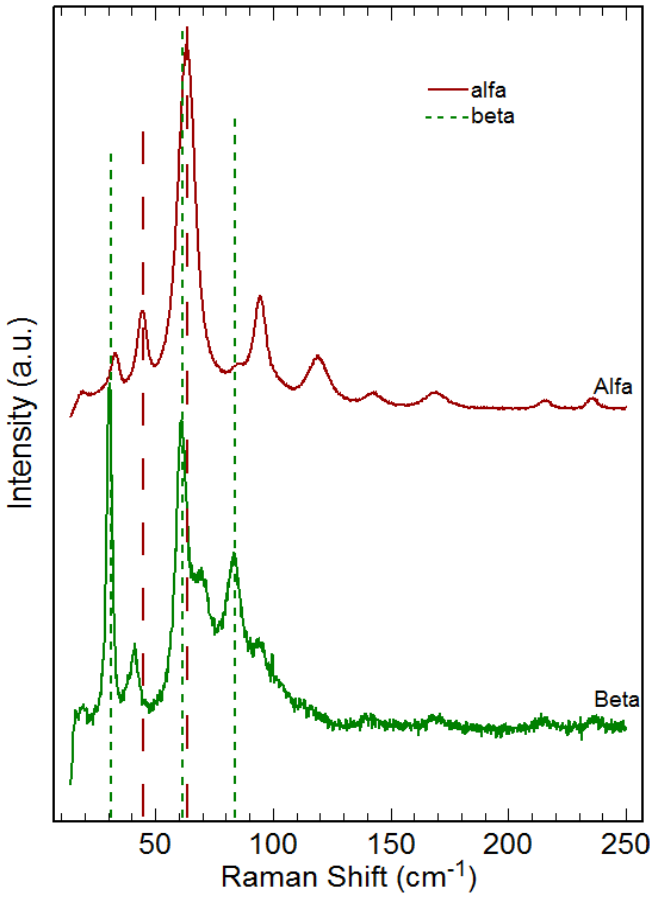

Figure 3.38 Lattice phonon Raman spectra of the two 9ACA polymorphs.

The factor group analysis of the 24 lattice modes at $\boldsymbol{k}$ = 0 shows that 12 of them are Raman active, with symmetries $6A_g + 6B_g$. To identify all the expected bands of α-9ACA, the polarized Raman spectra of Figure 3.39 were measured. This approach was needed as the spectrum of the cis-dimer solid phase, which could not be synthesized in solution, is unknown. Therefore, we wanted to make sure that any changes observed in the spectrum of α-9ACA under irradiation were not due merely to polarization effects as a result of sample movements and re-orientation.

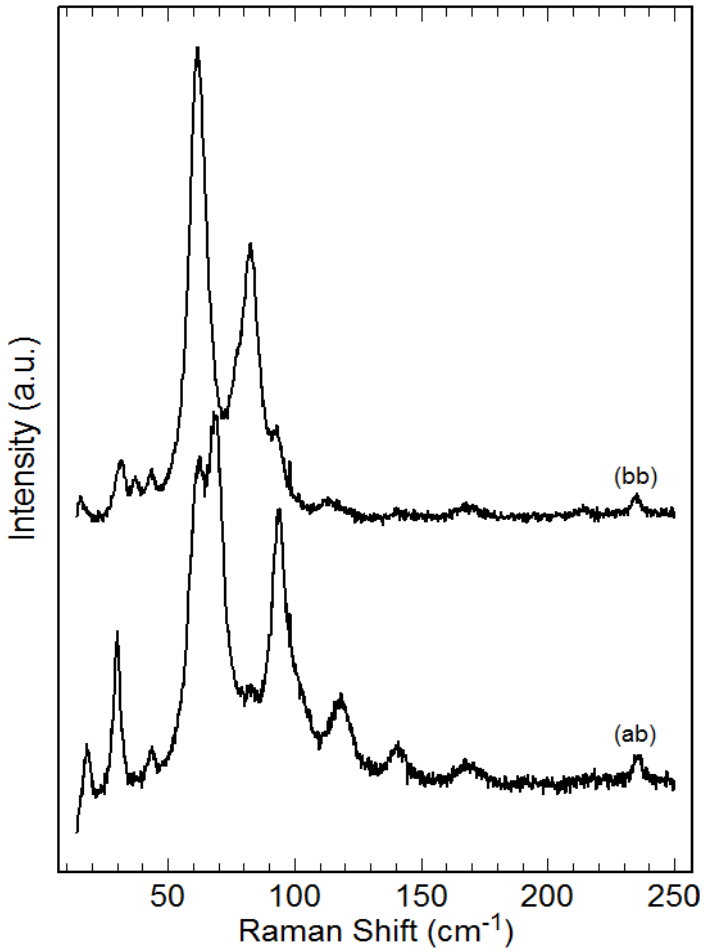

Figure 3.39 Polarized phonon Raman spectra of α-9ACA

The long axis of the α-9ACA needle crystal, that is the direction of its fastest growth, was assumed to be coincident with the shortest *a* crystallographic axis. The crystal placed between the crossed polarizers of an optical microscope gave extinction in the direction nearly perpendicular to the needle axis, and such a direction was identified with the *b* crystallographic axis of the monoclinic structure. Accordingly, the needle was placed vertically aligned on the spectrometer measuring stage, and the Raman spectra of Figure 3.39 were thus

recorded in such a way to keep the polarization direction of the excitation light either parallel or perpendicular to the *b* monoclinic axis, while the Raman scattering was analyzed with a polarization always parallel to the axis. The spectra obtained are then labeled as (bb) and (ab) respectively following the Porto's notation. In the top spectrum of Figure 3.39 only the modes of A_g symmetry can be observed. The B_g modes can instead be detected when the ab matrix elements are probed, as in the bottom spectrum of Figure 3.39. Residual polarization should account for features common to the two spectra.

The triclinic $P\bar{1}$ structure [49] of β-9ACA has cell parameters *a* = 3.8896 Å, *b* = 9.384 Å, *c* = 14.852 Å, α = 101.784°, β =95.457°, γ = 90.220°. The two molecules per unit cell lie in generic positions and are exchanged by the crystal centre of symmetry. Out of the 12 lattice modes, the 6 of A_g symmetry are Raman active. Measuring polarized Raman spectra is not necessary here, as all the A_g bands can be detected in Figure 3.39, and in any other orientation of the triclinic structure. Intensity variations among bands in different spectra may nonetheless occur, as a result of different selections of the polarizability matrix elements when the crystal orientation changes.

3.4.2.2 Molecular arrangements and reactivity

The two 9ACA structures (Figure 3.40) have almost identical densities (1.397 and 1.398 g/cm^3 for monoclinic and triclinic phase, respectively) and therefore higher density, usually corresponding to a more efficient packing, is not in this case a criterion that can be used to predict the more stable polymorph. On the other hand, either form can be obtained by simply changing the re-crystallization solvent, and predictably their energies are very close.

To verify which polymorph is the more stable, we performed crystal lattice energy minimization calculations with a model potential. A detailed description of the computational approach and the potential model used will be given and can be found in Chapter 4. A comparison between the molecular geometries in the two crystal structures confirms that these are virtually identical. The carboxyl group is in both cases (nearly) planar and its plane forms a dihedral angle of ≈ 54° with the plane defined by the anthracene skeleton. The *ab-initio* optimized geometry for the molecule in the gas phase is very similar to that found in the crystal, with a dihedral angle of 47.8°. Since it was very reasonable to assume the same starting molecular geometry for both polymorphs, it was also reasonable to calculate their crystal lattice energies adopting identical molecules for them, especially in view of the very close

energy values. The choice of the *ab-initio* geometry did not appear to be the one to prefer. In fact, the hydrogen bonds involving the COOH groups are very important features in the molecular packing of these systems and certainly the small, but significant difference in the experimental dihedral angle can be attributed to the solid state pattern of interactions. For these reasons, the molecular geometry selected for our calculations was the one calculated as the average of all the asymmetric units of both the monoclinic and the triclinic structures. Minimum potential energy structures for the two structures are reported in Table 3.3, along with the computed cell unit parameters. For the latter, the match with the experimental parameters is excellent, thus confirming that the chosen potential model properly describes this crystal structures. As a matter of fact, from our calculations emerges that the two polymorphs have almost identical energies, and the monoclinic is calculated to be more stable just by less than 4.0 10^{-2} kcal/mol. This is also in agreement with the experimental findings and an analysis of the molecular packings.

Table 3.3 The experimental structures of the known 9ACA polymorphs [86,49] are compared to the minimum potential energy Φ. Energies are in kcal/mole, unit cell axes *a*, *b*, *c* are in Å , angles α, β, γ in degrees, and cell volumes V in Å³.

	a	***b***	***c***	***α***	***β***	***γ***	**V**	**Energy**
	Polymorph α							
Experimental	3.897	9.355	28.98	90.0	90.79	90.0	1056.407	
Minimum ϕ	3.727	9.505	29.90	90.0	88.0	90.0	1058.620	-27.5752
	Polymorph β							
Experimental	3.8896	9.3840	14.8520	101.784	95.457	90.220	528.117	
Minimum ϕ	3.747	9.470	15.356	100.97	98.52	87.35	528.865	-27.5379

A detailed discussion on the similarities and differences of the two structures can be found in reference [49], and is only resumed here.

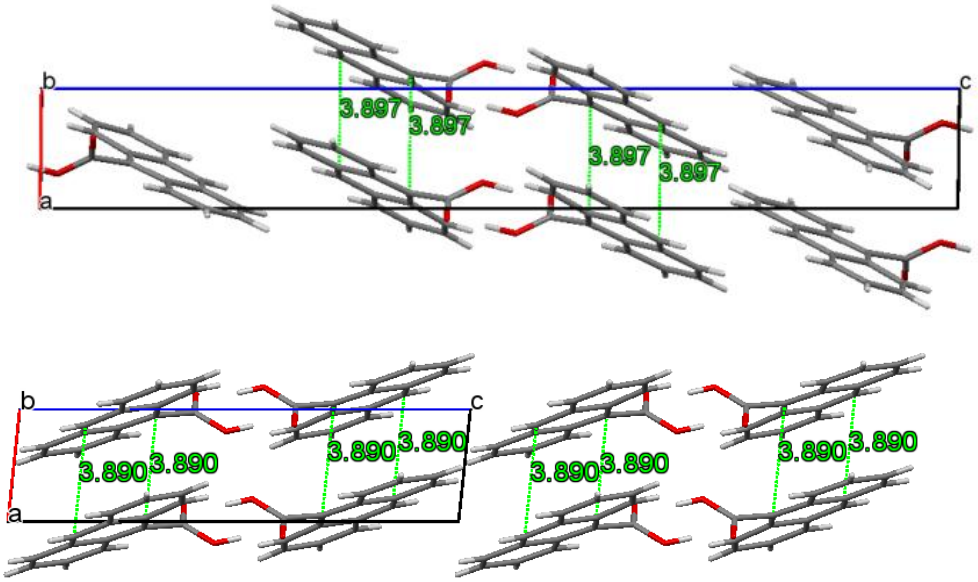

Figure 3.40 Comparison of the two polymorph structures: α-9ACA (top) and β-9ACA (bottom).

In both 9ACA structures there is a single type of hydrogen bond (or motif) which forms a cyclic dimer around a site of C_i symmetry, as clearly illustrated in Figure 3.41, in which the carboxylic groups are rotated by about 55° with respect to the nearly planar anthracene backbone. Each molecule belongs to a stack formed by the anthracene cores, and the hydrogen bonds link pairs of molecules belonging to neighboring stacks. The solid state dimerization reaction is an intra-stack process, which should only perturb the inter-stack hydrogen bonds. Since there are only 2 molecules per cell in the β-9ACA structure, only one type of stack pairing is possible. Instead, in the monoclinic α-9ACA structure with Z = 4, two distinct pairs of stack can be identified, rotated with respect to each other, while the intra-stack distances and relative molecular orientations within the stacks are virtually the same for both structures. This means that no large differences should be expected in the photo-reactivity of the two polymorphs.

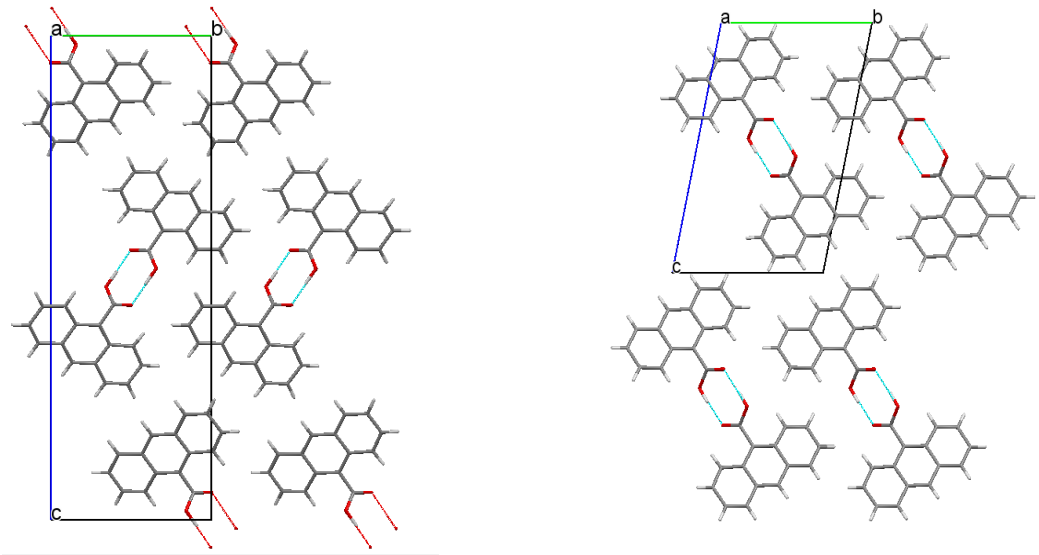

Figure 3.41 Hydrogen bond type in α-9ACA (left) and β-9ACA (right).

3.4.2.3 Lattice phonon Raman spectra of 9ACA single crystals under irradiation

Figure 3.42 shows the lattice phonon Raman spectra of a crystal of α-9ACA irradiated with the unfocused light of a diode laser at 405 nm, as a function of the irradiation time, together with the image of the sample.

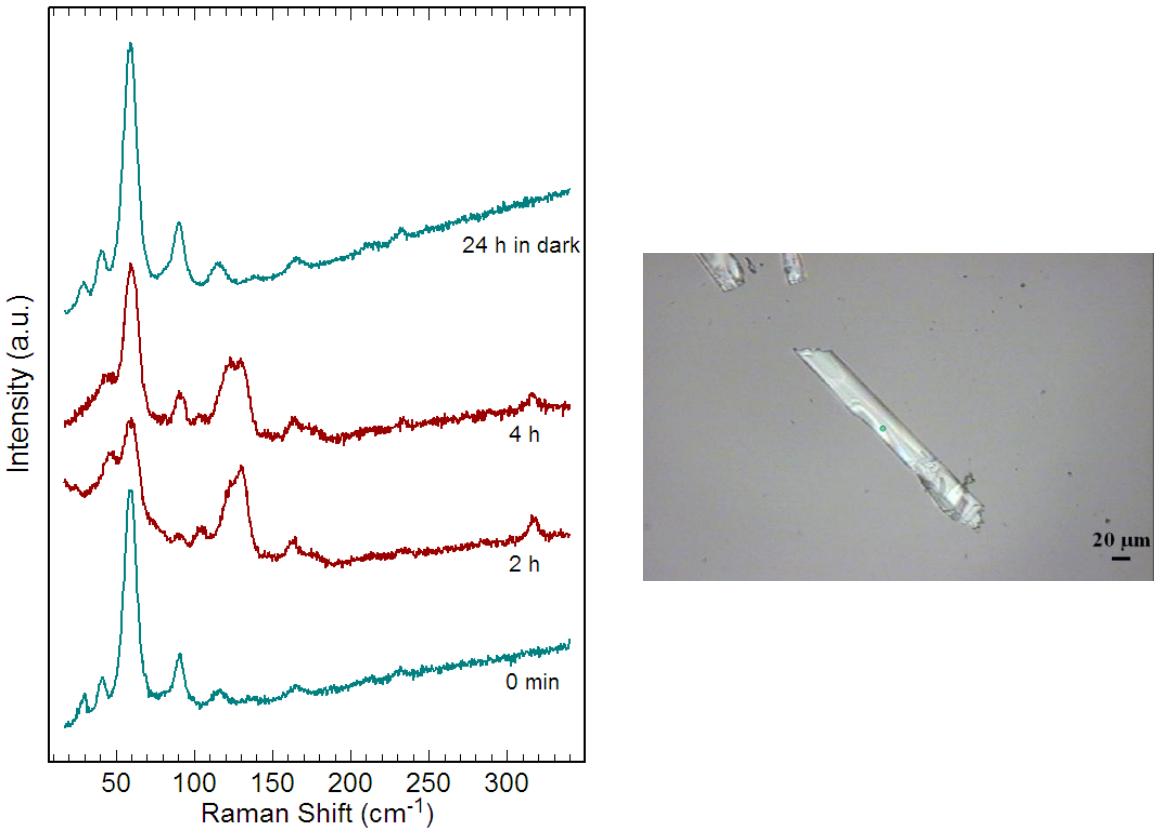

Figure 3.42 Left: Lattice phonon Raman spectra of α-9ACA crystal irradiated by unfocused diode laser (left); Right: image of the irradiated specimen.

The choice of using the laser beam unfocused was dictated by the need of irradiating in a uniform way in area as large as possible of a macroscopic sample (Figure 3.42 right). This allowed us to identify easily the irradiated spot also in the Raman measurements taken at very different times and in the case of bending and twisting of the specimen.

As can be seen from Figure 3.42, α-9ACA proved to be very resilient to reacting, and spectra taken at intervals of 30' of light exposure did not show any change up to 2h, when finally, and suddenly, new phonon bands appeared. In the meantime, no macroscopic movements of the sample were detected, and the Raman measurements in the energy interval of the internal vibrations (here not shown) turned out to be very noisy for all the tested samples and did not give a clear hint of a chemical process. In fact, we could not monitor unambiguously a decrease of the intensity in the vibrational bands characteristic of the anthracene aromatic cores, decrease which would be the evidence of the dimerization reaction. However, the outcome of the spectrum taken after 2h is unmistakable: the monomer lattice is transforming into a new one, with new spectral features at 44 cm^{-1} and between 110 and 145 cm^{-1}. Such a transformation must be accompanied by a chemical process, marked by the observed changes in the intramolecular vibrational bands which fall in the same spectral range of the lattice phonons, like the band at 318 cm^{-1}. Two more hours of continuous irradiation, did not produce any further progression of the reaction. The study of this photodimerization by UV-vis absorption spectroscopy [87] revealed that in 9ACA powder the behaviour of the monomer concentration with time is accounted for by a kinetic equation which includes a step of autoinhibition or negative catalysis. The origin of the inhibition process is not clear, but, as a result of it, the more product is formed the more the reaction slows down, never reaching completion. Indeed, also for the sample of Figure 3.43, no further spectral changes were observed during an illumination of hours. Besides, the transformations undergone by the crystal were found to be totally reversible, as the Raman lattice phonon spectrum of the α-9ACA polymorph is fully recovered after 24 h in the dark, as seen in Figure 3.42. Note that the spectrum does not even display band broadening and increased spectral noise, as it would be expected if the systems turned back into its monomeric state but with some structural disorder. It would be worth mentioning that the sequence of spectra of Figure 3.42 is in fact the first evidence of a structural transformation linked to the dimerization of the α-9ACA system. As reported above, no dimer structure could be found by single crystal X-ray diffraction [87], as the only effect of long hours of irradiation of crystals larger than 50 μm was

an apparently more disordered monomer structure, with unit cell parameters only slightly changed with respect to the original crystal. Not all the irradiated samples of α-9ACA showed the evidence of structural changes, but in some, instead, an increase of disorder was detectable from the lattice phonon spectra.

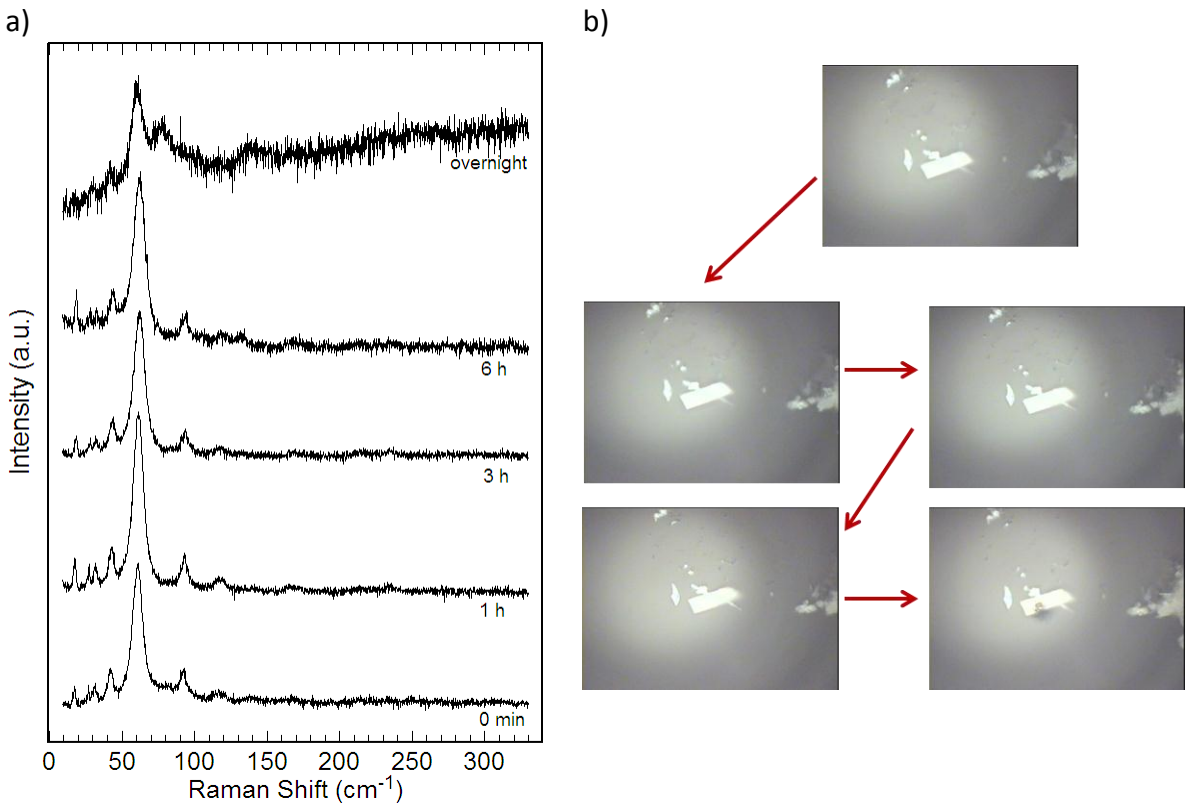

Figure 3.43 Time sequence of Raman spectra and images of irradiated sample.

In Figure 3.43a, for instance, the time sequence of the spectra recorded upon irradiation with focused laser light for the sample in Figure 3.43b is reported. It can be noticed that, after several hours of illumination, the Raman spectrum has retained the feature of the monomer, but it has become more noisy and intensity variations in the bands can be observed. Either structural changes did not occur or they were reversible even on the timescale of each single experiment. In the latter case the variation of intensity could be ascribed to the fact that at the end of the sequence of transformations, the crystal must be formed by many micro-domains differently oriented.

Finally, irradiating single crystals of the triclinic β-9ACA did not produce instead any change in the lattice phonon spectra despite the high number of tested samples and prolonged irradiation. As in the example mentioned above, long illumination times yielded

monomer spectra noisier than at the beginning, and affected the intensity ratios of the various bands, but what lies behind it could not actually be disclosed.

3.4.2.4 Lattice phonon Raman spectra of 9ACA microribbons under irradiation

The reversible photoinduced twisting of microribbons of α-9ACA under spatially uniform irradiation were studied in Ref. [11], and a detailed analysis of the movement was performed in that work. The microribbons prepared for this thesis work were found by the Raman lattice phonon spectra to have the structure of α-9ACA, as expected [11]. In Ref. [11], the orientation of the crystallographic planes in the microribbons was determined by X-rays, and the ribbon face was found to be parallel to the *ab* crystal plane. In fact, through the comparison between the microribbon spectra (Figure 3.44) and the bulk single crystal polarized spectra, we were able to confirm the correctness of the orientations assumed for the bulk α phase of section 3.4.2.1.

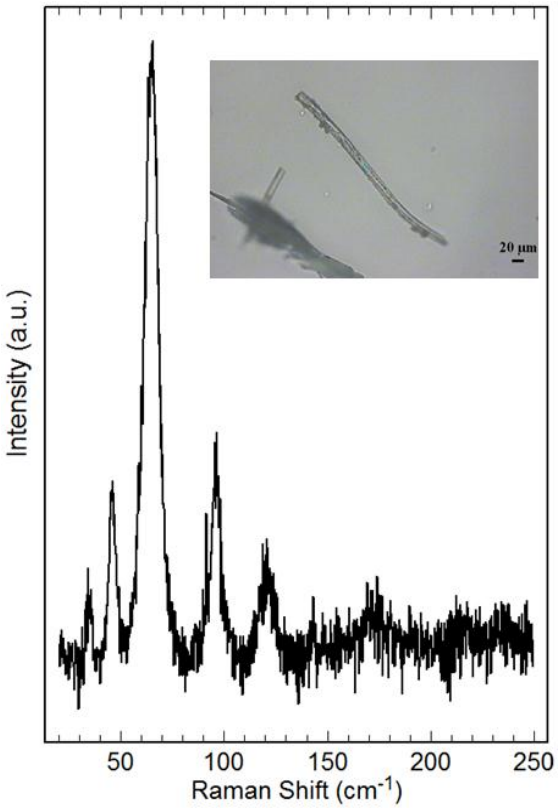

Figure 3.44 Raman spectra and image of a microribbon (α-phase).

In the case of the microribbons, the onset of the photodimerization reaction [47] is given by the intensity decrease of the green-yellow excimer fluorescence, which is partly replaced by an exciton-like blue-shifted emission, assigned to unreacted, isolated monomers,

trapped in the environment of the dimer species, as in the case of 9CNA. The X-ray determination of the dimer structure was not possibile neither in the bulk or in the microribbons of 9ACA and of a series of its derivatives [47], as only the monomer structure was found after the time elapsed between the end of the irradiation and the actual X-ray measurement. The most remarkable feature of the microribbon is, however, their twisting under irradiation, which was present also in all our samples. This motion, proceeds by cycles, at the end of which the initial conformation of the sample is restored, and it is assumed to be caused from the building-up in the crystal lattice of the strain resulting from the coexistence of two or more chemical species. In our system the different species could be identified in the monomer and the dimer molecules, but could also be reaction intermediates. The phenomenon is generally called heterometry [11]. It is not clear what role lattice distortions and modifications can play in this kind of process.

In our experiments, microribbons were seen to twist and bend, qualitatively in the same way as described in ref [11]. However, despite the fact that the time elapsing between the switching off of the irradiation and the positioning of the sample on the micro-Raman stage was less than a minute, no changes in the Raman lattice phonon spectra were ever detected. This means that no structural modification could be seen, at least on the time scale of our experiments. Therefore, the origin of the motion cannot be likely ascribed the adjustment of the product lattice into the one of the reactant. No aid in the interpretation of the cause of the motion came from the analysis of the spectra in the internal vibrations modes, because, as in the case of the α-9ACA bulk crystal, the results were affected by the high noise present in the spectra and small changes were observed only in the fingerprint region. The difficulties encountered in the spectral analysis is also probably due to the large concentration of unreacted monomer left in the samples. The only possible way of interpreting these results is assuming that, while the chemical reaction (reversibly) occurs, with the microribbon motion being the effect, no phase reconstruction does take place.

In conclusion, we have attempted the study of the reversible [4+4] photodimerization reaction of 9ACA. In the literature, the spectroscopic evidence of the chemical reaction in the solid state is based on the change of the fluorescence emission [47] and of the absorption spectrum [87], but so far there is no clear evidence of a phase transformation linked to the chemical step. We have recorded a significant change in the lattice phonon Raman spectra of an α-9ACA single crystal, which also proved to be fully reversible. This means that, at least in

some specimens, the lattice transformation occurs. There are hints that something is happening in the lattice under irradiation also when we are dealing with microribbons of the same α-polymorph, but they are very elusive, whereas, at least for the few samples tested, the β-polymorph seems to be definitely (and unexpectedly) photostable.

Both polymorphic forms of 9ACA are characterized by the same hydrogen bond motif. Each potentially reacting pair of monomers in a stack is linked to another pair in a neighboring stack. However, statistically, two dimerization reactions in the two stacks may not involve the molecules connected by two adjacent centres of symmetry. In other words, at any stage of the reaction, the hydrogen bond patterns can be highly disrupted because the bonds may be now exerted between pairs of dimers, pairs of monomers or dimers and monomers. This constitutes an important source of strain, and the necessary rearrangements of the interaction patterns may produce the macroscopic crystal motion and also contribute to the intrinsic instability of the product. Statistically, of course, this prevents the completion of the reaction, but it could also be the origin of the negative autocatalytic step identified by Moré and coworkers [87]. In these conditions, it is not perhaps unrealistic to think that the concomitant steric hindrance of the dimers and the hydrogen bonds dynamic disruption concur to drive the reaction backwards, so that, when the light is switched off, the system fully reverts to its initial chemical state. In the meantime, with high probability, the product lattice has never formed.

Given the strong similarities between the two polymorphs of 9ACA, we cannot really explain why the β form appears to be photostable, and we believe that the subject is still worth pursuing.

3.5 Pseudo-polymorphism

Pseudo-polymorphism was first defined by McCrone in 1965 [91] and occurs when different crystal structures of a specific compound differ in the nature or stoichiometry of solvent molecules included in its lattice [92]. Actually, there is a still open debate about the exact definition of the terms pseudo-polymorph, co-crystal and solvate (hydrate when the solvent is water) [93] but a clarification about that distinction has been made by Bernstein [94] and a schematic representation of his classification is shown in Figure 3.45.

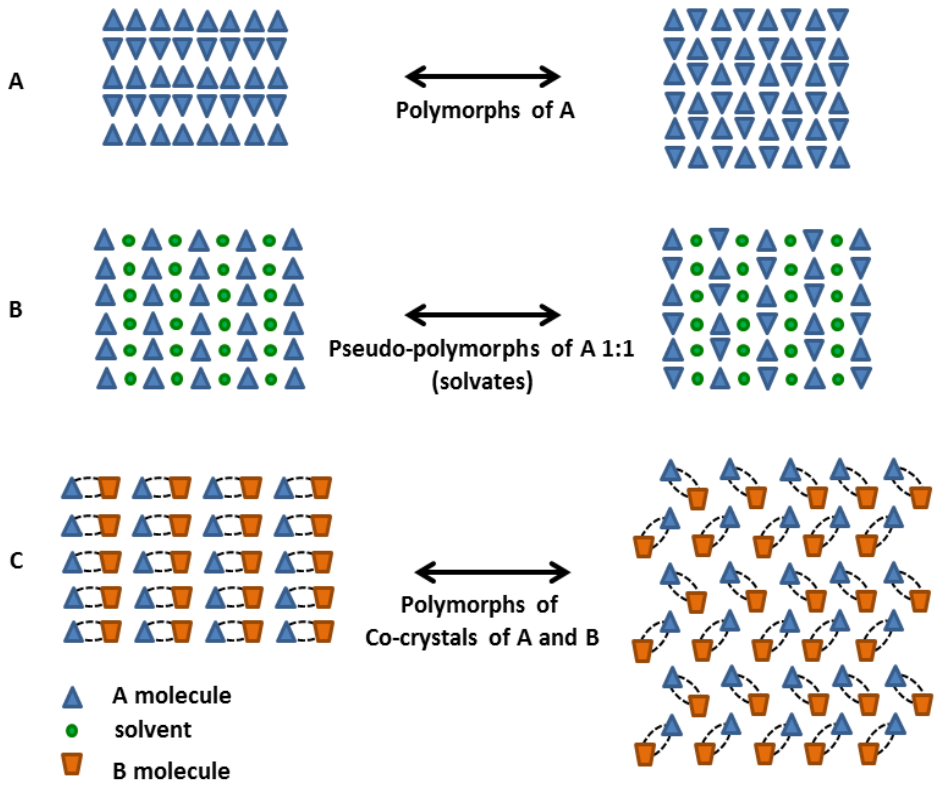

Figure 3.45 Schematic representation of polymorphs (A), pseudo-polymorphs (B) and co-crystals (C) [94].

A first distinction among the different crystal structures can be made on the basis of the number of different molecules involved in the packing. When the structure is composed only of molecules of a single chemical species the phenomenon of different packings is called polymorphism (Figure 3.45a). When more chemical species are involved, different names are conventionally adopted, depending on the physical status and the nature of one of the components at room temperature. If this component is found as a liquid at room T the term "solvate" (Figure 3.45b) should be used, otherwise the denomination of co-crystal (Figure 3.45c) is the correct one. The term "solvate" is usually substituted with the more common

term “pseudo-polymorph”, which will be used hereafter to conform with the current nomenclature [94].

In the recent years the interest in the regulation and manipulation of the crystal pseudo-polymorphism of organic compounds has been subject of several studies in different scientific fields including pharmaceutical chemistry and materials science [95].

The pseudo-polymorphs of a certain compound are distinct chemical structures in a supramolecular sense, and should be therefore treated like the normal crystal polymorphs encountered in molecular crystals, as they exhibit different physical and chemical properties due to their different molecular packing or conformational modifications in the crystal [96].

The variety of crystal packings found in molecular crystals originates from subtle differences in the non-covalent interactions between molecules, as described in chapter 4, which determine the complex phase diagram of most solid systems. The various alternative packing arrangements of the pseudo-polymorphic structures arise from the nature of the interactions between the molecules of the material and the molecules of the solvent in which the crystallization process takes place: hydrogen-bonding is often at play, with the formation of typical hydrogen-bond motifs and influencing the final conformation of the species in the crystal structure [97].

In the literature it is possible to find several examples of compounds, such as aromatic amides and aromatic sulfonamides, that, additionally to polymorphism, also exhibit pseudo-polymorphism phenomena, depending on the crystallization conditions adopted [98].

The cause of the existence of pseudo-polymorphism is related to the tendency for a solvent to be retained in the crystal lattice via the formation of multipoint recognition hydrogen bonding synthons, involving the specific solvent used and the molecule during the crystallization process [99]. For this very reason the strong and directional nature of hydrogen bonds is the master key in crystal engineering, supramolecular chemistry, and biological recognition [100]. Interestingly, literature data show that solvents which have only a single hydrogen-bonding recognizing site are not included in molecular crystal as often as solvents with many sites. The stability of a solvated structure is connected to the balance between the entropic gain made in releasing the solvent molecules of the crystal nuclei into the bulk solution, and the enthalpic gain, given by the formation of strong and directional O/N – H· · ·O and/or C – H· · ·O hydrogen bonds (energy 2–10 kcal/mol^{-1}) [101]. Only when the enthalpic

contributions override the negative enthalpy variations, the solvent can be retained in the nucleating crystal to give a stable system [99].

An interesting subject of investigation is how the presence of the "guest" solvent molecules modifies the arrangement in the "host" system. Clearly this must depend both on the nature and strength of the interactions and on the size and shape of the guest. Consequently, a guest can either induce small changes, so that even the lattice parameter of the solvated and non-solvated form are very close, or lead to dramatic modifications of the host solid state architecture [102].

Desolvation processes in pseudo-polymorphic structures are the object of several studies, as several stable and metastable polymorphs can be so obtained. The possibility of having a stable structure after desolvation, instead of the collapse of the crystal structure and therefore an amorphous material, is the complex function of many parameters, such as the kinetics of the reaction, the thermodynamic relation between solvated and solvent free forms, the nature of the solvate and the specific conditions and method for the removal of the solvent [103].

The main challenge in crystal design and engineering is the understanding of how to use, modulate and rule strong and weak hydrogen bonds to govern the resulting crystal structure [104]. Certainly, the understanding of the forces that govern recognition between multifunctional molecules is still a goal in the field of supramolecular chemistry for building nanoscale architectures from molecular scaffolds [105].

3.5.1 9-anthracene carboxylic acid dimer (9ACAD) pseudo-polymorphs

As mentioned in the paragraph 3.4, we tried to obtain the 9ACA dimers by synthesizing them in solution, with the aim to have the reference crystals for the product of the solid state reaction. However, the process gave unexpected results, which, we thought, deserved a separate discussion and some consideration of the phenomenon of pseudo-polymorphism. In fact, the crystal phases isolated and analyzed, all turned out to be pseudo-polymorphs, or solvates, formed by the head-to-tail (or trans) 9ACA dimer (9ACAD) and the solvent used for the synthesis in a stoichiometric ratio. It was not fully unexpected that the formation of the trans isomer would be favored in solution (despite the fact that according to the literature [88,89] the formation of both isomers was predicted). It was nonetheless surprising that it was impossible to find the conditions in which to obtain directly from the solution crystals of the

pure trans-9ACAD. This happened regardless of the specific nature of the solvents used. As a matter of fact, the solvent molecules appear to play distinct roles in the building of the resulting lattice of the dimer, as they either get engaged in hydrogen bond interactions with the 9ACAD molecules or enter the composition of the unit cell by filling the cavities left by the spatial organization of the dimer units. While it is well known that the larger the solute, the higher is the probability that crystallization in solution occurs via the formation of solvates [106,107], 9ACAD can be still classified as a relatively small molecule, and it would be reasonable to assume that it should be possible to obtain it in the solid state also in a unsolvated form. The pursuing of this goal, linked to our general interest for polymorphism, took our research on anthracene derivatives solid state reactivity on a side track. Thermodynamics and kinetics of desolvation mechanisms in crystals have been studied for the past 20 years [107-109] especially for pharmaceutical compounds, identifying structural and phenomenological parameters which allow for a classification of a wide range of phenomena. Also, a number of techniques are available for studying solid state transitions in solvates. Heating in controlled conditions, for instance, is a common technique of desolvation, yielding either into amorphous material or a polymorphic phase of the pure compound, often metastable. Unfortunately, the technique turned out to be unsuited for our samples, in which the 9ACAD dimer undergoes a thermal dissociation into two 9ACA monomers. Analogously, the thermal instability of 9ACAD, prevented the use of techniques usually applied in the study of solvates, such as TGA and DSC. The spectroscopic approach, however, turned out to be quite useful to give some insight of the processes concerning solvation in 9ACAD crystals.

Following the procedure already described in Chapter 3.2 for 9CNA, the stirred solutions of 9ACA in a number of solvents were irradiated in inert atmosphere with the broadband light of a 250 W Xe lamp, using as a container a pyrex flask, which effectively stops the light transmission at wavelengths below 300 nm and prevents the back reaction of photodissociation of the dimer product. The dimer was far less soluble than the monomer in all the solvents used, and could be recovered as a crystalline precipitate after 8 hours of irradiation, washed with fresh solvent and then dried. As solvents, ethyl-acetate, methanol, ethanol/$CHCl_3$, acetone, methyl-tert-butyl-ether (MTBE), anisole and methyl-anisole were used. The solvate crystals were treated with vacuum drying (≈ $8x10^{-3}$ bar) to promote evaporation of solvent.

3.5.1.1 9ACAD from ethyl acetate: Crystal Structure and Raman Spectra

The X-ray diffraction analysis of crystals obtained from ethyl-acetate (EtOAc) gave the triclinic $P\bar{1}$ structure of a solvate, with parameters *a* = 8.4667(9) Å, *b* = 9.3649(10) Å, *c* = 10.2262(11) Å, α = 63.2800(10)°, β= 70.8870(10)° and γ = 69.5030(10)° and cell volume of 664.25(12) Å^3. There is one asymmetric unit per cell with a 1:1 ratio of 9ACAD and EtOAc. The asymmetric unit is made by half a molecule of 9ACAD and one molecule of EtOAc. Both entities lie on distinct inversion centers of the lattice. Whereas the dimer molecule is centrosymmetric, EtOAc is not. However, statistically, 50% of the EtOAc molecules can be generated by applying the inversion symmetry operation to the remaining 50%. The calculated crystal density is 1.331 g/cm^3. In Figure 3.46 the packing in the crystal is shown in a projection along the *b* crystallographic axis. As can be seen, each 9ACAD molecule is engaged in two dimer synthons in trans position to each other, with the hydrogen bonds aligned along the *c* crystallographic axis. The way the chains of hydrogen bonds assemble, generates a channel-type skeleton in which the solvent molecules are located. The CO group of the solvent presents a short contact of 2.553 Å with a hydrogen of the dimer aromatic ring.

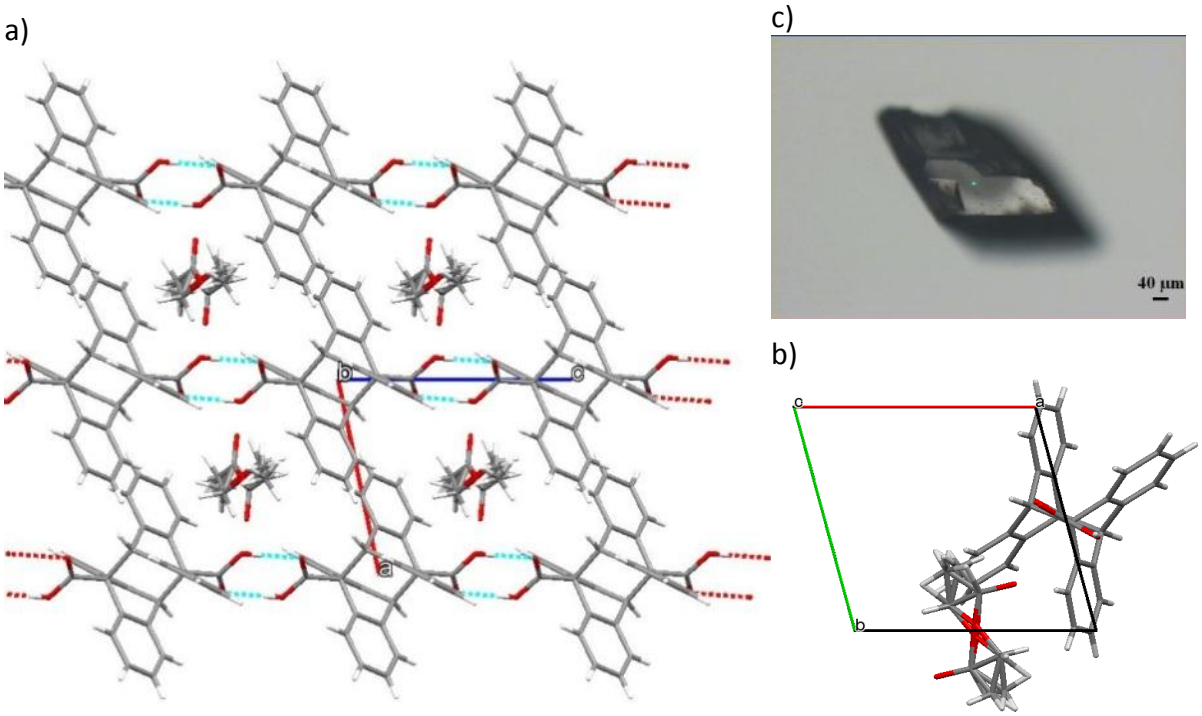

Figure 3.46 X-ray structure of the 1:1 9ACAD-EtOAc solvate: a) cell axes and extended packing viewed along the *b* crystallographic axis. Dotted blue lines show hydrogen bond interactions between the carboxyl groups. Occupancies are shown for disordered EtOAc molecules; b) a projection along the *c* crystallographic axis displays the molecular geometry of the dimer; c) picture of the actual crystal.

The Raman spectrum of the 9ACAD-EtOAc system in the lattice phonon wavenumber interval is reported in Figure 3.47a. Despite the fact that lattice phonon Raman spectra have recently become an important tool for phase recognition in a number of in pharmaceutical solvate solid compounds, the technique has been used exclusively with an analytical approach. Different polymorphs or pseudo-polymorphs have been identified by their different spectra, without attempting the assignment of the bands. We have adopted the same approach in the present analysis of the 9ACAD pseudo-polymorphs. Indeed, a rigorous assignments of the crystal vibrational bands can be cumbersome especially when, as in the cases we are dealing with, a supramolecular framework is generated via the strong intermolecular interaction due to the hydrogen bonds. In this situation, in fact, a clear distinction between inter- and intra-molecular vibrational modes is not be possible, as a result of the cooperative behavior of the hydrogen bond structures. In the 9ACAD-EtOAc system, a further complication arises from the presence of a statistically disordered solvate, for which, to the best of our knowledge, a specific lattice dynamics treatment does not exist.

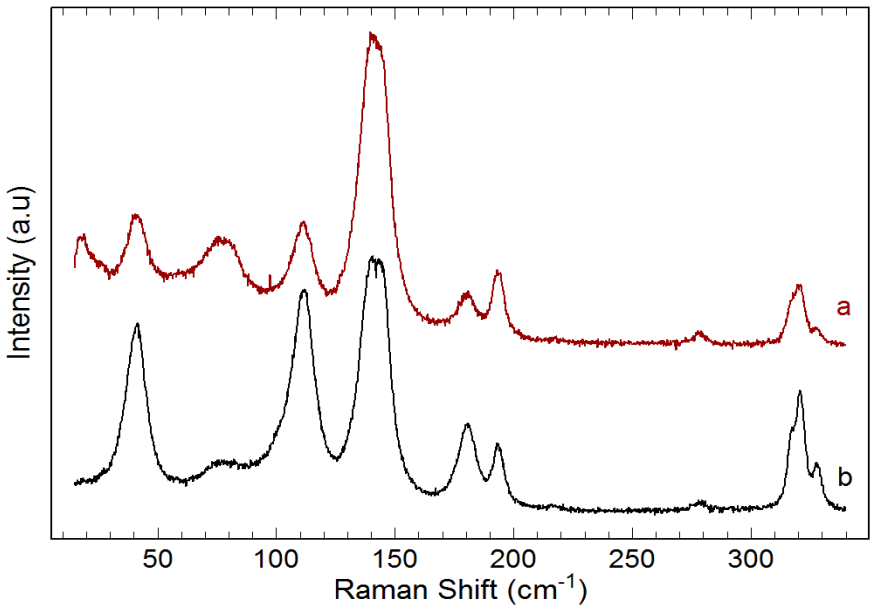

Figure 3.47 Raman phonon spectrum of the 9CAD-EtOAc crystal in the lattice phonon region. a) Crystal obtained by crystallization in EtOAc; b) the same crystal kept 24h at 8 mbar.

9ACAD-EtOAc crystals were put in vacuum drying for 24h at RT. Since the structure is characterized by the absence of hydrogen bonds with the solvent molecules located in channels of the structure, promoting the solvent evaporation was expected to be easy in the operation conditions (the vapor pressure of EtOAc is ≈ 0.1 mbar at 22 °C). However, a comparison of the lattice phonon patterns recorded before and after the permanence in vacuum (figure 3) does not reveal changes in the phonon peak positions. A different intensity

distribution throughout the entire spectrum is accounted for by a partial reorientations of the anisotropic crystal domains after the drying process. NMR measurements confirm that EtOAc is still present in the sample in the initial stoichiometric amount, even after evacuation in mild heating conditions (40 °C).

3.5.1.2 9ACAD from methanol: Crystal Structure and Raman Spectra

The crystals obtained from methanol (MeOH) have a monoclinic C2/m structure with cell parameters *a* = 12.051(6) Å, *b* = 14.248(6) Å, *c* = 8.656(4) Å and β = 115.774(11)°. There is one asymmetric unit per cell with a 1:2 ratio of 9ACAD and MeOH and a calculated density of 1.257 g/cm^3. There are two 9ACAD molecules per unit cell and each one is located on a center of inversion which lies on a C_2 axis, which corresponds to the *b* crystallographic direction. In this structure the 9ACAD molecules thus belong to the C_{2h} punctual symmetry group. There are four MeOH molecules per unit cell, with the C-O bond lying on the symmetry plane perpendicular to the C_2 axis. The methyl group is statistically disordered as its hydrogen atoms can rotate around the axis passing through the C-O bond. Each MeOH molecule forms hydrogen bonds with the carboxyl groups of two adjacent 9ACAD molecules, as shown in the projection of Figure 3.48.

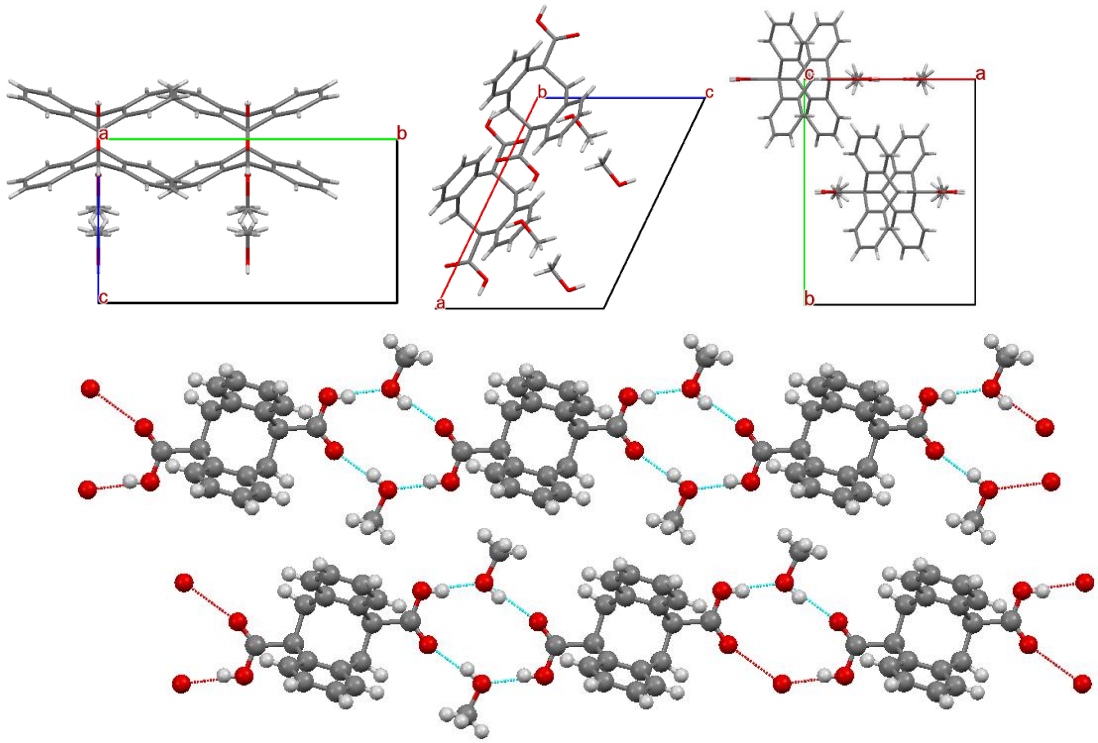

Figure 3.48 X-ray structure of the 1:2 9ACAD-MeOH solvate: top) cell axes and extended packing viewed along the *a* and *b* crystallographic axes; bottom) z-clipped projection to show the hydrogen bond motif. Dotted blue lines are for hydrogen bonds between the carboxyl groups and the MeOH. Note that in the measurements the position of the MeOH hydrogen bonds was not resolved.

The 9ACAD-MeOH crystals were subjected to vacuum drying for 24 hours at room *T*. Due to the presence of the hydrogen bonds with the 9ACAD molecules, MeOH in the crystal was assumed to be less volatile than in its pure liquid form, but considering that MeOH has a vapor pressure of ≈ 130 mbar at 20 °C, the conditions and the timing could be sufficient to remove it from the lattice.

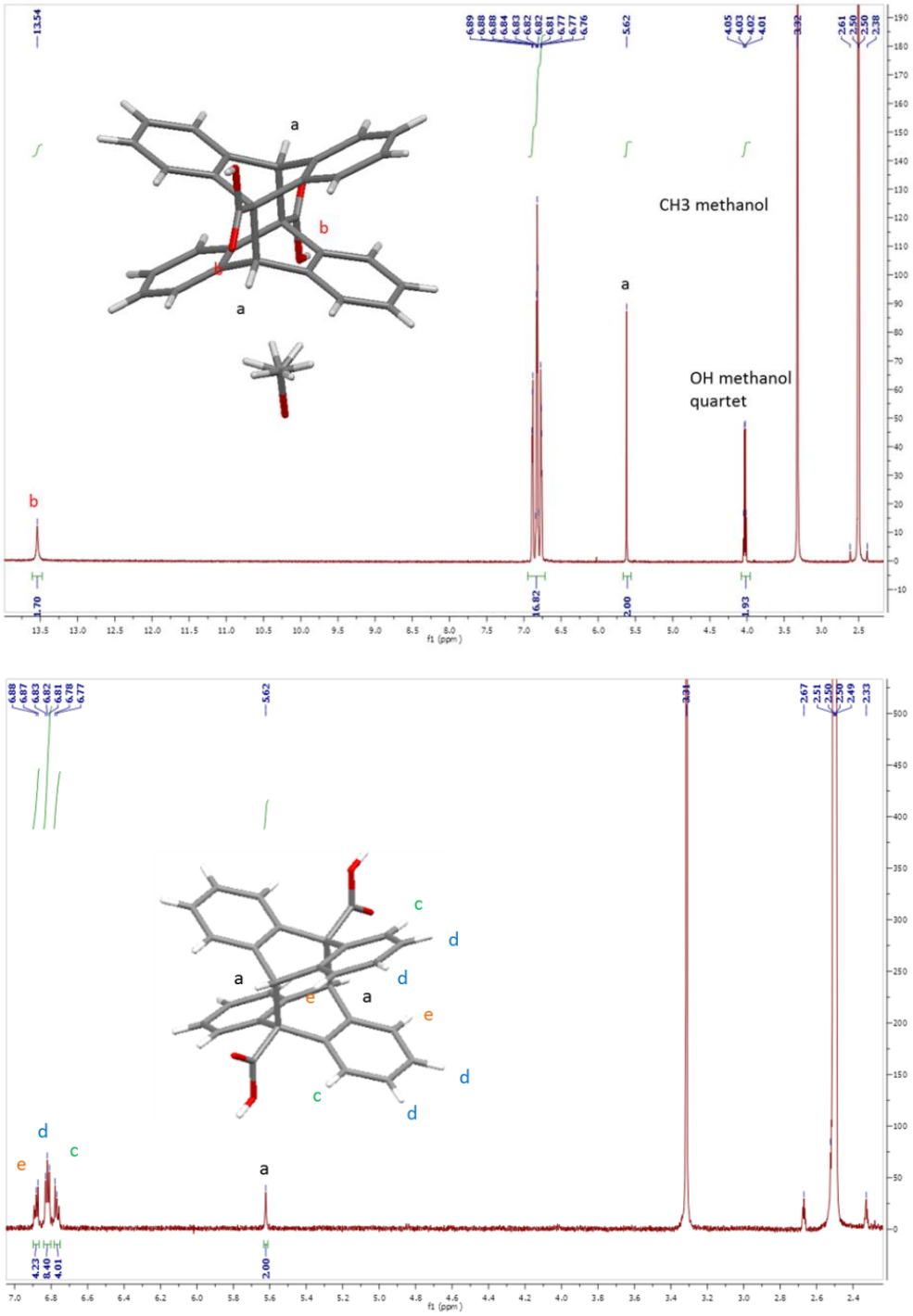

Figure 3.49 a) (top) NMR spectrum of the 9ACAD-MeOH solvate recorded as freshly prepared, b) (bottom) NMR spectrum of the 9ACAD-MeOH after vacuum drying the sample.

NMR spectra of the solvate crystals were recorded before and after the drying procedure (Figures 3.49a and 3.49b) and the analysis clearly showed that MeOH was removed. No further X-ray analysis was then performed, also because the dried crystals got cracked or their quality deteriorated at such an extent to prevent the measurement. The Raman spectra in the lattice phonon region are shown in Figure 3.50.

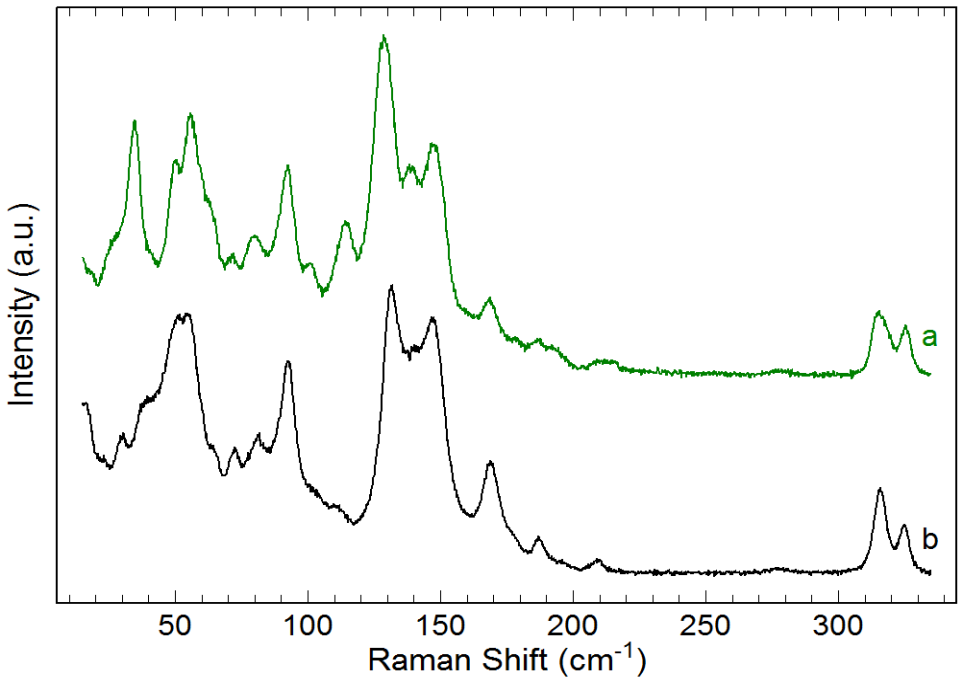

Figure 6. a) Raman Spectrum of the 9ACAD-MeOH 1:2 crystal in the lattice phonon region. b) Raman spectrum of the same crystal after desolvation for 24h by vacuum drying.

As expected, the Raman spectrum was found to change upon solvent removal. Although the analysis is not trivial, the comparison of the two spectra in the figure 6 indicates that the bands missing after the drying process can be easily accounted for by the contribution of the solvent. After desolvation, a total of two rigid bodies are left in the unit cell of the C_2/m centrosymmetric system. By considering the primitive pseudo-triclinic cell (Z=1), a total of 3 ***k***=0 lattice phonons of gerade symmetry would be Raman active. However, the rigid body approximation very unlikely applies here, and a clear boundary between internal and external vibrations is therefore not present. As a result, more bands in the low wavenumber region are observed, having an inter/intra-molecular mixed character. Certainly, the NMR datum is confirmed by Raman spectroscopy, as the spectra before and after desolvation differ, even though not dramatically so. Indeed, it has been recently reported [106,107] that when the solvent is removed in a smooth way, the unary phase so obtained can have a strong structural filiation with the mother solvated phase, so much as to display very little differences at the X-

ray diffraction analysis. The new phase is generally a metastable polymorph of the pure component, obtained from the cooperative release of the solvent molecules, with little or no relaxation at all of the entire structure. This would be what is called topotactic or quasi-topotactic desolvation in ref [106]. If this is what happens in our system, the Raman spectra identify a new metastable polymorph, the packing of which is very close to that of mother phase.

3.5.1.3 9ACAD from ethanol/$CHCl_3$: Crystal Structure and Raman Spectra

The precipitate obtained from the photodimerization reaction of 9ACA in methyl-t-butyl ether was dissolved in a 1:1 solvent mixture of ethanol (EtOH) and $CHCl_3$ and single crystals were grown by slow evaporation. These crystals were found to have a triclinic $P\bar{1}$ structure with cell parameters *a* = 8.456(13) Å, *b* = 9.607(15) Å, *c* = 10.861(17) Å and α = 105.494(16)°, β= 101.120(17)° and γ = 113.570(17)°, with cell volume of 773.086(12) $Å^3$. There is one asymmetric unit per cell, formed by half a molecule of 9ACAD (lying on a center of mass) and a molecule of ethanol (lying in a general position, and with some rotational disorder) with a 1:2 ratio of 9ACAD and EtOH. Similarly to the solvate with MeOH, the solvent forms hydrogen bonds with the carboxylic groups of 9ACAD, yielding a hydrogen bond motif very similar to that of the former case, as can be seen in Figure 3.51. However, due to the larger molecular volume of the alcohol, the entire structure is much less dense (calculated density = 1.211 g/cm^3).

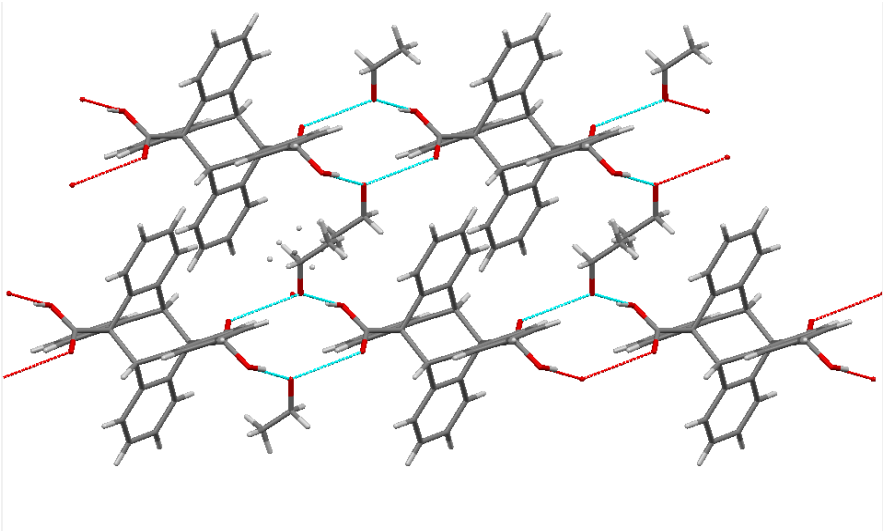

Figure 3.51 X-ray structure of the 1:2 9ACAD-ETOH solvate: Extended packing viewed to show the hydrogen bond motif. Dotted blue lines show hydrogen bond interactions between the carboxyl groups and the ethanol molecules. Multiple occupancies are shown for disordered EtOH molecules.

NMR spectra taken after prolonged vacuum drying at RT (a few days) showed un unchanged stoichiometric ratio of 9ACAD and alcohol. Clearly the solvent could not be released in these conditions and no further attempt was made. Raman phonon spectra in the low wavenumber region, accordingly, showed no change.

3.5.1.4 9ACAD from other solvents: Raman Spectra

Single crystals of solvates of 9ACAD were also grown from a number of other solvents, namely: acetone, anisole, methyl-anisole and methyl-t-butyl ether for which we have no X-ray determination since the work is still in progress. For these, we only have the NMR spectra to indicate that the solvent is anyway present in a stoichiometric ratio in the lattice of 9ACAD, and that the RT vacuum drying is not sufficient for its release, evidence which is confirmed by the Raman lattice phonon spectra which remain unchanged after the drying process. The only exception is for crystals grown from acetone, for which NMR spectra show that all the solvent has disappeared after drying. Indeed, for this case only, we correspondingly observe marked differences in the Raman spectra before and after drying, most noticeable in the 40-120 cm^{-1} wavenumber range, as documented in Figure 3.52.

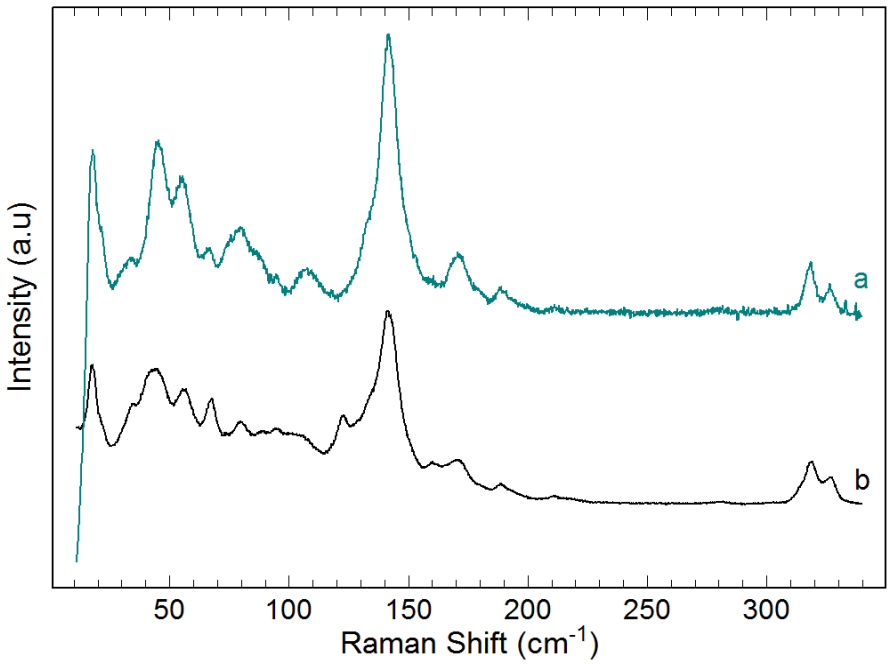

Figure 3.52 a) Raman Spectrum of the 9ACAD-Acetone crystal in the lattice phonon wavenumber range. b) Raman spectrum of the same crystal after desolvation for 24h by vacuum drying.

Once the crystal structure is known from X-ray data, the energy contribution of the solvent to the stability of a crystal structure can be estimated in an inexpensive and fast way, starting from the total energy of the pseudo-polymorphs structure at the minimum of a chosen potential model. We have done this for the structures of 9ACAD EtOAc -and 9ACAD-MeOH, as representative of cases in which desolvation failed or was successful, respectively. The method for lattice energy minimization is described elsewhere in this thesis and will not be given here. In the energy minimization calculations for both of the solvates the rigid body approximation was adopted, employing the potential model which had already reproduced satisfactorily the 9ACA monoclinic and triclinic structures. The molecular geometries of both solute and solvent used for the calculations was that obtained from the X-rays. In fact, for 9ACAD the value of the torsional angle between the anthracene backbone and the plane of the carboxylic group determined for the crystal does not coincide with that determined by *ab-initio* calculations for the molecule in the gas phase. This is not surprising, as the solid state geometry is governed by the formation of hydrogen bond network.

As already illustrated above, the space group symmetry of 9ACAD-EtOAc is the result of the statistically disordered solvent. The same happens for 9ACAD-MeOH, for which the source of disorder is the methyl group of the solvent, that is free of rotating about the C-O bond.

In both cases, symmetry cannot be used in generating the input structure for the lattice dynamics calculations, where the entire crystal unit cell is therefore used as an asymmetric in which only one of the solvent possible orientations must be selected.

The minimum potential energy structures both for the EtOAc and MeOH solvates are reported in Table 3.4, along with their energy Φ_0. The value of Φ_0 originates from the sum of three distinct intermolecular contributions:

$$\Phi_{0=} \Phi_{9ACAD\text{-}9ACDA} + \Phi_{solv\text{-}solv} + \Phi_{9ACAD\text{-}solv}$$

$\Phi_{9ACAD\text{-}9ACDA}$ and $\Phi_{solv\text{-}solv}$ are the terms for the interactions involving the 9ACAD and the solvent molecules, respectively, while $\Phi_{9ACAD\text{-}solv}$.is the term describing the interaction between 9ACAD and the solvent.

Once the minimum energy structure has been determined, $\Phi_{9ACAD\text{-}9ACDA}$ and $\Phi_{solv\text{-}solv}$ can be computed by removing the 9ACAD and the solvent molecules, respectively, without

further minimization of the energy of the resulting system. The remaining term can thus be obtained as $\Phi_{9ACAD\text{-}solv} = \Phi_0 - (\Phi_{9ACAD\text{-}9ACDA} + \Phi_{solv\text{-}solv})$. The various contributions are also listed in Table 3.4 both for the EtOAc and MeOH solvates.

Tab 3.4 Calculated minimum potential energy Φ_0 (kcal/mol) and structural parameters for the pseudo-polymorph structures of 9ACAD-EtOAc and 9ACAD-MeOH. The experimental structural values are given for comparison. The terms contributing to the total energy Φ_0 are also reported.

	Φ_0	$\Phi_{9ACAD9ACDA}$	$\Phi_{solv\text{-}solv}$	$\Phi_{9ACAD\text{-}solv}$	a(Å)	b(Å)	c(Å)	α	β	γ	V(Å^3)
9ACAD-EtOAc (Z=2)											
Exp					8.4667	9.3649	10.2262	63.280	70.887	69.503	664.246
Cal	-49.117	-25.849	-0.7895	-22.4786	8.2836	9.5326	10.7448	59.963	69.816	67.383	665.567
9ACAD-MeOH (Z=4)											
Exp					8.6560	14.2480	11.3770		107.470		1338.413
Cal	-33.238	-23.0575	-0.1490	-10.0316	8.4667	13.9250	11.5192		103.914		1318.252

Let us analyze first the case of EtOAc. It is worth noting that the term $\Phi_{solv\text{-}solv}$ is in fact negligible. The solvent molecules, located in the structure quite far apart from each other, interact very little. On the contrary, $\Phi_{9ACAD\text{-}solv}$ is very large, and accounts for about the 45% of the total lattice energy. The solvent actually acts like the glue holding together the entire scaffold of the quasi- 1D arrays generated by the hydrogen bond network. By minimizing the energy of the structure deprived of the solvent molecules, unexpectedly the system relaxes onto a new local minimum, which, however, has very little resemblance with the mother structure.

Also in the 9ACAD-MeOH structure the actual interaction between solvent molecules is very small, as can be seen from the table. The $\Phi_{9ACAD\text{-}solv}$ term is found instead to contribute to the total energy for no more than the 30%. This may be unexpected, as in the packing of this solvate, as we have seen, the solvent actively participates in the highly directional hydrogen bonds. However, if this computed datum is be trusted, it would explain why the desolvation for this system was made possible by applying mild experimental conditions. In support to the idea that here we are dealing with a topotactic desolvation, we have found that by removing the MeOH molecules from the structure, the system does relax onto a new minimum which is strongly affiliated with the original one.

At this stage of our investigation we conclude that, under the mild drying conditions used, the release of the solvent has proven unsuccessful in all cases, with the only exceptions

of MeOH and acetone, perhaps owing to their lower boiling temperatures. In either case, what has been obtained is likely to be a metastable polymorph of the unary system. Interestingly, both solvates underwent the desolvation process without transforming into an amorphous phase, as can be verified by the permanence of a lattice phonon pattern in the Raman spectra. This means that in the energy landscape of the solid state diagram of the unary system there is a local minimum accessible from the solvate system, with a closely related structure. This thesis appears to be confirmed by our preliminary calculations of crystal structure minimum energy.

A summary of the Raman phonon spectra of the all pseudo-polymorphs is given in Figure 3.53.

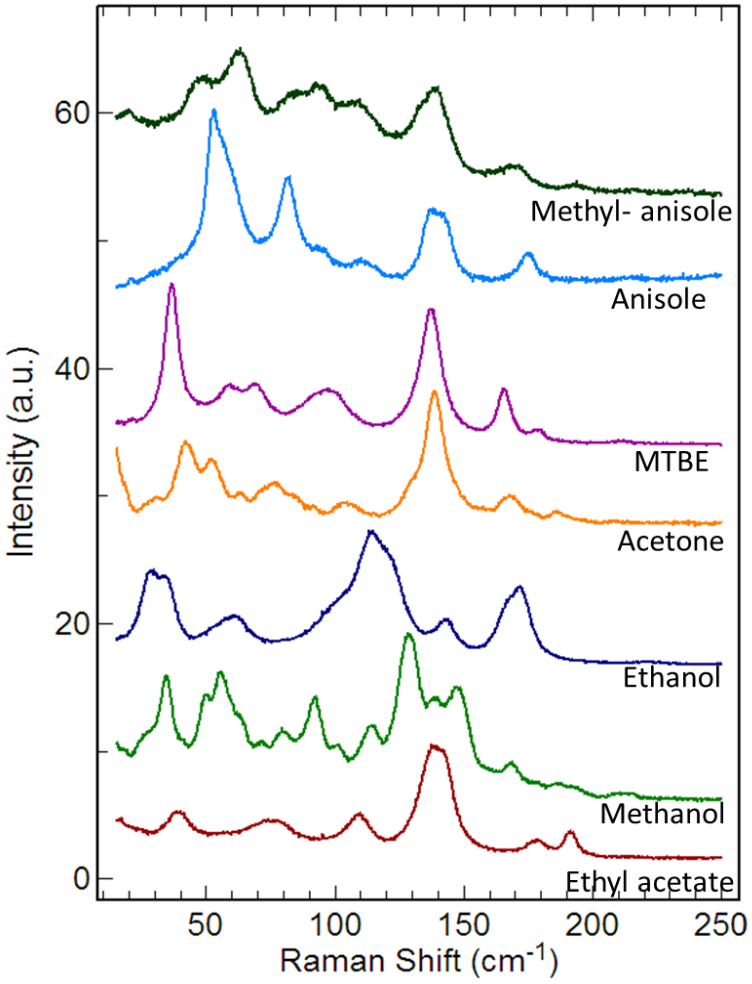

Figure 3.53 Lattice phonon Raman spectra of all pseudo-polymorphs of 9ACAD obtained.

The total of seven dimers insofar synthesized certainly does not represent the upper limit for 9ACAD, because, following the Mc Crone rule [91], still a number of solvents are planned to be tried. We believe that 9ACAD is going to become an exemplary case of a

molecular crystal showing a high number of pseudo-polymorphs, which is explained by the inspection of its structure, easily prone to host solvent molecules, as units or chains, in the interstices of its cage-like framework. Furthermore, the hydrogen bonds, originating between solvent molecules and the carboxylic group of the aromatic core, establish a kind of supramolecular structure with a variety of options of closely packed architectures.

The second important information that can be extracted from Figure 3.52 is that lattice phonon spectra efficiently constitute a sort of database for a fast and easy identification of polymorphs or pseudo-polymorphs, a technique which can be transferred to pharmaceutical investigations for a faster screening of their products.

As to the understanding of the lattice dynamics of these systems, we remark that it is still lacking a solid theoretical basis to fully describe the complex behavior of these disordered, or partly disordered, systems. The lack of periodicity should apparently wash away the phonon spectral features, though solvents molecules statistically contribute to the partial ordering of the overall solvate packed structure and might anyway have a role in the dynamics of the system. What would result in the actual lattice phonon spectra requires more experiments and more thinking.

References

[1] H.D. Becker, Chem Rev. 93, 145 (1993).

[2] E.F. Plaza-Medina, W. Rodríguez-Cordoba, R. Morales-Cueto, J. Peon, J. Phys. Chem. A 115, 577 (2011).

[3] A. Brillante, I. Bilotti, R.G. Della Valle, E. Venuti, A. Girlando, CrystEngComm. 10, 937 (2008).

[4] G. J. Piermarini, S. Block, J. D. Barnett, R. A. Forman, J. Appl. Phys. 46, 2774 (1975).

[5] L. Farina, R. G. Della Valle, A. Brillante, High Press. Res. 18, 233 (2000).

[6] A. Brillante, R.G. Della Valle, R. Farina, E. Venuti, Chem. Phys. 191, 177 (1995).

[7] J. Trotter, Acta Cryst. 12, 232 (1959).

[8] G. Turrel, *Infrared and Raman Spectra of Crystals*, Academic Press, London 1972.

[9] Y. Fu and C. P. Brock, Acta Cryst. B54, 308 (1998).

[10] D.P. Craig, J. and Proc. Royal Soc. New South Wales 61, 115 (1982).

[11] L. Zhu, R.O. Al-Kaisy, C. J. Bardeen, J. Am. Chem. Soc. 133, 12569 (2011).

[12] K. Syassen and R. Sonnenschein, Rev. Sci. Instrum. **53**, 644 (1982).

[13] A. Brillante, M. Hanfland, K. Syassen, Chem. Phys. Lett. 119, 42 (1985).

[14] A. Brillante, M. Cau, R. D. Della Valle, E. Venuti, Chem. Phys. Lett. 218, 568 (1994).

[15] M. D. Cohen, G. M. J. Schmidt,. J. Chem. Soc. 1996 (1964).

[16] E. Heller, G. M. Schmidt, Israel J. Chem. 9, 449 (1971).

[17] V. Ramamurthy, K. Venkatesan, Chem. Rev. 87, 433 (1987).

[18] Frisch, M. J.; Trucks, G. W.; Schlegel, H. B.; Scuseria, G. E.; Robb, M. A.; Cheeseman, J. R.; Montgomery Jr., J. A.; Vreven, T.; Kudin, K. N.; Burant, J. C.; Millam, J. M.; Iyengar, S. S.; Tomasi, J.; Barone, V.; Mennucci, V.; Cossi, M.; Scalmani, G.; Rega, N.; Petersson, G. A.; Nakatsuji, H.; Hada, M.; Ehara, M.; Toyota, K.; Fukuda, R.; Hasegawa, J.; Ishida, M.; Nakajima, T.; Honda, Y.; Kitao, O.; Nakai, H.; Klene, M.; Li, X.; Knox, J. E.; Hratchian, H. P.; Cross, J. B.; Bakken, V.; Adamo, C.; Jaramillo, J.; Gomperts, R.; Stratmann, R. E.; Yazyev, O.; Austin, A. J.; Cammi, R.; Pomelli, C.; Ochterski, J. W.; Ayala, P. Y.; Morokuma, K.; Voth, G. A.; Salvador, P.; Dannenberg, J. J.; Zakrzewski, V. G.; Dapprich, S.; Daniels, A. D.; Strain, M. C.; Farkas, O.; Malick, D. K.; Rabuck, A. D.; Raghavachari, K.; Foresman, J. B.; Ortiz, J. V.; Cui, Q.; Baboul, A. G.; Clifford, S.; Cioslowski, J.; Stefanov, B. B.; Liu, G.; Liashenko, A.; Piskorz, P.; Komaromi, I.; Martin, R. L.; Fox, D. J.; Keith, T.; Al-Laham, M. A.; Peng, C. Y.; Nanayakkara, A.; Challacombe, M.; Gill, P. M. W.; Johnson, B.; Chen, W.;

Wong, M. W.; Gonzalez, C.; Pople, J. A. Gaussian 03, Revision C.02, (Gaussian, Inc., Wallingford CT, 2004).

[19] D. E. Williams, D. Houpt, J. Acta Cryst. B 42, 286 (1986).

[20] W. R. Busing, M. Matsui, Acta Cryst. A 40, 532 (1984).

[21] M. Born, K. Huang, Dynamical Theory of Crystal Lattices, Oxford University Press, New York 1954.

[22] Weighted average of nine published data, NIST database, http://webbook.nist.gov/.

[23] P.J. Kraulis, J. Appl. Cryst. 24, 946 (1991).

[24] K. Otsuka, C. M. Wayman, *Shape Memory Materials*, Cambridge University Press 1998.

[25] G. M. J. Schmidt, J. Chem. Soc. 2014 (1964).

[26] G. M. J. Schmidt, Pure and Appl. Chem. 27, 647 (1971).

[27] D. P. Craig, C. P. Mallet, Chem. Phys. 65, 129 (1982).

[10] D. P. Craig, J. Proc. R. Soc. N. S. W. 115, 61 (1982).

[28] Kaftory, M., *Structural Aspects and Templation of Photochemistry in Solid-State Supramolecular Systems*. In: *Supramolecular Photochemistry: Controlling Photochemical Processes*; Ramamurthy, V., Inoue, Y., Eds.; John Wiley & Sons: Hoboken NJ, 2011, pp 229-266.

[29] M. Pope and C. E. Swenberg, *Electronic processes in organic crystals and polymers*, Oxford University Press, New York, 2nd edn, 1999.

[30] I. Zouev, D. Cao, T. V. Sreevidya, M. Telzhensky, M. Botoshansky, M. Kaftory, CristEngComm 13, 4376 (2011).

[31] D. P. Craig, P. Sarti-Fantoni, Chem. Commun. (London), 742 (1966).

[32] M. D. Cohen, Z Ludmer, J. M. Thomas, J. O. Williams, Proc. R. Soc. Lond. A 324, 459 (1971).

[33] M. D. Cohen, I. Ron, G. M. J. Schmidt, J. M. Thomas, Nature 224, 167 (1969).

[34] M. D. Cohen, Z. Ludmer, V. Yakhot, Phys. St. Sol. B 67, 51 (1975).

[35] T. Salzillo, I. Bilotti, R. G. Della Valle, E. Venuti, A. Brillante, J. Am. Chem. Soc. 134, 17671 (2012).

[36] E. M. Ebeid, S. E. Morsi, J. O. J. Williams, Chem. Soc., Faraday Trans.1 75, 1111 (1979).

[37] E. M. Ebeid, S. E. Morsi, J. O. J. Williams, J. Chem. Soc., Faraday Trans. 1 76, 2170 (1980).

[38] H. Rabaud, J. Clastre, Acta Cryst. 12, 911 (1959).

[39] C. R. Theocharis, W. Jones, J. Chem. Soc., Faraday Trans. 1 81, 857 (1985).

[40] J. Räsänen, F. Stenman, E. Penttinen, Spectrochim. Acta 29A, 395 (1973).

[41] J. M. L. Martin, J. El-Yazal, J. P. François, J. Phys. Chem. 100, 15358 (1996).

[42] T. Kim, L.; Zhu, L. J. Mueller, C. J.; Bardeen, CrystEngComm 14, 7792 (2012).

[43] S. Kobatake, S. Takami, H. Muto, T. Ishikawa, M. Irie, Nature 446, 778 (2007).

[44] H. Koshima, N. Ojima, H. Uchimoto, J. Am. Chem. Soc. 131, 6890 (2009).

[45] M. Morimoto, M. Irie, J. Am. Chem. Soc. 132, 14172 (2010).

[46] R. O. Al-Kaysi, C. J. Bardeen, Adv. Mater. (Weinheim, Ger.) 19, 1276 (2007).

[47] L. Zhu, R. O. Al-Kaysi, R. J. Dillon, F. S. Than, C. J. Bardeen, Cryst. Growth Des. 11, 4975 (2011).

[48] A. E. Keating, M. A. Garcia-Garibay, *Photochemical Solid-To-Solid Reactions. In Organic and Inorganic Photochemistry*; Ramamurthy, V., Schanze, K., Eds.; Marcel Dekker: New York, 1998; Vol. 2, pp 195-248.

[49] L. Zhu, A. Agarwal, J. Lai, R. O. Al-Kaysi, F. S. Tham, T. Ghaddar, L. Mueller, C. J. Bardeen, J. Mat. Chem. 21, 6258 (2011).

[50] A. K. Burnham, R. L. Braun, Energy & Fuels 13, 1 (1999).

[51] A. Khawam, D. R. Flanagan, J. Phys. Chem. B 110, 17315 (2006).

[52] E. E. Finney, R. G. Finke, Chem. Mater. 21, 4692 (2009).

[53] P.J. Skrdla, J. Phys. Chem A 108, 6709 (2004).

[54] M. A. Watzky, R. G. Finke, J. Am. Chem. Soc. 119, 10382 (1997).

[55] J. Kohout, J. Mater. Sci. 43, 1334 (2008).

[56] R. Moré, G. Busse, J. Hallmann, C. Paulmann, M. Scholz, S. Techert, J. Phys. Chem. C 114, 4142 (2010).

[57] M.E. Brown, Thermochim. Acta 300, 93 (1997).

[58] W. Johnson, R. Mehl, Trans AIME 135, 416 (1939).

[59] M. Avrami, J. Chem. Phys. 7, 1103 (1939).

[60] M. Avrami, J. Chem. Phys. 9, 177 (1941).

[61] M. Avrami, J. Chem. Phys. 8, 212 (1940).

[62] A. Kolmogorov, Akad. Nauk SSSR, Izv., Ser. Matem. 1, 355 (1937).

[63] B. V. Erofe'ev, Dokl. Akad. Nauk SSSR 52, 511 (1946).

[64] W. Anderson, R. Mehl, Trans. AIME 161, 140 (1945).

[65] E. Prout, F. C. Thompkins, Trans. Faraday Soc. 42, 468 (1944).

[66] D. L. Wernick, S. Schochet, J. Phys. Chem. 92, 6773 (1988).

[67] K. D. M. Harris, J. M. Thomas, D. Williams, J. Chem. Faraday Trans. 87, 325 (1991).

[68] D. De Loera, A. Stopin, M. A. Garcia-Garibay, J. Am. Chem. Soc. 135, 6626 (2013).

[69] M. D. Cohen, Tetrahedron 43, 1211 (1987).

[70] M. D. Cohen, *Structurally Controlled Reactions in Organic Crystals.* In: *Reactivity for Solids*; Anderson J. S., Roberts M. W., Stone, F. S., Eds.; Chapman and Hall: London, 1972, pp 456-471.

[71] Z. Ludmer, Chem. Phys. 26, 113 (1977).

[72] J. B. Birks, J. B. Aladekomo, Photochem. Photobiol. 2, 415 (1963).

[73] J. Ferguson, S. E. H. Miller, Chem. Phys. Lett. 36, 635 (1975).

[74] G. Kaupp, Angew. Chem., Int. Ed. 31, 595 (1992).

[75] I. Turowska-Tyrk, E. Trzop, Acta Crystallogr. B 59, 779 (2003).

[76] A. F. Mabied, M. Muller, R. E. Dinnebier, S. Nozawa, M. Hoshino, A. Tomita, T. Sato, S. Adachi, Acta Crystallogr. B 68, 424 (2012).

[77] T. Kim, L. Zhu, L. J. Mueller, and C. J. Bardeen*, J. Am. Chem. Soc.* 136, 18, 6617 (2014).

[78] S. Yamamoto, K. H. Grellmann, A. Weller, Chem. Phys. Lett. 70, 241 (1980).

[79] E. Z. M. Ebeid, A. F. M. Habib, S. A. Azim, React. Solids 6, 39 (1988).

[80] A. S. Dvornikov, P. M. Rentzepis, Res. Chem. Intermed. 22, 115 (1996).

[81] K. Takegoshi, S. Nakamura, T. Terao, Solid State Nuclear Magnetic Resonance 11, 189 (1998).

[82] J. C. J. Bart, G. M. J. Smith, Isr. J. Chem 9, 429 (1971).

[83] P. J. Cox, G. A. Sim, Acta Cryst. B 35, 404 (1979).

[84] T. Wolff, J. Photochem. 16, 343 (1981).

[85] T. Salzillo, S. Zaccheroni, R.G. Della Valle, E. Venuti, A. Brillante, J. Phys. Chem. C 118, 9628 (2014)

[86] L. J. Fitzgerald and R. E. Gerkin, Acta Cryst. C53, 71 (1997).

[87] R. Moré, G. Busse, J. Hallmann, C. Paulmann, M. Scholz, S. Techert, J. Phys. Chem. C 114, 4142 (2010).

[88] Y. Ito and H. Fujita, J. Org. Chem. 61, 5677 (1996).

[89] T. Wolff, N. Muller, J. Photochem. *23*, 131 (1983).

[90] J. T. Good, J. J. Burdett and C. J. Bardeen, Small 5, 24, 2902 (2009).

[91] W. C. McCrone, in Physics and Chemistry of the Organic Solid State, eds. D. Fox, M. M. Labes and A. Weissberger, Interscience Publishers, London, 1965, vol. 2, pp. 725-767.

[92] T.L. Therelfall, Analyst 120, 2435 (1995).

[93] J. Bernstein Cryst. Growth & Des. 5, 1661 (2005).

[94] J. Bernstein Chem. Commun. 5007 (2005).

[95] T. Sakai, K. Katagiri, Y. Uemura, H. Masu, M. Tominaga, and I. Azumaya Cryst.Growth & Des. 13, 308 (2013).

[96] Bernstein, J. Polymorphism in Molecular Crystals; Clarendon: Oxford, 2002

[97] R. Boese, G. D. Desiraju, Angew. Chem., Int. Ed. 46, 615 (2007).

[98] S. Terda, K. Katagiri, H. Masu, H. Danjo, Y. Sei, M. Kawahata, M. Tominaga, K. Yamaguchi, I. Azumaya, Cryst. Growth Des. 12, 2908 (2012).

[99] G. R. Desiraju Journal of Molecular Structure 656, 5 (2003).

[100] P. Vishweshwar, A. Nangia, V. M. Lynch, Crystal Growth & Design 3, 783 (2003).

[101] G. A. Jeffrey,An Introduction to Hydrogen Bonding , Oxford University Press, Oxford, (1997).

[102] R. K. R. Jetti, F. Xue, T. C. W. Mak and A. Nangia, J. Chem. Soc., Perkin Trans. 2, 1223 (2000).

[103] V. Suitchmezian, I. Jess and C. Näther, Crystal Growth & Design 9, 774 (2009).

[104] P. W. Baures , J. R. Rush , A. V. Wiznycia , J. Desper , B. A. Helfrich , and A. M. Beatty Crystal Growth & Design 2, 653 (2002).

[105] V. S. S. Kumar, A. Nangia, M. T. Kirchner and R. Boese, New J. Chem. 27, 224 (2003).

[106] B. Fours, Y. Cartigny, S. Petit and G. Coquerel, Faraday Discuss., 2015, Accepted Manuscript DOI: 10.1039/C4FD00222A.

[107] S. Petit and G. Coquerel, Chem. Mater., 1996**, 8**, 2247.

[108] K. R. Morris, Structural aspects of hydrates and solvates. in: Brittain, H.G. (Ed.), Polymorphism in Pharmaceutical Solids, 95. Marcel Dekker: New York, 1999, 125.

[109] A. K. Galwey, Thermochim. Acta, 355, 181 (2000).

4. Polymorphism and phase mixing in the organic semiconductor 9,10-diphenylanthracene

4.1 Organic Semiconductors

Organic semiconductors are a class of functional materials with a wide range of physical and chemical properties [1-3]. The interest for these compounds in organic electronics raised with the demand of supplementing Si-based electronics with materials which could at the same time be more easily processable and allow exploitable functionalization by chemical manipulation.

After early studies by the italian scientist Pochettino, who discovered the photoelectric effect in anthracene crystals at the beginning of the last century [4], the interest in the academic community, started from the 1980s for intriguing phenomena such as charge transport, photoconductivity, electroluminescence and superconductivity in organics, has grown enormously in the last years [5-8].

The common characteristic of the large class of compounds which displays the properties of interest is the presence of π-conjugated double bonds between carbon atoms of the molecular skeleton, leading to the electron delocalization in the π molecular orbitals, allowing for charge injection delocalization and charge transport [5]. The physical parameter which describes the charge carrier property of the material is the charge mobility μ ($cm^2s^{-1}V^{-1}$), expressed as the drift velocity of the charge when an electric field of 1 V/cm is applied.

Organic semiconductors can be classified in two main groups according to their molecular weight: a) low molecular weight compounds, usually called *small molecules or molecular semiconductors*, and b) high molecular weight compounds, which are *π-conjugated polymers*, with many thousands of g/mol of molecular weight.

Theoretical and experimental research on *molecular semiconductors* has been dealing in the last years with the characteristics of their solid state phases, either as single crystals or deposited as thin/ultra-thin films on substrates of technological interest [9] such as amorphous Si, Si/SO_2 [10,11] wafer or polymeric dielectric layers [12,13], having as main application the field effect transistors [14]. Figure 4.1 shows the chemical structures of some small molecules organic semiconductors.

Experimental procedures for obtaining suitable single crystals and thin films are

available, while the mobility has increased over the time and is now comparable to that of amorphous silicon [15]. Crystalline organic materials are therefore ideal candidates for low cost electronic devices, whenever high speed components are not required. Further advantages are the easy of the processability and the modulation of the properties, as *via* chemical synthesis it is possible not only to improve the charge carrier mobility but also tailor solubility in different solvents, spectral range of the light emission, crystal packing.

Excellent reviews and books on these topics have been published [1-5,16] and give a wide overview of the field.

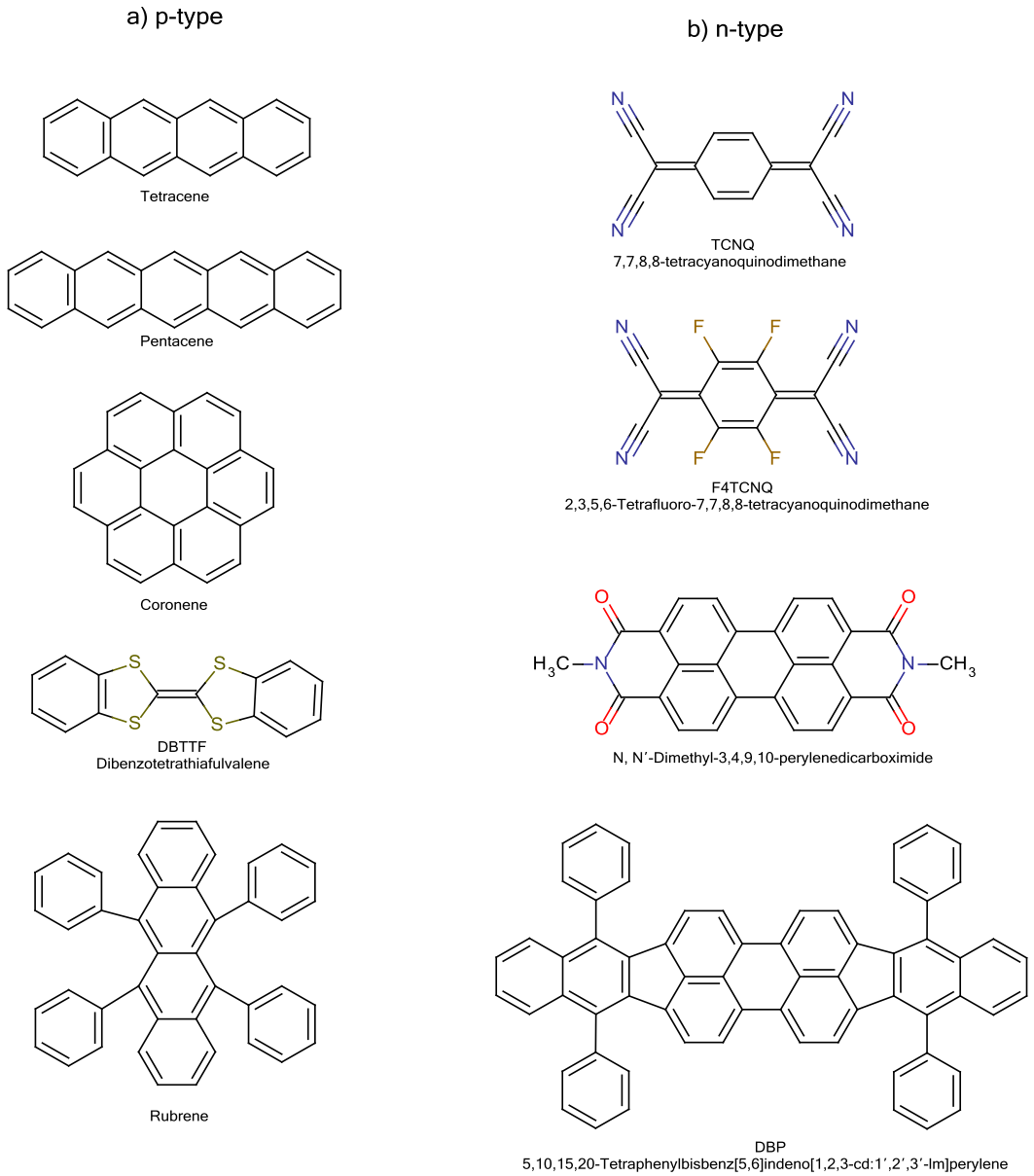

Figure 4.1 Chemical structure of some small molecule organic semiconductors: a) p-type; b) n-type.

The electronic structure of a molecular crystal and its charge carrier properties depend both on the electronic molecular structure and on the packing of the molecular units in the crystal lattice, driven by the nature and the strength of the intermolecular interactions.

The relationship between solid state organization and material properties is not clarified yet and it is very difficult to make predictions about the arrangement of the molecules in the crystal. In fact, not only small chemical changes may correspond to different packings, but the same compound may happen to have several polymorphic modifications, which differ only by a few kcal/mol in energy.

Single crystals represent suitable model systems to assess the structure/dynamics-property correlation, as in principle they are free of all the other factors, such as disorder, traps, defects, chemical and physical impurities, which affect the charge transport parameters.

In this thesis we have focused our attention on the spectroscopic study of *small molecules* organic semiconductors and their properties in single crystals. In particular, we have addressed the issue of the occurrence of polymorphism on changing method of crystal preparation.

4.2 Organic molecular crystal

Organic semiconductor compounds are characterized by the presence of extended π-conjugation of the intramolecular bonds, given by the alternation of single (σ) and double (π) bonds. In π-conjugated systems, the carbon atoms are sp^2 hybridized, with the three sp^2 orbitals involved in σ bonds occupied by highly localized σ-electrons. The nonhybridized p_z orbitals form instead the molecular orbitals involved in π bonds, described by wavefunctions orthogonal to the those of the σ skeleton of the molecule and delocalized over the entire molecule. The σ electrons are lower in energy than π electrons and therefore σ bonds are stronger. The filled molecular π-bonding orbitals form the valence band and the last one, which has the highest energy, is called Highest Occupied Molecular Orbital (HOMO). The empty molecular π*-antibonding orbitals form instead the conduction band and the lowest one is called Lowest Unoccupied Molecular Orbital (LUMO). In Figure 4.2 the scheme of the bonds for a pair of sp^2 hybridized carbon atoms is given, together with the representation of valence and conduction bands in a conjugated system.

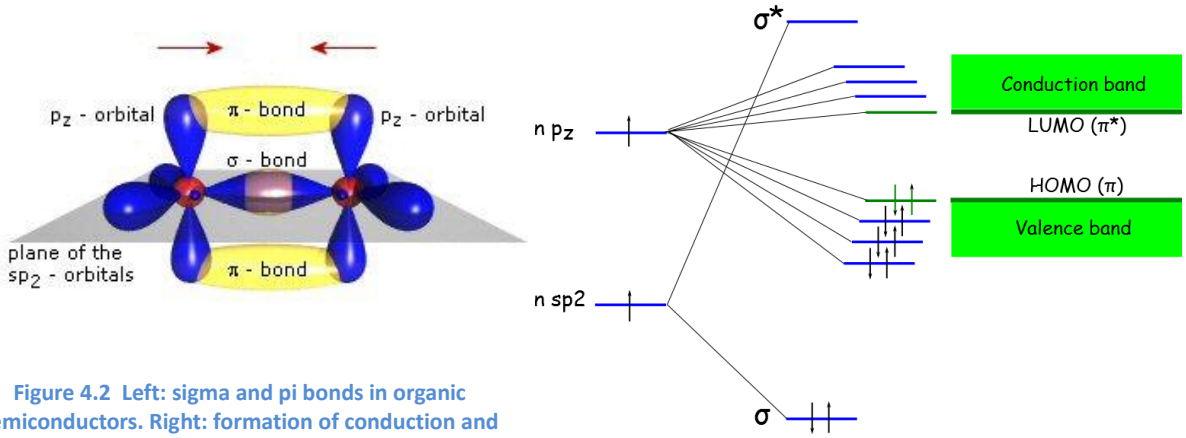

Figure 4.2 Left: sigma and pi bonds in organic semiconductors. Right: formation of conduction and valence bands in organic crystals [17].

In organic molecular crystal the intermolecular interactions are weak and mostly consist of dispersion (van der Waals) and electrostatic interactions between permanent multipoles. Hydrogen and halogen bonds can also be present. The van der Waals forces are non directional and attractive for the interplanar distances typical of organic molecular crystals ($d > 3.4$ Å [18]). The electrostatic forces [19] may be either attractive or repulsive, depending on the relative orientations of the molecules. In fact, van der Waals interactions favor packing geometries in which the molecules are oriented face-to-face, because this results in the optimization of the overlap of the π systems. The presence of the electrostatic interactions, mainly quadrupolar, favors edge-to-face or herringbone arrangements where the hydrogen of a molecule points towards the π-network of the adjacent one. The final crystal structure is the result of a balance of both interactions, which promote molecular arrangements that minimize the energy. Many organic molecular crystals display herringbone arrangements, and despite the fact that efforts have been spent in the search of systems with cofacial configurations, particularly attractive for an extended π-overlap, allowing for the largest electronic splitting in the HOMO and LUMO levels with theoretical improvement of charge carrier mobilities [20], perfect co-facial arrangements are not known, as adjacent molecules show relative displacements either along the short or the long molecular axes, so to decrease the large electrostatic repulsion between the conjugated backbones [21].

The electron mobility is basically quantified by two parameters: the *transfer integral t* [20,22], which expresses the electronic coupling between adjacent molecular units and therefore charge delocalization and the reorganization energy λ. This latter is made of two contributions: λ_i which accounts for the geometry deformation undergone by the molecule in the charge transfer, and λ_s, which instead derives from the polarization effects in the

surrounding medium [23]. To achieve high mobility, the transfer integral must be large and the reorganization energies small. Transport in generally described in two limiting cases or regimes: the band-like regime *versus* the hopping regime. In conditions of strong electronic coupling, the charge can be highly delocalized, and the system is in a band-like regime of charge transport, as found for inorganics, in which lattice phonons hamper conductivity. In this regime the mobility decreases with increasing temperature with a power law $\mu \propto T^{-a}$.

At ambient temperature, however, many organic semiconductors display a thermally activated mobility, and the hopping of charge transfer applies, in which charge carriers are localized on molecular units and move from one molecule to its neighbor. Indeed, many organic systems display a band-like regime at low temperature and switch to a hopping regime at higher T so that the total mobility can be expressed to a good approximation as a sum of two contributions:

$$\mu = \mu_{band} + \mu_{hop}$$

The first term is due to band-like regime (or coherent electron transfer) and the second term is related to the hopping motion (incoherent electron transfer). Clearly, what determine the charge transport behavior of organics are the much weaker interactions present in the molecular solids, compared to the inorganic systems which are instead characterized by high bonding energies [5]. The difference in electronic structure yields the smaller electronic bandwidths, the strong electron-lattice couplings and the polaron formation characteristic of the organics. Charge carrier mobility is strictly connected with the electronic bandwidth and differs by more than one order of magnitude between organic semiconductors (10^{-5} – 10 cm^2/Vs) [6,7,8] and crystalline silicon (50-500 cm^2/Vs) [24].

Many factors, such as chemical impurities, crystal defects, static and dynamic disorder, can affect charge transport in organics. Similarly to inorganic, organic semiconductors can be classified by the sign of the carrier transported in n- or p-type (Figure 4.3) if it is electron or hole, respectively. These characters are determined by the ionization potential (IE) and the electronic affinity (EA) and some materials shows an ambipolar charge transport behavior [25,26] ,even though hole and electron mobilities are usually not perfectly balanced. P-type organic semiconductors are in large majority compared to n-type and this is reflected by the fact that the conditions for the formation of organic molecular anions are generally less favorable.

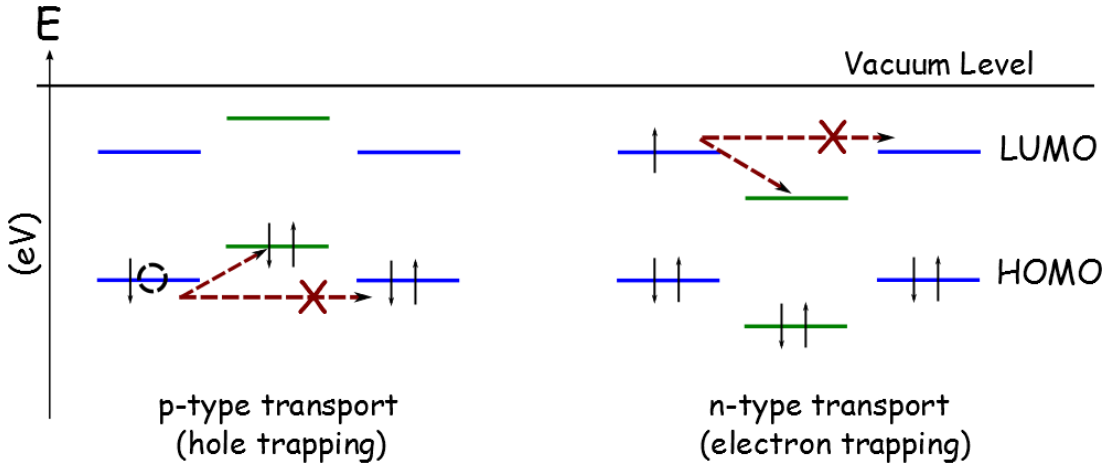

Figure 4.3 Electronic levels configuration for p-type and n-type semiconductors [27].

4.3 9,10-diphenylanthracene and its polymorphs

Polycyclic aromatic compounds in the solid state have been the subject of intense research aimed to their employment in devices like thin film transistors, photovoltaic cells, or light emitting diodes. Indeed, in the crystal phase these materials often display strong π-π interactions, and therefore can behave as semiconductors of electrons and holes and may have good charge transport properties combined to interesting optical characteristics.

9,10-Diphenylanthracene (DPA), shown in Figure 4.4, is a polyciclic aromatic compound in which the positions 9 and 10 of the anthracene backbone carry phenyl groups. The compound is structurally quite similar to rubrene, and has been shown to have both high hole and electron mobilities in the solid state [28-30], linked to an intense photoluminescence.

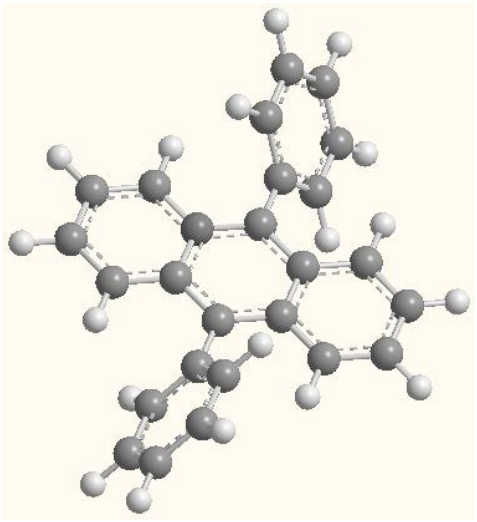

Figure 4.4 Chemical structure of 9,10-diphenylanthracene

Unlike many organics, DPA is characterized by a very good chemical stability and a melting point which is above the operating temperature of the electronic devices. Besides, DPA melts without decomposition, and this means that purification by melting and zone refining techniques can be used.

The main limitation of DPA in organic electronics applications arises from the large energy barriers to the injection of charge carriers at the electrode-organic layer interface [28,29]. This is, however, a drawback common to many organic materials, which could be overcome by using conducting polymers with tunable work functions as electrodes. Therefore DPA, with its comparable hole and electron mobilities can be selected as a model system of ambipolar compounds.

It is indisputable that high chemical purity is a key factor when reproducible intrinsic electronic mobilities in organics are sought. However, it has also been shown that in these systems charge transport also dramatically depends on the polymorphic phase of the compound. In fact, different polymorphs may correspond to very different molecular packings in the crystal unit cell and thus to altogether different intermolecular orbital overlaps of the π systems responsible for the charge carrier properties [31-35]. Furthermore, the possible coexistence of more solid phases in a sample, which is called phase mixing or structural inhomogeneity, is an intrinsic source of disorder and has detrimental effects on the mobility, as any kind of defect provides a small barrier to charge transport.

By changing method and physical conditions, the crystal growth can be driven towards the formation of a specific polymorph, and the structure obtained is not necessarily the most thermodynamically stable, especially when dealing with thin films or single crystals in the form of micro- or nano-structures.

For this reason, the definition of the experimental conditions in which a certain stable solid phase can be obtained is important, as it is the understanding of the link between optimal transport properties and solid state molecular organization. Indeed, the phenomenon of polymorphism in molecular crystals has attracted attention of pharmaceutical research for a long time [36], but only recently there has been an increasing interest for polymorphs of small molecule organic semiconductors [35-40].

As for DPA, until now only one solution grown crystal structure has been reported in detail in the literature [41-43]. However, in the first crystallographic report on this compound [41] the Authors also refer to a private communication concerning a different structure obtained from the melt, for which unfortunately only cell parameters were given. Electron and hole mobilities [28] were measured in highly pure crystals grown by Bridgman's method (and therefore from melt), which were found to have the same structure as the solution grown literature samples [41-43]. In his thesis work Tripathi [29] reported on another structure, which also displayed ambipolar behaviour, and was instead obtained by vapor growth.

Altogether, we felt that the situation about polymorphism in DPA had not been quite clarified yet and that, especially in view of the possible applications of this compound, some advancements were needed in the knowledge of the number of its polymorphs, the way each of them could be obtained and their relative thermodynamic stability.

Therefore, in this thesis work, DPA crystals were grown in a number of ways and characterized by micro-Raman spectroscopy in the low-wavenumber region (10-150 cm^{-1}), where lattice phonon vibrations can be observed and different crystal structures readily discriminated. Calculations of crystal potential energy were also performed, to assess the energy of the structures for which the atomic coordinates in the crystal unit cell were known from X-ray diffraction methods, following a joint experimental and computational approach which has been proved to be very efficient in aiding the characterization of polymorphs in functional molecular materials. The analysis of the lattice phonon Raman spectra allowed us to identify three different DPA polymorphs, named in this work α, β and γ. Polymorph α is the well known form, grown from solution in this work, also present in commercial DPA, and corresponding to that obtained by Bridgman's technique [28]. Polymorph β has been grown from the melt in this work but corresponds to that grown by sublimation in the thesis of Tripathy [29]. A third, new polymorph, γ, has been seen for the first time by Raman spectroscopy in a phase mixing with either α or β and has also been identified as the only form present in nanostructures obtained in solutions.

4.3.1 Sample Preparation

DPA was purchased from Sigma Aldrich (purity 99%), and the pristine material was formed by small needles of pale yellow color. By slow re-crystallization from a toluene solution in a 2 ml vial at ambient conditions, needle-like crystals a few mm long of the α polymorph were grown. Solution crystallized DPA was melt in a sealed vial, and crystals of β-DPA with varying morphologies were obtained, while the vapor condensed on the vial walls formed colorless thin platelet-like crystals of the γ polymorph. Yellow microcrystals of γ-DPA were also grown by sublimation at 160 °C at low pressure (10 Pa) of N_2 and at the optical microscope they appeared like platelets of elongated irregular hexagonal shape. In the same growth, it was possible to identify and select for the measurements needle crystals of α-DPA. Following the literature [44], γ-DPA nanostructures were grown at room temperature by injecting 100 µl of a 2×10^{-3} M solution of DPA in THF in 5 ml of milli-Q water under vigorous stirring. The sample was kept under stirring for three minutes and then left overnight to allow for the crystal growth. In Figure 4.5 the optical image of the nanostructures, collected with a confocal laser scanning microscope (CLSM), is shown.

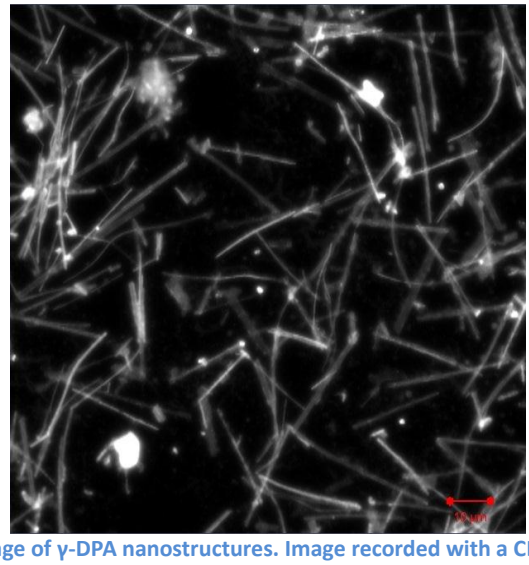

Figure 4.5 Optical image of γ-DPA nanostructures. Image recorded with a CLSM with λ_{exc} = 405 nm

4.3.2 Experimental set-up

The micro-Raman setup described in chapter 2 was employed for the spectroscopic characterization. The Raman excitation was from a krypton laser tuned at 647.1 nm, a wavelength chosen to avoid fluorescence, as DPA solutions in toluene were not found to absorb significantly above 450 nm.

4.3.3 Computational methods

Quasi harmonic lattice dynamics (QHLD) calculations can be used to determine the equilibrium crystal structure and binding energy at non zero temperatures and pressures, together with lattice phonon frequencies, possibly estimating the extent of the coupling between lattice and internal (molecular) vibration modes.

In the QHLD method [45] the Gibbs free energy of the crystal is computed as the free energy of an ensemble of phonons of frequency v_i

$$G(p,T) = \Phi_0 + pV + \sum_i \frac{h\nu_i}{2} + k_B T \sum_i ln\left[1 - exp\left(-\frac{h\nu_i}{k_B T}\right)\right]$$

Here ϕ_0 is the total potential energy of the crystal in its average structure (the electronic ground state energy), pV is the pressure-volume term, $\sum_i h\nu_i/2$ is the zero-point energy, and the last term is the entropic contribution. Given an initial crystal structure, one computes ϕ_0 and its second derivatives with respect to the displacements of the molecular coordinates. The second derivatives form the dynamical matrix, which is numerically diagonalized to obtain the phonon frequencies v_i and the corresponding eigenvectors. The structure as a function of p and T is then determined self-consistently by minimizing $G(p,T)$ with respect to lattice parameters, molecular positions and orientations. The total potential ϕ_0 is made of inter- and intra-molecular terms, ϕ_{inter} and ϕ_{intra}, respectively.

In the present treatment, the molecules do vibrate but maintain their average geometry. The interactions are represented by ϕ_{inter}, expressed as a pairwise additive atom-atom potential to which an electrostatic term is added. This term is expressed as a Coulomb interaction represented by a set of charges residing on the atoms. The Ewald's method is applied to accelerate the convergence of the Coulombic interactions [46]. *Ab-initio* methods are usually used to compute atomic charge distributions fitted to the molecular electrostatic potential, which are better suited than the Mulliken values, derived from molecular orbital coefficients. *Ab-initio* methods are often employed also for the input molecular geometry, although the experimental X-ray data can also be used.

To compute the phonon frequencies one needs all second derivatives $\partial^2\phi_0/\partial Q_{ri}\partial Q_{sj}$ of the total potential with respect to all pairs of molecular coordinates Q_{ri} and Q_{sj}. Here r and s indexes label molecules in the crystal, while i and j distinguish between molecular

coordinates. An efficient way to evaluate the effect of the internal modes is the exciton-like model [47], in which ϕ_{intra} corresponds to the harmonic potential of an isolated molecule. Thus the diagonal derivatives of ϕ_{intra} coincide with those of an isolated molecule, and correspond to the frequencies of the normal modes of the molecule, while off diagonal derivatives are zero. The coupling between the molecular coordinates is given solely by the intermolecular potential ϕ_{inter}, which is a function of the interatomic distances. Since the distances depend on the Cartesian coordinates X_{ra} of the atom a, ϕ_{inter} second derivatives can be computed in terms of X_{ra}, and then converted to molecular coordinates Q_{ri} using the derivative chain rule, $\frac{\partial f}{\partial x} = \frac{\partial f}{\partial y}\,\frac{\partial y}{\partial x}$:

$$\frac{\partial^2 \phi_{inter}}{\partial Q_{ri} \partial Q_{sj}} = \sum_{ra,sb} \frac{\partial^2 \phi_{inter}}{\partial X_{ra} \partial X_{sb}} \frac{\partial X_{ra}}{\partial Q_{ri}} \frac{\partial X_{sb}}{\partial Q_{sj}}$$

Here a and b label the Cartesian coordinates of the atoms in molecules r and s, and the matrix $\partial X_{ra}/\partial Q_{ri}$ describes the Cartesian displacements which correspond to each molecular coordinate Q_{ri}.

The displacements corresponding to rigid translations and rotations of the molecules can be derived by simple geometric considerations [47]. The displacements associated to the intramolecular degrees of freedom are the cartesian eigenvectors of the normal modes of the isolated molecule, which are usually computed with *ab-initio* methods.

In the treatment of DPA crystal structures, free energy minimizations were performed using the WMIN program [48] for rigid molecules. The intermolecular interactions were represented by an atom-atom potential with Buckingham terms and Coulomb's terms with atomic charges fitted to the *ab-initio* electrostatic potential, calculated using the B3LYP/6-31G(d) combination of density functional and basis set. The parameters of the intermolecular potentials were taken from the Williams's model [49].

The experimental X-ray data were the input parameters in the energy minimization procedure. This allowed us to locate the local minimum for the model potential, which corresponds to the potential energy ϕ of the structure at its mechanical equilibrium. The effects of temperature were accounted for by computing the structures of minimum Gibbs energy G(p,T) with the QHLD method [50,51], that is by determining the structure at thermodynamical equilibrium.

The isolated molecule properties needed for the crystal energy calculations or the interpretation of the vibrational features, that is, optimized geometry, atomic charge distribution and harmonic vibrational frequencies, were computed with the GAMESS program [52], using the B3LYP/6-31G(d) combination. As a starting molecular geometry for the *ab-initio* calculations, the molecular conformations obtained from the X-ray atomic coordinates were chosen, adding the constraint of a C_{2h} symmetry. Such a choice was made because, despite the fact that for all structures the molecules lie in sites with symmetry C_i, the C_{2h} symmetry describes very well the experimental molecular geometry.

The harmonic frequencies for the isolated molecule were calculated at the optimized *ab-initio* structure, to identify the internal modes which could couple, by symmetry and energy, with the lattice phonon modes, thus determining the vibrational features in the low energy range of the Raman spectrum. Also, they were calculated to test whether the C_{2h} molecular conformation corresponded to an energy minimum for the molecule, by assuring that all the vibrational eigenvalues were positive.

4.3.4 Crystal Structures

Three X-ray structures of crystalline DPA have been published complete of atomic coordinates [41-43] and they all concern the same monoclinic phase, obtained from solution in a variety of solvents such as toluene, xylene and n-pentane. The structural parameters of this phase, which we name polymorph α, also correspond to those given in the work by Tripathi *et al.* [28].

The monoclinic structure belongs to the standard space group C2/c (C_{2h}^6), with Z=4 and room temperature unit cell parameters *a* = 10.683 Å, *b* = 13.552 Å, *c* = 12.2570 Å and β = 90.54° [42]. A projection of the unit cell of α-DPA is given in Figure 4.6. The conventional cell is non-primitive (C side-centered), the molecules lie on inversion sites with centers of mass at (1/4,1/4,0.0), (3/4,3/4,0.0), (1/4,3/4,1/2), (3/4,1/4,1/2), and the asymmetric unit is therefore a half-molecule, while the C_2 rotation axis is parallel to the b crystallographic axis. The molecular geometry is C_i, with very small deviations from C_{2h}. The dihedral angle formed by the plane of the anthracene and the phenyl substituent is ≈ 67°. The short C-C contacts between atoms in the anthracene skeletons along the *c* axis are shown in figure 6 and is 3.778 Å while the shortest intermolecular C-C distance, between an atom of the anthracene skeleton and an atom of the phenyl group of an adjacent molecule is 3.673 Å.

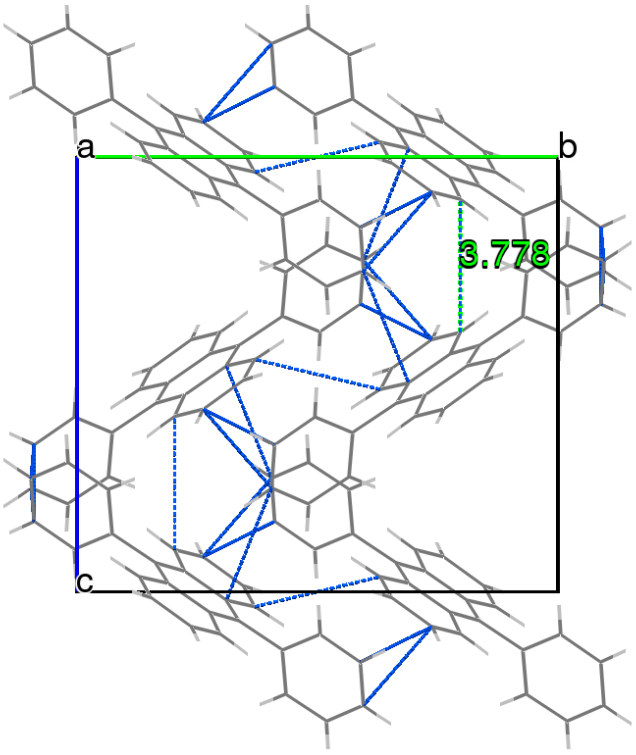

Figure 4.6 Unit cell of the α-DPA polymorph (C2/c symmetry): view along the *a* crystallographic axis. Short C-C contacts between atoms in the anthracene skeletons along the *c* axis are also shown, together with short C-C between anthracene skeletons and phenyl group in adjacent molecules.

In the primitive cell (Z=2), used for the analysis of the Raman spectra, there are two equivalent molecules per cell, with parameters $a' = b' = 8.628$ Å, $c' = c$, $\alpha' = \beta' = 90.33$ and $\gamma' = 105.503°$. In a vector form, the transformation from conventional to primitive is:

$$\boldsymbol{a}' = \frac{(\boldsymbol{a} - \boldsymbol{b})}{\mathbf{2}};\ \boldsymbol{b}' = \frac{(\boldsymbol{a} + \boldsymbol{b})}{\mathbf{2}}$$

Room temperature cell parameters for the $P2_1/a$ structure named polymorph β are *a*=9.4976 Å, *b*= 20.413 Å, *c*=10.0843 Å and β= 112.307°. In the unit cell, shown in Figure 4.7, two non equivalent molecules lie on inversion centres at (0,0,0) and (0,0,1/2). The dihedral angles between the anthracene backbone and the phenyl groups are slightly different in the two molecules, being ≈ 77° and 74° respectively, and differ from the value found in polymorph α. Also in this case, the deviations from the C_{2h} symmetry are small.

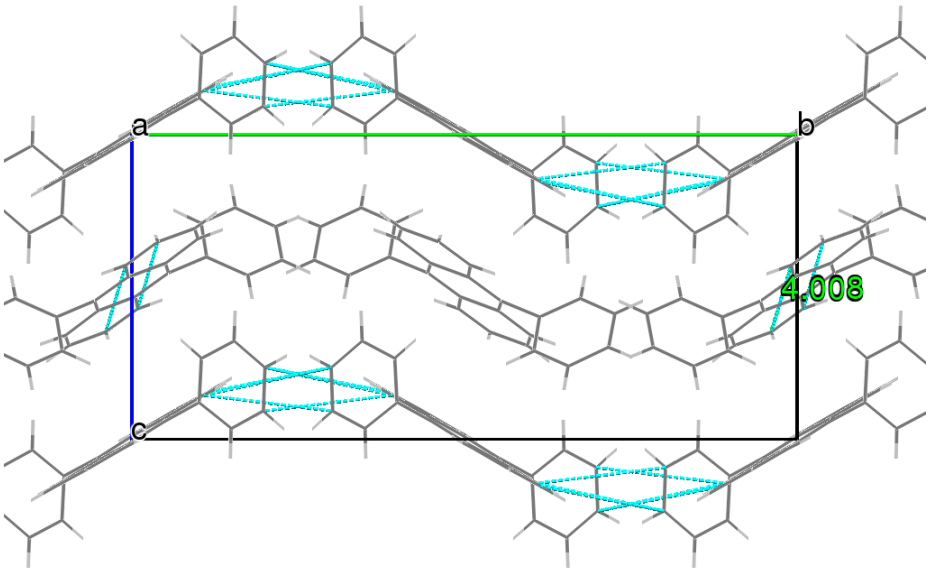

Figure 4.7 Unit cell of the β-DPA polymorph ($P2_1/a$ symmetry): view along the *a* crystallographic axis. Short C-C contacts between atoms in the anthracene skeletons along the *c* axis are also shown, together with short C-C between anthracene skeletons and phenyl groups in adjacent molecules.

The structures α and β present very different ways of packing pairs of molecules, as shown in Figure 4.8. Indeed, a phase transformation from α to β (and viceversa) may be hindered by the high energetic cost to be paid to perform the molecular motions which would rearrange one structure into the other.

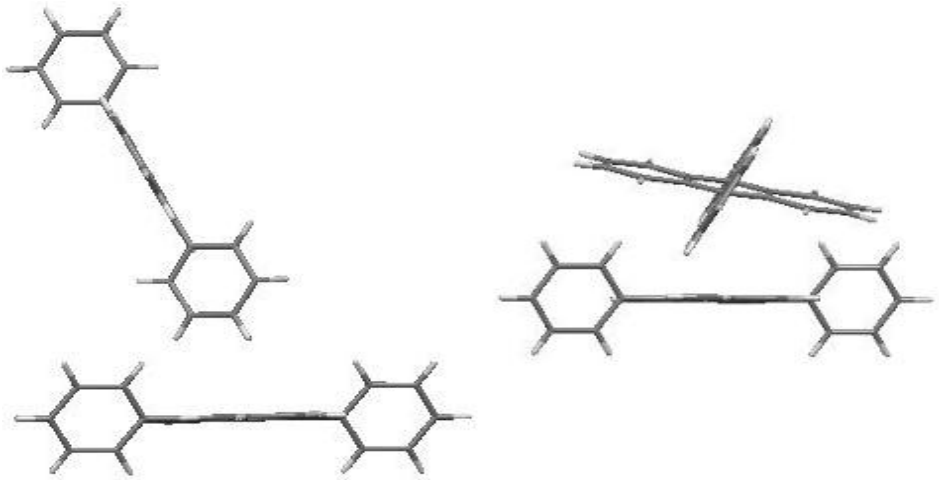

Figure 4.8 Molecular arrangement in DPA polymorphs; left: α-DPA; right: β-DPA

Despite the fact that DSC measurements [29] do not show a phase transition before melting [28], Adams and Ramdas [41] reported on a P2/m crystalline DPA phase obtained from the melt [41], with parameters a = 9.99 Å, b = 21.06 Å, c = 9.11 Å, β = 112.0°. As no atomic

coordinates are available, it is difficult to establish whether this structure does correspond to that of the crystals obtained from the vapor by Tripathy [29] and from the melt in this thesis.

A third polymorphic phase has been detected by lattice phonon Raman spectroscopy only (*vide infra*) in batches where either α-DPA or β-DPA were also obtained, and, in a pure form, as nanocrystals.

4.3.5 Raman Spectra

The Raman spectra of a number of DPA crystals, prepared as illustrated above, were recorded, giving a special emphasis to the spectral region of lattice phonons.

The crystal planes of our samples could not be directly identified by X-ray measurements, with the exception of a few platelets of the β polymorph. As the Raman technique is here mainly used as a diagnostic tool in identifying different solid phases, the punctual knowledge of the crystal faces from which the Raman scattering is observed is not strictly important. That said, in many cases it was possible to make a reasonable guess of the crystal face probed in the experiment on the basis of considerations on the crystal morphology and on symmetry selection rules, and therefore measure Raman polarized spectra. These are extremely helpful when the phonon spectra are very crowded and more bands overlap, so that it is difficult to disentangle them all, a procedure sometimes necessary to ascertain the purity of the phase.

4.3.5.1 The Polymorph α

Figure 4.9 shows the Raman spectra of a DPA needle grown from a toluene solution in the region of the lattice phonons and of the lowest energy molecular vibrations. For the sake of clarity, we show also the spectral deconvolution and the peak assignments. The image of the typical thin-needle morphology which accompanies this lattice phonon spectrum is also given in the figure.

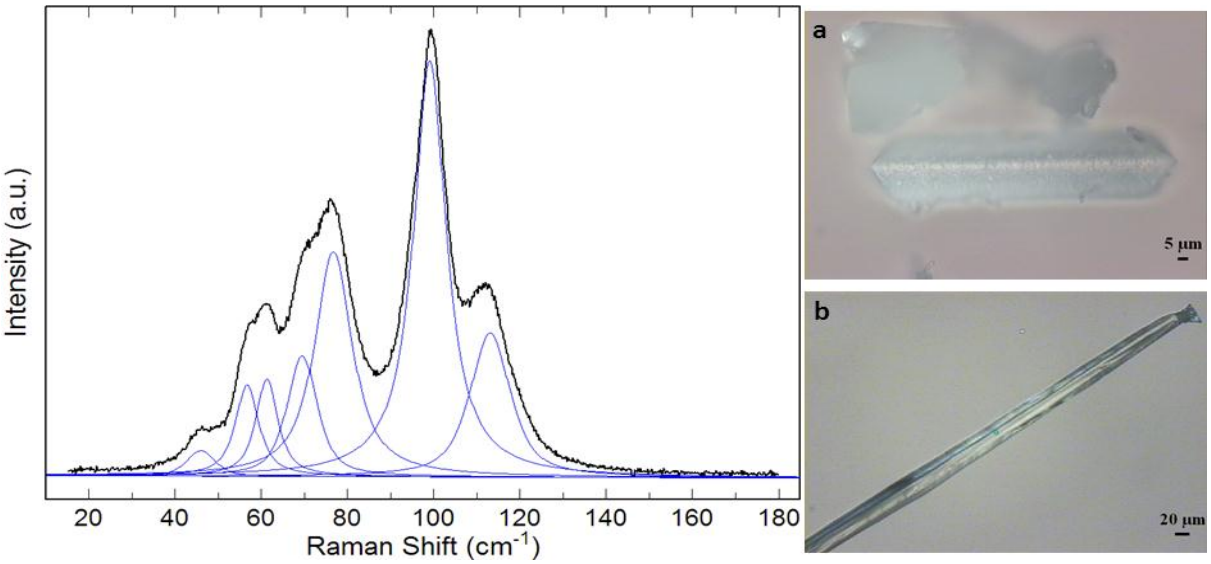

Figure 4.9 Left: Raman spectrum of a α-DPA sample in the wavenumber region 10-150 cm^{-1}; right: optical images of α-DPA samples: a) prism-like and b) needle.

The same spectrum is observed in commercial DPA, prior to re-crystallization, and is the only one we have found in solution grown specimens. Although thin needle crystals characteristically display this spectrum, microcrystals of different morphology, obtained by slow cooling of the melt or by sublimation, such as those shown in Figure 4.9b, still yield the same spectral features.

The lattice phonon spectrum of polymorph α of figure 9 can be discussed in the light of the crystal structure and of the vibrational dynamics of the system. In the frame of the rigid molecule approximation [40], that is when internal molecular degrees of freedom are neglected, the number and the symmetry of the Raman active lattice modes (***k***=0) in the C2/c structure can be determined by considering the corresponding reduced primitive cell with Z = 2, obtained as described above. Out of a total of 12 lattice modes, 6 are of gerade symmetry ($3A_g$ + $3B_g$) and are Raman active. However, as in the case of rubrene [54], molecular vibrational modes of low frequency, which involve the phenyl groups attached to the anthracene skeleton, can strongly couple with lattice vibrations. Indeed the *ab-initio* calculations show that five molecular vibrational modes with gerade symmetry, suitable for coupling, lie below 200 cm^{-1} and three of these lie below 100 cm^{-1}. As the site symmetry in the crystal is C_i, each internal mode of gerade symmetry splits in two components of symmetry A_g and B_g, respectively, according to the C_{2h} factor group [40]. This easily explains why the number of the bands observed in our experiments at low energy is always higher than six.

Polarized Raman spectra were recorded for a needle-like single crystal oriented, with

an aid of a polarized microscope, in the extinction direction, which was found to be at 45° with respect to the needle axis. In the back scattering geometry of our set-up, the spectra of Figure 4.10 were collected with a polarization parallel to that of the horizontally polarized incoming bean, (namely, H-H) or perpendicular (V-H), respectively. After allowing for residual polarization, each spectrum displays below 125 cm^{-1} at least five distinct not overlapping bands, which can be assigned to A_g (H-H) and B_g (V-H) modes. This implies that the face probed in the experiment is not ac where B_g transitions would not be observable. Polarized spectra recorded in the range of the pure internal vibrations revealed that most bands are actually split in two components, thus confirming that B_g modes are observable on the analyzed face.

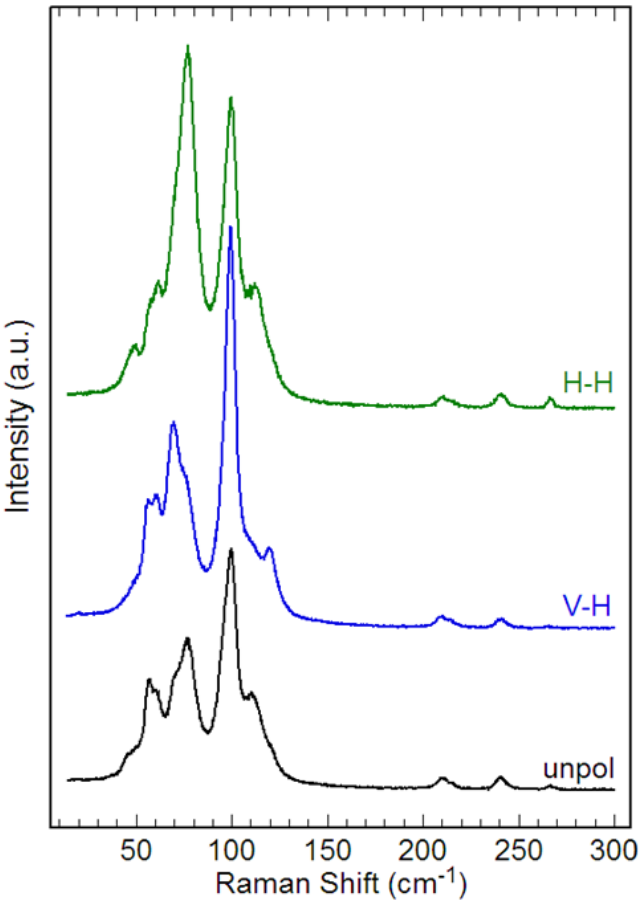

Figure 4.10 Polarized Raman spectrum of α-DPA single crystal (needle) in the wavenumber region 10-150 cm^{-1}; H-H and H-V polarizations (see text for explanation of the symbols) are compared to the full spectrum of the crystal (unpol).

4.3.5.2 The Polymorph β

The Raman spectrum of a sublimation grown $P2_1/a$ DPA crystal is shown in Figure 4.11 together with its optical image (Figure 4.11a). The deconvolution of the spectrum is also shown. It should be noticed that the same spectrum is also found in samples grown by fast cooling from the melt (Figures 4.11b,c,d). As in the case of the α phase, morphology can vary and the shape of the crystals is never a good diagnostics for the phase identification, unlike what happens in other organics [40]. We can, however, confidently assign our samples to β-DPA, because they all present the same Raman spectrum and this coincides with the spectrum recorded for a sample of DPA grown from sublimation [55].

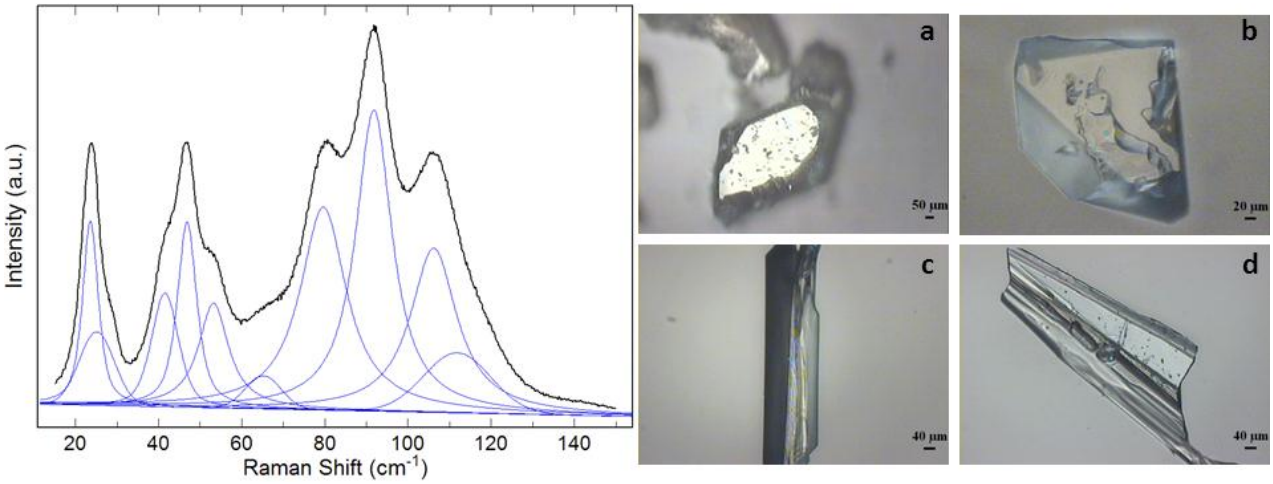

Figure 4.11. Left: Raman spectrum of β-DPA polymorph in the wavenumber region 10-150 cm^{-1}; right: optical images of α-DPA samples in the various morphologies displayed.

X-rays analysis [29] has shown that platelet-like crystals of the β polymorph show a preferential growth in the *ac* plane. This knowledge allows for a more detailed analysis of the vibrational features of this polymorph. The incident laser light is, in this case, parallel to the monoclinic *b* axis which also coincides with one of the crystal optical directions of the biaxial indicatrix. Maximum birifrangence conditions can be acquired, but the extinction conditions in polarized light do not correspond either to *a* or *c* crystallographic axes.

On the basis of selection rules of the $P2_1/a$ crystal space group, 12 out of the 21 optical lattice modes ($6A_g+6B_g$) are expected to be Raman active in the rigid molecule approximation. By symmetry, when the back-scattered radiation from the *ac* face is analyzed, only the six modes of A_g symmetry can be detected, as the *aa*, *cc* and *ac* components of the polarizability tensor all belong to the total symmetric representation of the factor group C_{2h}. By allowing the coupling with molecular internal vibrations, as in the case of α-DPA, the number of bands

increases, due to the mixing with the total symmetric contributions of the molecular vibrations. Depending on the specific component of the Raman tensor which is probed in each experiment, different intensity patterns of the A_g bands can be observed in the oriented sample, as a result of the relative polarization of incident and scattered light.

An example of this is reported in Figure 4.12 for an oriented platelet. The spectra of the Figure have been recorded by collecting the Raman scattering polarized either parallel (H-H) or perpendicular (V-H) to the excitation. While the total number of bands remains unchanged, the relative intensities change.

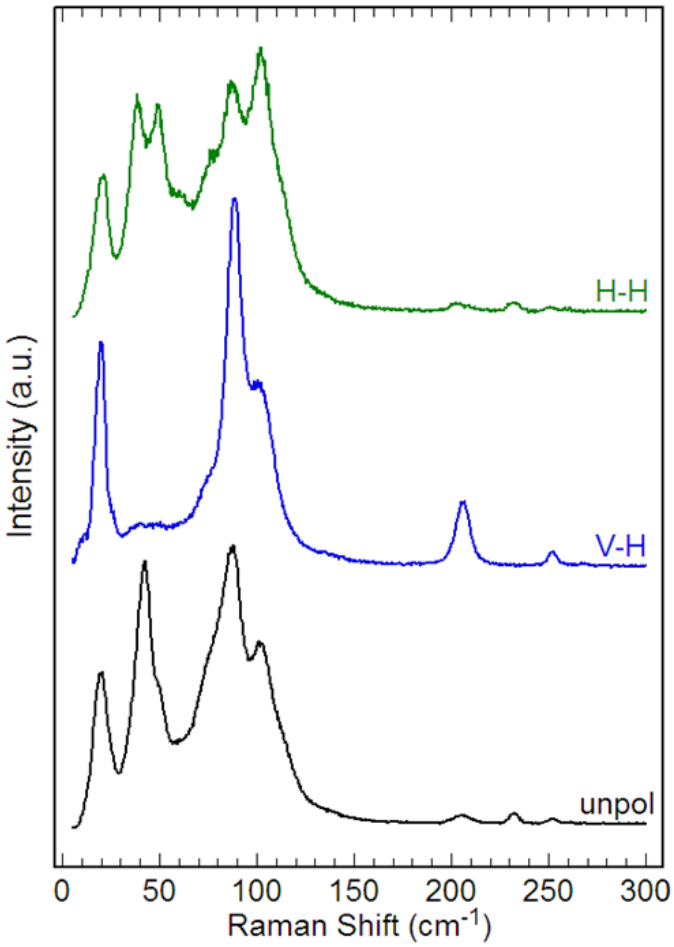

Figure 4.12 Polarized Raman spectra of a β-DPA platelet in the low wavenumbers region. The platelet was in polarized light, with the ac crystal face normal to the incident (horizontally) polarized laser radiation. Next to each spectrum, the relative polarization of excitation and scattering (see text for explanationof the symbols).

4.3.5.3 The Polymorph γ

The Raman spectrum of the DPA nanocrystals is shown in Figure 4.13 together with the optical image of the sample, showing structures of the same morphology and dimensions as those given in Zhang and coworkers [44]. As reported above, the same spectrum was obtained for bulk crystals found in the growth of either the α or the β polymorph.

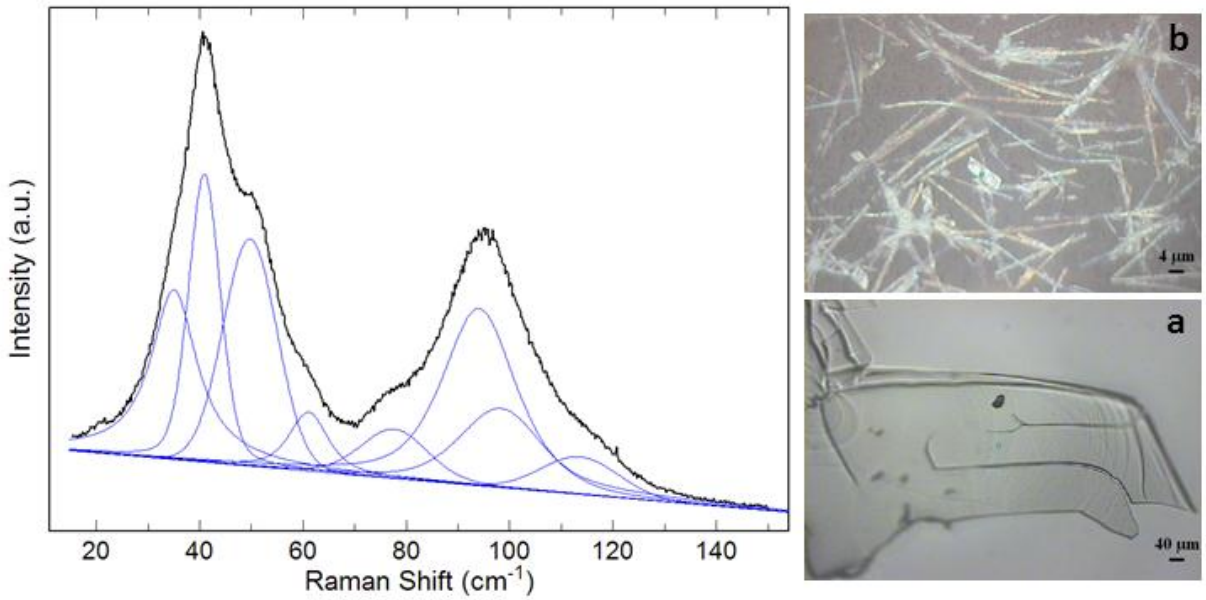

Figure 4.13 Left: γ-DPA Raman spectrum in the wavenumber region 10-150 cm^{-1}; right: optical images of γ-DPA samples: (a) nanocrystals and (b) platelet.

The bad quality of the crystals grown in batches where other polymorphs were present did not allow us to determine the structure of this phase by single crystal X-ray diffraction methods. The quantity of nanostructures so far obtained would be certainly suitable for powder X-ray determination. However, we are quite certain that this is a new polymorph and that we are not looking at a different face of either of the known ones for at least two reasons: the Raman spectra of ground samples of α-DPA and β-DPA were recorded, in such a way to have data as complete as possible of both of them for all the possible orientations, and a satisfactory match or overlap with the spectrum of the unknown phase was never found; on the other hand, as shown in Figure 4.14, it is possible to measure polarized spectra of a micro-crystal of the unknown phase oriented along a direction of maximum extinction. Despite residual polarization, probably due to the fact that we are not dealing with a single crystal, the band pattern is quite clear, and, again, no overlaps with the spectra of the other phase are clearly detectable.

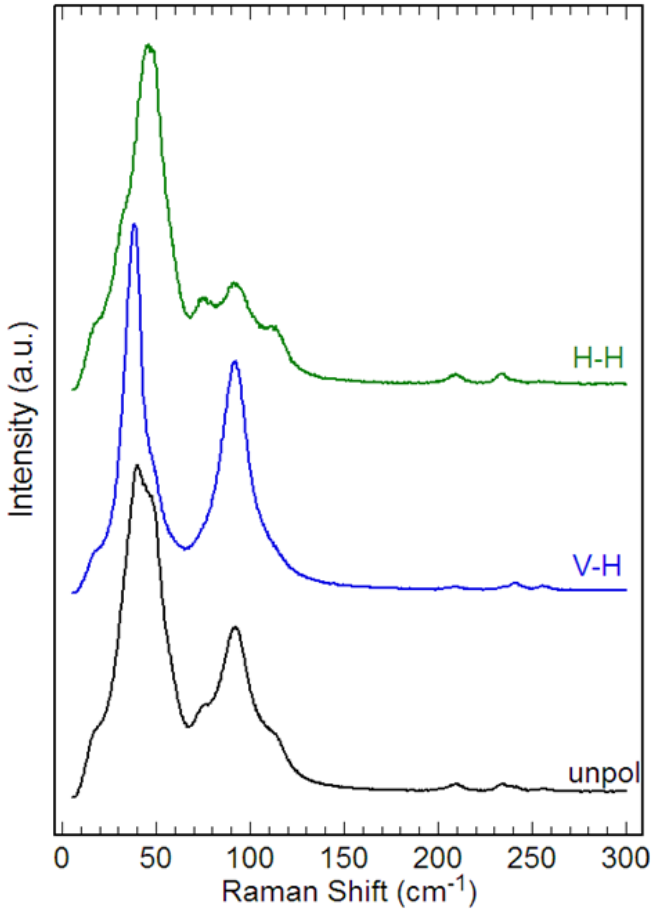

Figure 4.14 Polarized Raman spectra of a y-DPA platelet in the low wavenumbers region.

4.3.6 Computational Results

In Table 4.1 the results of the crystal structure calculations for the DPA polymorphs are reported. The structural parameters, calculated at the minimum of the potential energy ϕ and at the minimum of the free energy G(T), are compared to the X-ray data [29,55]. G(T) values are given at the temperature of the experiments. Note that the computed cell volumes at minimum ϕ are systematically smaller than the experimental ones, and this is expected as no thermal effects are included. Once thermal effects are accounted for, the volume increases, and the agreement with the experiments improves. It should be pointed out that the agreement with the experiments has been found excellent only by employing in the calculations the molecular geometry as given by the X-rays measurements. The attempt to use the optimized C_i geometry obtained from the *ab-initio* calculations leads to structures with large deviations from the experiments (results not shown), especially for the α polymorph.

In fact, the main difference between calculated and experimental geometries involves the torsional angles between the anthracene skeleton and the phenyl groups, which is ≈ 75° in the former and, as given in section ≈ 67° in the latter. This is a strong indication that the slight conformational changes between polymorphs, driven by the different crystal packing, cannot be overlooked.

The α polymorph turns out to be the most stable, corresponding both to the deepest potential minimum ϕ and to the structure with the lowest free energy G at ambient conditions. This was expected, as polymorph α has been the only one known for a long time. Note that is also the most dense structure, and thus again, predictably, the most stable, following the rule of thumbs for relative polymorph stability. Interestingly, the calculated free energy for α is the lowest over the 0-500 K temperature range. Therefore, from the computational point of view, no solid-phase transitions are expected for this polymorph before the melting point. This result agrees with the experimental finding for which α and β are in a monotropic phase relationships [29,36].

Table 4.1 The experimental structures of the known DPA polymorphs [41,42,43,44] are compared to the minimum potential energy Φ and minimum free energy structures, Energies are in kcal/mole, unit cell axes *a*, *b*, *c* are in Å , angles α, β, γ in degrees, and cell volumes V in Å³.

	a (Å)	*b* (Å)	*c* (Å)	*α* (deg)	*β* (deg)	*γ* (deg)	V (Å³)	Energy (Kcal/mole)
	Polymorph α							
Experimental	10.683	13.552	12.257	90.00	90.54	90.00	1774.441	
Minimum ϕ	10.521	13.576	12.238	90.00	91.05	90.00	1747.664	-64.89
Minimum G (293K)	10.627	13.645	12.371	90.00	91.164	90.00	1793.484	-73.59
	Polymorph β							
Experimental	9.4976	20.413	10.0843	90.00	112.307	90.00	1808.8	
Minimum ϕ	9.4894	20.386	9.9642	90.00	112.124	90.00	1785.6	-62.59
Minimum G (293K)	9.5534	20.557	10.0241	90.00	112.006	90.00	1825.169	-71.80

4.4 Discussion and Conclusions

Although polymorphism is widely encountered in organic materials for electronics [56-58], and in particular in polyaromatics hydrocarbons (PAHs) [59], there are, however, few instances of 9,10-anthracene derivatives which show this behavior and in this DPA represents an interesting case. Besides, the α and β polymorphs of DPA may constitute an example of polymorphs in a monotropic relationship. The energy barrier for the transformation from α-DPA to β-DPA (or viceversa) could be too high to be overcome by heating before melting. As the calculations and the experiments indicate that the α phase is the one thermodinamically

stable, no precaution should be taken to preserve it in devices and applications, once it has been obtained. Instead, the β phase could be metastable, yielding the α phase in a range of *p,T* conditions. However, a kinetically controlled transformation β to α is made particularly unlikely by the large molecular reorganization that such a transformation would require. Interestingly, the two polymorphs can form in very similar conditions, although the observation that β is obtained in "fast processes" is a further indication that its formation is kinetically controlled. In all the growth conditions tested in this work, α and β forms have never found to coexist in the same batch, and this allowed us to conclude they are never concomitant polymorphs. The γ phase, instead, is found concomitantly with either form, even though phase mixing, in the meaning of a sample appearing as homogeneously belonging to a single phase, but actually formed instead by domains of two [55], has not been observed. The most interesting finding about γ-DPA is the possibility of obtaining it in nano and micro-structures, because these kind of one- and two-dimensional morphologies has attracted recently much interests for application in devices [60,61]. Note that in reporting for the first time DPA nanostructures [60], Zhang mentioned that they were found to have the same structure as the most common polymorph α. However, in Reference [44], variable surfactant concentration was used (unlike here) to guide the growth morphologies and indeed, the presence of surfactant could also selectively drive the polymorph formation. Mobility measurements could say whether the occurrence of γ-DPA is to be avoided in DPA samples or, instead, the packing of this structure could be exploited to improve its charge transport performances.

It is worth mentioning that it is not the first time that a new polymorph is spotted by Raman microscopy before being identified by X-ray or other methods. Among the examples to remember we mention those of dibenzo-tetrathiafulvalene and of tetraphenylbutadiene [40,57,58,62].

References

[1] R. H. Friend, R. W. Gymer, A. B. Holmes, J. H. Burroughes, R. N. Marks, C. Taliani, D. D. C. Bradley, D. A. Dos Santos, J. L. Brédas, M. Logdlund, and W. R. Salaneck, Nature 397, 121 (1999).

[2] A. Dodabalapur, H. E. Katz, L. Torsi, and R. C. Haddon, Science 269, 1560 (1995).

[3] G. Malliaras, and R. Friend, Physics Today May 2005, 53 (2005).

[4] A. Pochettino, *Atti della R. Accademia dei Lincei. Rendiconti della classe di scienze fisiche, matematiche e naturali* 15, 355 (1906).

[5] M. Pope and C. E. Swemberg, *Electronic processes in organic crystals*. Oxford: Claredon Press (1982).

[6] E. J. Meijer, D. M. de Leeuw, S. Setayesh, E. van Veenendaal, B. H. Huisman, P. W. M. Blom, J. C. Hummelen, U. Scherf, and T. M. Klapwijk, Nature Materials 2, 678 (2003).

[7] D. V. Lang, X. Chi, T. Siegrist, A. M. Sergent, and A. P. Ramirez, Physical Review Letters 93, 086802 (2004).

[8] O. D. Jurchescu, J. Baas, and T. T. Palstra, Applied Physics Letters 84, 3061 (2004).

[9] M. M. Ling and Z. Bao Chem. Mater. 16, 4824 (2004).

[10] C. Bartic, H. Jansen, A. Campitelli, S. Borghs, Org. Electron. 3, 65(2002).

[11] A. Salleo, M. L. Chabinyc, M. S. Yang, R. A. Street, Appl. Phys. Lett. 81, 4383 (2002).

[12] Z. Bao, V. Kuck, J.A. Rogers, M. Paczkowski, Adv. Funct. Mater. 12, 526 (2002).

[13] L. L. Chua, P. K. H. Ho, H. Sirringhaus, R. H. Friend, Appl. Phys. Lett. 84, 3400 (2004).

[14] H. Koezuka, A. Tsumura, T. Ando, Synthetic Metals 18, 699 (1987).

[15] A. R. Moore Appl. Phys. Lett. 31, 762 (1977).

[16] G. Schweicher, Y. Olivier, V. Lemaur and Y.H. Geerts, Isr. J. Chem**.** 54, 595-620 (2014).

[17] Organic Semiconductor World www.iapp.de/orgworld

[18] K. A. Williams, P. T. M. Veenhuizen, B. G. de la Torre, R. Eritja, and C. Dekker, Nature 394, 52 (2002).

[19] C. A. Hunter, and J. K. M. Sanders, Journal of American Chemical Society 112, 5525 (1990).

[20] J. Cornil, D. Beljonne, J. P. Calbert, and J. L. Brédas, Advanced materials 13, 1053 (2001).

[21] V. Coropceanu, J. Cornil. D.A. Da Silva Filho, Y. Olivier, R. Silbey and J.L. Brédas, Chem. Rev. 107, 926 (2007).

[22] A. Troisi, and G. Orlandi, Physical Review Letters **96**, 086601 (2006).

[23] J.L. Brédas, D. Beljonne, V. Coropceanu, J. Cornil, Chem. Rev. 104, 4971 (2004).

[24] J. M. Shaw, and P. F. Seidler, IBM J. Res.&Dev 45, 3 (2001).

[25] N. W. Ashcroft, and N. D. Mermin, *Solid state physics*, Saunders College Publishing, 1979.

[26] L. L. Chua, J. Zaumseil, J. F. Chang, E. W. Ou, P. H. Ho, H. Sirringhaus, and R. H. Friend, Nature 434, 194 (2005).

[27] A. Köhler, Nature Materials 11, 836 (2012).

[28] A. K. Tripathi, M. Heinrich, T. Siegrist, and Jens Pflaum, Adv. Mater. 19, 2097 (2007).

[29] A. K. Tripathi; *PhD Dissertation*, University of Stuttgard (Germany), 2008.

[30] T. P. Vaid, A. K. Lytton-Jean, and B. C. Barnes; Chem. Mater. 15, 4292 (2003)

[31] G. Schweicher, Y. Olivier, V. Lemaur, and Y. H. Geerts; Isr. J. Chem. 53, 1 (2013).

[32] S. Bergantin, M. Moret; Cryst. Growth Des. 12, 6035 (2012).

[33] T. Matsukawa, M. Yoshimura, K. Sasai, M. Uchiyama, M. Yamagishi, Y. Tominari, Y. Takahashi, J. Takeya, Y. Kitaoka, Y. Mori, T. Sasaki; Journal of Crystal Growth 312, 310 (2010).

[34] A. Troisi, G. Orlandi; J Phys Chem B. 109, 1849 (2005).

[35] Y. Yuan, G. Giri, A. L. Ayzner, A. P. Zoombelt, S. C. B. Mannsfeld, J. Chen, D. Nordlund, M. F. Toney, J. Huang and Z. Bao; Nat. Commun. 5:3005 (2014).

[36] J. Bernstein; *Polymorphism in Molecular Crystals* Clarendon Press, Oxford, 2002.

[37] A. M. Hiszpanski, R. M. Baur, B. Kim, N. J. Tremblay, C. Nuckolls, A. R. Woll, and Y.-L. Loo, J. Am. Chem. Soc. 136 (44), 15749 (2014).

[38] M. Lipman, M. Leufgen, G. Schmidt, L. W. Molenkamp, V. Laukhin, J. Veciana, C. Rovira, Adv. Mater. 22, 4198 (2010).

[39] R.G. Della Valle, E. Venuti, A. Brillante, A. Girlando, J. Phys.Chem. A 112, 6715 (2008).

[40] A. Brillante, I. Bilotti, R. G. Della Valle, E. Venuti, S. Milita, C.Dionigi, F. Borgatti, A. N. Lazar, F. Biscarini, M. Mas-Torrent, N. S. Oxtoby, N. Crivillers, J. Veciana, C. Rovira, M. Leufgen, G. Schmidt, L W. Molenkamp, CrystEngComm 10, 1899 (2008).

[41] J. M. Adams and S. Ramdas; Acta Cryst. B35, 679 (1979).

[42] V.Langer, H.-D. Becker; Z.Kristallogr 199, 313 (1992).

[43] M. Munakata, L. Ping Wu, T. Kuroda-Sowa, M. Maekawa, Y. Suenaga, T. Ohta, and H. Konaka; Inorg. Chem. 42, 2553 (2003).

[44] X. Zhang, G. Yuan, Q. Li, B. Wang, X. Zhang, R. Zhang, J. C. Chang, C. Lee, and S. Lee; Chem. Mater. 20, 6945 (2008).

[45] R. G. Della Valle, E. Venuti, A. Brillante, Chem. Phys. 202, 231 (1996).

[46] G. F. Signorini, R. Righini, V. Schettino, Chem. Phys. 154, 245 (1991).

[47] S. Califano, V. Schettino, N. Neto, *Lattice Dynamics of Molecular Crystals*, Springer and Verlag, Berlin, 1981.

[48] W. R. Busing and M. Matsui; Acta Cryst. A 40, 532 (1984).

[49] D. E. Williams; J. Mol. Struct. 321, 458 (1999).

[50] W. Ludwig; Springer Tracts in Modern Physics, Vol. 43 (Springer-Verlag, Berlin, 1967).

[51] R.G. Della Valle, E. Venuti Phys. Rev. B 58, 206 (1998).

[52] "*General Atomic and Molecular Electronic Structure System*" M.W.Schmidt, K.K.Baldridge, J.A.Boatz, S.T.Elbert, M.S.Gordon, J.H.Jensen, S.Koseki, N.Matsunaga, K.A.Nguyen, S.Su, T.L.Windus, M.Dupuis, J.A.Montgomery J. Comput. Chem., 14, 1347 (1993).

[53] E. Venuti, I. Bilotti, R.G. Della Valle, A. Brillante, P. Ranzieri, M. Masino, A. Girlando. J. Phys. Chem. C 112, 17416 (2008).

[54] G. Turrel. Infrared and Raman spectra of crystals. Academic Press London and New York. (1970).

[55] Siegrist & Pflaum, private communication.

[56] A. Brillante, I. Bilotti, R.G. Della Valle, E. Venuti, M. Masino, A. Girlando Adv. Mater. 17, 2549 (2005).

[57] A. Brillante, I. Bilotti, R.G. Della Valle, E. Venuti, A. Girlando; CrystEngComm 10, 937 (2008).

[58] A. Brillante, I. Bilotti, R.G. Della Valle, E. Venuti, M. Mas-Torrent, C. Rovira, Y. Yamashita Chem. Phys. Lett. 523, 74 (2012).

[59] O. D. Jurchescu, D. A. Mourey, S. Subramanian, S. R. Parkin, B. M. Vogel, J. E. Anthony, T. N. Jackson, and D. J. Gundlach Phys. Rev. B 80, 085201 (2009).

[60] C. Zhang, Y. Yan, Y. S. Zhao and J. Yao; Annu. Rep. Prog. Chem., Sect. C: Phys. Chem. 109, 211 (2013).

[61] B. Yang, J. Xiao,, J. I. Wong, J. Guo, Y. Wu, L. Ong, L. L. Lao, F. Boey, H. Zhang, H. Y. Yang, and Q. Zhang; J. Phys. Chem. C 115, 7924 (2011).

[62] A. Bacchi, I. Bilotti, A. Brillante, D. Crocco, R.G. Della Valle, A. Girlando, M. Masino, P. Pelagatti, E. Venuti. J. Raman Spectr. **44**, 905 (2013)

5. Crystal growth and spectroscopic characterization of charge transfer crystals of Perylene – F_xTCNQ

5.1 Charge transfer crystals

The application of organic materials in the field of electronics and photonics still requires the use of inorganic layers, usually in the form of metal contacts. Recently, it has been discovered that the charge injection efficiency is greatly improved by the use of an *organic metal-organic semiconductor* interface. This has resulted in the employment of several organic metals such as carbon nanotubes, graphene, polymers and mixed crystals like tetrathiafulvalene-7,7,8,8-tetracyanoquinodimethane (TTF-TCNQ) [10-18]. TTF-TCNQ has been found to better the performances of an organic semiconductor with respect to devices with silver or gold contacts, even though the intrinsic conductivity of the organic metals is still much lower than that of inorganics [18]. The higher charge mobilities and low contact resistance at the interfaces of two the organic materials are also linked to the possibility of improving the matching of their Fermi levels by acting on the chemical modification of the compounds [19-21]. The versatility of organic materials thus suggests that manipulating organic-organic interfaces is a robust way to improve the electronic properties.

Apart from the lower device performances displayed by the organic with respect to the inorganic materials, a further drawback of the former in applications arises from their having generally unipolar characteristics, with the majority of them classified as p-type [22].

Recently, some research groups have focused again their attention on a class of crystalline materials which were known and had been widely studied in former times: the so-called organic Charge-Transfer (CT) compounds or complexes [23-26]. CT complexes are combinations of charge donating (D) and charge accepting (A) molecules, usually assembled in a stoichiometric ratio in the crystal state, thus forming co-crystals. While the single compounds have usually unipolar semiconducting properties, the complexes may display a wide range of different characteristics such as ambipolarity when the binary system acts as a semiconductor, or metal and even superconductor behavior in a number of cases [27].

In the past decades, the interest for CT compounds was focused not only on their potential conductivity and high temperature superconductivity, but also on several interesting physical phenomena observed in these systems, like charge density waves or Peierls transitions

[28]. A renewed interest in CT complexes arose just recently, based on a study by Alves and coworkers, who described some surprising properties observed at the interface between donor and acceptor compounds and which were not present in the parent materials [29]. Later, a mechanism for the generation of these properties was proposed [30]. Indeed, Mathis and coworkers, in their studies of the interface between TTF and TCNQ single crystals, suggested that the increase in conduction observed in TTF-TCNQ salts occurs when such an interface is formed by sublimation and not by physical contact only [30]. A more recent work by Tsunami and coworkers describes the photoconduction of single crystals of Perylene-F_4TCNQ, showing that the diffusion length of the photocarriers is strictly correlated to the CT complex energy gap [31,32].

Of course, the properties displayed by the various CT materials strongly depend on the choice of the molecules used as donor and acceptor (see examples in Figure 5.1), as well as on their packing arrangements in the crystal or in a thin film phase. A molecule that has a stable anionic state, and is therefore easily reduced, is the electron acceptor (A). A molecule with a stable cationic state, and is therefore easily oxidized, is the electron donor (D).

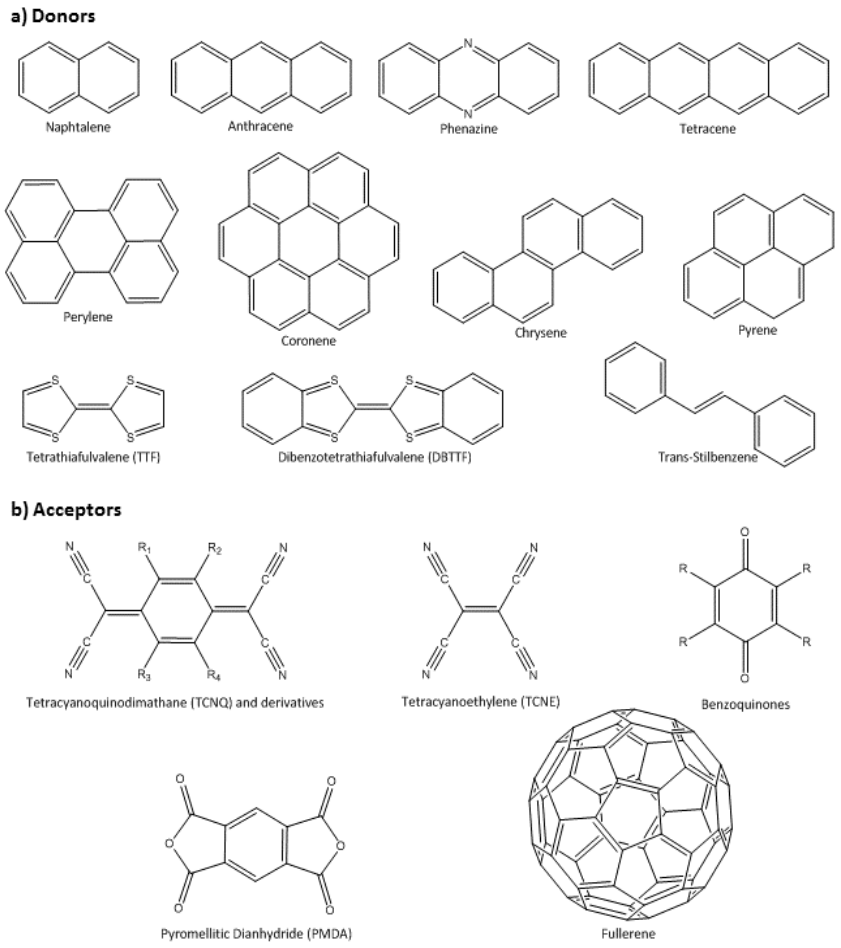

Figure 5.1 Examples of typical donor and acceptor molecules in CT mixed crystals.

Based on the definitions of the molecular orbitals theory, an electron donor is a compound with a relatively high energy of the highest occupied molecular orbital (HOMO). The ionization potential (I_p) of the molecule is defined as the energy needed to remove the electron from the HOMO. On the other hand, an electron acceptor is characterized by a low energy of the lowest unoccupied molecular orbital (LUMO). The molecular electron affinity (E_A) is the energy needed to accept an extra electron in the LUMO. The electronic interaction between different molecules couples of the HOMO orbital of the donor to the LUMO orbital of the acceptor, with a partial degree of charge transfer, ρ, between the two systems (Figure 5.2). The partial transfer of the charge from the donor to the acceptor results in a ground state of the complex characterized by a degree of ionicity, $D^{\rho+}A^{\rho-}$, related to I_p and E_A of D and A, respectively [33]. The so called CT band energy is represented by $E_{G,CT} = I_p - E_A - E(D^{\rho+}A^{\rho-})$, where $E(D^{\rho+}A^{\rho-})$ is the Madelung energy term.

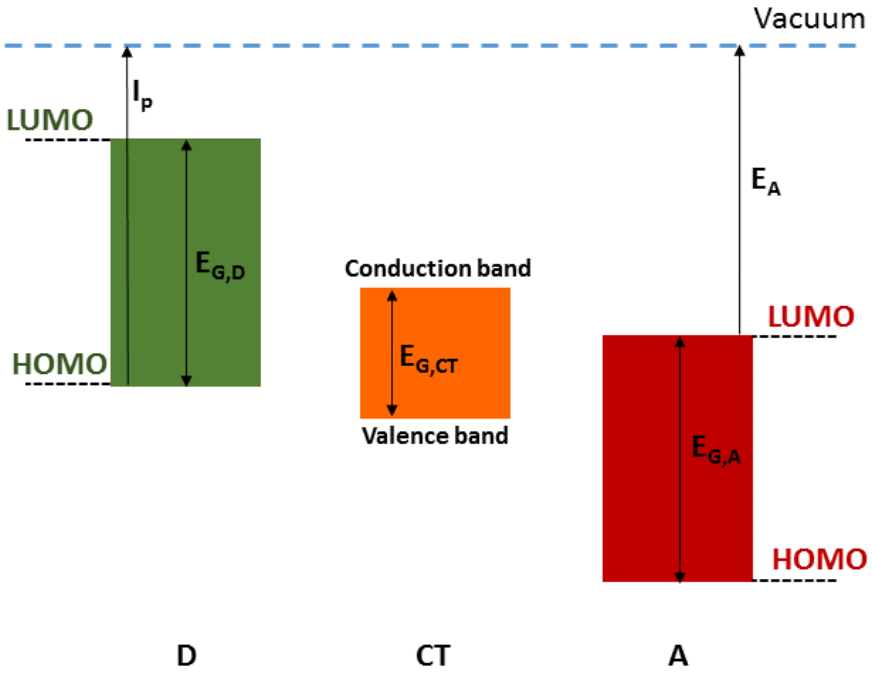

Figure 5.2 The donor band structure (green), acceptor band structure (red) and the resulting CT band structure (orange).

From this relation it is possible to classify the CT complexes as neutral or quasi neutral with $\rho < 0.5$, with a D-A combination for which $I_p - E_A >> E(D^{\rho+}A^{\rho-})$, and as ionic or quasi ionic with $\rho > 0.5$, with a D-A combination for which $I_p - E_A << E(D^{\rho+}A^{\rho-})$ [33].

Herbstein described the CT systems using two relevant parameters which are assumed to be responsible for their characteristic properties: the difference between the energy levels of D and A and the molecular conformation [34]. Further reports on these systems stated that the Herbstein parameters alone are not sufficient to fully describe the CT complexes and the

relationship between electronic properties and crystal structure is still the subject of an open debate.

5.1.1 Crystal arrangements

The crystal structure of D_n-A_m CT complexes can have, in theory, all possible combinations of n and m. The stoichiometry 1:1 is quite commonly reported in the literature and many examples have been studied, whereas the information on more complex structures such as 1:3, 2:3, *etc.* is still quite scanty. For the 1:1 stoichiometry found in several CT complexes, two types of crystal packing have been observed, as shown in Figure 5.3. The first packing is defined as segregated stack, in which D and A molecules are arranged in separate stacks as A-A-A-A and D-D-D-D. An instance of this arrangement is the case of black TMTSF-TCNQ [35]. The second type of packing is defined as mixed stack, and in this the D and A molecules are organized in a single π-stacking sequence D-A-D-A. Examples of this are the anthracene-PMDA [36] and perylene-TCNQ [37] systems, with the latter being also treated in this thesis.

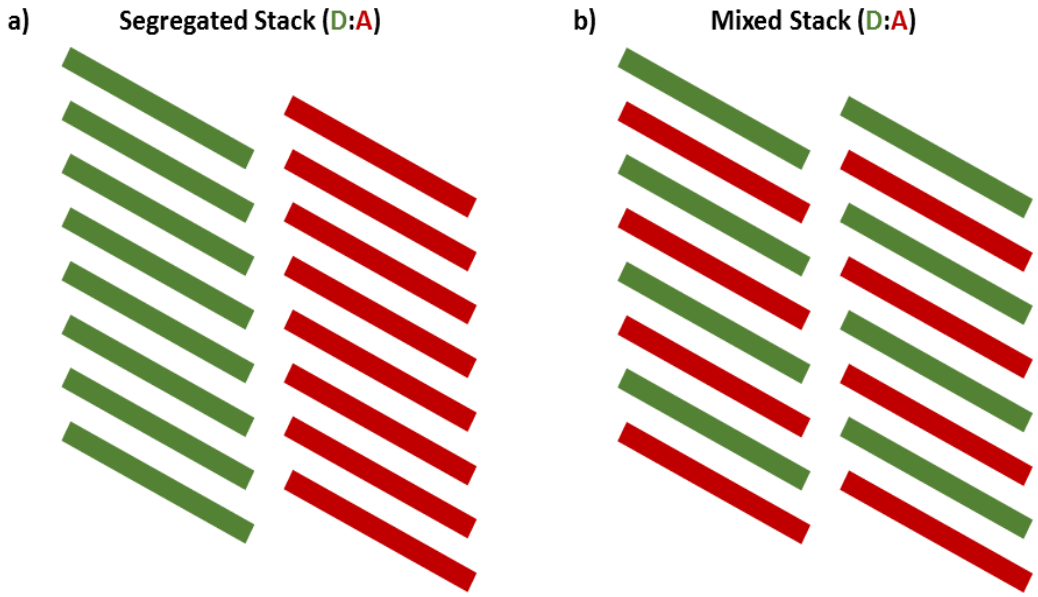

Figure 5.3 Typical packing motifs for crystalline charge transfer compounds with 1:1 stoichiometry: segregated stack (left) and mixed stack (right).

In the case of more complex structures with higher stoichiometric ratios, 2:1, 3:1, 3:2, some molecules are located outside the CT stacking and as a matter of fact they do not participate in charge transfer processes. The same stoichiometry of the CT binary system might also display different packings with completely different physical properties, and this true for

all the ratios, the 1:1 or the more complex ones. Predictably, the molecular solid state arrangements of CT complexes must be strictly dependent on the experimental conditions of their crystal growth.

5.1.2 Electronic properties and the interplay between the degree of CT and the electrical properties

The electronic properties of the CT complexes can vary depending on their band gap, passing from insulator to superconductor. The strong temperature dependence of these properties constitutes a further source of interest. Basically, two important parameters can be used to classify the compounds: i) electrical conductivity and mobility and ii) degree of charge transfer.

The electrical conductivity can be determined with a variety of methods and the high anisotropy of these system structures [38] requires that its measurement must be done in different geometries. A high conductivity is important for the characterization and evaluation of a good metal, but the determination of the mobility of holes and electrons is more useful for the semiconductors. Among the several methods to measure the conductivity and the mobility of charge in the CT systems, the mostly used are: space-charged-limited current (SCLC) [28,39], time of flight (TOF) [40] and organic field-effect transistor (OFET) [28]. The measure of the space-charged-limited current is used mostly for unipolar compounds, because the result does not discriminate between holes or electrons mobility and the value, in the case of ambipolar compounds, is a combination of both of them. Time of flight is another method which uses two contacts deposited on the material to be examined and allows for the evaluation of the mobility of both holes and electrons. OFET measurements can also be used as a comparative method to determine mobilities, since, differently from the previous techniques, the data obtained are more dependent on the surface than on the bulk [41].

The second parameters useful to characterize CT complexes is the degree of charge transfer ρ from the donor to the acceptor at a given composition, $D^{\rho+}A^{\rho-}$, with $0 \leq \rho \leq 1$.

In the literature several methods are described for the estimation of ρ. A common one is based on X-ray diffraction studies, and uses the differences found between the bond lengths of neutral and ionic forms of donor and acceptor moieties. According to a theoretical study by Johanson [42] TCNQ becomes more benzenoid on passing from neutral to ionic, therefore undergoing an appreciable change in the bond lengths. In the last decades, four different

equations [43-46] have been proposed for the determination of ρ for the acceptor TCNQ, with small differences from one to the other. The four equations were chosen in reason of the precision of the bond length measurements and they are listed below:

$$\rho_{TCNQ} = 7.25(b-c) - 8.07(c-d) - 1 \qquad \text{eq.1 [43]}$$

$$\rho_{TCNQ} = 22.43 - 23.81[(a+c)/(b+d)] \qquad \text{eq.2 [44]}$$

$$\rho_{TCNQ} = 19.83 - 41.67c/(b+d) \qquad \text{eq.3 [45]}$$

$$\rho_{TCNQ} = -1.374 + 8.13[(b+d) - (a+c)] \qquad \text{eq.4 [46]}$$

a, *b*, *c*, and *d* are the bond lengths as indicated in Figure 5.4. The values of the different constants in the equations depend on the selected set of bond lengths.

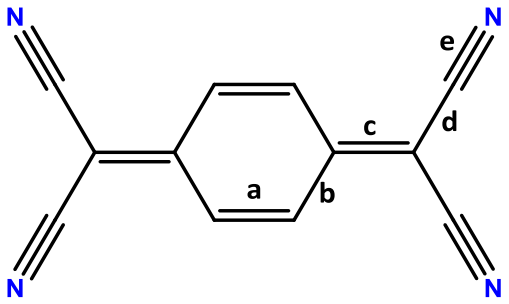

Figure 5.4 Definition of characteristic bonds of the TCNQ skeleton

Another method for the estimation of ρ is based on spectroscopic parameters. By using Raman and Infrared spectroscopies, one can probe the stretching frequencies of selected bonds, which are sensitive to the degree of charge transfer. By assuming a linear dependence of the frequency mode on going from the fully neutral to the fully ionic species, ρ can be determined for any intermediate case. When comparing the results of the two methods proposed for estimating ρ, a particular attention should be paid to the CN functional group, whose stretching frequency is very sensitive to even slight variations of the charge transfer .

In a recent review [27] the conductivity σ of several D:A CT complexes has been plotted as a function of ρ, so that distinctive trends could be identified, leading to the general definition of two distinct groups of systems. The first one, in the limiting cases of low and high value of ρ, is typical of materials with insulator or semiconductor character, whereas the second one is typical of materials which exhibit metallic behavior and refers to the limited range of ρ from 0.59 to 0.74.

5.2 Charge transfer crystals Perylene-F_xTCNQ

We have focused our work on the crystal growth of a new class of CTs, the Perylene-F_xTCNQ compounds, where the amount of fluorine content of the acceptor (x = 0 to 4) is varied, with the aim of modulating the degree of charge transfer of the resulting system. The crystals were grown by the physical vapour transport method, described in chapter 2, in a closed system with inert atmosphere, mixing perylene and functionalised 7,7,8,8-tetracyanoquinodimethane (Figure 5.5). By changing the crystal growth conditions, it was possible to obtain various D:A stoichiometric ratios, with different outcomes on crystal packing and CT properties.

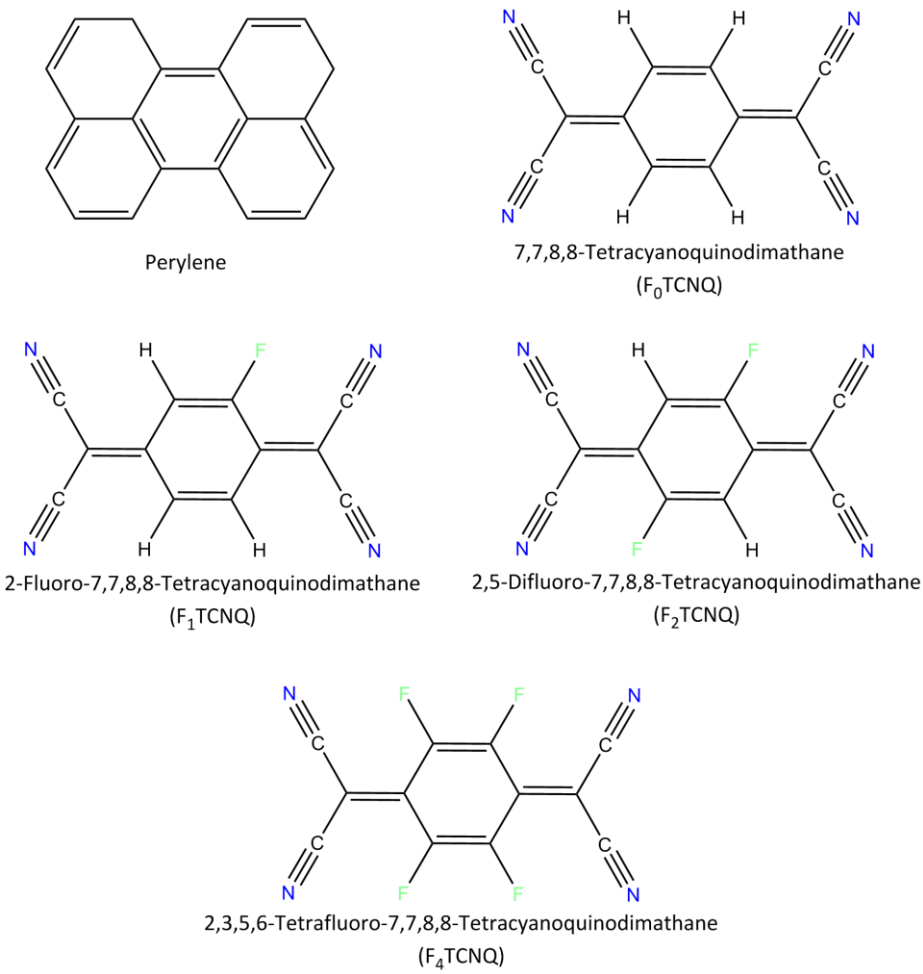

Figure 5.5 Molecular structures of donor (perylene) and acceptor (F_xTCNQ)

The study is therefore based on the association of perylene with four different TCNQ isostructural acceptors having a different degree of fluorination. All the acceptor compounds (F_0TCNQ, F_1TCNQ, F_2TCNQ and F_4TCNQ) present a different electronic structure, as shown in Figure 5.6, with the HOMO-LUMO values modulating ρ and the CT electronic band.

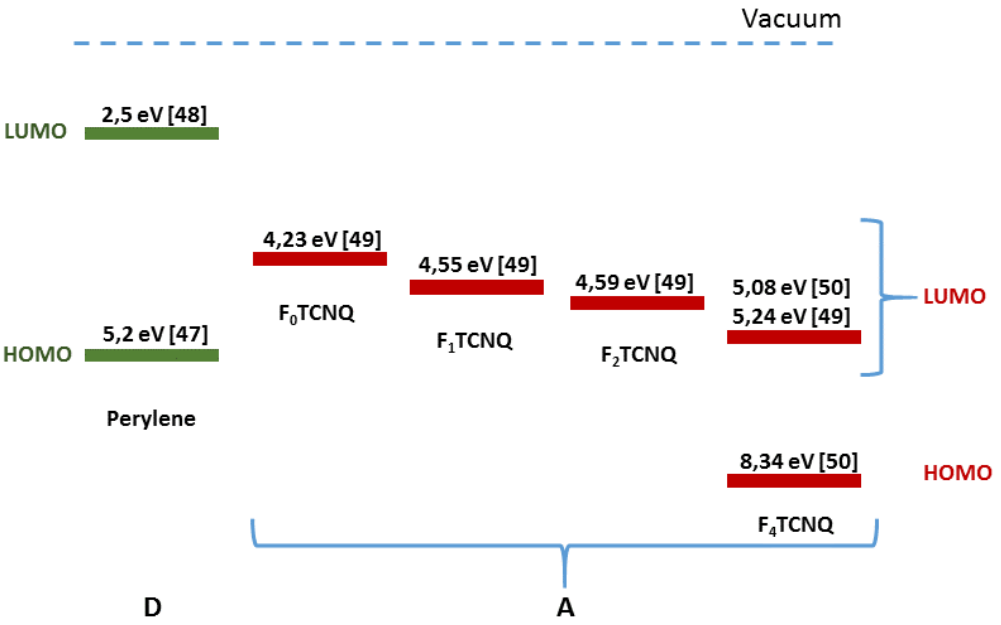

Figure 5.6 Homo and LUMO levels of the donor and the different acceptor molecules used.

The donor perylene ($C_{20}H_{12}$) presents two monoclinic polymorphs. The α form was described for the first time by Donaldson et al. [51], whereas the first report for the β form was by Tanaka [52]. A complete and revisited report of both crystal structures of perylene has been published by Botoshansky and coworkers [53]. The cell structures of the polymorphs are shown in Figure 5.7. In the α form the molecules are arranged in a pair-like packing. The structure belongs to the space group $P2_1/c$ with four molecules per unit cell and cell parameters: a = 10.2390(7) Å, b = 10.7860(8) Å, c = 11.1320(11) Å, β = 100.924(3)°. The β form shows the more common herring-bone arrangement, with space group symmetry $P2_1/c$ and two molecules per unit cell. The cell parameters are: a = 9.7630(15) Å, b = 5.8430(9) Å, c = 10.608(2) Å, β = 96.770(6)°. Tanaka et al. [52] described the transformation of the β form into the α form at 140 °C. Below this temperature both structures can be found.

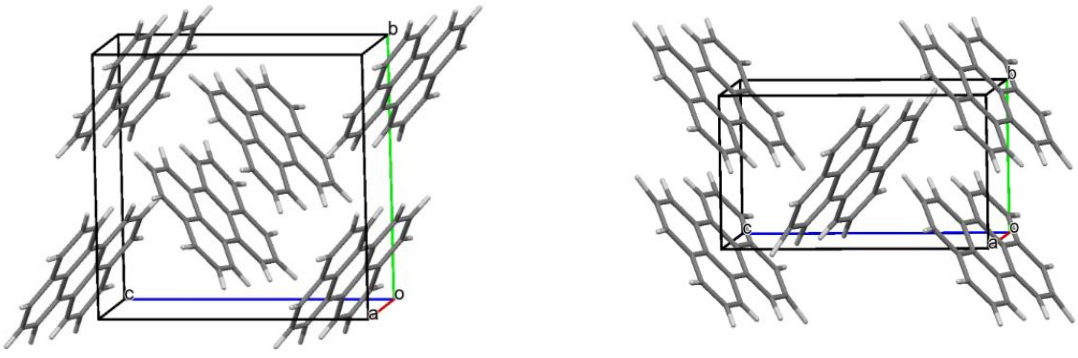

Figure 5.7 Crystal structures of α-perylene (left) and β-perylene(right).

The acceptor 7,7,8,8-Tetracyanoquinodimethane, or TCNQ, is the compound with the lowest electronegativity, having is no functionalization of the aromatic core by fluorine atoms. We have adopted here the convention of naming it F_0TCNQ, to stress the absence of fluorine in this member of the acceptor series. F_0TCNQ crystallizes in a monoclinic structure belonging to space group C2/c with four molecules per unit cell [54]. The crystal parameters are: *a* = 8.906(6) Å, *b* = 7.060(4) Å, *c* = 16.395(5) Å and β = 98.54(4)°. The crystal lattice and the bond lengths are shown in Figure 5.8.

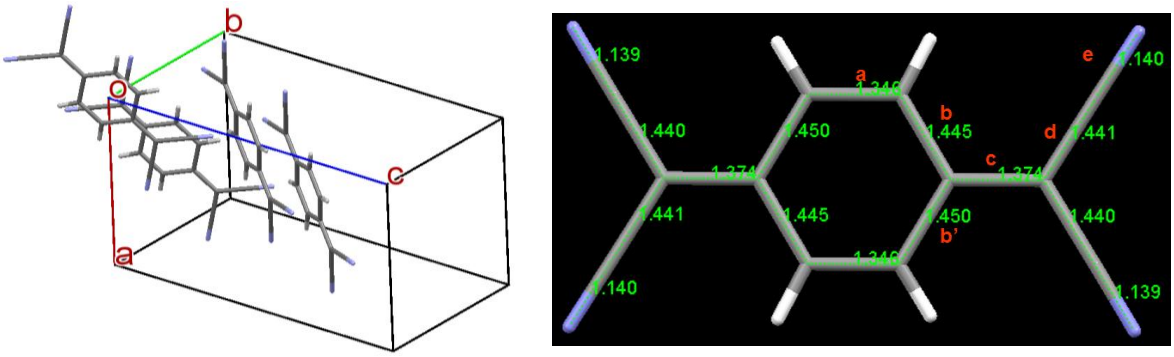

Figure 5.8 Crystal structure of F_0TCNQ and bond lengths.

The crystal structure of the 2-fluoro-7,7,8,8-tetracyanoquinodimethane, F_1TCNQ, has been determined by X-ray diffraction by Wiygul et al [55] (Figure 5.9). It is the only acceptor used in this work with a molecular structure which lacks any symmetry in the fluorine substitution. F_1TCNQ crystallizes in a monoclinic structure with two molecules per unit cell. The structure belongs to space group $P2_1/n$ with cell parameters *a:* = 7.596(3) Å, *b* = 8.204(4) Å, *c* = 8.428(2) Å and β = 90.90(3)°.

In the crystal structure the fluorine atom has been found to be intrinsically disordered, due to the rotational disorder of the molecule. This can be described saying that, by keeping fixed in the structure all the atoms of the molecule apart from F, this has a 50% probability to be located either at the position 2 or position 5 of the aromatic core of TCNQ skeleton.

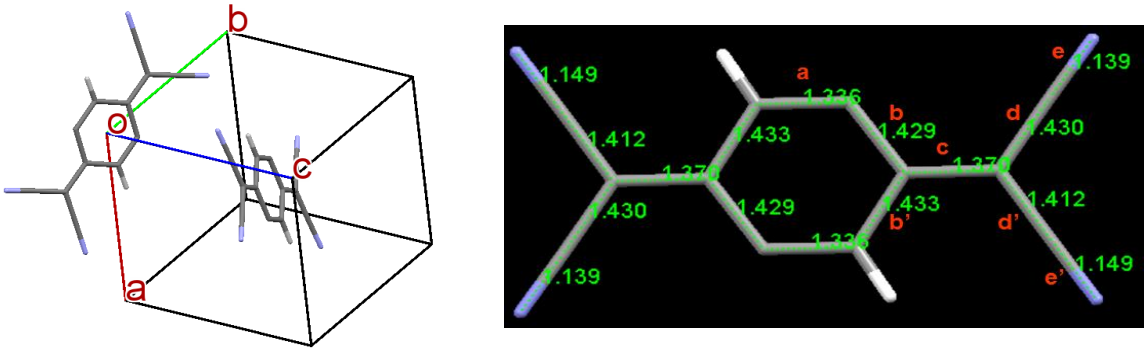

Figure 5.9 Crystal structure of F_1TCNQ and bond lengths.

The crystal structure of 2,5-difluoro-7,7,8,8-tetracyano-p-quinodimethane, F_2TCNQ, has also been published by Wiygul et al [56]. It belongs to the monoclinic space group C2/m with two molecules per unit cell and cell parameters *a* = 10.208(4) Å, *b* = 6.026(2) Å, *c* = 8.836(3) Å and β=106.64(3)°. The structure and the bond lengths are shown in Figure 5.10.

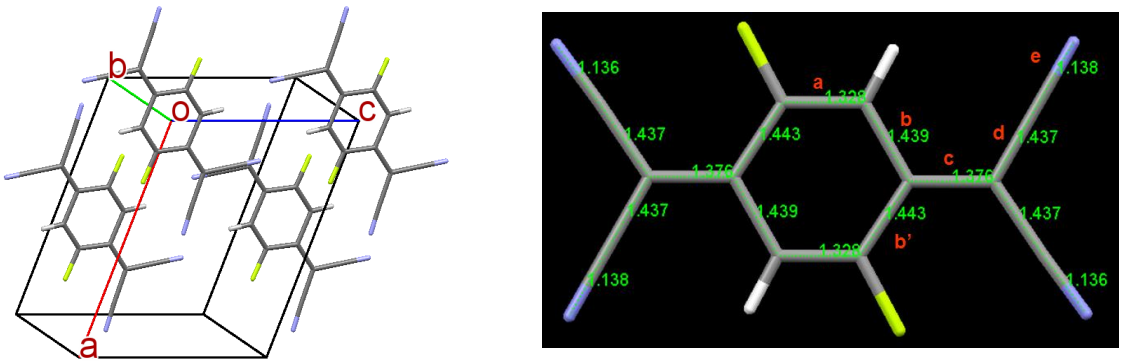

Figure 5.10 Crystal structure of F_2TCNQ and bond lengths.

The 2,3,5,6-tetrafluoro-7,7,8,8-tetracyanoquinoedimethane (F_4TCNQ) is the electron acceptor with the highest electronegativity used in this work. Its crystal structure has been reported by Emge and coworkers in 1981 [57], but in it has been determined again in this work by single crystal X-ray diffraction of a crystal grown by PVT method (see Table 5.1) and compared with the previous results [57]. The parameters of its orthorhombic structure were found in agreement with those given by Emge and coworkers [57], who used a single crystal grown by slow evaporation from an acetonitrile solution. The structure with the bond lengths is shown in Figure 5.11.

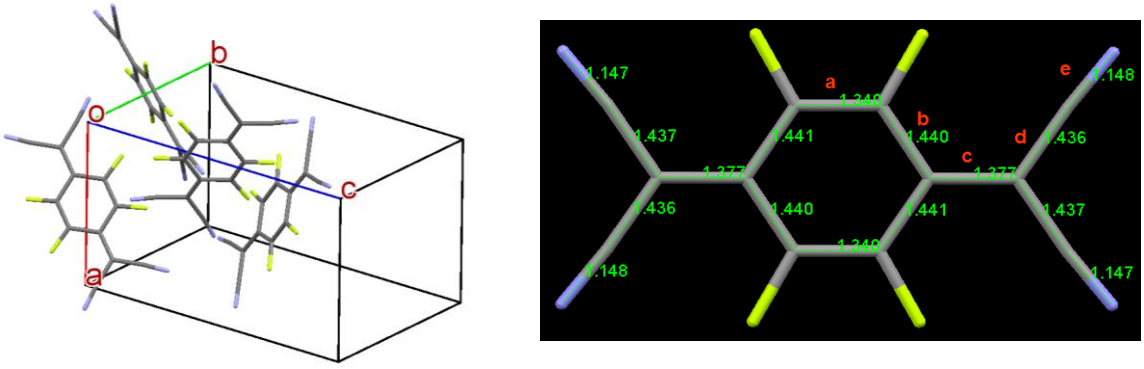

Figure 5.11 Crystal structure of F_4TCNQ and bond lengths.

Table 5.1 Crystal data and structure refinement for F_4TCNQ.

Empirical formula	$C_{12}F_4N_4$
Formula weight	276.16 g mol^{-1}
Temperature	150(2) K
Wavelength	0.71073 Å
Crystal system	Orthorhombic
Space group	P c a b
Unit cell dimensions	*a* = 8.0828(2) Å α = 90°
	b = 9.2231(2) Å β = 90°
	c = 14.5974(4) Å γ = 90°
Volume	1088.21(5) $Å^3$
Z	4
Density (calculated)	1.686 Mg/m^3
Absorption coefficient	0.155 mm^{-1}
F(000)	544
Crystal size	0.500 x 0.500 x 0.250 mm^3

The binary systems Perylene-F_0TCNQ in the ratios 1:1 and 3:1 and Perylene-F_4TCNQ in the ratio 3:2, have already been described in the literature [23,24,32]. All the other structures of Perylene-F_1TCNQ, Perylene-F_2TCNQ in both ratios 1:1 and 3:2 and Perylene-F_0TCNQ-F_2TCNQ are reported in this work for the first time. In the following paragraphs, all the structures obtained by physical vapor transport, are described in details.

5.2.1 Perylene-F_0TCNQ 1:1 crystals (Low T)

An ampoule of 100 mm length and 10 mm diameter was cleansed with soap, distilled water, isopropanol and acetone in this sequence and then left to dry overnight at 110 °C. The ampoule was loaded with 28 mg of perylene (0.111 mmol), Sigma Aldrich sublimed grade, > 99% of purity, and 28.9 mg of F_0TCNQ (0.142 mmol), Sigma Aldrich, 98% of purity. The amount of perylene and F_0TCNQ were calculated to have a molar ratio of 1:1 in the starting powder.

A second ampoule, of the same dimensions and cleansed with the same procedure, was filled with 9.9 mg of perylene (0.039 mmol) and 28.1 mg of F_0TCNQ (0.138 mmol) to have a starting powder molar ratio of 3:1 for perylene and F_0TCNQ, respectively.

Before sealing with an oxygen-natural gas burner, the ampoules were evacuated in N_2 at a final pressure of 10^{-4} mbar. Both ampoules were placed in a two-zone furnace for the crystal growth by PVT method. The temperature was set at 140°C and 100 °C at the hot and cold end, respectively (see Figure 5.12).

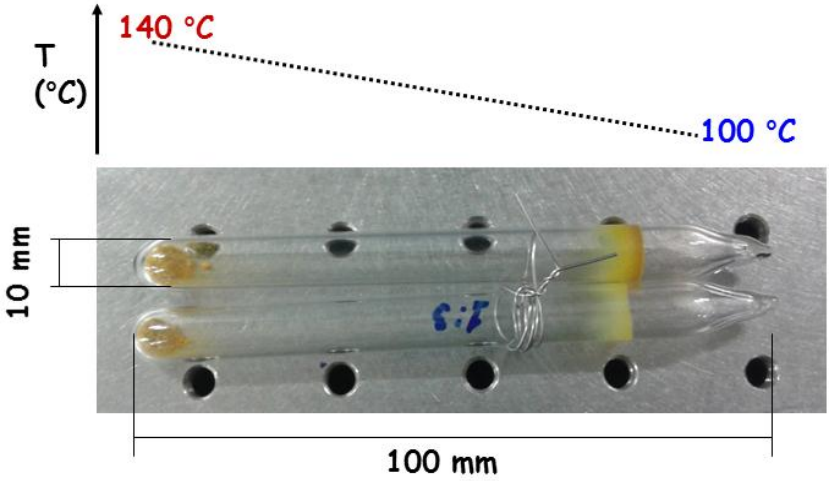

Figure 5.12 Schematic representation of the temperature gradient applied along the ampoule.

After 15 days the ampoules were cooled down by turning off the furnace and left inside it to avoid a too fast condensation of the material in the vapor phase. Both ampoules, regardless of the perylene-F_0TCNQ starting ratio, still showed a large amount of the starting material at the hot ends. In the growth region, orange platelet-like crystals were found, mixed to black prismatic crystals which could also be seen at the hot end together with the starting material (see Figure 5.13).

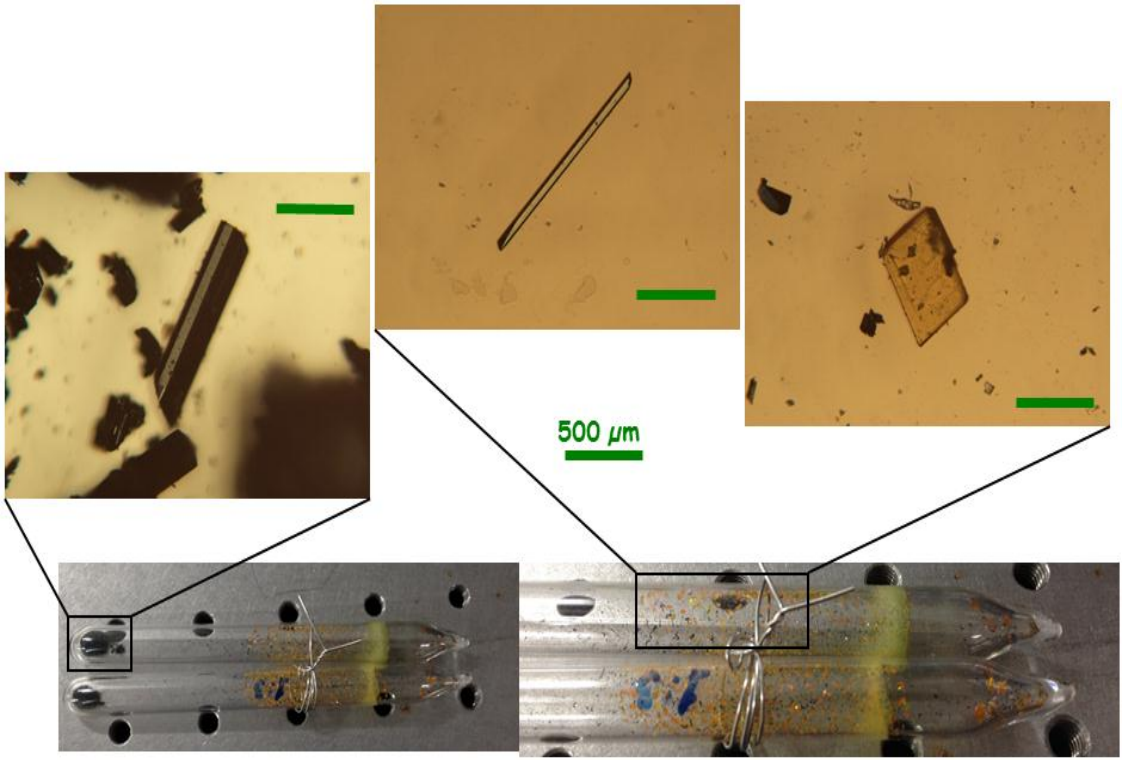

Figure 5.13 Morphologies of the crystals obtained after experiment and distribution along the ampoule.

The black and orange crystals were characterized by X-ray single crystal diffraction. The black ones resulted to be mixed crystals of perylene-F_0TCNQ with ratio 1:1 and their lattice phonon spectra proved that all of them had the same crystal structure.

The binary system Perylene-F_0TCNQ 1:1, already described in the literature, was found to crystallize in a monoclinic structure, space group $P2_1/c$, with 2 molecules per unit cell and unit cell parameters at 150 K: a = 7.2013 Å, b = 10.8390 Å, c = 14.4747 Å and β = 90.324°. Further details of the structure are reported in Table 5.2, while the packing is sketched in Figure 5.14. The cell parameters of this work compare very well with those previously published by Tikle et al. [58] and Vermeulen et al. [59], as the small differences in the length of the cell axes can be accounted for by the different temperatures used in the various experiments. In the structure of Figure 5.14 each perylene molecule is paired to a F_0TCNQ molecule, forming a mixed stack structure with stacking direction along the a crystallographic axis.

Table 5.2 Crystal data and structure refinement for Perylene-F_0TCNQ 1:1.

Empirical formula	$C_{32}H_{16}N_4$
Formula weight	456.49 g mol^{-1}
Temperature	150(2) K
Wavelength	1.54184 Å
Crystal system	Monoclinic
Space group	$P2_1/c$
Unit cell dimensions	a = 7.2013(5) Å α = 90°
	b = 10.8390(8) Å β = 90.324(4)°
	c = 14.4747(11) Å γ = 90°
Volume	1129.80(14) Å^3
Z	2
Density (calculated)	1.342 Mg/m^3
Absorption coefficient	0.634 mm^{-1}
F(000)	472
Crystal size	0.290 x 0.080 x 0.050 mm^3

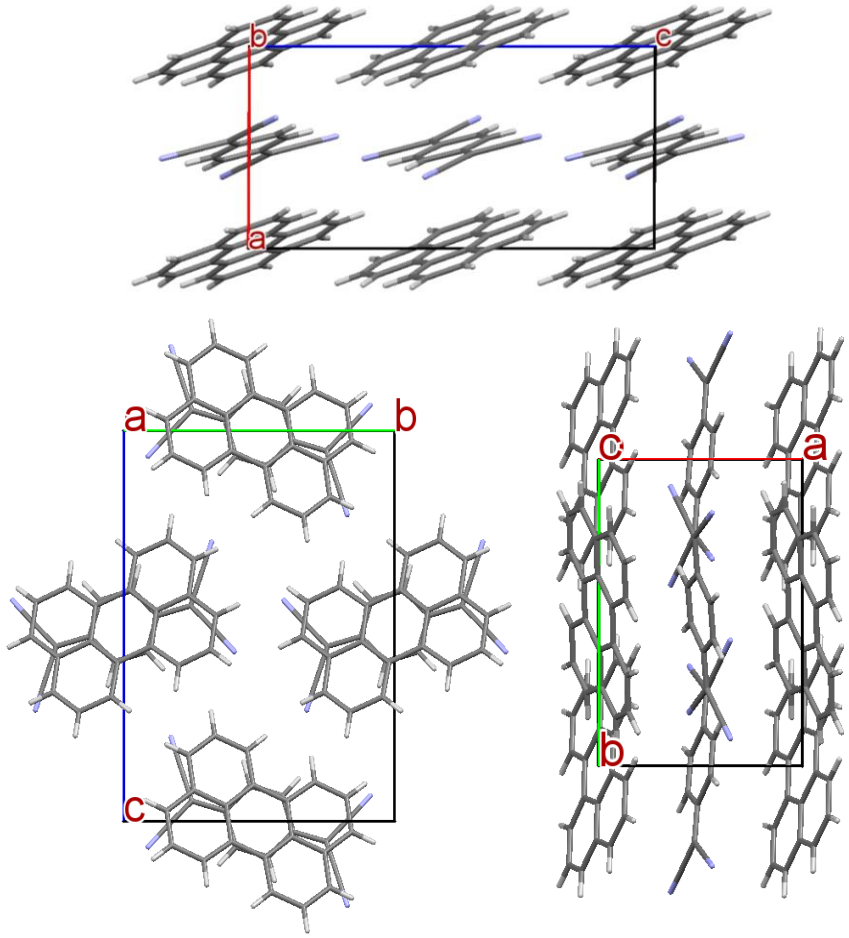

Figure 5.14 Crystal packing of binary system Perylene-F_0TCNQ 1:1.

The X-ray data of the orange crystals corresponded instead to those of a single crystal of pure F_0TCNQ, which clearly also grows in the furnace conditions. The cell parameters at 150 K are reported in Table 5.3, and compare well with the data previously published at a different temperature [54].

Table 5.3 Crystal data and structure refinement for F_0TCNQ.

Empirical formula	$C_{12}H_4N_4$
Formula weight	204.19 g mol^{-1}
Temperature	150(2) K
Wavelength	1.54184 Å
Crystal system	Monoclinic
Space group	C2/c
Unit cell dimensions	*a* = 8.8746(4) Å α = 90°
	b = 6.9335(3) Å β = 98.315(4)°
	c = 16.4071(6) Å γ = 90°
Volume	998.95(7) Å^3
Z	4
Density (calculated)	1.358 Mg/m^3
Absorption coefficient	0.710 mm^{-1}
F(000)	416
Crystal size	0.290 x 0.080 x 0.050 mm^3

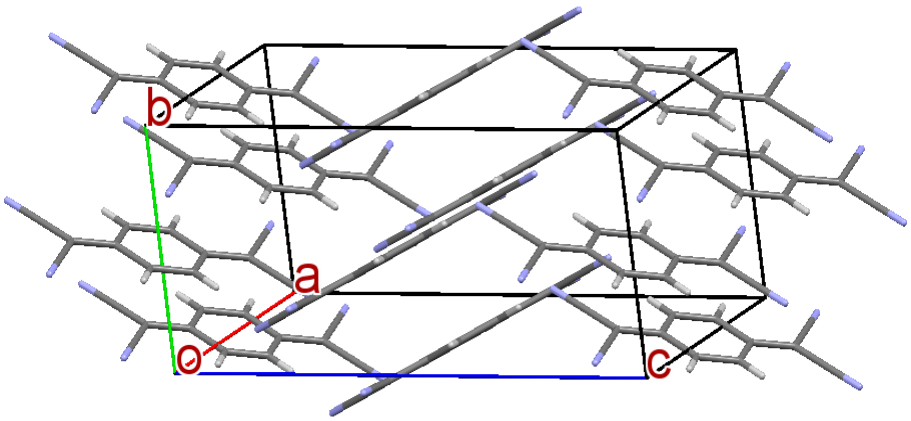

Figure 5.15 Crystal packing of pure F_0TCNQ obtained by PVT.

5.2.2 Perylene-F_0TCNQ 3:1 crystals (High T)

20.4 mg of perylene (0.081 mmol) and 18.4 mg of F_0TCNQ (0.090 mmol) were placed in the furnace into an evacuated quartz glass ampoule. The sample was prepared following the same protocol as described above. This time the furnace was set at 170 °C at the hot end

and at 110 °C at the cold end. Both ends were covered with glass wool caps to avoid heat dispersion. The temperature profiles of the system with and without the end caps are drawn in Figure 5.16, where the position of the ampoule in the furnace is also shown.

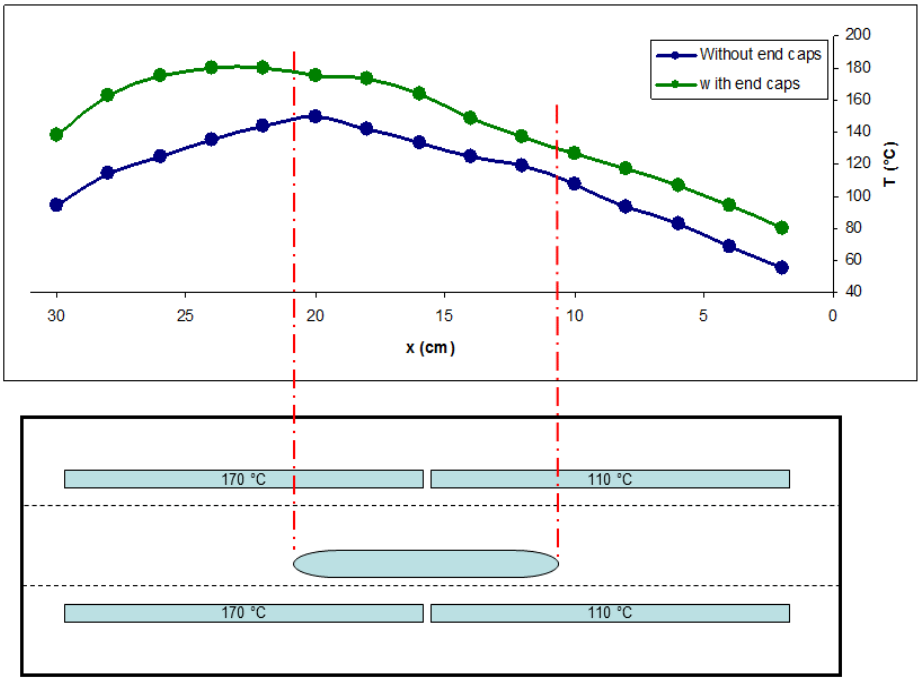

Figure 5.16 Comparison of temperature distributions in the two zones furnace.

After 7 days the furnace was turned off, the end caps removed and the ampoule left to cool down slowly inside the ceramic holder tube. Before opening it, the ampoule was placed under the microscope to observe the spatial distribution of the various crystals grown during its stay in the furnace. By looking at the pictures of Figure 5.17, three different zones of the ampoule can be identified, starting from the left hand side: in the first one a small amount of the starting powder is still present; in the middle, black needle-like and platelet crystals are observed and, finally, a few orange crystals are located in the right hand side.

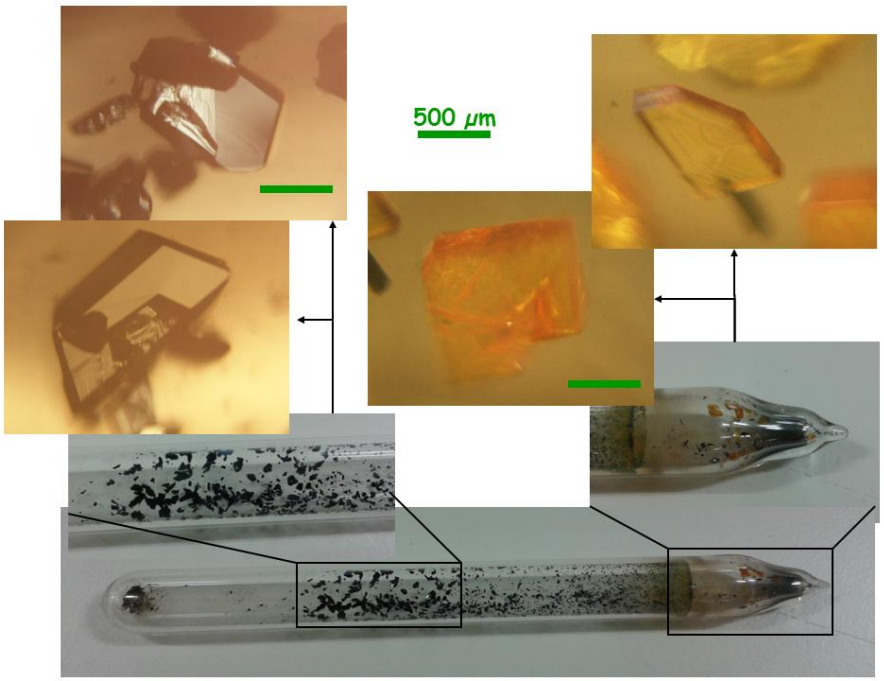

Figure 5.17 Morphologies of the crystals obtained after experiment and distribution along the ampoule.

The orange crystals were characterized by Raman spectroscopy and were readily identified as the more volatile compound F_0TCNQ. The black crystals with two distinct morphologies of the central zone were characterized both by X-ray diffraction and Raman spectroscopy. The needle-like crystals, which grow prevalently in the zone with a lower temperature of the middle section, resulted to be the mixed system perylene-F_0TCNQ 1:1, already described in paragraph 5.2.1.

Table 5.4 Crystal data and structure refinement for Perylene-F_0TCNQ 3:1.

Empirical formula	$C_{72}H_{40}N_4$	
Formula weight	961.08 g mol^{-1}	
Temperature	150(2) K	
Wavelength	0.71073 Å	
Crystal system	Triclinic	
Space group	$P\bar{1}$	
Unit cell dimensions	*a* = 10.3446(2) Å	α= 112.4861(13)°
	b = 10.8429(3) Å	β= 114.2810(14)°
	c = 12.5107(3) Å	γ = 91.3733(13)°
Volume	1154.20(5) Å^3	
Z	1	
Density (calculated)	1.383 Mg/m^3	
Absorption coefficient	0.081 mm^{-1}	
F(000)	500	
Crystal size	0.400 x 0.350 x 0.200 mm^3	

The platelet-like crystals, isolated at the higher temperature side of the section, were found to be the mixed system perylene-F_0TCNQ 3:1. The cell parameters and the crystal structure of this system are reported in Table 5.4 and Figure 5.18, respectively.

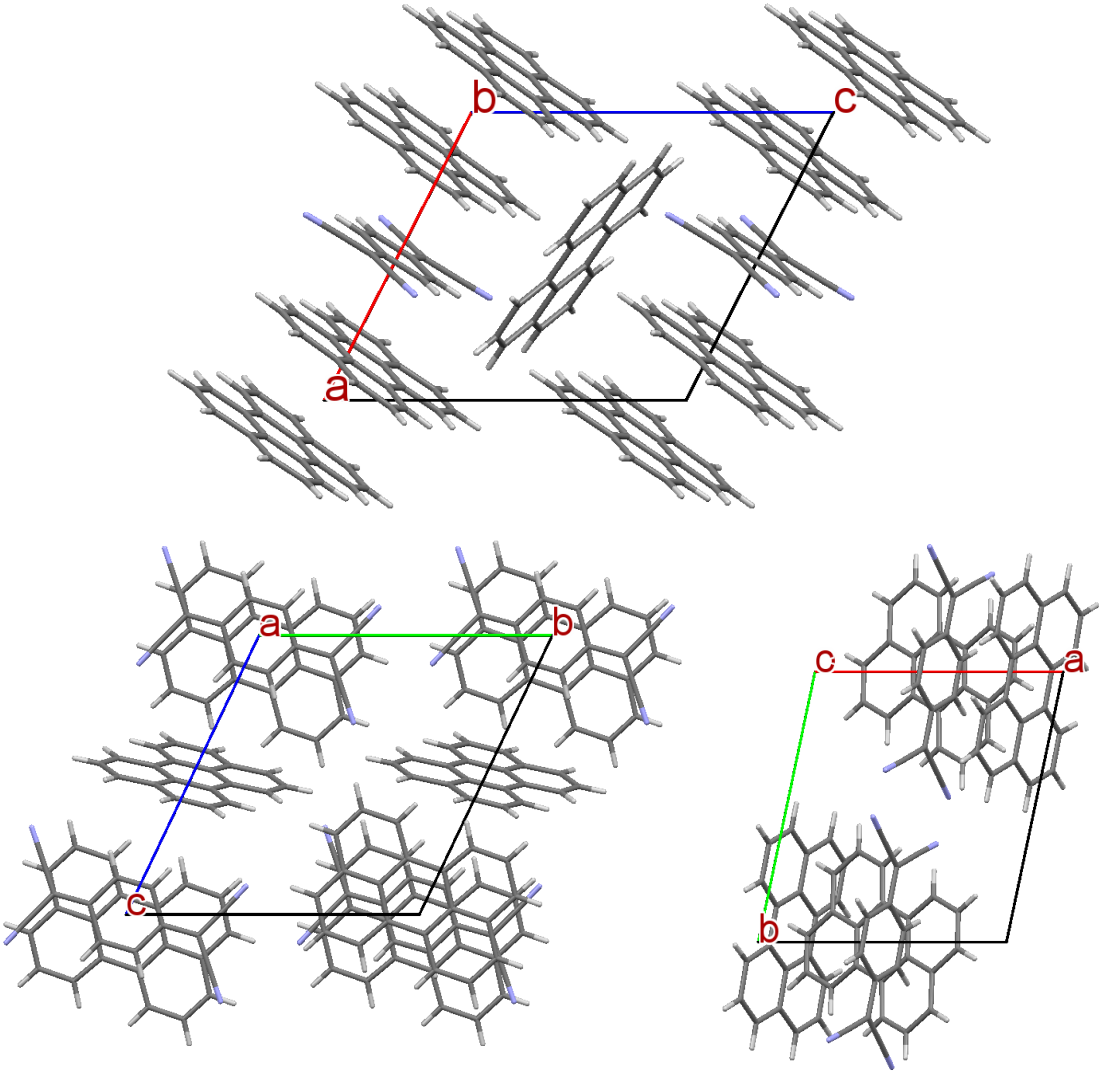

Figure 5.18 Crystal packing of binary system Perylene-F_0TCNQ 3:1.

As can be seen from the table, the binary Perylene-F_0TCNQ 3:1 system crystallizes in a triclinic structure, space group $P\bar{1}$, with one molecule per unit cell and unit cell parameters (at 150K): *a* = 10.3446 Å, *b* = 10.8429 Å, *c* = 12.5107 Å, α = 112.4861°, β = 114.2810° and γ = 91.3733°. The parameters are agreement with those previously published by Hanson et al. [60] and Vermeulen et al. [59] Again, small differences are due to the lower temperature used for the collection of our diffraction data. In the structure reported in Figure 5.18, one F_0TCNQ molecule is sandwiched between two perylene molecules to form a mixed stack along the *a* crystallographic direction, with a resulting sequence DDADDADDA. The third perylene of the crystal stoichiometry is instead found in the interstitial sites located between the

DDADDADDA stacks, thus forming a row of molecules with the molecular planes perpendicular to the crystallographic direction *c*.

5.3 Charge transfer crystals Perylene-F_1TCNQ

The protocol already adopted for the growth of crystals by the PVT method was used for a mixture of 22.8 mg of perylene (0.090 mmol) and 18.0 mg of F_1TCNQ (0.081 mmol), TCI chemicals 98% of purity. The two ends of the two-zone furnace were kept at the temperatures of 170 °C and 110 °C, respectively, and the ampoule was placed in the furnace in the suitable position displayed in Figure 5.19, together with the temperature profile of the crystal growth apparatus.

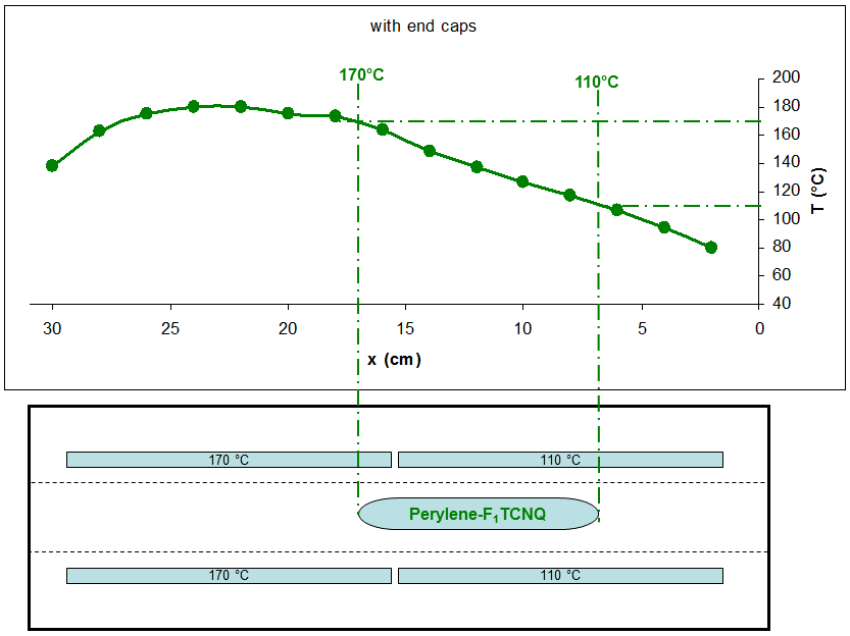

Figure 5.19 Temperatures distribution in the furnace for perylene-F_1TCNQ crystal growth.

The crystal growth process was prolonged to 9 days and, after the cooling of the furnace to room temperature, different kinds of crystals were found to be present, as shown in Figure 5.20. As already observed, roughly three different zones and crystals could be identified along the direction of the ampoule temperature gradient. The widest one lay in the middle, with needle-like black crystals which needed identification by XRD. At a short distance from the starting powder (hot end of the ampoule), there were yellow crystals which were identified as perylene, that is the component with the lower volatility. At the opposite side, right at the cold end, the growth of F_1TCNQ, which is the component with higher volatility, could be found. The presence of the crystals of both the parent molecules was quickly detected by Raman and Infrared spectroscopies.

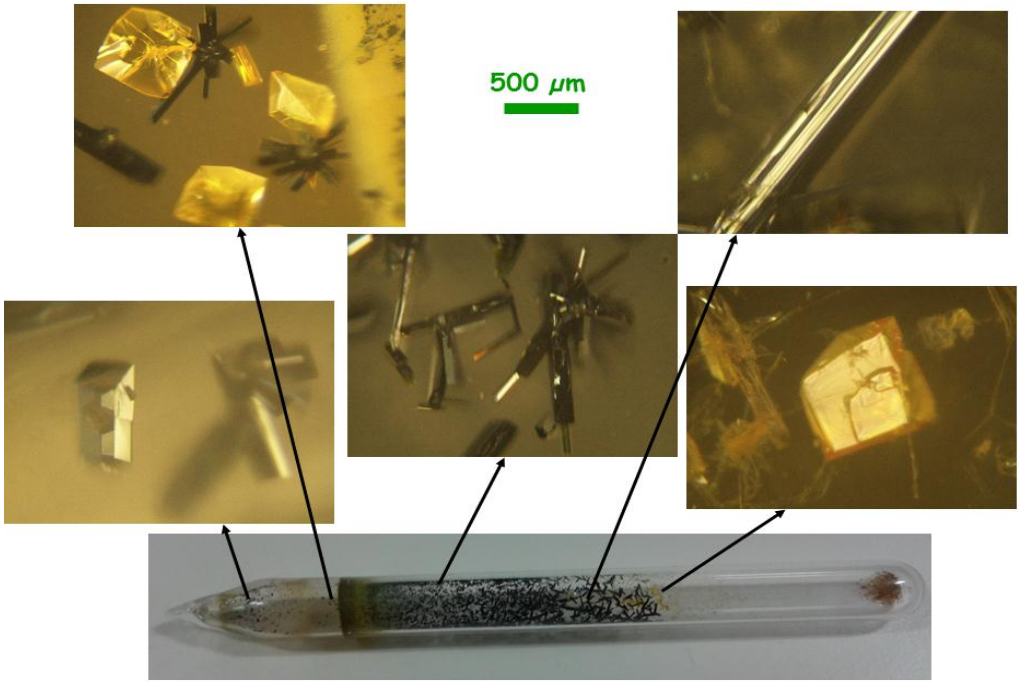

Figure 5.20 Morphologies of the crystals obtained after experiment and distribution along the ampoule.

By X-ray single crystal diffraction analysis, the black needle crystals grown in the middle section resulted to be the mixed perylene-F_1TCNQ system with the stoichiometric ratio 3:2. Cell parameters and crystal packing are reported in Table 5.5 and Figure 5.21, respectively.

Table 5.5 Crystal data and structure refinement for Perylene-F_1TCNQ 3:2.

Empirical formula	$C_{84}H_{38}F_2N_8$	
Formula weight	1197.22 g mol^{-1}	
Temperature	150(2) K	
Wavelength	0.71073 Å	
Crystal system	Triclinic	
Space group	P-1	
Unit cell dimensions	*a* = 7.2254(2) Å	α= 112.2658(14)°
	b = 19.1275(4) Å	β= 90.2346(10)°
	c = 22.3203(6) Å	γ= 94.0322(15)°
Volume	2846.09(13) Å^3	
Z	2	
Density (calculated)	1.397 Mg/m^3	
Absorption coefficient	0.088 mm^{-1}	
F(000)	1232	
Crystal size	0.430 x 0.200 x 0.100 mm^3	

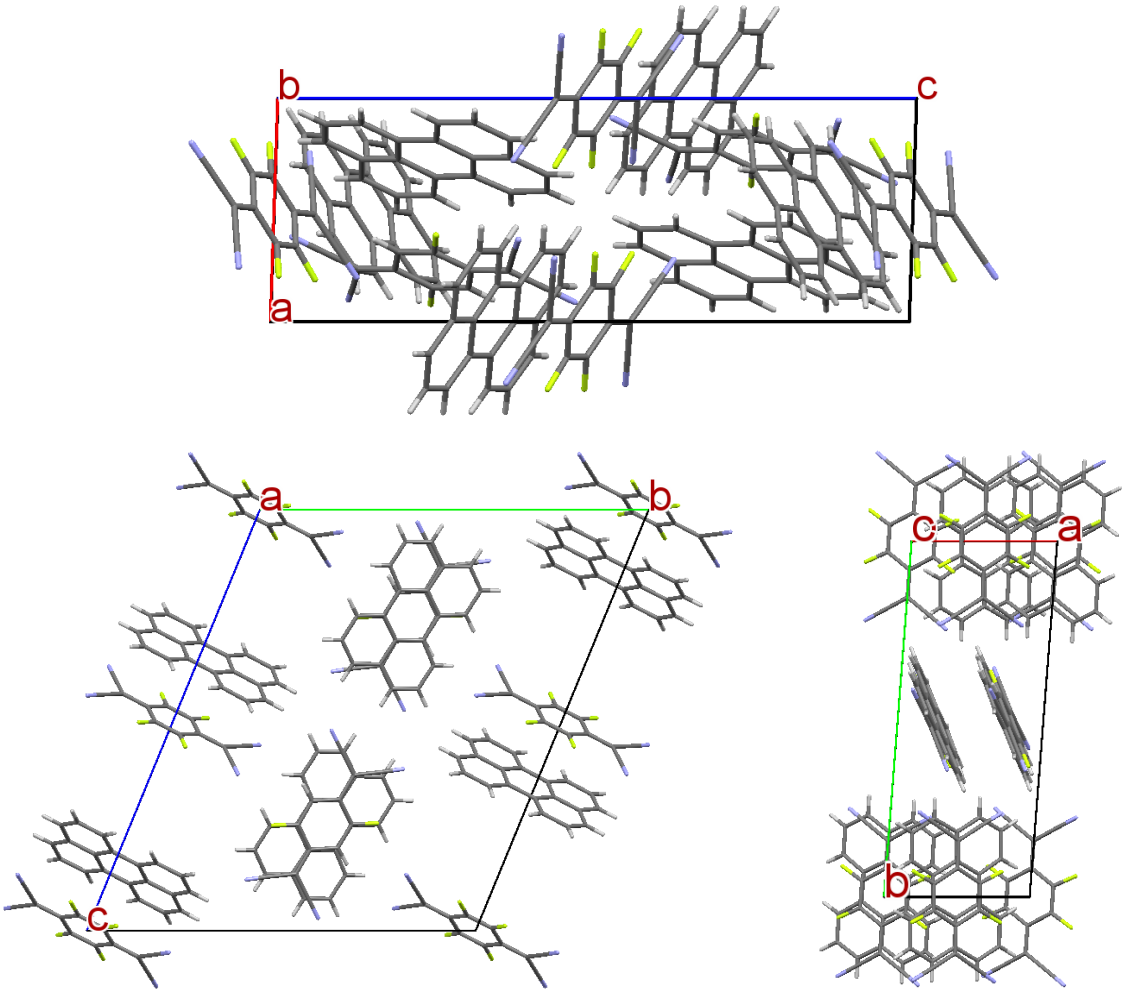

Figure 5.21 Crystal packing of binary system Perylene-F_1TCNQ 3:2.

The binary system Perylene-F_1TCNQ 3:2 crystallizes in a triclinic structure, space group $P\bar{1}$, with two molecules per unit cell and unit cell parameters (at 150 K): *a* = 7.2254 Å, *b* = 19.1275 Å, *c* = 22.3203 Å, α = 112.2658°, β = 90.2346° and γ = 94.0322°. The structure has not been reported in the literature as yet. As can be seen in Figure 5.21, F_1TCNQ and perylene form two distinct mixed stacks, along the *c* and *a* crystallographic axes, respectively. The mixed stack along *a* is characterized by a sequence DADADA with the F_1TCNQ molecules presenting rotational disorder, so that the F atom is found to have an average occupation of the 50% in positions 2 and 5 of the aromatic ring. The second mixed stack aligned along *c* is characterized by the sequence DDADDADDA with a Perylene:F_1TCNQ ratio 2:1. In the latter stack the average occupation of the F atoms for all the four aromatic positions is 25%. Therefore, in this structure the positions of the F atoms in F_1TCNQ result all partially occupied, with the best fit yielding a global occupation average of 37 %, in agreement with the values of 50 % and 25% given for the two sequences.

5.4 Charge transfer crystals Perylene-F_2TCNQ

5.4.1 Perylene-F_2TCNQ 1:1 crystals (Low T)

10.1 mg of perylene (0.040 mmol), and 11.9 mg of F_2TCNQ (0.045 mmol), TCI chemicals 98% of purity, were placed in the ampoule prepared following the protocol described above. The ampoule was located in the furnace, setting the temperatures of the hot and cold end at 180 °C and 110 °C, respectively. An accurate measurement of the temperature at the cold end showed that this was actually slightly higher (114 °C) (Figure 5.22).

Figure 5.22 Ampoule before crystal growth with temperature of hot and cold ends set.

After 7 days, the furnace was turned off and the ampoule left inside to cool down to room T. Very little amount of material was deposited at the cold end, but it was anyway possible to identify three kind of crystals in the growth: yellow needles, black platelets and orange prism-like crystals (see Figure 5.23).

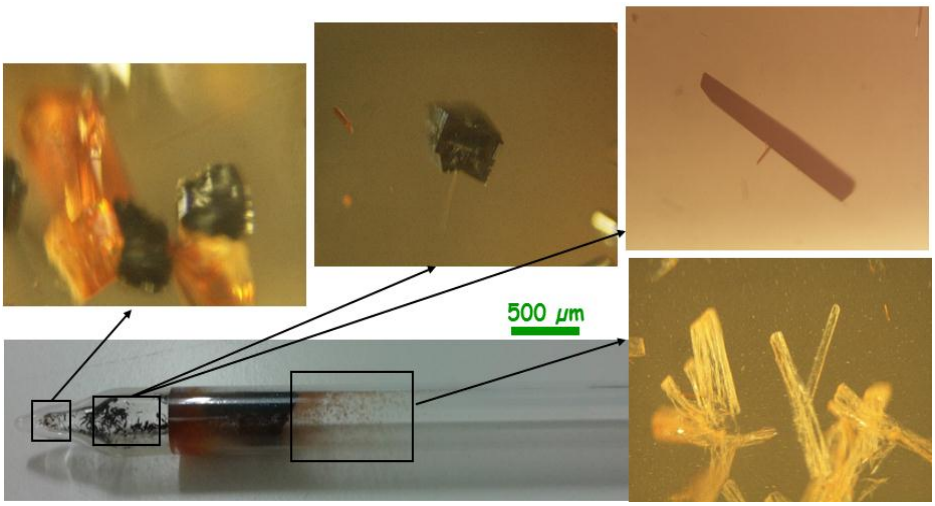

Figure 5.23 Morphologies of the crystals obtained after experiment and distribution along the ampoule.

The parents materials Perylene and F_2TCNQ, crystallized as pure compounds, could be recognized by infrared and Raman spectroscopies, and no further analysis was needed for those. The black crystals were characterized instead by XRD, and resulted to be the binary system Perylene-F_2TCNQ in a 1:1 ratio. This system crystallizes in a monoclinic structure, with space group $P2_1/n$, two molecules per unit cell and cell parameters (at 150 K): a = 7.0425 Å, b = 8.4114 Å, c = 19.117 Å and β = 96.086°. No structural data for this crystal have been reported as yet. Cell parameters and more details of the structure are reported in Table 5.6 and Figure 5.24, respectively.

Table 5.6 Crystal data and structure refinement for Perylene-F_2TCNQ 1:1.

Empirical formula	$C_{32}H_{12}F_2N_4$
Formula weight	490.46 g mol^{-1}
Temperature	150(2) K
Wavelength	0.7107 Å
Crystal system	Monoclinic
Space group	$P2_1/n$
Unit cell dimensions	a = 7.0425(10) Å α = 90°
	b = 8.4114(9) Å β = 96.086(6)°
	c = 19.117(3) Å γ = 90°
Volume	1126.1(3) $Å^3$
Z	2
Density (calculated)	1.447 Mg/m^3
Absorption coefficient	0.099 mm^{-1}
F(000)	500
Crystal size	0.500 x 0.250 x 0.100 mm^3

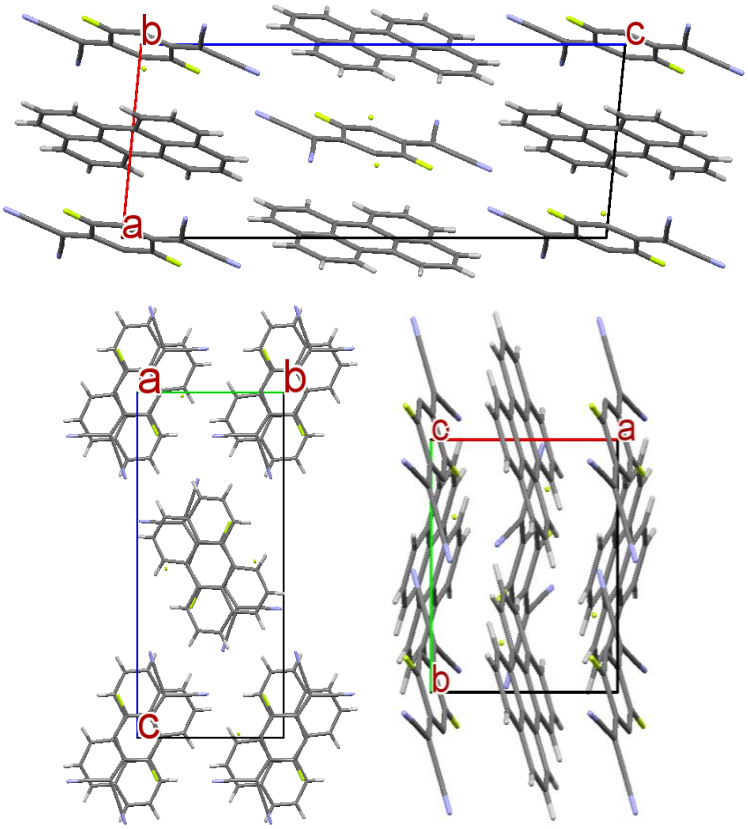

Figure 5.24 Crystal packing of binary system Perylene-F_2TCNQ 1:1.

The figure shows that perylene and F_2TCNQ make a perfect mixed stack along *a* axis. The F atoms are disordered as a result of the rotational disorder of F_2TCNQ and the average occupation of the position pairs (2,5) and (3,6) is 70:30.

5.4.2 Perylene-F_2TCNQ 3:2 crystals (High T)

19.60 mg of perylene (0.078 mmol) and 18.66 mg of F_2TCNQ (0.078 mmol), TCI chemicals 98% of purity, were transferred into a the quartz glass ampoule and treated as previously described. In the experimental conditions given in the previous paragraph the perylene-F_2TCNQ 1:1 structure can be obtained. If the same rationale found for the binary system perylene-F_0TCNQ described in the paragraphs 5.2.1 and 5.2.2 applies, a higher T setting should produce a different structure, with a different stoichiometric ratio. With this goal in mind, the ampoule was placed in the furnace setting the high temperature at 200 °C and the low temperature at 140 °C. After just seven days, binary crystals of perylene-F_2TCNQ in the expected stoichiometric ratio 3:2 were isolated. This result is especially remarkable because it is the first clear indication that it is possible to drive the system towards a desired structure while working in the gas phase.

This system crystallizes in a triclinic structure, with space group $P\bar{1}$, two molecule per unit cell and cell parameters (at 150 K): *a* = 7.23070 Å, *b* = 19.1407 Å, *c* = 22.2723 Å, α = 112.2834°, β = 96.086°and γ = 93.7559°. No structural data for this crystal have been reported as yet. Cell parameters and details of the crystal structure of perylene-F_2TCNQ 3:2 are reported in Table 5.7 and Figure 5.25, respectively.

Table 5.7 Crystal data and structure refinement for Perylene-F_2TCNQ 3:2.

Empirical formula	$C_{84}H_{36}F_4N_8$	
Formula weight	1233.21	
Temperature	150(2) K	
Wavelength	0.71073 Å	
Crystal system	Triclinic	
Space group	P-1	
Unit cell dimensions	*a* = 7.23070(10) Å	α = 112.2834(8)°
	b = 19.1407(3) Å	β = 90.1900(8)°
	c = 22.2723(5) Å	γ = 93.7559(12)°
Volume	2844.85(9) $Å^3$	
Z	2	
Density (calculated)	1.440 Mg/m^3	
Absorption coefficient	0.095 mm^{-1}	
F(000)	1264	
Crystal size	0.500 x 0.400 x 0.150 mm^3	

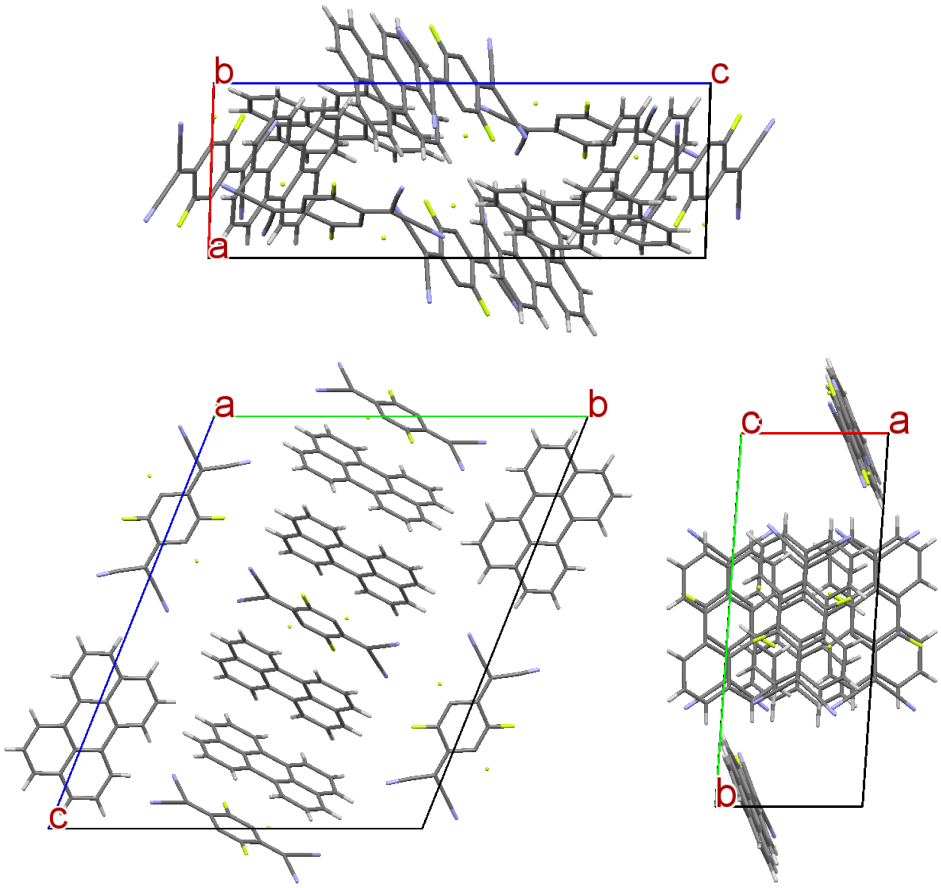

Figure 5.25 Crystal packing of binary system Perylene-F_2TCNQ 3:2

The crystal packing of this binary system is characterized by two separated different stacks. One mixed stack has a configuration ADDADDA along the *c* crystallographic axis, the other and has a configuration ADADA along the *a* axis and can be easily identified in the crystal structure shown in Figure 5.25. The F atoms present an intrinsic disorder with different occupation factors.

5.5 Charge transfer crystals Perylene-F_4TCNQ

5.5.1 Perylene-F_4TCNQ 3:2 crystals (by PVT)

10.7 mg of F_4TCNQ (0.0387 mmol) and 11.2 mg of perylene (0.0444 mmol), were used for the growth of the binary system. As shown in Figure 5.26, the sealed ampoule was placed in the two-zones furnace setting the left hand side at 200 °C and the right hand side at 130 °C.

Figure 5.26 Ampoule before crystal growth with temperature of hot and cold ends set.

The crystals obtained after 7 days were examined under the optical microscope (Figure 5.27). At the right hand side of the ampoule the crystallization of black needles was observed, together with a small amount of the starting material.

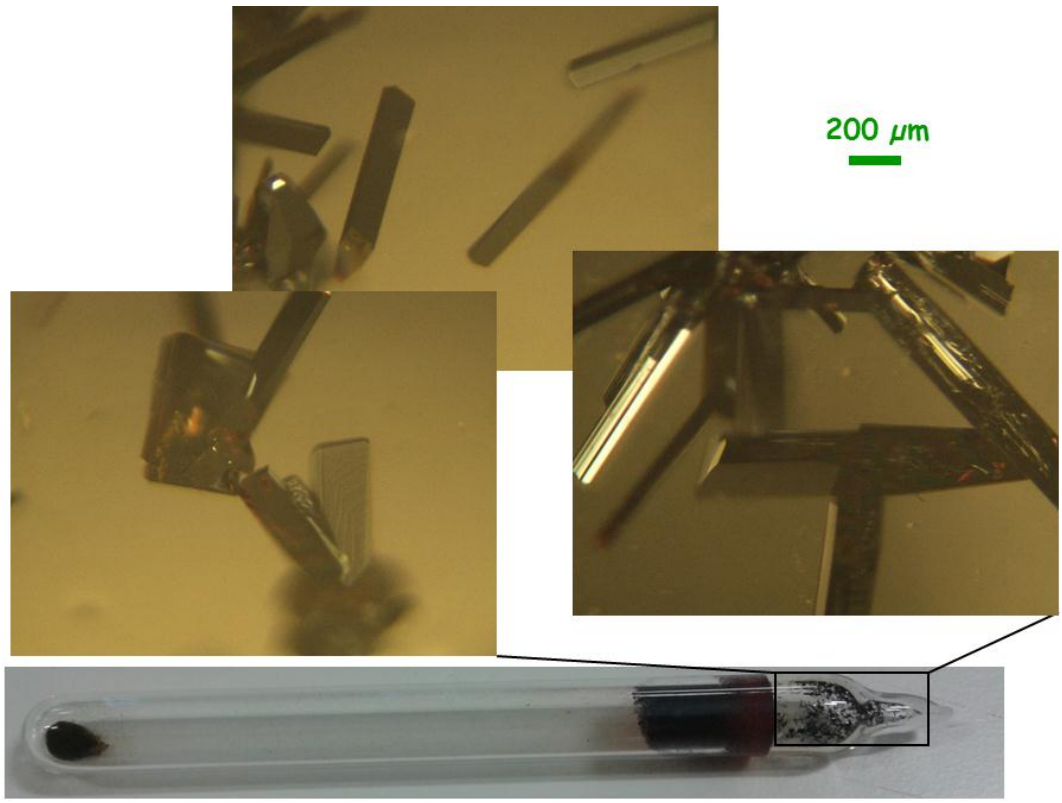

Figure 5.27 Morphologies of the crystals obtained after experiment and distribution along the ampoule.

The black crystals were first probed by Raman and Infrared spectroscopies. When it was determined that they belonged to a structure not yet obtained, they were analyzed by XRD diffraction.

Perylene-F_4TCNQ 3:2 binary system crystallizes in a triclinic structure, with space group $P\bar{1}$, two molecules per unit cell and cell parameters (at 150 K): *a* = 7.2066 Å, *b* = 19.0974 Å, *c* = 22.4050 Å, α = 111.8014°, β = 90.0472°and γ = 94.1283°. The structural parameters reported in Table 5.8 and Figure 5.28 are in agreement with those of the previous work by Tsunami et al. [32].

Table 5.8 Crystal data and structure refinement for Perylene-F_4TCNQ 3:2.

Empirical formula	$C_{84}H_{36}F_8N_8$	
Formula weight	1309.21 g mol^{-1}	
Temperature	150(2) K	
Wavelength	0.71073 Å	
Crystal system	Triclinic	
Space group	P-1	
Unit cell dimensions	*a* = 7.2066(2) Å	α = 111.8014(14)°
	b = 19.0974(6) Å	β = 90.0472(17)°
	c = 22.4050(7) Å	γ = 94.1283(17)°
Volume	2854.30(15) $Å^3$	
Z	2	
Density (calculated)	1.523 Mg/m^3	
Absorption coefficient	0.109 mm^{-1}	
F(000)	1336	
Crystal size	0.500 x 0.250 x 0.050 mm^3	

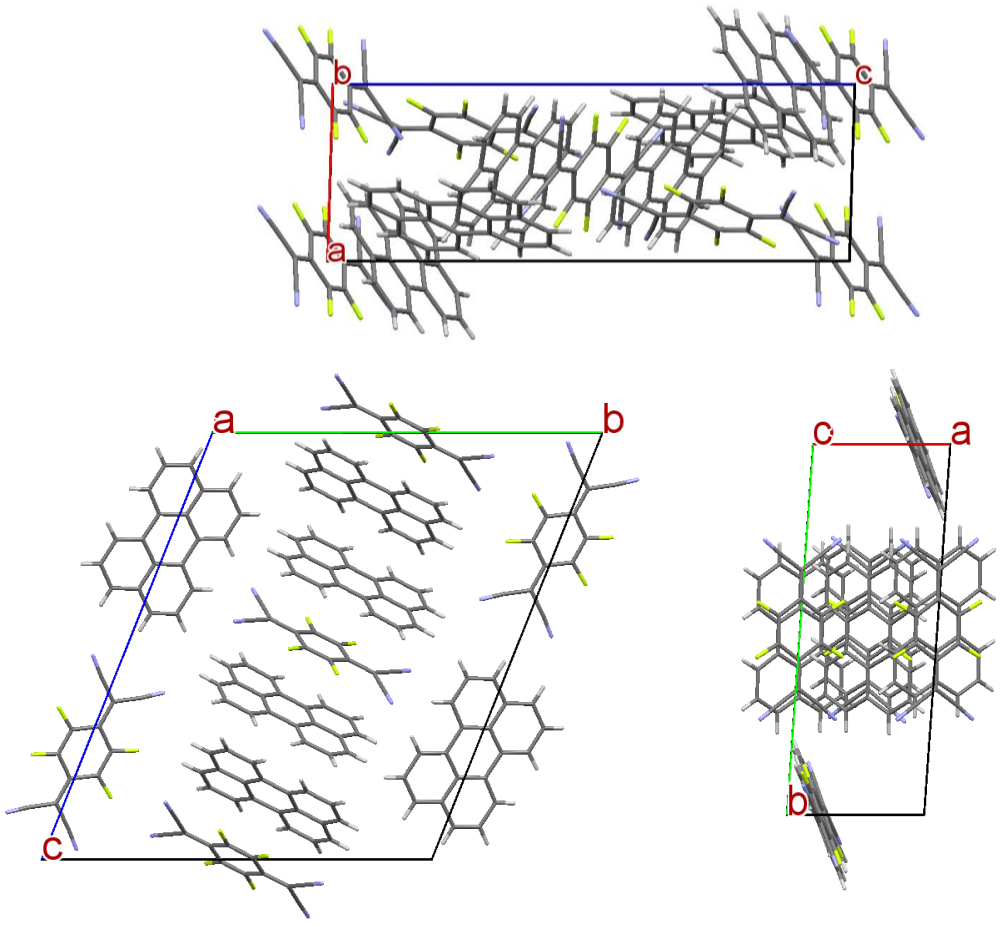

Figure 5.28 Crystal packing of binary system Perylene-F_4TCNQ 3:2.

The crystal structure of the binary system Perylene-F_4TCNQ is similar in cell parameters and crystal packing to that of the Perylen-F_2TCNQ 3:2 system. The molecular arrangements in the two structures are basically identical and the same two stacks can be identified in the crystal packing of Figure 5.28: a mixed stack in configuration ADDADDA along the *c* crystallographic axis and a mixed stack ADADA along the *a* axis.

5.5.1 Perylene-F_4TCNQ 1:1 crystals (from solution)

1.04 mg of F_4TCNQ (0.0387 mmol) and 0.96 mg of perylene (0.0444 mmol), were dissolved in a solution of toluene/acetonitrile 5:1 and placed in a ultrasound bath for 10 min at room temperature. After complete dissolution of two compounds, the solution was heated to 80 °C for 30 minutes and then left cooling down to ambient conditions overnight. The black needle like crystals so obtained are shown in Figure 5.29.

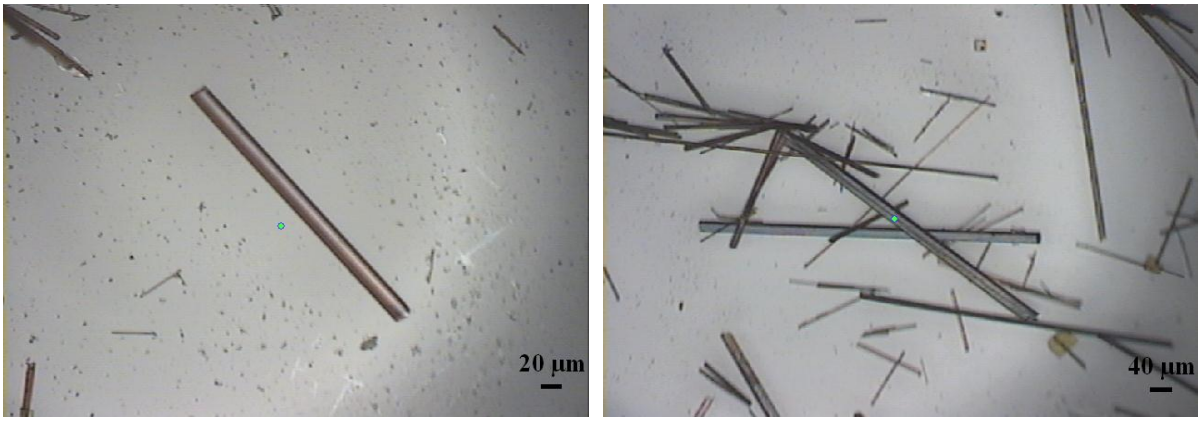

Figure 5.29 Crystal shape of the binary system by solution method Perylene-F_4TCNQ 1:1 * 1 toluene

The Perylene-F_4TCNQ 1:1 binary system was found to crystallize in a triclinic structure, with space group $P\bar{1}$, one molecule per unit cell and cell parameters (at 150 K): *a* = 7.0293 Å, *b* = 8.4804 Å, *c* = 11.8703 Å, α = 89.557°, β = 81.968°and γ = 86.069°. In the crystal refined structure the molecule of the solvent toluene is also present, with an intrinsic disorder.

Structural details and the packing of this structure, not yet reported in the literature, are given in Table 5.9 and Figure 5.30, respectively.

Table 5.9 Crystal data and structure refinement for Perylene-F_4TCNQ 1:1 * 1 toluene.

Empirical formula	$C_{39}H_{20}F_4N_4$	
Formula weight	620.59 g mol^{-1}	
Temperature	150(2) K	
Wavelength	1.54184 Å	
Crystal system	Triclinic	
Space group	P-1	
Unit cell dimensions	*a* = 7.0293(4) Å	α = 89.557(8)°
	b = 8.4804(8) Å	β = 81.968(7)°
	c = 11.8703(12) Å	γ = 86.069(6)°
Volume	699.01(11) $Å^3$	
Z	1	
Density (calculated)	1.474 Mg/m^3	
Absorption coefficient	0.887 mm^{-1}	
F(000)	318	
Crystal size	0.200 x 0.020 x 0.020 mm^3	

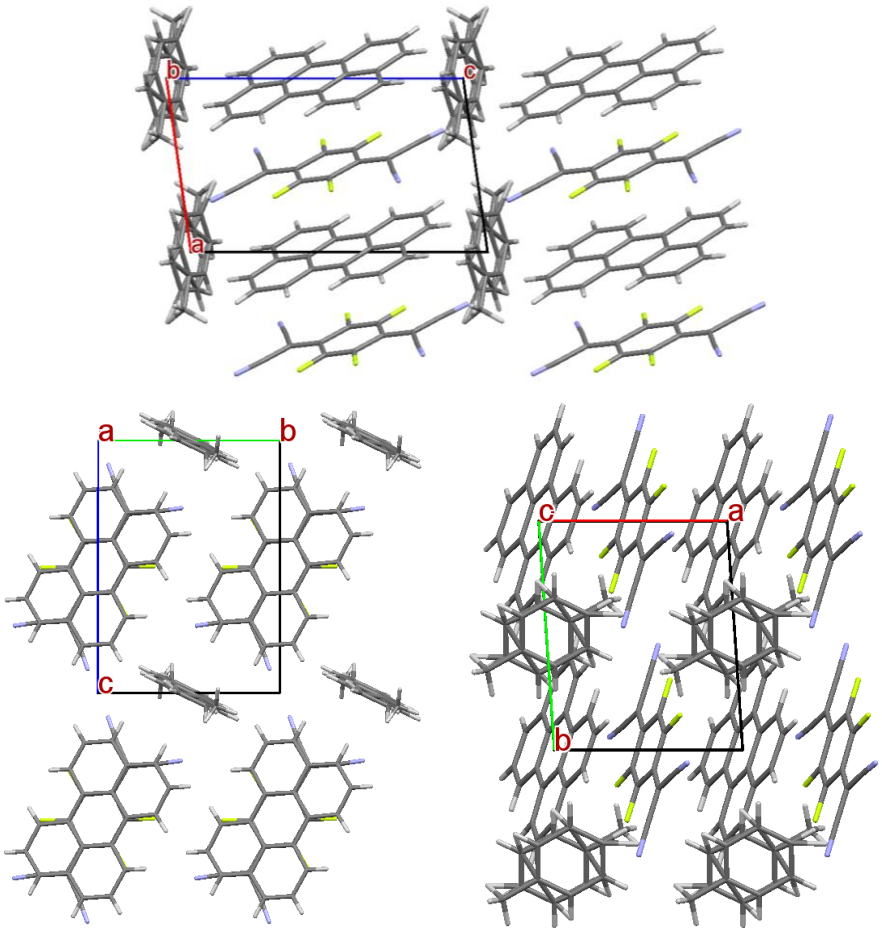

Figure 5.30 Crystal packing of binary system Perylene-F_4TCNQ 1:1

Apart from the presence of the solvent molecules, the crystal structure of the binary system Perylene-F_4TCNQ is similar both in cell parameters and crystal packing to the other Perylene-F_xTCNQ systems of ratio 1:1 already reported in the previous paragraphs. The molecules are packed in the same way in all systems, with each donor paired to an acceptor in a mixed stack ADADA parallel to *a* crystallographic axis (Figure 5.30). The disordered solvent molecules are located in interstitial sites between the CT stacks.

5.6 Charge transfer crystals Perylene-F_0TCNQ-F_2TCNQ

A mixture of 16.2 mg of perylene (0.064 mmol), 12.5 mg of F_0TCNQ (0.061 mmol) and 15.3 mg of F_2TCNQ (0.064 mmol) was used in the attempt of growing a ternary system. In this case, the temperatures selected for the hot and cold end were 170 °C at 110 °C, respectively. The temperature profile along the furnace axis is drawn in Figure 5.31, where the temperatures actually measured for the two ends (178 °C and 128 °C) are indicated.

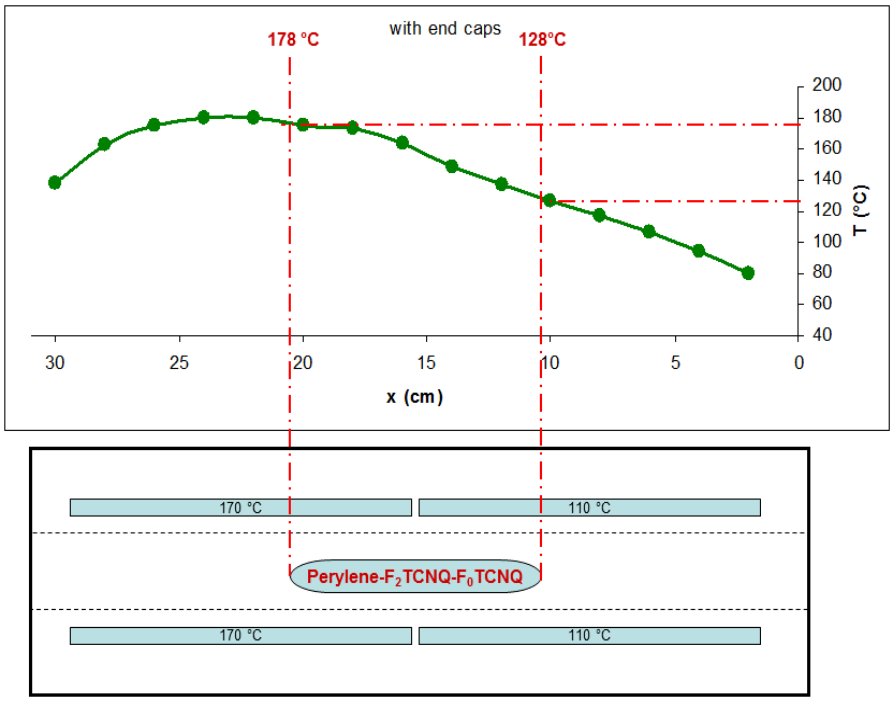

Figure 5.31 Temperatures distribution in the furnace for perylene-F_0TCNQ-F_2TCNQ crystal growth.

Crystals were left to grow for 12 days. Images of the variety of crystals that were recovered from the ampoule are shown in Figure 5.32. The black crystals were present in a large portion of the middle section of the ampoule and were found mixed with the yellow crystals of pure perylene. The orange crystals of the pure compounds F_0TCNQ and F_2TCNQ were instead recovered at the right end of the ampoule.

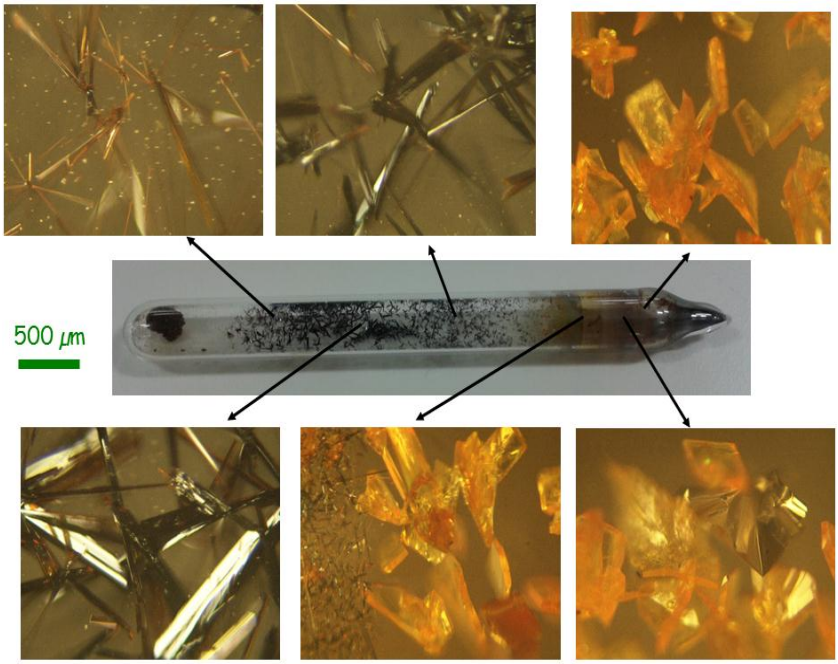

Figure 5.32 Morphologies of the crystals obtained after experiment and distribution along the ampoule.

Spectroscopic measurements showed that the black crystals were a mixed system and XRD confirmed that ternary system perylene-F_0TCNQ-F_2TCNQ had been obtained.

Perylene-F_0TCNQ-F_2TCNQ crystallizes in a triclinic structure, with space group $P\bar{1}$, one molecule per unit cell and cell parameters (at 150 K): *a* = 7.2289 Å, *b* = 19.1347 Å, *c* = 22.2851 Å, α = 112.2496°, β = 90.1547°and γ = 93.8456°. The cell parameters and the crystal structure are reported in Table 5.10 and Figure 5.33, respectively.

Table 5.10 Crystal data and structure refinement for Perylene-$F_{0\text{-}2}$TCNQ 3:2.

Empirical formula	$C_{168}H_{76}F_7N_{16}$	
Formula weight	2451.44 g mol^{-1}	
Temperature	150(2) K	
Wavelength	0.71073 Å	
Crystal system	Triclinic	
Space group	P-1	
Unit cell dimensions	*a* = 7.2289(2) Å	α = 112.2496(15)°
	b = 19.1347(6) Å	β = 90.1547(15)°
	c = 22.2851(8) Å	γ = 93.8456(16)°
Volume	2845.28(16) A^3	
Z	1	
Density (calculated)	1.431 Mg/m^3	
Absorption coefficient	0.093 mm^{-1}	
F(000)	1259	
Crystal size	0.500 x 0.250 x 0.100 mm^3	

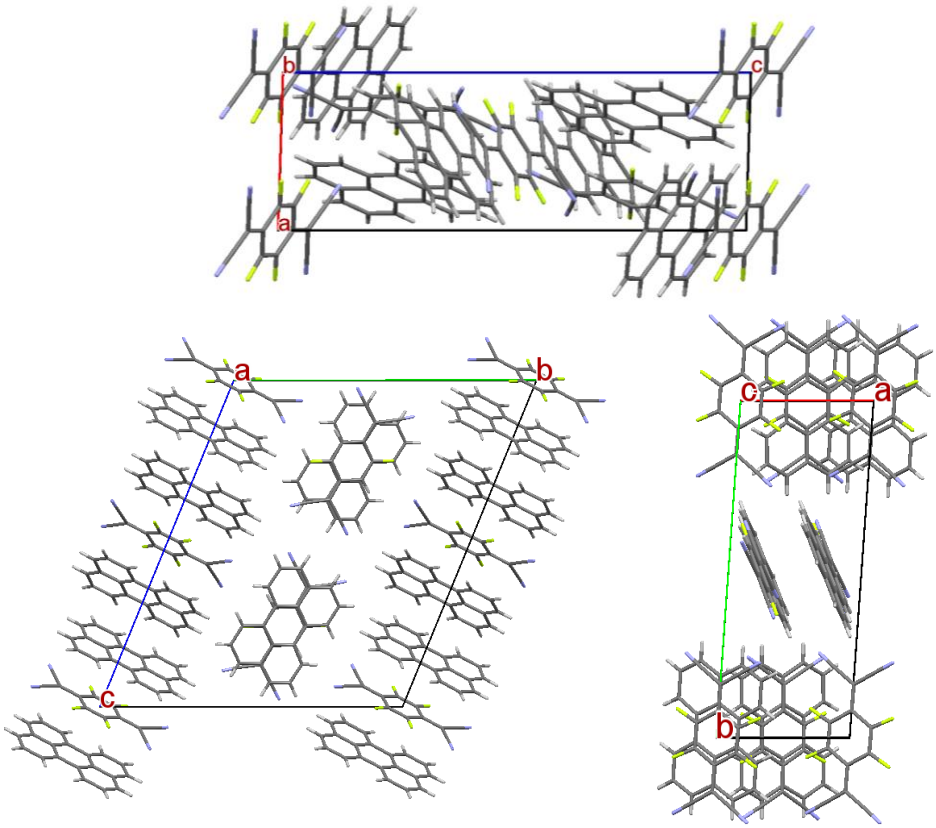

Figure 5.33 Crystal packing of ternary system Perylene-F_0TCNQ-F_2TCNQ.

The unit cell contains six perylene and four F_xTCNQ molecules with different occupations of the F atoms as follows: F1 and F2 = 75%, F3 and F4 = 50%, F5 = 40% and F6 = 60%. The positions of the different F atoms in the crystal packing are shown in Figure 5.34. Note that the unit cell parameters are similar to those of both crystal systems perylene-F_2TCNQ 3:2 and perylene-F_4TCNQ 3:2. Indeed, this system crystallizes in the same ratio 3:2 with the CT stacks ADDADDA along the *c* axis and ADADA along the *a* axis.

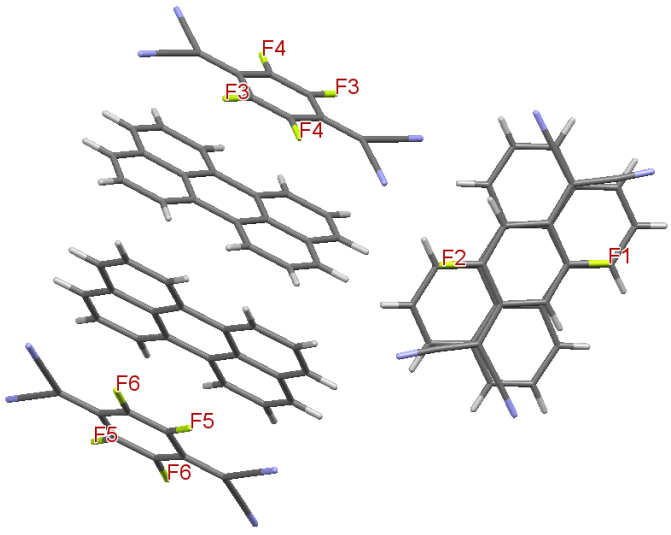

Figure 5.34 Numbering of the F atoms with different occupation factors in the crystal packing.

5.7 Vibrational and charge transfer properties of binary systems Perylene-F_xTCNQ

As already described at the beginning of this chapter, the magnitude of the charge transfer from the HOMO of the donor to the LUMO of the acceptor is related to the ionization potential of the former (Perylene), to the electron affinity of the latter (F_xTCNQ), and to the energetic gain upon the formation of an ionic structure [61]. A partial charge transfer may take place in systems where the difference between the ionization potential of the donor and the electron affinity of the acceptor is moderately negative. In classes of compounds such as salts of donor and acceptor molecules, the degree of charge transfer is closely related to the stoichiometry of the solid.

A comparison between the bond lengths of the neutral species and of the salt shows, as expected, that the geometry varies with the electron population of the molecular orbitals. In the case of TCNQ and its derivatives, a larger electron population implies a less quinoid character of the molecule, with C-C bonds more equal in value. Thus, the experimental geometry can provide information on the degree of charge transfer through the bond length variation between neutral and charged TCNQs.

Systematic studies to this effect have been carried out by several authors for F_0TCNQ [23,24,43-46,62], to seek relationships based on a the interpolation of the data for the neutral compound (ρ=0) and the fully charge salt (ρ=1). The four different expressions already reported in paragraph 5.1.2 are commonly used for the estimation of the unknown ρ values of binary systems with F_0TCNQ. To apply them to our F_0TCNQ complexes, we must make the approximation (very reasonable in terms of available precision of crystallographic data) that the bond lengths are not dependent on temperature. This has allowed us to calculate the ρ_{F0TCNQ} values for the systems perylene-F_0TCNQ 1:1 and perylene-F_0TCNQ 3:1 given in Table 5.11, in which the data obtained for each equation are reported.

Table 5.11 Molecular parameters of the F_0TCNQ molecule in the binary systems of perylene-F_0TCNQ and values of ρ determined by using equations 1-4 of this chapter.

compound	T [K]	a [Å]	b [Å]	c [Å]	d [Å]	ρ_{F0TCNQ}
Perylene-F_0TCNQ 1:1	150	1.348	1.445	1.378	1.430	0.095 (eq.1)
						0.146 (eq.2)
						0.143 (eq.3)
						0.163(eq.4)
Perylene-F_0TCNQ 3:1	150	1.353	1.440	1.386	1.434	0.217 (eq.1)
						0.258 (eq.2)
						0.262 (eq.3)
						0.272 (eq.4)

In a recent work, Lieffrig and coworkers [63] report on the charge transfer degree in binary systems where iodinated tetrathiafulvalene derivatives (EDT-TTFI$_2$) are associated with F_1TCNQ and F_2TCNQ. Based on X-ray data for neutral F_1TCNQ and F_2TCNQ [55,56] and radical anion states [64,65], the authors derive for these compounds the parameters A and B of the equation 3 given by Kistenmacher [46] and already reported in paragraph 5.1.2: $\rho = A[c/(b+d)] + B$. The A values of that work are -57.87 and -56.78, for F_1TCNQ and F_2TCNQ, respectively; the B values are 27.79 and 27.15, respectively.

The calculated values ρ_{F_1TCNQ} and ρ_{F_2TCNQ}, together with the bond lengths used for their estimation, are given in Table 5.12.

Table 5.12 Calculated values of ρ for the binary systems perylene-F_1TCNQ and perylene-F_2TCNQ.

compound		T [K]	a [Å]	b [Å]	c [Å]	d [Å]	ρ_{FxTCNQ} (x = 1,2)
Perylene-F_1TCNQ 3:2	Mixed stack ADADAD (along x axis)	150	1.348	1.440	1.384	1.435	0.068
	Mixed stack ADDADDADD (along x axis)	150	1.344	1.445	1.378	1.431	0.052
Perylene-F_2TCNQ 1:1	Mixed stack ADADAD	150	1.341	1.444	1.386	1.435	0.060
Perylene-F_2TCNQ 3:2	Mixed stack ADADAD (along x axis)	150	1.341	1.444	1.382	1.437	0.032
	Mixed stack ADDADDADD (along x axis)	150	1.382	1.445	1.377	1.432	0.082

Note that for the binary systems with ratio 3:2, in which two different kinds of mixed stacks are present, ρ must be estimated for each of them, as the F_xTCNQ molecules in the two arrangements are not symmetry equivalent and display differences in bond lengths. The values of ρ based on the geometries of the acceptor molecules in the crystal structures of these binary systems lie all in the range 0.03-0.08, an indicator that these complexes are essentially neutral, despite the presence of the fluorine atoms.

For the binary systems perylene-F_4TCNQ, ρ cannot be estimated with this method, because of the lack of literature crystallographic data and the experimental difficulty of obtaining single crystals suitable for the X-ray analysis of the F_4TCNQ salts. For the ternary

system, the employment of the equations is instead complicated by the occupational disorder of F_0TCNQ and F_2TCNQ, which does not permit to disentangle the bond lengths.

As reported above, the frequency of several vibrational modes of TCNQ and its derivatives is sensitive to the charge transfer [66]. Girlando et al. [67] and Bozio et al. [68] reported that the C=C stretching mode exhibits a considerable shift towards lower frequencies with increasing negative charge and it is therefore a very sensitive probe of the ionization degree.

In Figure 5.35 the polarized IR spectra the perylene-F_0TCNQ 1:1 crystal are reported. The polarization directions indicated are those parallel and perpendicular to the extinction direction.

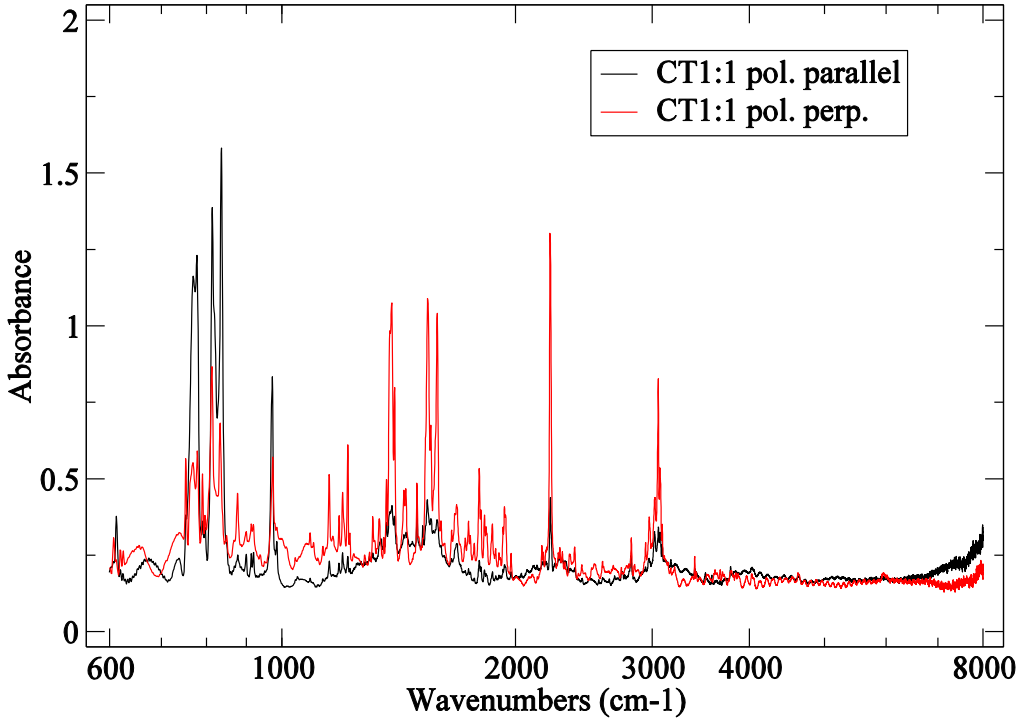

Figure 5.35 IR spectra of Binary system Perylene-F_0TCNQ 1:1 in different polarizations: parallel (black line) and perpendicular (red line) to the extinction direction.

The interpretation of these spectra has been based on the infrared spectrum of perylene reported by Ambrosino and Califano [69] and the vibrational spectrum of TCNQ and its alkali salts reported by Girlando et al. [70]. The potassium salt of F_0TCNQ was prepared in this work following Melby et al. [71], using the reaction of the iodide with TCNQ. When the hot solutions of KI and TCNQ in acetonitrile were mixed, the potassium salt precipitated as a purple crystalline solid. TCNQ and potassium iodide were mixed in ratio 2:3 using the excess of metal iodide to scavenge the iodine by-product as I_3^-. The infrared spectra of neutral F_0TCNQ and the potassium salt $K^+F_0TCNQ^-$ are reported in Figure 5.36, with the picture of the diagnostic

mode used for the estimation of ρ. The mode at 1543 cm^{-1} is the C=C stretching vibration of neutral F_0TCNQ and is shifted by 34 cm^{-1} in the potassium salt (1509 cm^{-1}).

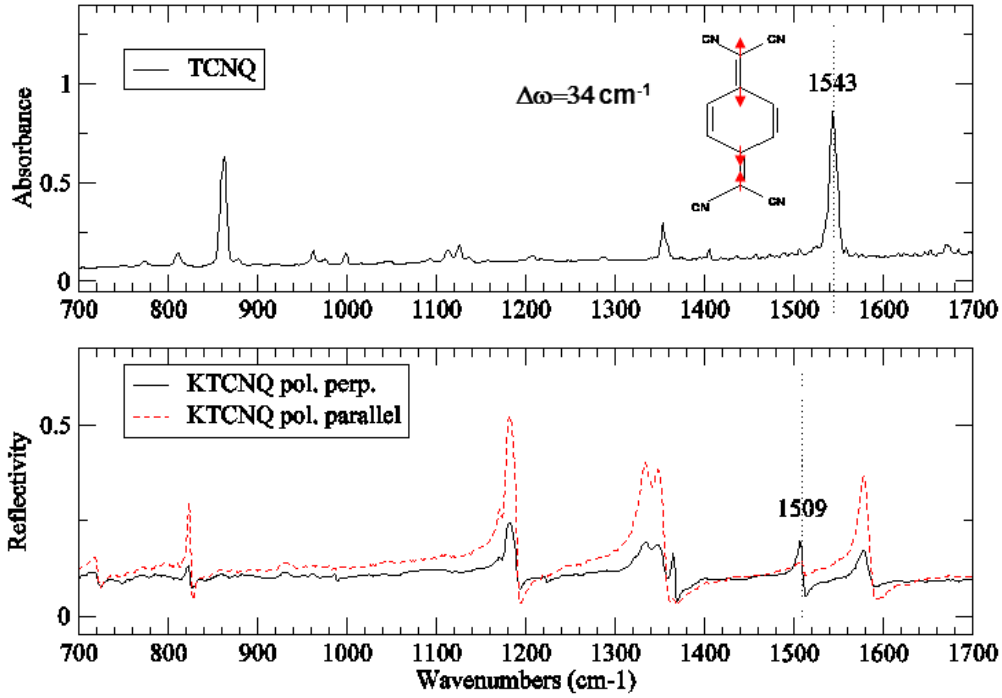

Figure 36 IR spectra of the salt K^+F_0TCNQ in different polarizations and IR spectrum of the neutral compound.

When the spectra of neutral F_0TCNQ and of system perylene-F_0TNQ 1:1, this latter in both polarizations, are compared (Figure 5.37), it is clear that no shift of the diagnostic mode is detected. For this reason, the binary system can be considered as neutral (ρ=0).

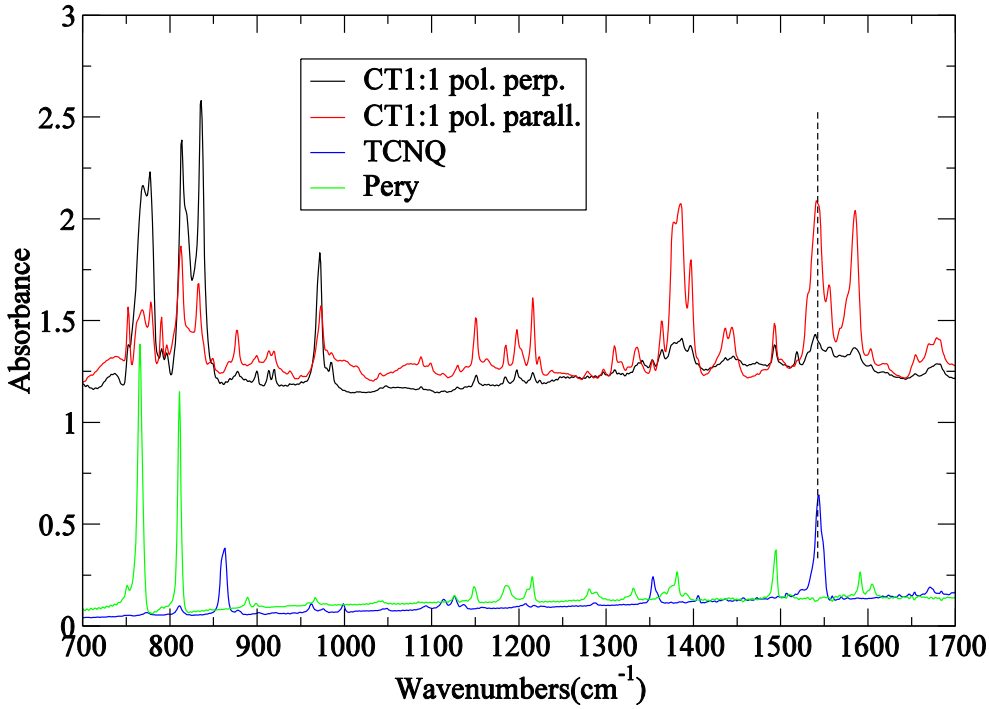

Figure 5.37 IR spectra of the pure single compounds F_0TCNQ (blue line) and perylene (green line) and polarized spectra of the Perylene- F_0TCNQ 1:1 binary system.

The same procedure was followed for the analysis of the system perylene-F_0TCNQ with ratio 3:1 and the complete IR spectra in the parallel and perpendicular polarizations are reported in Figure 5.38.

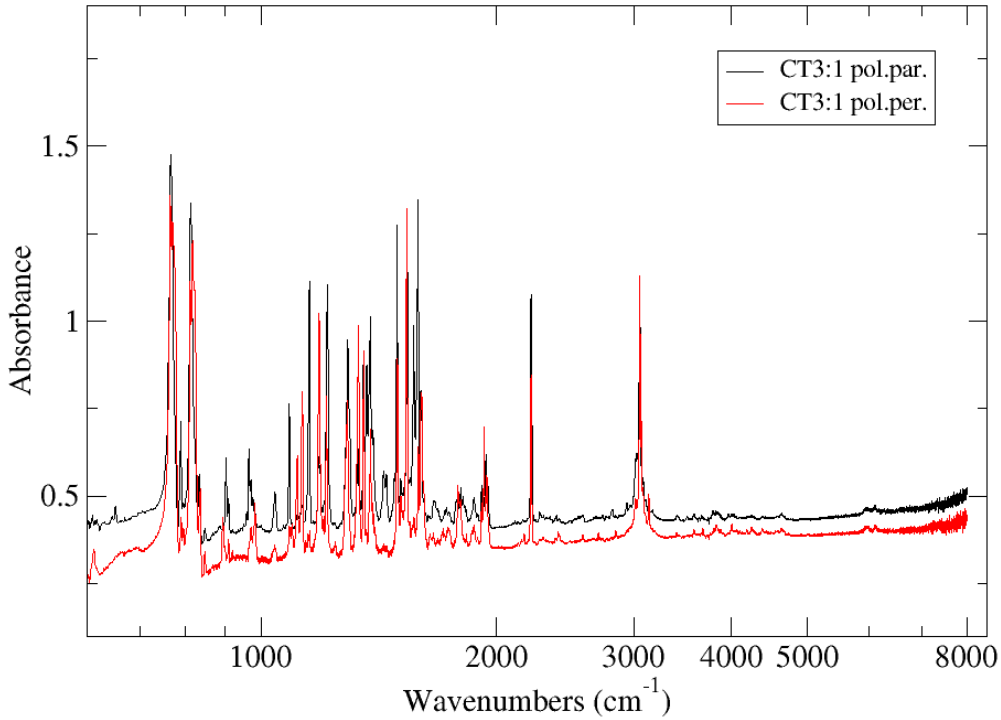

Figure 5.38 IR spectra of Binary system Perylene-F_0TCNQ 3:1 in different polarizations: parallel (black line) and perpendicular (red line) to the extinction direction.

The diagnostic band, detected at 1543 cm^{-1} in the neutral compound, is present in both polarizations at the two slightly different frequencies of 1538 and 1536 cm^{-1} (Figure 5.39). The perylene-F_0TCNQ 3:1, as described in the previous paragraph, crystallizes in a triclinic structure with one molecule per unit cell, and for this reason no splitting is expected. Nonetheless, the splitting of this band has been reported for the first time by Truong and Bandrauk [72], who described this effect as a consequence of the strong interaction of F_0TCNQ with perylene, thus confirming that in the complex 3:1 there is a partial ionicity. In fact, the ρ value calculated from the mean value the shift of the diagnostic infrared band is ≈ 0.2.

The electronic absorption spectra of both 1:1 and 3:1 perylene-F_0TNQ have been reported by Bandrauk and coworkers [73]. The absorption spectra of these complexes are characterized by the presence of the so called charge transfer bands, which are transitions from electronic states localized (mostly) on the donor moiety of the complex to states localized (mostly) on the acceptor moiety. These transitions, usually weak and broad, can be found in the near IR or in the visible portion of the electromagnetic spectrum.

The absorption spectra of the 1:1 system displays a band at 950 nm, which does not

occur in the spectra of the isolated molecules [74] and is therefore assigned to the CT transition. In the case of the system 3:1 the maximum of the CT band is shifted to 1000 nm, as a consequence of the stronger perylenes -TCNQ interaction.

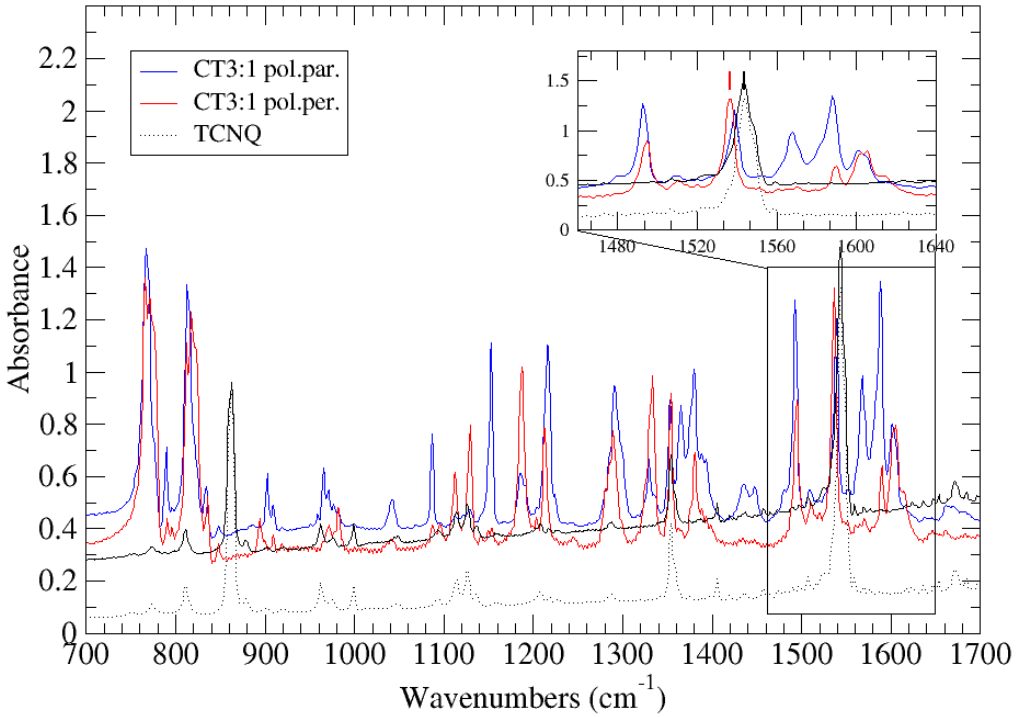

Figure 5.39 Comparison of the IR spectra of the pure single compounds F_0TCNQ (black line) and the different polarizations of the corresponding binary system 3:1. In the onset a magnification of the range examinated.

The Perylene-F_2TCNQ 1:1 complex, described previously, is a typical 1D system with a regular mixed stack along the *a* crystallographic axis, with considerable side-by-side interactions between the stacks, driven by C-H----F bonds. Unlike the perylene-F_0TCNQ systems previously described, the IR spectra of the complex Perylene-F_2TCNQ 1:1 (Figure 5.40) show a strong absorption starting from 7000 cm^{-1} in both polarization conditions. This absorption can be assigned to the CT band, although the reason why we can detected in both polarizations must be investigated.

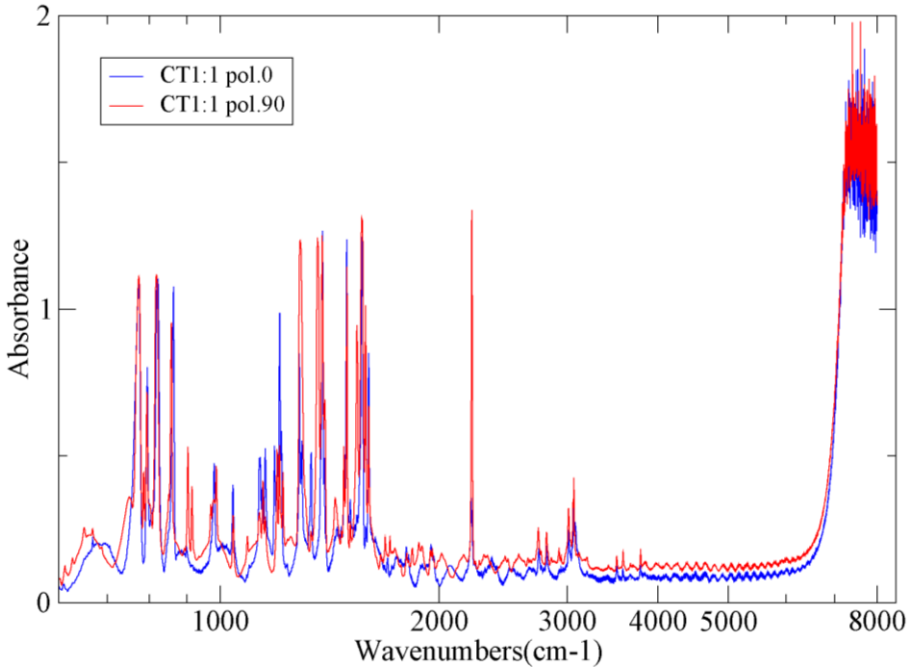

Figure 5.40 IR spectra of Binary system Perylene-F_2TCNQ 1:1 in different polarizations: parallel (blue line) and perpendicular (red line) to the extinction direction.

The estimation of ρ with the spectroscopic method was based on the analysis of the diagnostic C=C stretching modes of F_2TCNQ, falling at 1383, 1543 and 1567 cm^{-1}. The infrared spectra of the binary system 1:1 in both polarizations, together with those of neutral F_2TCNQ and of the corresponding potassium salt, are given in Figure 5.41. The salt was obtained with the same procedure described for $K^+F_0TCNQ^-$. The frequency shifts of the complex correspond to an estimated charge transfer ρ in the range 0.1-0.15.

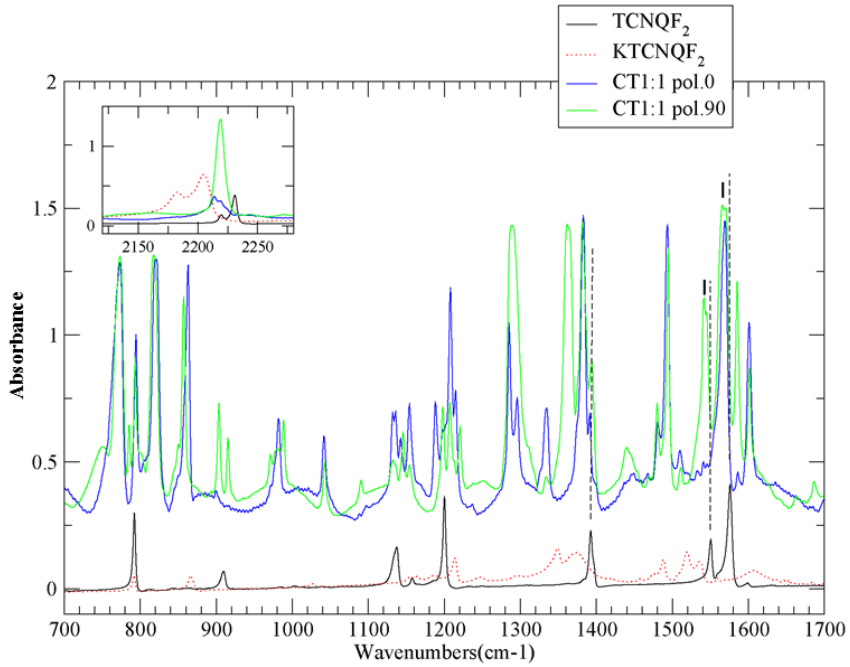

Figure 5.41 Comparison of the IR spectra of the pure single compounds F_2TCNQ (black line), the potassium salt (dotted red line) and different polarizations of the corresponding binary system 1:1. In the onset the shift of the C-N stretching.

Perylene-F_2TCNQ 3:2 crystal displays a more complicate packing, with a herringbone arrangement of the DAD trimer in the *ac* plane and a slightly dimerized mixed stack along the *a* crystal direction. By analysing the crystal arrangement, one can deduce that intra-trimer interactions must be the most important. From the spectra in the infrared region shown in Figure 5.42, a CT band around 7000 cm^{-1} can be detected. The band was found to be strongly polarized along the direction of the longer axis of the crystal sample. By looking at the cell parameters, it can be noticed that most probably the polarization direction of the CT band coincides with the direction of *a* crystallographic axis, which is by far the shortest and should correspond to the direction of fastest growth.

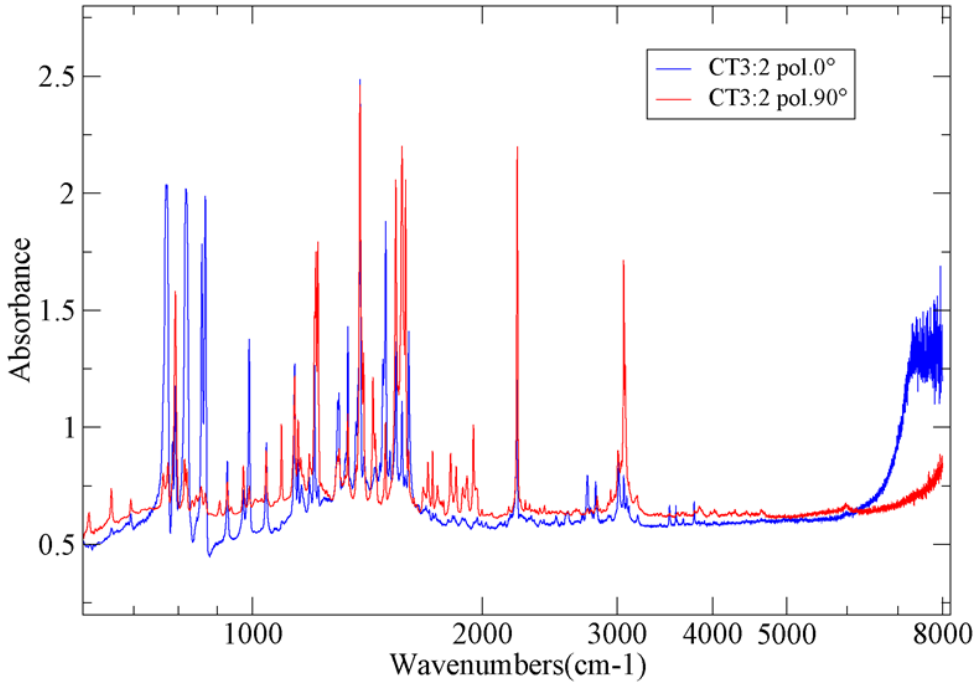

Figure 5.42 IR spectra of Binary system Perylene-F_2TCNQ 3:2 in different polarizations: parallel (blue line) and perpendicular (red line) to the extinction direction.

The selected diagnostic vibrational modes are those used the analogous 1:1 complex. The analysis of the infrared spectra (shown in figure 43) confirms the presence of differently interacting F_2TCNQ molecules, with a different degree of ionicity. A first set of vibrational modes can be found at 1.383, 1541 and 1569 cm^{-1}, and therefore with no frequency shifts. This behavior suggests the presence of F_2TCNQ molecules with $\rho = 0$. A second set of modes displays bands at 1396, 1551 and 1577 cm^{-1}, which correspond to F_2TCNQ molecules with a degree of charge transfer $\rho = 0$.

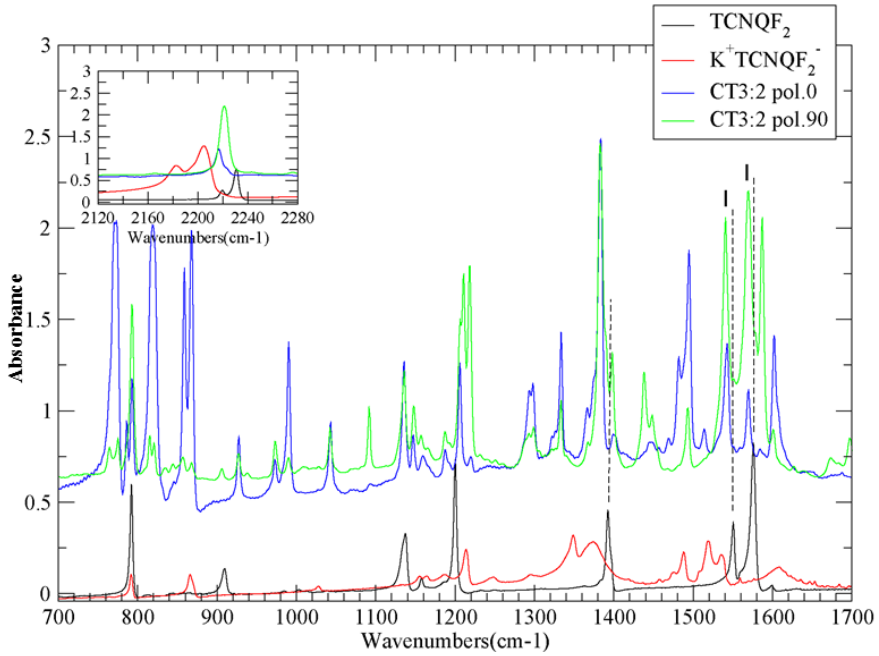

Figure 5.43 Comparison of the IR spectra of the pure single compounds F_2TCNQ (black line), the potassium salt (dotted red line) and different polarizations of the corresponding binary system 3:2. In the onset the shift of the C-N stretching.

Finally, the binary system with the strongest electron acceptor F_4TCNQ was analyzed by IR spectroscopy. The structure of perylene-F_4TCNQ 3:2 is similar to perylene-F_2TCNQ with the same stoichiometry, with a herringbone arrangement of the DAD trimer in the *ac* plane and a dimerized mixed stack along the *a* axis direction. The CT band can be detected in the polarized infrared spectra of Figure 5.44 at 6000 cm^{-1}.

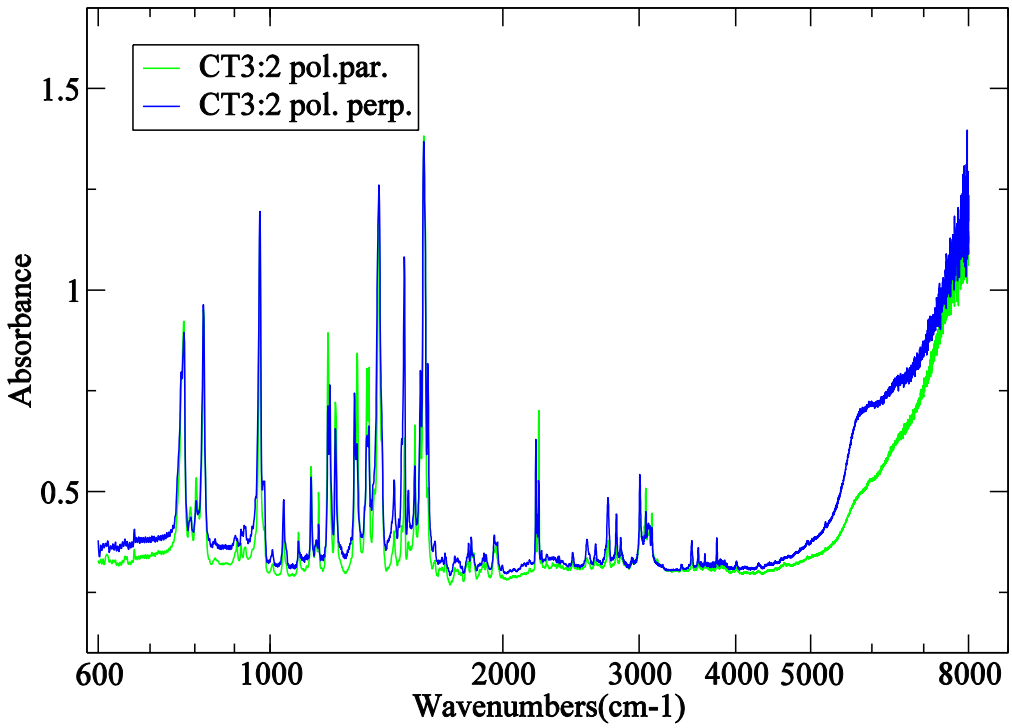

Figure 5.44 IR spectra of Binary system Perylene-F_4TCNQ 3:2 in different polarizations: parallel (green line) and perpendicular (blue line) to the extinction direction.

The three diagnostic bands used for the estimation of the degree of charge transfer are found in neutral F_4TCNQ at 1396, 1550 and 1599 cm^{-1}. They are marked as ν_3, ν_2 and ν_1, respectively, in figure 45. The same bands in the potassium salt are shifted at lower energies and found 1353, 1501 and 1540 cm^{-1}. The normal modes corresponding to ν_3, ν_2 and ν_1 are also shown in Figure 5.45, together with the shifts between neutral compound and potassium salt.

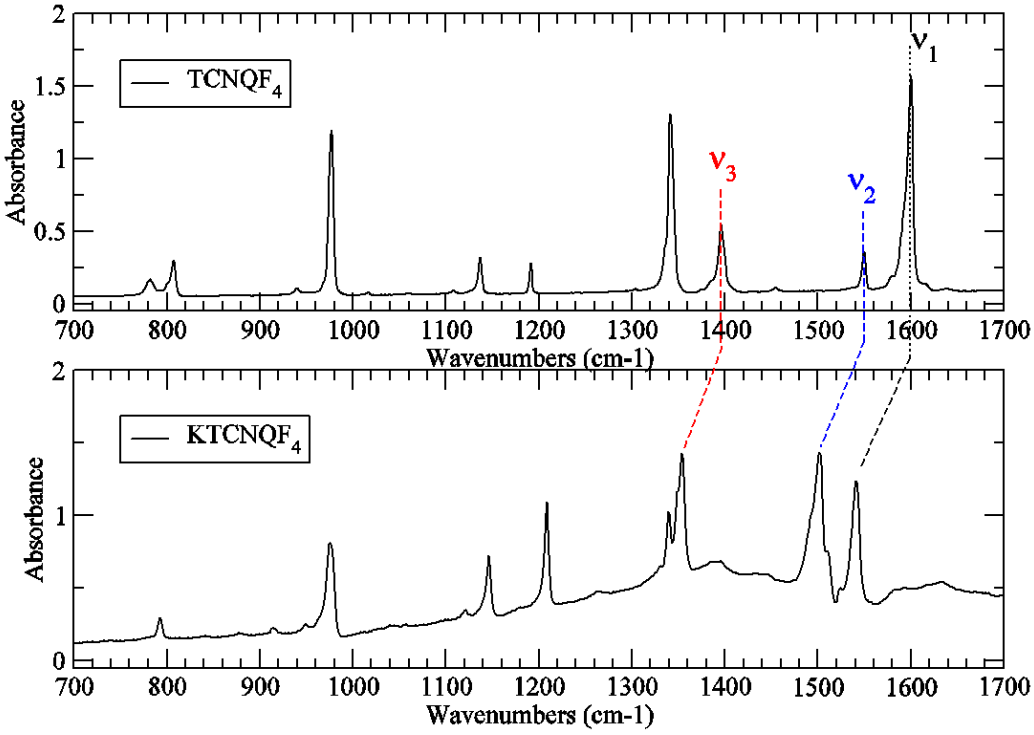

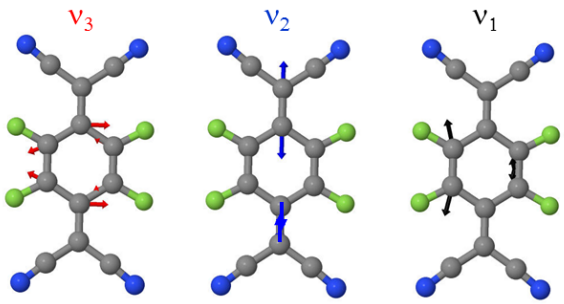

	ν_3 (cm^{-1})	ν_2 (cm^{-1})	ν_1 (cm^{-1})
F_4TCNQ^0	1396	1550	1599
F_4TCNQ^-	1353	1501	1540
$\Delta\omega$	43	49	59

Figure 5.45 IR spectra of the salt $K^+F_4TCNQ^-$ in different polarizations compared with the IR spectrum of the neutral compound.

In the Figure 5.46 the infrared spectra of the binary crystal is compared to that of the neutral acceptor, to quickly identify the shift due to the charge transfer effect. The three bands are marked. The ρ values calculated separately for each band are slightly different from each other: $\rho_{\nu1} = 0.29$, $\rho_{\nu2} = 0.22$ and $\rho_{\nu3} = 0.28$.

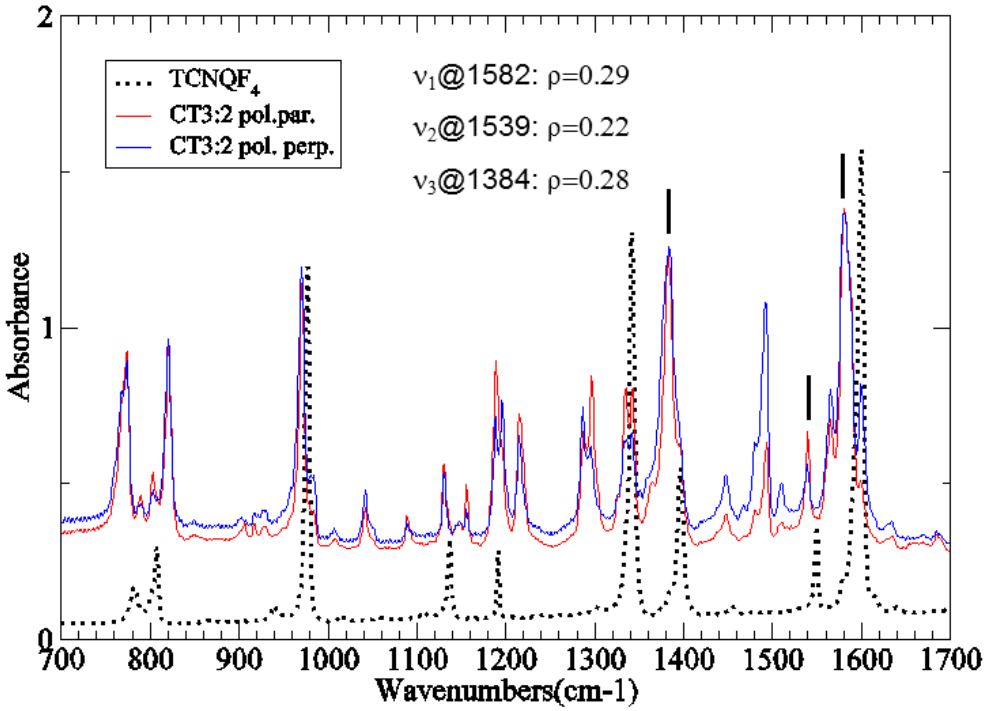

Figure 5.46 Comparison of the IR spectra of the pure single compounds F_4TCNQ (dotted black) and of the different polarizations of the corresponding binary system 3:2.

In conclusion, reliable and reproducible procedures for the growth of single crystals of several charge transfer perylene-F*x*TCNQ have been defined. All the pure charge transfer crystals were grown by physical vapor transport method, with the only exception of the binary system perylene-F_4TCNQ, which was obtained only from solution and contains some toluene inclusions as an impurity. Altogether, five new complexes perylene-F_xTCNQ based were synthesized: perylene-F_1TCNQ, perylene-F_2TCNQ both in 1:1 and 3:2 ratios, perylene-F_4TCNQ 1:1 and the ternary system perylene-F_0TCNQ-F_2TCNQ. We obtained the crystals of the already known systems perylene-F4TCNQ 3:2 and perylene-F_0TCNQ in both stoichiometric ratios 1:1 and 3:1. The structures of the systems perylene-F_0TCNQ 1:1 and 3:1 have been recently re-determined after growing a mix of both stoichiometries by physical vapor [23] and the pure phases by slow evaporation method [24]. In our procedure, the stoichiometry of the crystals could be controlled by setting the temperature conditions. In fact, low (1:1) and high (3:1, 3:2) stoichiometry ratios can be achieved at low and high temperature conditions of the crystal growth, respectively. By comparing the growth conditions and the resulting crystal packings, we suggest that the actual packing, and the stoichiometry with it, is driven by the perylene polymorphism. As already mentioned in paragraph 5.2, perylene exists in two different polymorphic modifications. In the β form, the perylene molecules are arranged in a herringbone fashion, while in the α form display a pair-like structure. It looks as if the β-form

drives the formation of the 1:1 complex, whereas the α-form induces the formation of the 3:1 or 3:2 complexes, with perylene molecules replaced by F_xTCNQ molecules in the unit cell. Considerations on the growth temperature conditions support this hypothesis. Indeed, the 1:1 systems were obtained with a temperature of crystal growth below 140 °C, *i.e.*, in the temperature range where the perylene β-form is stable, while all the systems with higher stoichiometry grow in the temperature range where only the α-form is stable.

Crystal structures, interactions and structural motifs in our complexes have been determined and identified. All the system are characterized by the presence of a face-to-face arrangement of at least of donor molecule with one acceptor, which leads to an extended π overlap. This overlap is driven by the charge transfer interaction of the HOMO of perylene and the LUMO of F_xTCNQ. In Figure 5.47, the contours of the calculated perylene HOMO and F_0TCNQ LUMO orbitals are compared with the molecular overlaps as found in the X-ray analysis of the 1:1 and 3:1 stoichiometries. Molecules are oriented in the crystal in such a way, both in the 1:1 and 3:1 structures, as to maximize the overlap of the HOMO and LUMO orbitals of donor and acceptor.

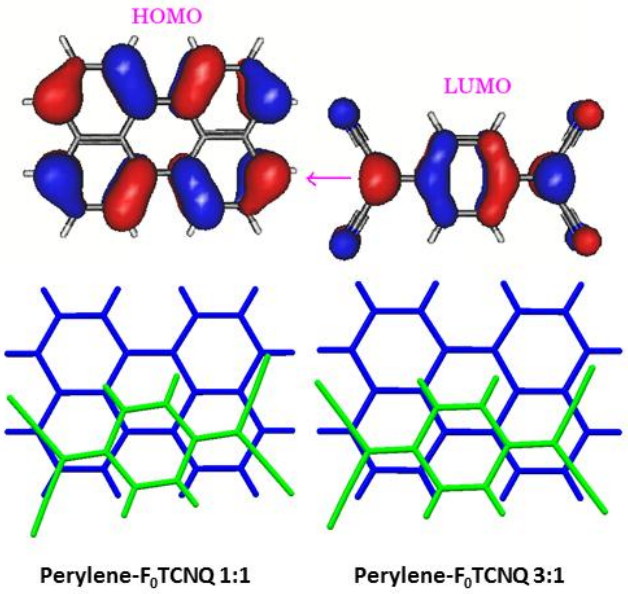

Figure 5.47 HOMO and LUMO orbitals of donor perylene and acceptor F_0TCNQ and molecular overlap observed for both 1:1 and 3:1 stoichiometries.

Importantly, we have assessed the degree of charge transfer in the complexes, estimating its values both from molecular geometries data and by infrared spectroscopy, when possible. A reliable comparison between the two methods cannot really be made, as for F_4TCNQ no molecular geometry is available for the anion. However, The results of the two approaches do not seem to agree to full extent. As an example, the data for the F_0TCNQ system

should be considered: whereas the spectroscopy data clearly indicate that a charge transfer does not take place, the values calculated by all the equations reported and using molecular geometries parameters of the TCNQ system are, albeit small, different from zero. We have the feeling, that should be confirmed by more numerical tests, that the method based on the X-ray determination of the molecular geometries is over-sensitive to slight variations of the input values for the bond lengths. This leads to a large scattering of the calculated values of ρ, depending on the set of atomic coordinates selected.

In general, the addition of F atoms in the structure of the TCNQ derivative should increase significantly the degree of charge transfer. However, ours is a work in progress and we are still performing experiments to complete the description of our systems.

References

[1] A. Pochettino, Acad. Lincei Rend. 15, 355 (1906).

[2] D. D. Eley, Nature 162, 819 (1948).

[3]M. E. Gershenson, V. Podzorov and A. F. Morpurgo, Rev. Mod. Phys. 78, 973 (2006).

[4] E. J. Meijer, D. M. De Leeuw, S. Setayesh, E. Van Veenendaal, B. H. Huisman, P. W. M. Blom, J. C. Hummelen, U. Scherf and T. M. Klapwijk, Nat. Mater. 2, 678 (2003).

[5] Y. Kim, S. Cook, S. M. Tuladhar, S. A. Choulis, J. Nelson, J. R. Durrant, D. D. C. Bradley, M. Giles, I. McCulloch, C. S. Ha and M. Ree, Nat. Mater. 5, 197 (2006).

[6] H. Klauk, M. Halik, U. Zschieschang, G. Schmid, W. Radlik and W. Weber, J. Appl. Phys. 92, 5259 (2002).

[7] Z. N. Bao,Adv. Mater. 12, 227 (2000).

[8] A. F. Hebard, M. J. Rosseinsky, R. C. Haddon, D. W. Murphy, S. H. Glarum, T. T. M. Palstra, A. P. Ramirez and A. R. Kortan, Nature 350, 600 (1991).

[9] M. J. Rosseinsky, A. P. Ramirez, S. H. Glarum, D. W. Murphy, R. C. Haddon, A. F. Hebard, T. T. M. Palstra, A. R. Kortan, S. M. Zahurak and A. V. Makhija, Phys. Rev. Lett. 66, 2830 (1991).

[10] H. Sirringhaus, T. Kawase, R. H. Friend, T. Shimoda, M. Inbasekaran, W. Wu and E. P. Woo, Science 290, 2123 (2000).

[11] P. C. Taylor, J. K. Lee, A. A. Zakhidov, M. Chatzichristidi, H. H. Fong, J. A. DeFranco, G. C. Malliaras and C. K. Ober, Adv. Mater. 21, 2314 (2009).

[12] Y. F. Lim, S. Lee, D. J. Herman, M. T. Lloyd, J. E. Anthony and G. G. Malliaras, Appl. Phys. Lett. 93, 193301 (2008).

[13] H. Rost, J. Ficker, J. S. Alonso, L. Leenders and I. McCulloch, Synth. Met. 145, 83 (2004).

[14] I. Valitova, M. Amato, F. Mahvash, G. Cantele, A. Maffucci, C. Santato, R. Martel and F.Cicoira, Nanoscale 5, 4638 (2013).

[15] F. Cicoira, N. Coppede, S. Iannotta and R. Martel, Appl.Phys. Lett. 98, 183303 (2011).

[16] G. Eda and M. Chhowalla, Adv. Mater. 22, 2392 (2010).

[17] G. Eda, Y. Y. Lin, C. Mattevi, H. Yamaguchi, H. A. Chen, I. S. Chen, C. W. Chen and M. Chhowalla, Adv. Mater. 22, 505 (2010).

[18] Y. Takahashi, T. Hasegawa, Y. Abe, Y. Tokura, K. Nishimura and G. Saito, Appl. Phys. Lett. 86, 063504 (2005).

[19] X. J. Xian, K. Yan, W. Zhou, L. Y. Jiao, Z. Y. Wu and Z. F. Liu, Nanotechnology 20, 5050204 (2009).

[20] M. Kraus, S. Richler, A. Opitz, W. Brutting, S. Haas, T. Hasegawa, A. Hinderhofer and F. Schreiber, J. Appl. Phys. 107, 094503 (2010).

[21] K. Shibata, K. Ishikawa, H. Takezoe, H. Wada and T. Mori, Appl. Phys. Lett. 92, 023305 (2008).

[22] H. Klauk, Chem. Soc. Rev. 39, 2643 (2010).

[23] D. Vermeulen, L. Y. Zhu, K. P. Goetz, Peng Hu, Hui Jiang, C. S. Day, O. D. Jurchescu, V. Coropceanu, C. Kloc and L. E. McNeil., J.Phys.Chem.C 118, 24688 (2014).

[24] P. Hu, L. Ma, K. J. Tan, H. Jiang, F. Wei, C. Yu, K. P. Goetz, O. D. Jurchescu, L. E. McNeil, G. G. Gurzadyan, and C. Kloc., Crystal Growth & Design 14, 12, 6376 (2014).

[25] A. Mänz , T. Breuer , and G. Witte., Crystal Growth & Design 15, 1, 395 (2015).

[26] W. Zhu, Y. Yi, Y. Zhen and W. Hu, Small (early view) DOI: 10.1002/smll.201402330

[27]K. P. Goetz, D. Vermeulen, M. E. Payne, C. Kloc, L. E. McNeil and O. D. Jurchescu. J. Mater Chem. C. 2, 3065 (2014).

[28] M. Pope and C. E. Swenberg, Electronic processes in organic crystals and polymers, Oxford University Press, New York, 2nd edn, 1999.

[29] H. Alves, A. S. Molinari, H. X. Xie and A. F. Morpurgo, Nat. Mater. 7, 574 (2008).

[30] T. Mathis, K. Mattenberger, P. Moll and B. Batlogg, Appl. Phys. Lett. 101, 023302 (2012).

[31]J. Tsutsumi, T. Yamada, H. Matsui, S. Haas and T. Hasegawa, Phys. Rev. Lett. 105, 226601 (2010).

[32] J. Tsutsumi, H. Matsui, T. Yamada, R. Kumai and T. Hasegawa, J. Phys. Chem. C 116, 23957 (2012).

[33] T. Mori and T. Kawamoto, Annu. Rep. Prog. Chem., Sect. C: Phys. Chem. 103, 134 (2007).

[34] F. H. Herbstein, Crystalline molecular complexes and compounds: structures and principles, Oxford University Press, Oxford, New York, 2005.

[35] K. Bechgaard, T. J. Kistenmacher, A. N. Bloch and D. O. Cowan, Acta Crystallogr., Sect. B: Struct. Crystallogr. Cryst. Chem. 33, 417 (1977).

[36] A. Brillante and M. R. Philpott., J. Chem. Phys. 72, 4019 (1980).

[37] I. J. Tickle and C. K. Prout, J. Chem. Soc., Perkin Trans. 2, 720 (1973).

[38] L. Y. Zhu, Y. P. Yi, Y. Li, E. G. Kim, V. Coropceanu and J. L. Bredas, J. Am. Chem. Soc. 134, 2340 (2012).

[39] G.T. Wright., Solid-State Electronics 2, 2–3, 165 (1961).

[40] K. S. Haber, A. C. Albrecht J. Phys. Chem. 88, 24, 6025 (1984).

[41] G. Horowitz., Adv. Mater. 10, 5, 365 (1998).

[42] H. Johanson, Int. J. Quantum Chem. 9, 459 (1975).

[43] S. Flandrois and D. Chasseau., Acta Cryst. B33, 2744 (1977).

[44] T. C. Umland, S. Allie, T. Kuhlmann and P. Coppens., J. Phys. Chem., 92, 6456 (1988).

[45] P. Coppens, and T. N. Guru Row., Ann. N.Y. Acad. Sci. 313, 244 (1978).

[46] T. J.Kistenmacher, T. J. Emge, A. N. Bloch, and D. O. Cowan., Acta Cryst. B38, 1193 (1982).

[47] K. H. Frank, P. Yannoulis, R. Dudde, and E. E. Koch, J Chem Phys 89, 7569 (1988).

[48] N. Sato, K. Seki and H. Inokuchi J. Chem. Soc., Faraday Trans. 2, 77, 1621 (1981).

[49] K. Kanai, K. Akaike, K. Koyasu, K. Sakai, T. Nishi, Y. Kamizuru, T. Nishi, Y. Ouchi, K. Seki, Applied Physics A. 95, 309 (2009).

[50] W. Gao, A. Kahn Organic Electronics. 3, 2, 53 (2002).

[51] D. M. Donaldson, J. M. Robertson, J. G. White, Proc. R. Soc., London, A220, 311, (1953).

[52] J. Tanaka, Bull. Chem. Soc. Jpn. 36, 1237, (1963).

[53] M. Botoshansky, F. H. Herbstein, M. Kapon, Helv. Chim. Acta 86, 1113, (2003).

[54]R. E. Long, R. A. Sparks and K. N. Trueblood., Acta Cryst. 8, 932 (1965).

[55] F. M. Wiygul, T. J. Emge, J. P. Ferraris and T. J. Kistenmacherab., Mol. Cryst. liq. Cryst. 71, 3-4, 303, (1981).

[56] F. M. Wiygul, J. P. Ferraris, T. J. Emge and T. J. Kistenmacher., Mol. Cryst. liq. Cryst. 78, 1, 279 (1981).

[57] T. J. Emge, M. Maxfeld, D. O. Cowan and T. J. Kistenmacher, Mol. Cryst. liq. Cryst. 65, 161, (1981).

[58] I. J. Tickle, C. K. Prout, J. Chem. Soc., Perkin Trans. 2, 720 (1973).

[59] D. Vermeulen, L. Y. Zhu, K. P. Goetz, Peng Hu, Hui Jiang, C. S. Day, O. D. Jurchescu, V. Coropceanu, C. Kloc, and L. E. McNeil, J. Phys. Chem. C 118, 24688 (2014).

[60] A. W. Hanson, Acta Crystallogr., Sect. B: Struct. Crystallogr. Cryst. Chem. 34, 2339 (1978).

[61] G. Saito, J. P. Ferraris, Bull Chem Soc. Jpn 53, 2141 (1980).

[62] M. D. Dobrowolski, G. Garbarino, M. Mezouar, A. Ciesielski, M K. Cyranski, Cryst Eng Comm 16, 415 (2014).

[63] J. Lieffrig, O. Jeannin, A. Frackowiak, I. Olejniczak, R. Swietlik, S. Dahaoui, E. Aubert, E. Espinosa, P. Auban-Senzier and M. Fourmiguè, Chem. Eur. J. 19, 14804 (2013).

[64] T. Murata, K. Nakamura, H. Yamochi, G. Saito, Synth. Met. 159, 2375 (2009).

[65] T. J. Emge, F. M. Wiygul, J. P. Ferraris, T. J. Kistenmacher, Mol. Cryst. Liq. Cryst. 78, 295 (1981).

[66] M. Meneghetti, C. Pecile, J. chem. Phys 84, 8, 4149 (1986).

[67] A. Girlando, C. Pecile, Spectrochim. Acta A 29, 1859 (1973).

[68] R. Bozio, I Zanon, A. Girlando, C. Pecile, J. Chem. Soc. Faraday Trans. 2, 74, 235 (1978).

[69] F. Ambrosino, S. Califano, Spectrochimica Acta 21, 1401 (1965).

[70] A. Girlando, A. Morelli and C. Pecile, Chem. Phys. Lett. 22, 553 (1973).

[71] L. R. Melby , R. J. Harder , W. R. Hertler , W. Mahler , R. E. Benson , W. E. Mochel, J. Am. Chem. Soc. 84, 17, 3374 (1962).

[72] K. D. Truong and A. D. Bandrauk, Chemical Physics Letters 44, 2, 232 (1976).

[73] A. D. Bandrauk, K. D. Truong, C. Carlone, Canadian Journal of Chemistry 60, 589 (1982).

[74] K. D. Truong, A. D. Bandrauk, Chem Phys Letters 44, 232 (1976).

APPENDIX

6. Synthesis and characterization of platinum complexes with a perylene derivative ligand bi-functionalized for OLEDs applications

6.1 Introduction

In the past few decades, the search for highly emitting materials based on metal complexes not employing the relatively scarce iridium has attracted a great deal of attention, because of their potential applications in energy-saving organic light-emitting diodes (OLEDs) for full-color displays and solid state lighting [1].

Emitters based on transition metals such as rhenium, [2,3] osmium, [4,5] platinum [6,7] or gold [8,9] and on cheaper and less toxic ones such as copper [10-12] and zinc are suitable for this purpose due to the strong spin-orbit coupling exerted by the heavy metal. This effect produces both singlet and triplet electrogenerated excitons in devices with these compounds, leading to a potentially achievable 100% internal quantum efficiency. In the last years Pt(II) complexes have been considered as triplet emitters. The platinum complexes, having a d^8 electronic configuration exhibit a square planar coordination geometry, which induces the formation of aggregates in the ground state or excimers in the excited state, due to the Pt-Pt and π-π stacking interactions, with various effects on the photoluminescence[13-15].

This characteristic can be an advantage for the realization of white organic light-emitting diodes (WOLEDs) but it is also represents a drawback for applications where color purity is needed [16,17]. Terpyridine ligands [18,19] and their N^C^N and N^N^C analogues have been coordinated to Pt(II), [20-23] yielding neutral or singly or doubly charged complexes, some of them showing bright luminescence. These derivatives can form supramolecular structures like nanowires, nanosheets and polymeric mesophases, all with different interesting optical properties.

To control the processes of aggregation, which leads to undesired broadening of spectra, and to increase the solubility of these complexes, we have designed and synthesized a new class of neutral Pt(II) complexes bearing tridentate dianionic 2,6-bis(1H-1,2,4-triazol-5-yl)pyridine chelates [24-26]. Tuning of color, aggregation, and processability are key parameters for applications in electroluminescent devices.

Indeed, 1,2,4-triazoles have been easily functionalized at the C3 position. The substitution pattern of the triazole rings was varied by the alternative introduction of aliphatic adamantyl and PEG (Poly ethylen glycol) groups. The triazole rings bind the Pt(II) ion as anionic ligands by double N-deprotonation and in order to obtain neutral complexes, bifunctionalised pyridine perylene diimide was used as ancillar legant.

6.2 Synthesis and characterization of ancillary ligand: N,N'-bis[4-(2-aminoethyl)pyridine]perylene 3,4:9,10-bis(dicarboximide).

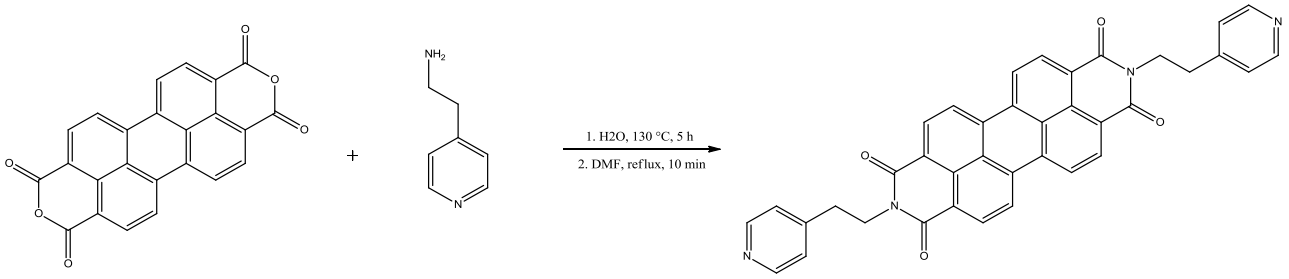

Figure 6.1 Synthetic procedure for ligand N,N'-bis[4-(2-aminoethyl)pyridine]perylene 3,4:9,10-bis(dicarboximide)

The ligand N,N'-bis[4-(2-aminoethyl)pyridine]perylene 3,4:9,10-bis(dicarboximide) was prepared by the reaction of perylene tetracarboxylic dianhydride (500 mg, 1.27 mmol) with aminoethylpyridine (388 mg, 3.17 mmol) in water (5 ml) at 130 °C for 6 h. The product was filtered and the red cake was then refluxed for 20 min in N,N'-dimethylformamide (figure 6.1). After cooling the product was filtered and dried in vacuum overnight. 518,8 mg (yield 70 %) of a red solid were obtained.

The NMR spectrum of the red solid (Figure 6.2) was recorded and compared with the NMR spectrum of the 4-(2-aminoethyl)pyridine (Figure 6.3) to check nature of the product obtained and its purity. The chemical shift of both reagent and product are reported below.

1H NMR (400 MHz, TFA-d, δ): 8.90, 8.88 (d, 4H, H py), 8.84, 8.82 (d, 4H, H py), 8.70, 8.68 (d, 4H, H peril.), 8.17, 8.15 (d, 4H, H peryl.), 4.75 (m, 4H, alif.), 3.55 (m, 4H, alif.).

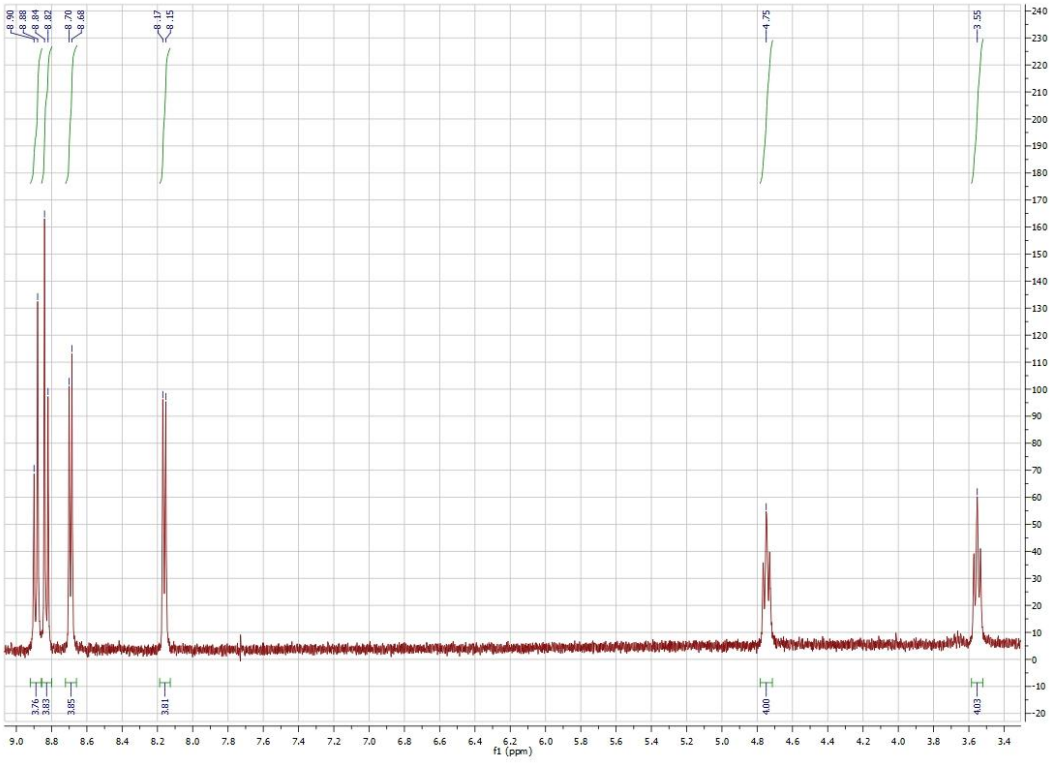

Figure 6.2 N,N'-bis[4-(2-aminoethyl)pyridine]perylene 3,4:9,10-bis(dicarboximide) NMR spectrum in trifluoro aceti acid (TFA)

1H NMR (400 MHz, $CDCl_3$, δ): 8.28, 8.27 (m, 2H, H py), 6.91 (d, 2H, H py), 2.76 (m, 2H, H alif.), 2.51 (m, 2H, H alif.), 1.06 (s, 2H, alif.).

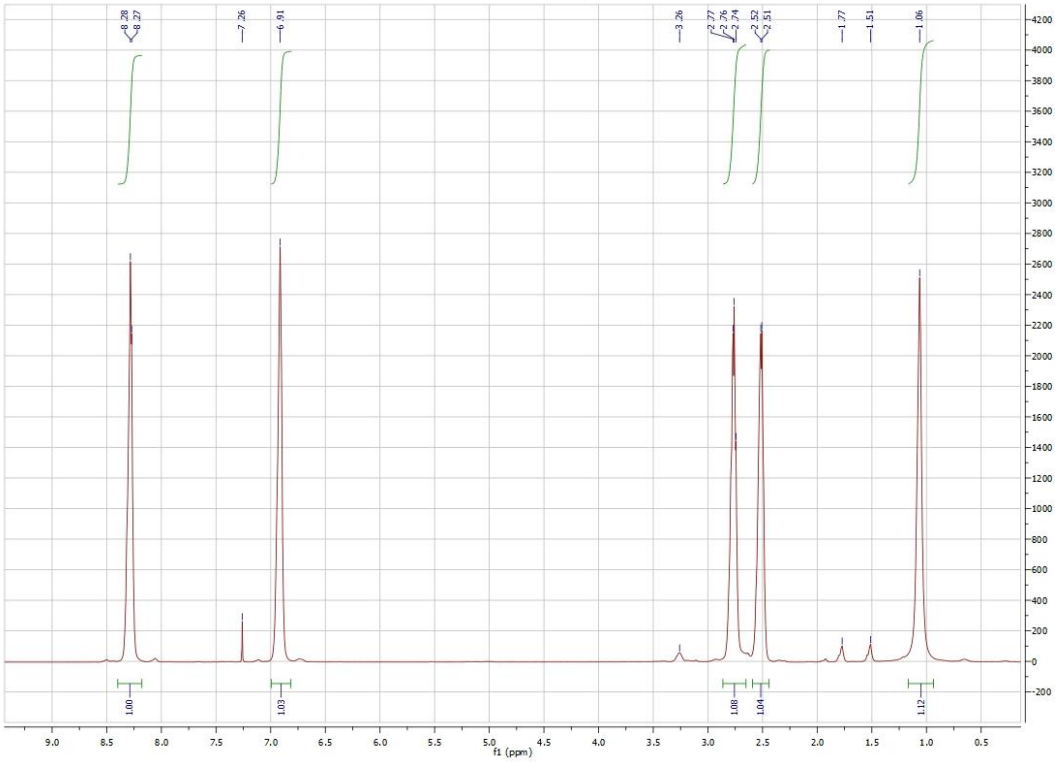

Figure 6.3 4-(2-aminoethyl) pyridine NMR spectrum of pure reagent in $CDCl_3$

The IR spectra of reagent perylene tetracarboxylic dianhydride and product N,N'-bis[4-(2-aminoethyl)pyridine]perylene 3,4:9,10-bis(dicarboximide) were recorded (Figure 6.4) in the solid state by an ATR instrument. The characteristic vibration frequencies are reported in Table 6.1.

In the perylene tetracarboxylic dianhydride spectrum, the typical bands the for symmetric and antisymmetric stretchings of C=O at 1772 and 1730 cm^{-1}, respectively, can be detected, together with the bands of the single C-O bond stretching at 1301, 1122 and 1016 cm^{-1} for the dianhydride group. In the IR spectrum of the product, the symmetric and antisymmetric stretching bands of the carbonyl group are still present, but shifted at low frequencies due to the presence of the nitrogen instead of the carbon atom, thus the formation of the diimide bond is confirmed. To confirm that the reaction has taken place, there are also the bands of the vibrations of the aromatic C-N at 1357 cm^{-1} and of the aliphatic C-N at 1172 cm^{-1}. No reactant impurity is present, as bands of the C-O single bond vibration cannot be detected.

Table 6.1 Functional group vibration frequencies for perylene tetracarboxylic dianhydride and N,N'-bis[4-(2-aminoethyl)pyridine]perylene 3,4:9,10-bis(dicarboximide)

perylene tetracarboxylic dianhydride		**N,N'-bis[4-(2-aminoethyl)pyridine]perylene 3,4:9,10-bis(dicarboximide)**	
C=O stretching	1772 cm^{-1}	C=O stretching	1693 cm^{-1}
	1730 cm^{-1}		1652 cm^{-1}
C-C stretching	1301 cm^{-1}	C-C stretching	1595 cm^{-1}
C-O stretching	1301 cm^{-1}	C-N aromatic	1357 cm^{-1}
	1122 cm^{-1}	C-N aliphatic	1172 cm^{-1}
	1016 cm^{-1}		

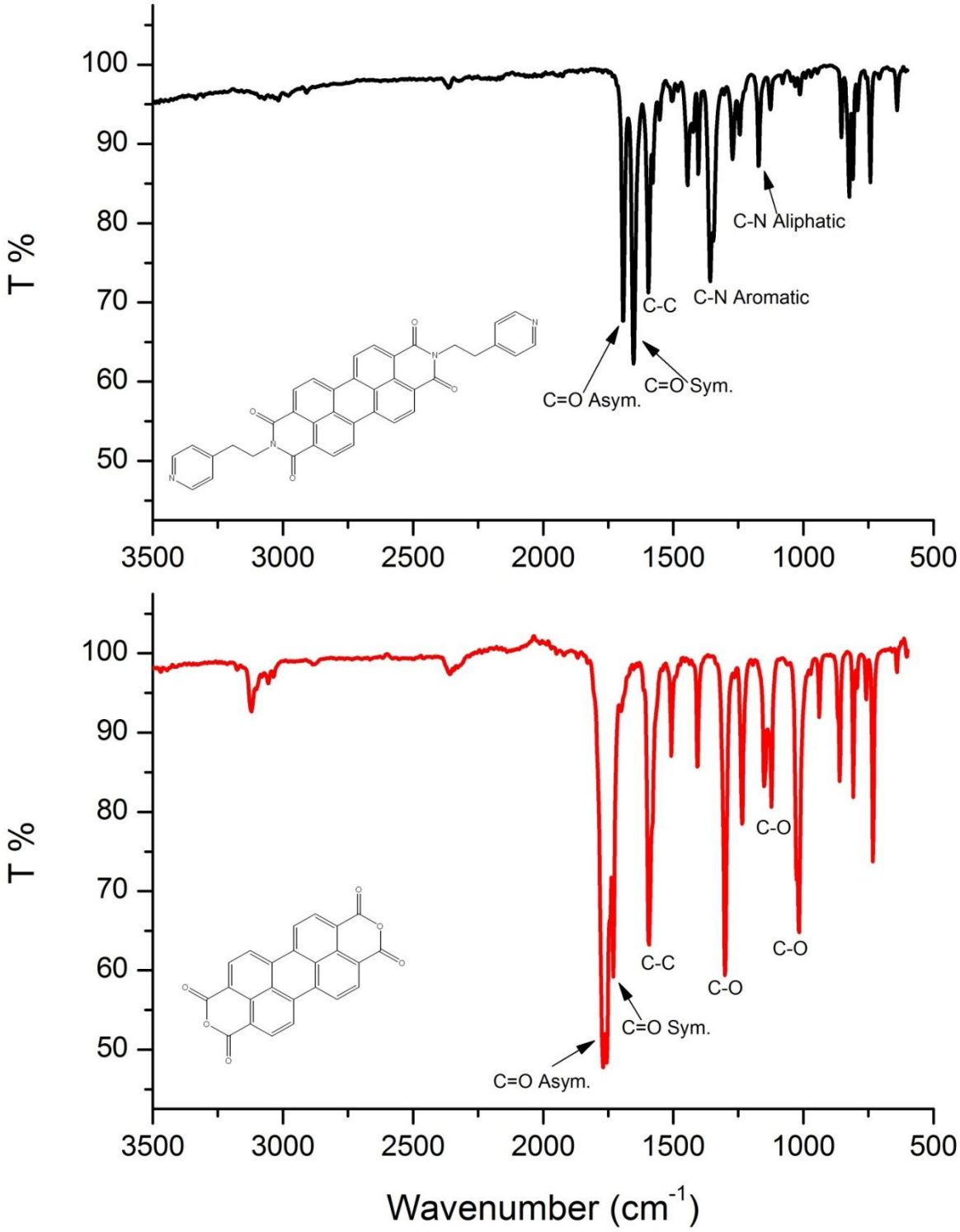

Figure 6.4 Comparison of the FT-IR spectra of perylene tetracarboxylic dianhydride(bottom) and N,N'-bis[4-(2-aminoethyl)pyridine]perylene 3,4:9,10-bis(dicarboximide) (top).

The results of the mass spectrum (Figure 6.5), and the mass value so obtained are in agreement with what expected for the desired product. HRMS (ESI+, CH_3Cl, m/z): [M+H]+ calcd for $C_{38}H_{24}N_4O_4$, 601.18; found, 601.19.

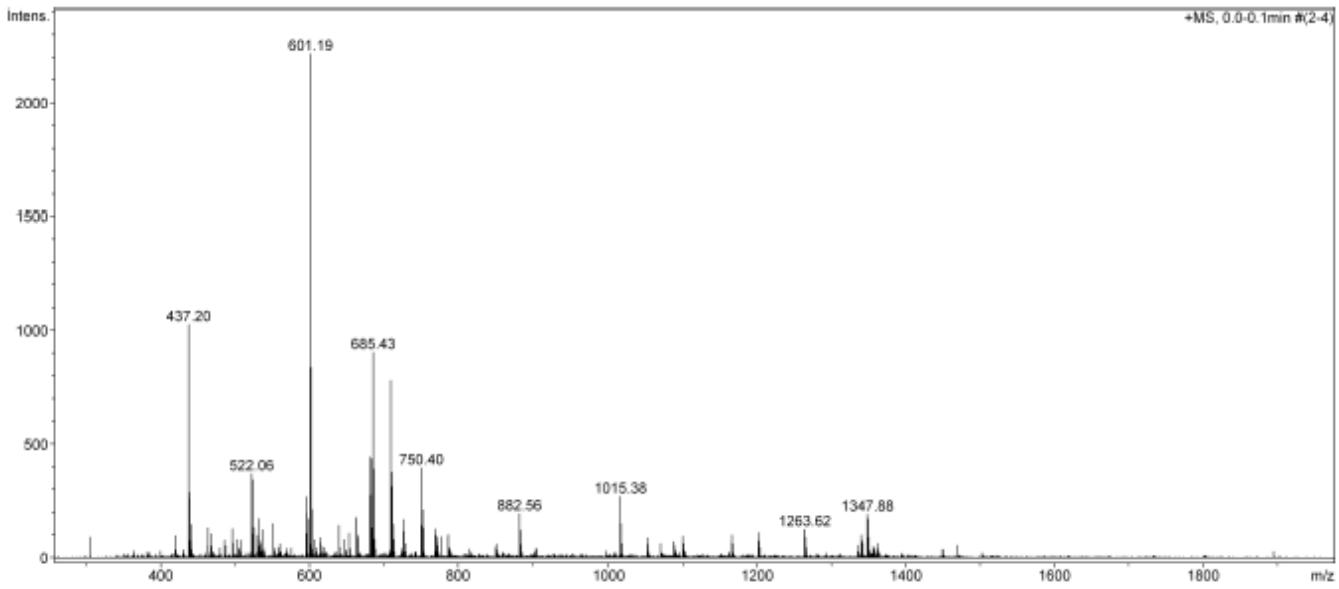

Figure 6.5 ESI-MS spectrum of N,N'-bis[4-(2-aminoethyl)pyridine]perylene 3,4:9,10-bis(dicarboximide).

6.3 Synthesis of the Platinum Complex Pt(trzpyttz)N,N'-bis[4-(2-aminoethyl)pyridine]perylene 3,4:9,10-bis(dicarboximide)

6.3.1 Synthesis of the tridentate ligand 2-(3-[Adamantan-1-yl]-1H-1,2,4-triazol-5-yl)-6-(1H-tetrazol-5-yl)pyridine (H_2trzpyttz)

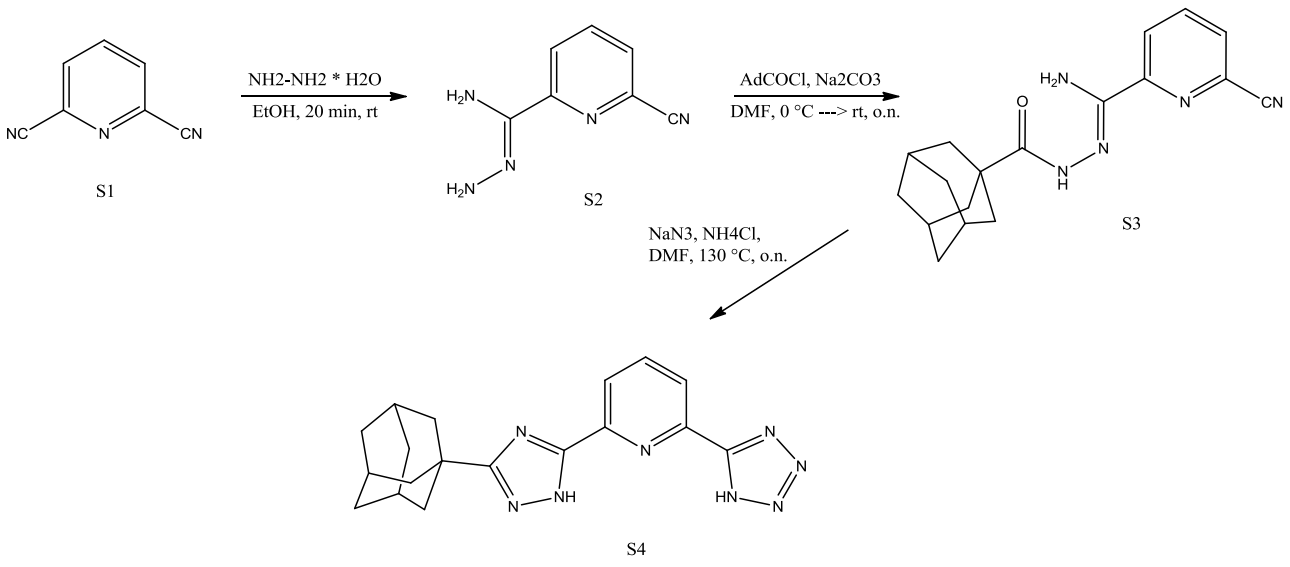

Figure 6.6 Synthetic procedure for ligand H_2trzpyttz

6-Cyanopicolinohydrazonamide (S2): To a solution of 2,6-pyridinedicarbonitrile (S1) (10 g, 77 mmol) in ethanol (500 mL), hydrazine monohydrate (76 mL, 1.55 mmol) was added. The reaction mixture was stirred at room temperature for 15–20 minutes, yielding a pale yellow

precipitate in a yellow solution. The precipitate was quickly filtered off, washed with cold ethanol and then dried, obtaining 6.95 g (yield 56%) of the desired compound.

(Adamantane-1-carbonyl)-6-cyanopicolinohydrazonamide (S3): Under inert atmosphere, a mixture of 6-cyanopicolinohydrazonamide (S2) (5 g, 31 mmol) and sodium carbonate (4.99 g, 47 mmol) in dry DMF (150 mL) was placed in a two-neck round-bottom flask, and the suspension so obtained was cooled down to 0 °C. A solution of 1-adamantanecarbonyl chloride (6.16 mg, 31 mmol) in dry DMF (50 mL) was slowly added to the cooled suspension under strong stirring. The pale yellow suspension cleared for some time to a darker yellow solution, (except for the presence of sodium carbonate). The reaction mixture was allowed to warm up to room temperature, and the precipitation of a yellow solid occurred overnight. Subsequently, the reaction volume was doubled by the addition of water, yielding more precipitate. The suspension was stirred strongly for another 1.5 h and then filtered and washed with water thoroughly. After drying under vacuum, 9.52 g (yield 95%) of a pale yellow solid were obtained, which was used without further purification for the following step.

2-(3-[Adamantan-1-yl]-1H-1,2,4-triazol-5-yl)-6-(1H-tetrazol-5-yl)pyridine (H2trzpyttz): A mixture of (adamantane-1-carbonyl)-6-cyanopicolinohydrazonamide (S3) (1 g, 3.09 mmol), sodium azide (333 mg, 5.12 mmol) and NH_4Cl (265 mg, 4.99 mmol) in dry DMF (80 mL) was placed in a two-neck round-bottom flask. The mixture was then heated to 130 °C for 22 hours. After cooling down to room temperature, the solvent was removed under vacuum and the solid residue was purified by refluxing with ethanol. The mixture was cooled to room temperature and, after filtration, dried under vacuum. 502 mg of the product were obtained (yield 46.48 %) as a white solid. The global reaction scheme is shown in Figure 6.6.

The NMR spectrum of the white solid (Figure 6.7) was recorded to identify the product obtained and check its purity. The chemical shift of both reagent and product are reported below.

1H NMR (400 MHz, DMSO-d6, δ): 8.25.8.11 (m, 3H, H-3, H py), 2.12.1.99 (m, 9H, Ad), 1.77 (s, 6H, Ad).

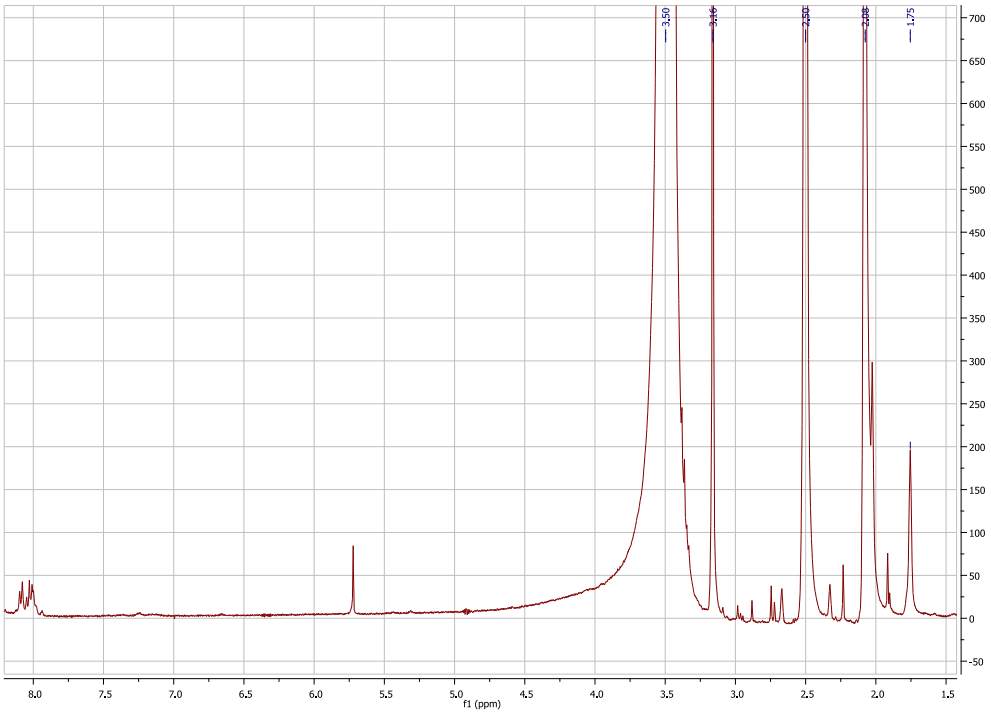

figure 6.7 ^{1}H NMR spectrum of (H2trzpyttz) in DMSO-d^{6}

The IR spectrum of the tridentate ligand H2trzpyttz (Figure 6.8) shows the strong characteristic bands of the adamantane C-H in the range 2800-3000 cm^{-1}, and the less intense but typical bands of the azide group at 2300 cm^{-1}. The presence of pyridine rings can be detected by the C-H and the C=C aromatic stretching bands at 3300 cm^{-1} and around 1500 cm^{-1}, respectively.

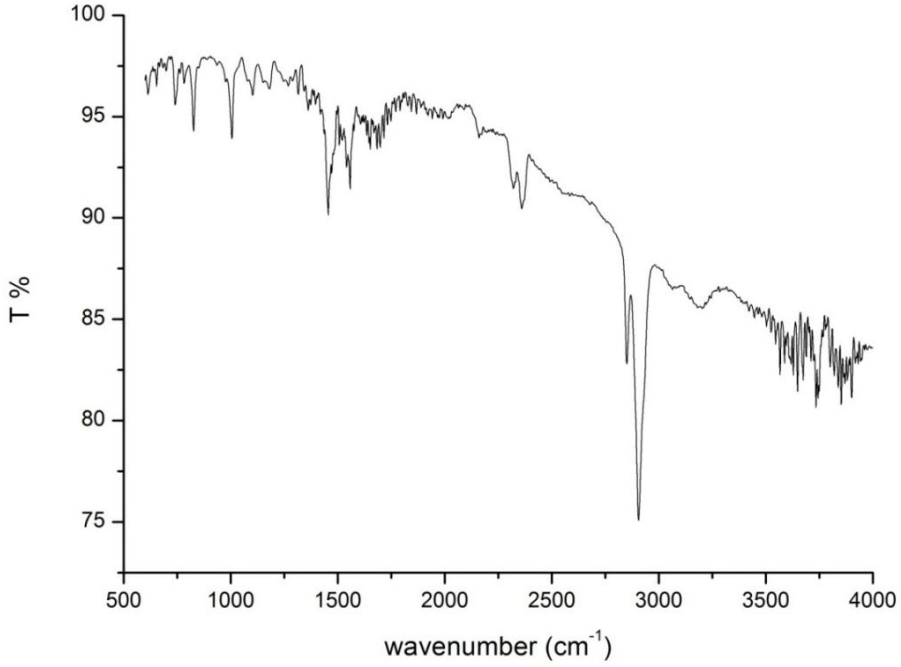

Figure 6.8 FT-IR spectrum of H_2trzpyttz

The mass spectrum (Figure 6.9) were recorded and the result and the calculated value are in agreement with the experimental one in the limit of the bar error. HRMS (ESI+, CH_3OH, m/z): [M+H]+ calcd for $C_{18}H_{20}N_8$, 349.1889; found, 348.93.

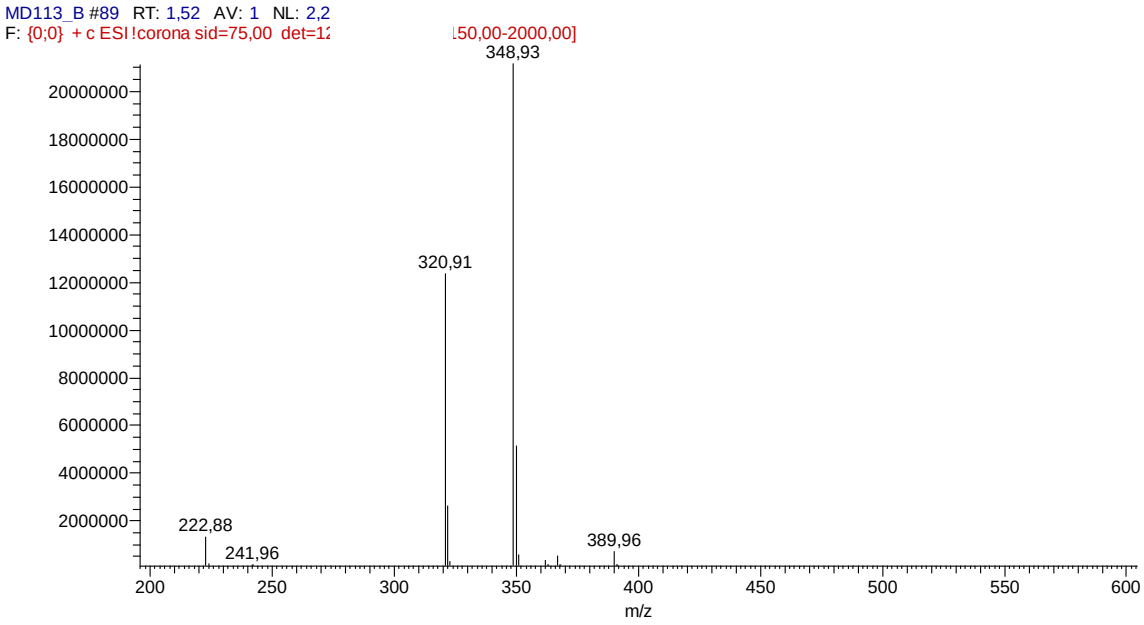

Figure 6.9 ESI-MS of H_2trzpyttz in CH_3OH

6.3.2 Synthesis complex Pt(trzpyttz)N,N'-bis[4-(2-aminoethyl)pyridine]perylene 3,4:9,10-bis(dicarboximide)

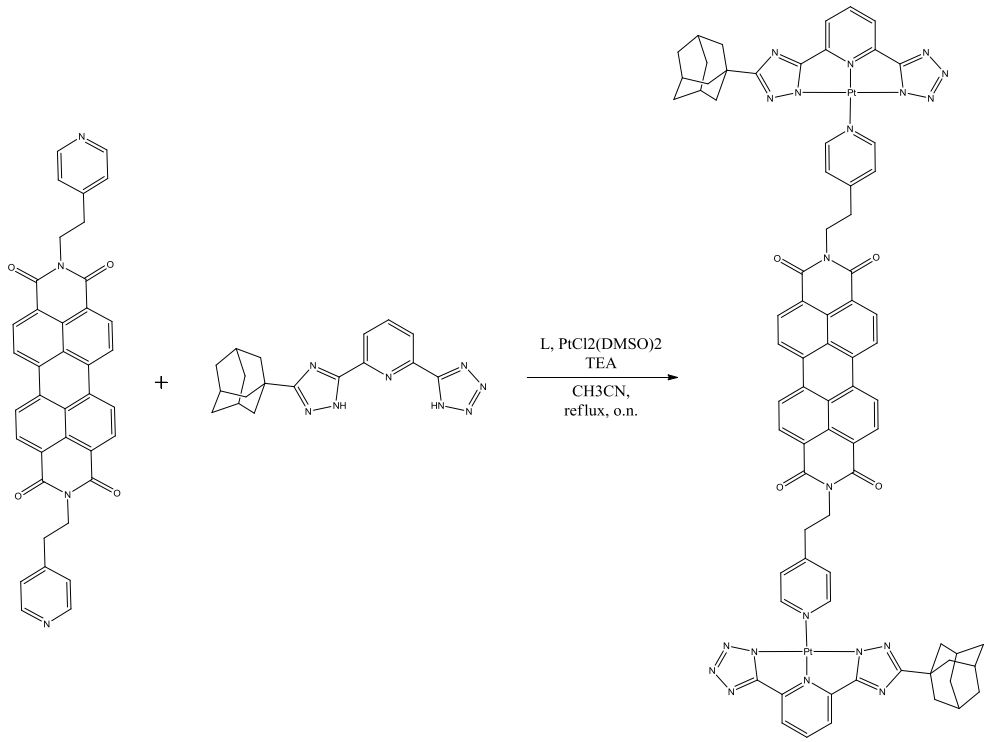

Figure 6.10 1 Synthetic procedure for complex Pt(trzpyttz)N,N'-bis[4-(2-aminoethyl)pyridine]perylene 3,4:9,10-bis(dicarboximide)

To a solution of $PtCl_2(DMSO)_2$ (2 equiv., 55.5 mg , 0.131 mmol) in CH3CN (20 mL) the tridentate ligand H_2trzpyttz (2 equiv., 51.2 mg, 0.133 mmol) and the base N,N-Diisopropylethylamine (2 equiv., 50 µl, 287 mmol) were added. The reaction mixture was stirred for 10 minutes to obtain a yellow solution to which the ancillary ligand L was added (1 equiv., 38.5 mg, 0.064 mmol). The precipitation of the product started just after the addition of the ancillary ligant. The mixture was then heated to 85°C under nitrogen for 24 hours, cooled to room temperature and stirred with 10 ml of water for 30 minutes. The mixture was finally filtered and washed first with 20 ml of methanol and then with diethyl ether. 80.1 mg of red solid (yield 73.48 %) were obtained. The reaction scheme is shown in Figure 6.10.

In Figure 6.11, the IR spectra of both reagents N,N'-bis[4-(2-aminoethyl)pyridine]perylene 3,4:9,10-bis(dicarboximide) and H_2trzpyttz are compared with the IR spectrum of the platinum complex Pt(trzpyttz)N,N'-bis[4-(2-aminoethyl)pyridine]perylene 3,4:9,10-bis(dicarboximide)

In the IR spectrum of the platinum complex, the symmetric and antisymmetric stretching bands of the carbonyl group of the ancillary legant are present at 1693 and 1652 cm^{-1}, respectively. The presence of the tridentate ligand H2trzpyttz is confirmed by the characteristic bands of the adamantane C-H in the range 2800-3000 cm^{-1} and by the typical bands of the azide group at 2300 cm^{-1}.

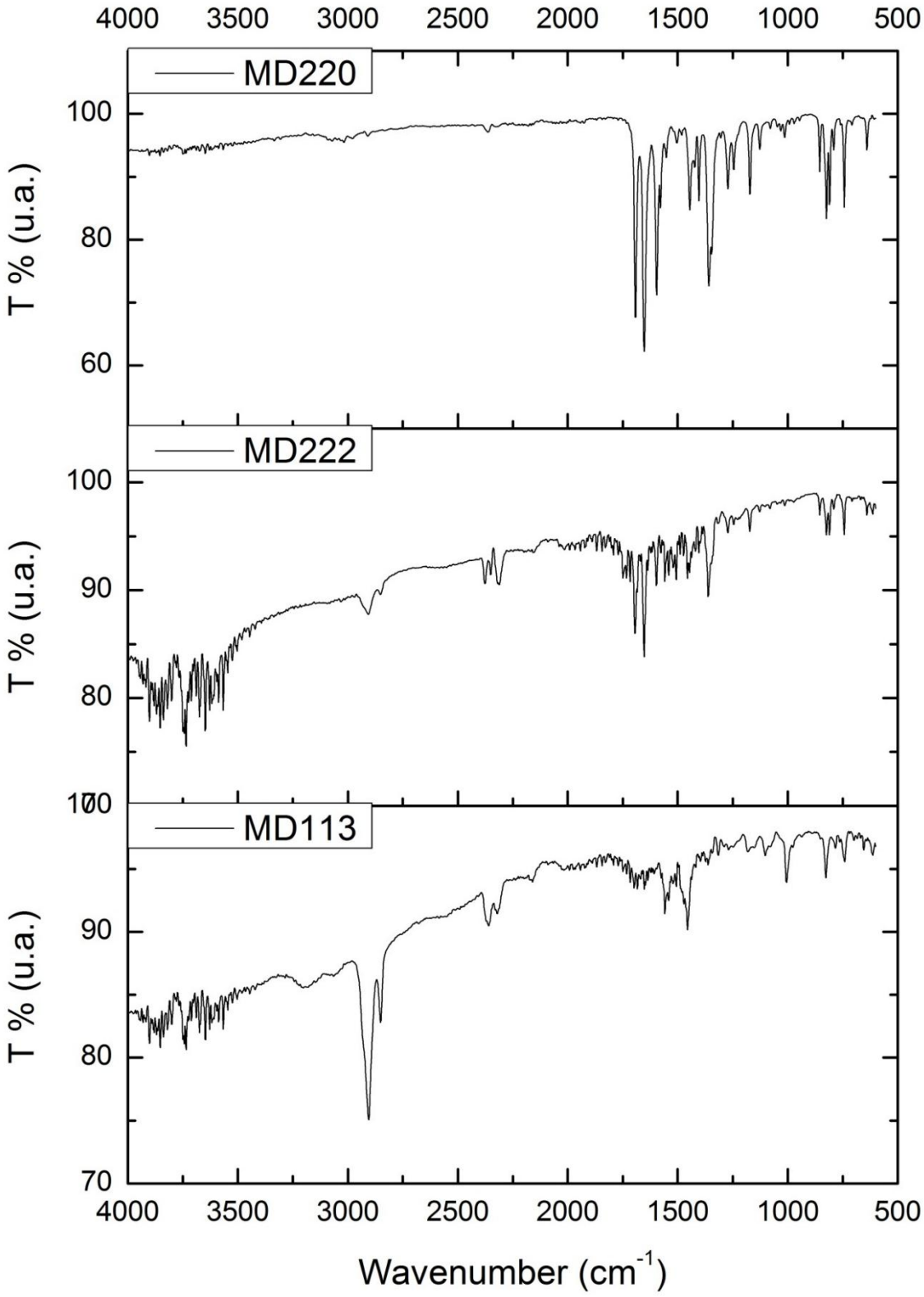

Figure 6.11 Comparison of the FT-IR spectra of (bottom) tridentate H_2trzpyttz (MD113), (centre) complex Pt(trzpyttz)N,N'-bis[4-(2-aminoethyl)pyridine]perylene 3,4:9,10-bis(dicarboximide) (MD222) and (top) ligand N,N'-bis[4-(2-aminoethyl)pyridine]perylene 3,4:9,10-bis(dicarboximide) (MD220).

The NMR spectrum of the red solid Pt(trzpyttz)N,N'-bis[4-(2-aminoethyl)pyridine]perylene 3,4:9,10-bis(dicarboximide) is reported in Figure 6.12. The chemical shift and the integrals are reported below.

1H NMR (400 MHz, TFA, δ): 8.90, 8.88 (d, 4H, H py), 8.84, 8.82 (d, 4H, H py), 8.55 (m, 1H, H lig.), 8.46 (m, 1H, H lig.), 8.39 (m, 1H, H lig.), 8.69 (m, 4H, H peril.), 8.17, 8.16 (d, 4H, H peryl.), 4.75 (m, 4H, alif.), 3.55 (m, 4H, alif.), 2.22 (m, 7H, Ad), 1.90 (s, 9H, Ad).

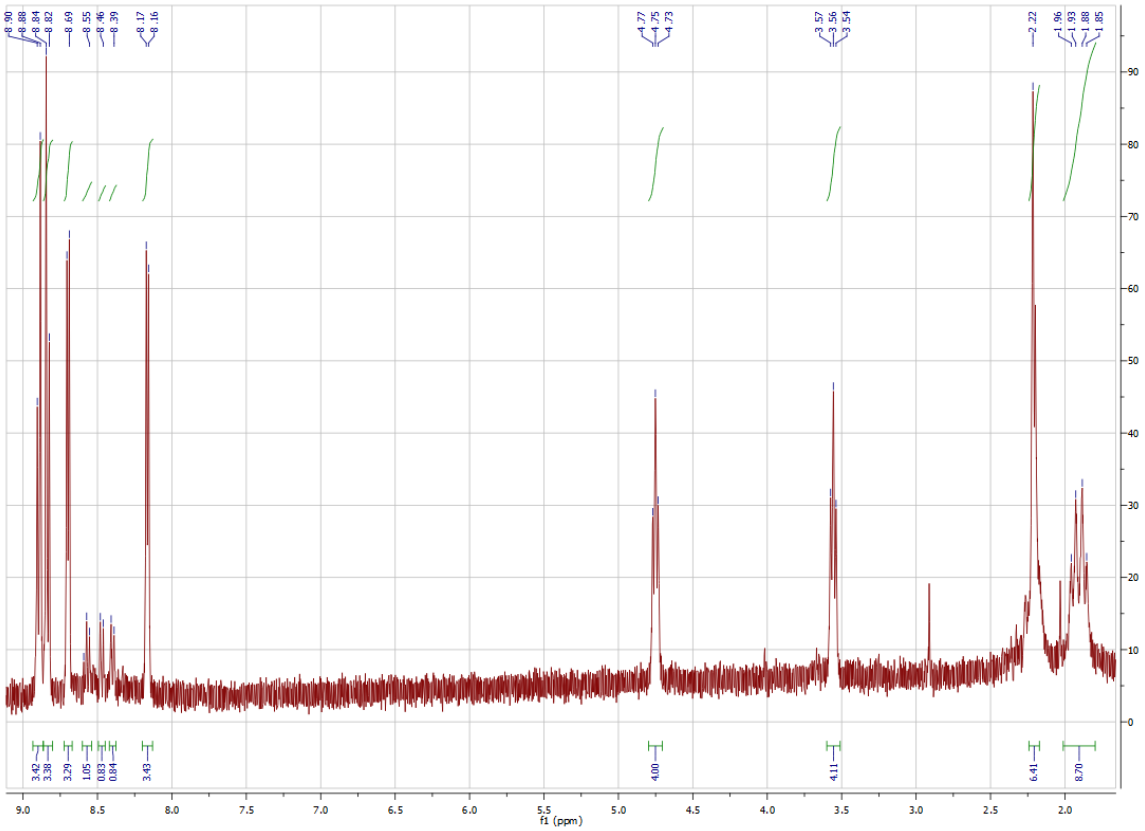

Figure 6.12 NMR spectrum of complex Pt(trzpyttz)N,N'-bis[4-(2-aminoethyl)pyridine]perylene 3,4:9,10-bis(dicarboximide) in TFA

Elemental analysys CHN:

	% N	% C	% H
Experimental	**13.84**	**55.15**	**4.13**
Theoretical	**16.64**	**52.79**	**3.59**

6.4 Complex Pt(2,6-Bis(3-((3R,5R,7R)-adamantan-1-yl)-1H-1,2,4-triazol-5-yl)-pyridine)N,N'-bis[4-(2-aminoethyl)pyridine]perylene 3,4:9,10-bis(dicarboximide)

6.4.1Synthesis tridentate 2,6-Bis(3-((3R,5R,7R)-adamantan-1-yl)-1H-1,2,4-triazol-5-yl)-pyridine

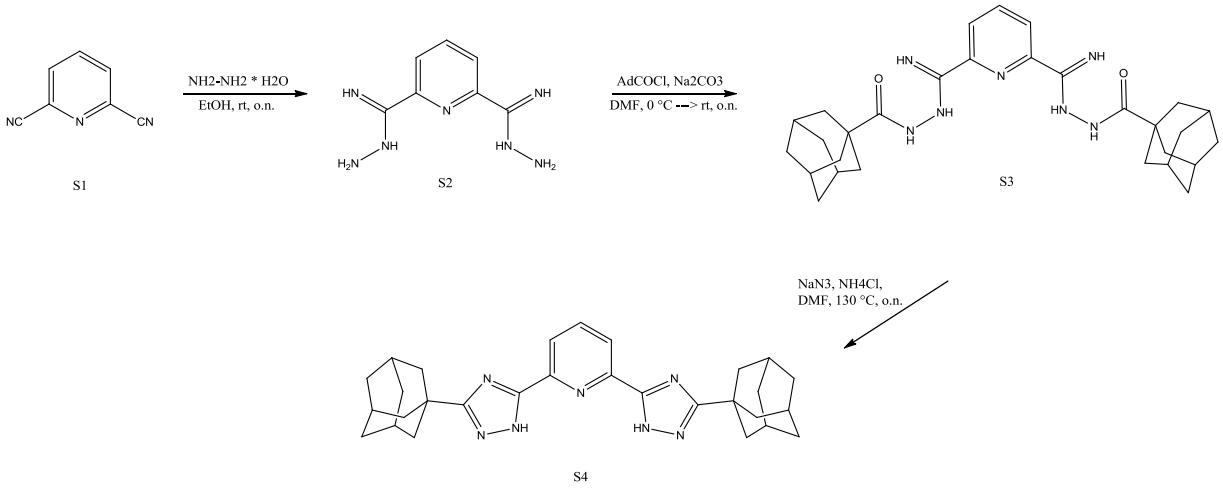

Figure 6.13 Synthetic procedure for ligand 2,6-Bis(3-((3R,5R,7R)-adamantan-1-yl)-1H-1,2,4-triazol-5-yl)-pyridine.

Pyridine-2,6-bis(carboximidhydrazide) (S2).

To a solution of 2,6-pyridinedicarbonitrile (20 g, 0.155 mol) in ethanol (1 L), hydrazine monohydrate was added (151 mL, 3.1 mol). The reaction mixture was stirred at room temperature (rt) overnight, yielding a pale yellow precipitate in a yellow solution. The precipitate was filtered off, washed with cold ethanol, and dried (12 g, 40%).

N′,N‴-(Pyridine-2,6-diylbis(iminomethylene))bis(adamantane-1-carbohydrazide) (S3).

A flame-dried, nitrogen-purged Schlenk tube was loaded with 1 (5 g, 26 mmol) and sodium carbonate (6.1 g, 58 mmol), evacuated, gently heated, and refilled with nitrogen after being cooled to rt. Next, dry N,N-dimethylformamide (N,N-DMF; 160 mL) was added, and the suspension was cooled to 0 °C. In a separately prepared Schlenk tube, a 1-adamantanecarbonyl chloride (10.3 g, 52 mmol) solution in dry N,N-DMF (60 mL) was prepared using the same procedure described above. This solution was then slowly added to the cooled suspension under strong stirring. The pale yellow suspension cleared for some time to a darker yellow solution, except for the presence of the sodium carbonate, followed by the precipitation of a yellow solid overnight, while the reaction mixture was allowed to warm to rt. Finally the reaction volume was doubled by water addition, yielding more precipitate. This

suspension was stirred strongly for another 1.5 h and then filtered and washed with water thoroughly. The yellow solid was dried under vacuum and used as such for the next step (11 g, 84%).

2,6-Bis(3-((3R,5R,7R)-adamantan-1-yl)-1H-1,2,4-triazol-5-yl)-pyridine (S4).

Product 2 was suspended in ethylene glycol in a 1 mL/100 mg ratio in an open round-bottom flask. The suspension was heated to 180 °C, eliminating water. Once the solution was clear, the reaction mixture was heated under reflux for another hour. After the reaction mixture was cooled to rt, the product was precipitated with water and stirred vigorously for 1 h longer. The white solid was filtered, washed with water, and dried under vacuum (8.5 g, 85%). The reaction scheme for the synthesis of the tridentate ligand is shown in detail in Figure 6.13.

6.4.2Synthesis complex Pt(2,6-Bis(3-((3R,5R,7R)-adamantan-1-yl)-1H-1,2,4-triazol-5-yl)-pyridine)N,N'-bis[4-(2-aminoethyl)pyridine]perylene 3,4:9,10-bis(dicarboximide)

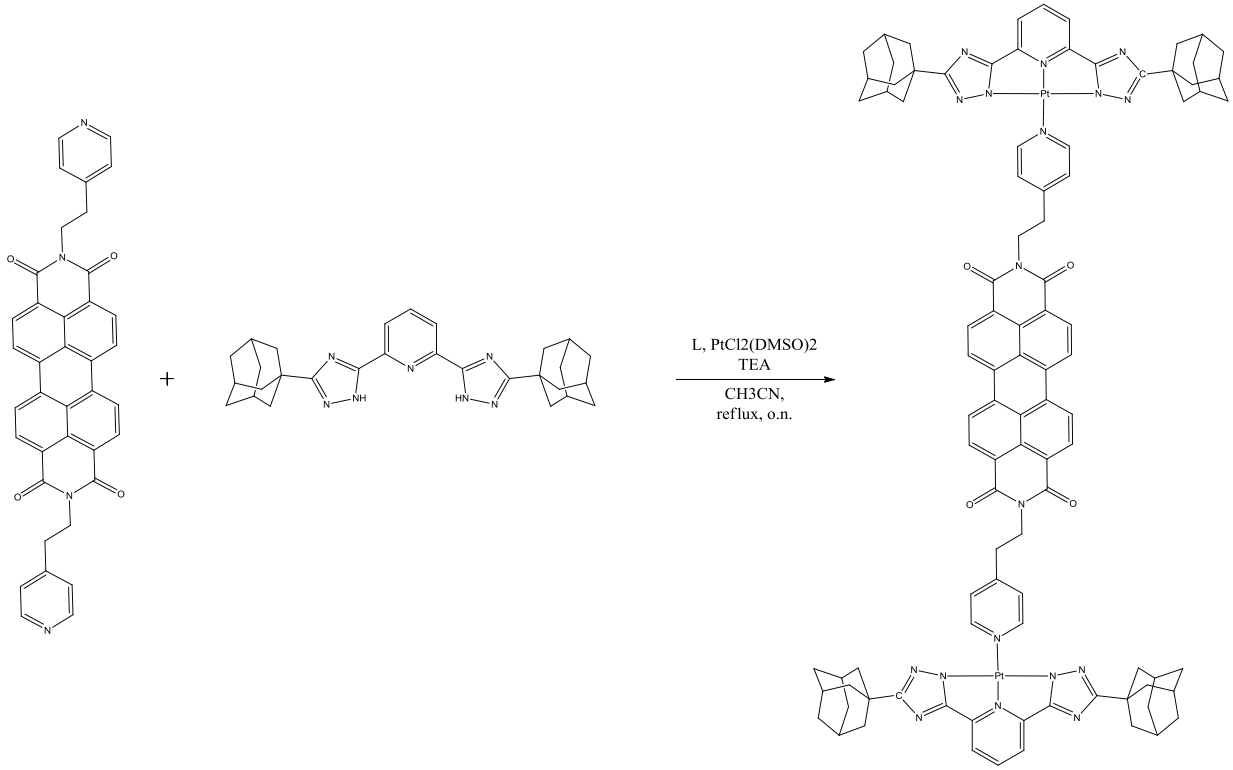

Figure 6.14 Synthetic procedure for complex Pt(2,6-Bis(3-((3R,5R,7R)-adamantan-1-yl)-1H-1,2,4-triazol-5-yl)-pyridine)N,N'-bis[4-(2-aminoethyl)pyridine]perylene 3,4:9,10-bis(dicarboximide)

The tridentate ligant 2,6-Bis(3-((3R,5R,7R)-adamantan-1-yl)-1H-1,2,4-triazol-5-yl)-pyridine (2 equiv., 50.7 mg, 0.105 mmol) and the base N,N-Diisopropylethylamine (2 equiv., 50 µl, 287 mmol) were added to a solution of $PtCl_2(DMSO)_2$ (2 equiv., 47.1 mg , 0.111 mmol)

in CH_3CN (20 mL). After stirring for about 10 minutes, a yellow solution was obtained and the ancillary ligand L was added (1 equiv., 31.1 mg, 0.052 mmol). The precipitation of the product started after the addition of the ancillary ligand. The mixture was then heated to 90°C under nitrogen flux for 24 hours. Afterwards, the solution was cooled to room temperature and stirred with 10 ml of water for 30 minutes. The mixture was filtered and washed first with 20 ml of methanol and then with diethyl ether. 48.5 mg of a red solid (yield 48.03 %) were obtained. The reaction scheme is reported in Figure 6.14 and the ^{1}H NMR spectrum (Figure 6.15) is recorded dissolving the complex in trifluoroacetic acid (TFA).

1H NMR (400 MHz, TFA, δ): 8.69 (m, 2H, H lig.), 8.68 (m, 4H, H py), 8.38 (m, 4H, H py), 8.09 (m, 8H, H peril.), 7.52 (m, 4H, H lig.), 2.68 (m, 4H, alif.), 2.34 (m, 4H, alif.), 2.26 (m, 28H, Ad), 1.81 (s, 36H, Ad).

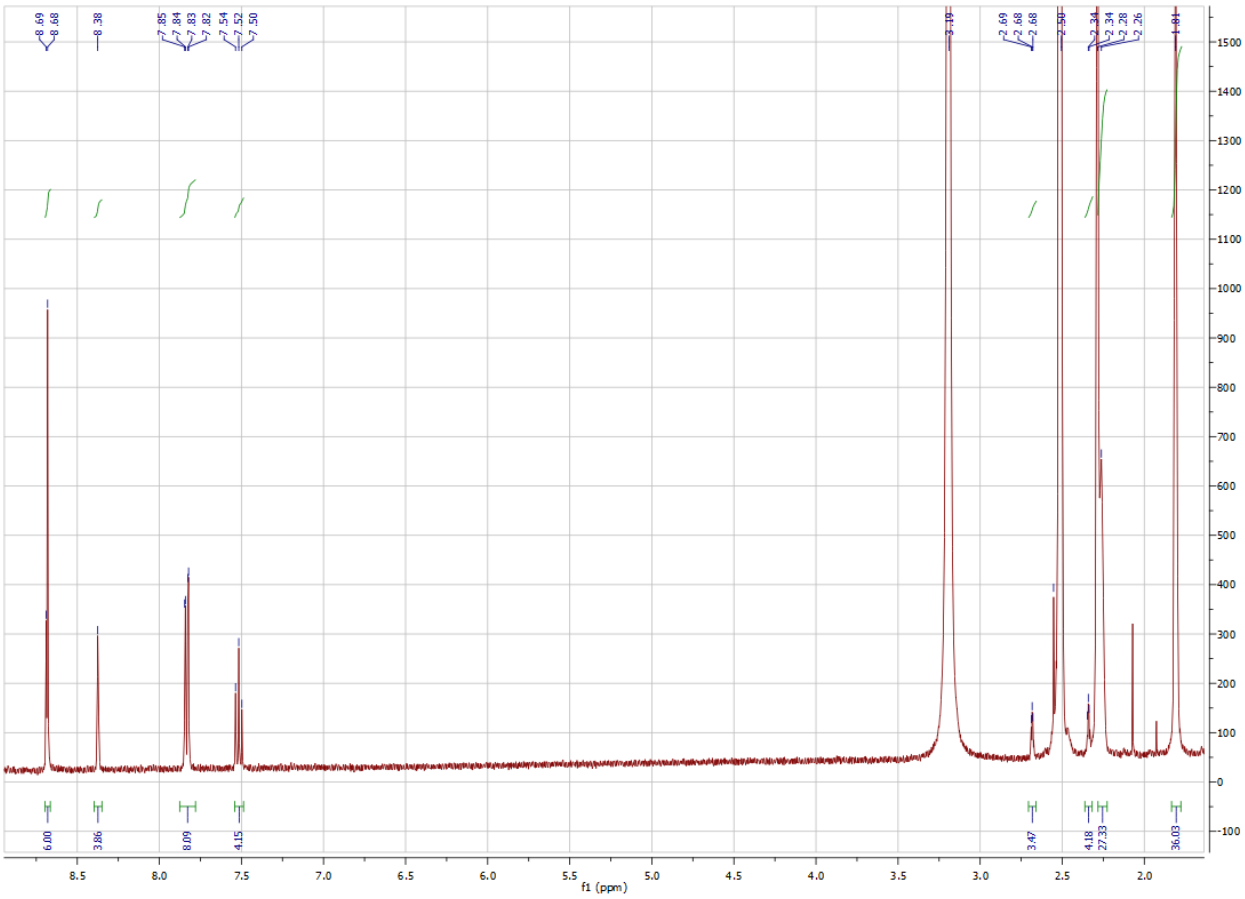

Figure 6.15 ^{1}H NMR spectrum of complex Pt(2,6-Bis(3-((3R,5R,7R)-adamantan-1-yl)-1H-1,2,4-triazol-5-yl)-pyridine)N,N'-bis[4-(2-aminoethyl)pyridine]perylene 3,4:9,10-bis(dicarboximide) in TFA.

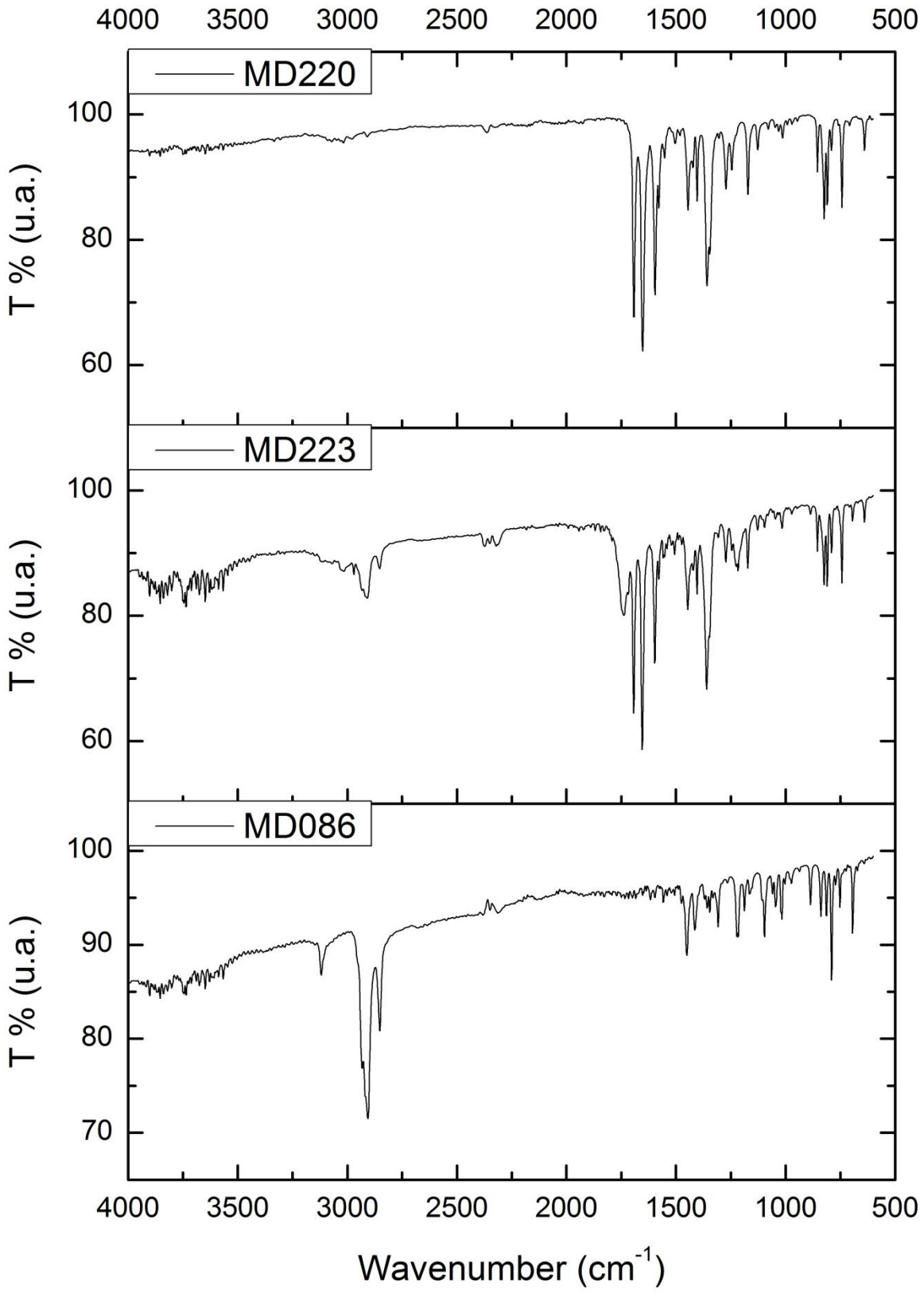

Figure 6.16 Comparison of the FT-IR spectra of (bottom) ligand 2,6-Bis(3-((3R,5R,7R)-adamantan-1-yl)-1H-1,2,4-triazol-5-yl)-pyridine (MD086), (centre) complex Pt(2,6-Bis(3-((3R,5R,7R)-adamantan-1-yl)-1H-1,2,4-triazol-5-yl)-pyridine)N,N'-bis[4-(2-aminoethyl)pyridine]perylene 3,4:9,10-bis(dicarboximide) (MD223) and (top) N,N'-bis[4-(2-aminoethyl)pyridine]perylene 3,4:9,10-bis(dicarboximide) (MD220).

Elemental analysys CHN:

	% N	% C	% H
Experimental	**11.73**	**67.75**	**5.26**
Theoretical	**12.93**	**59.13**	**4.65**

6.5 Complex Pt N,N'-bis[4-(2-aminoethyl)pyridine]perylene 3,4:9,10-bis(dicarboximide) 2,6-bis(3-((2-(2-methoxyethoxy)ethoxy)methyl)-1H-1,2,4-triazol-5-yl)pyridine

6.5.1 Synthesis tridentate 2,6-bis(3-((2-(2-methoxyethoxy)ethoxy)methyl)-1H-1,2,4-triazol-5-yl)pyridine

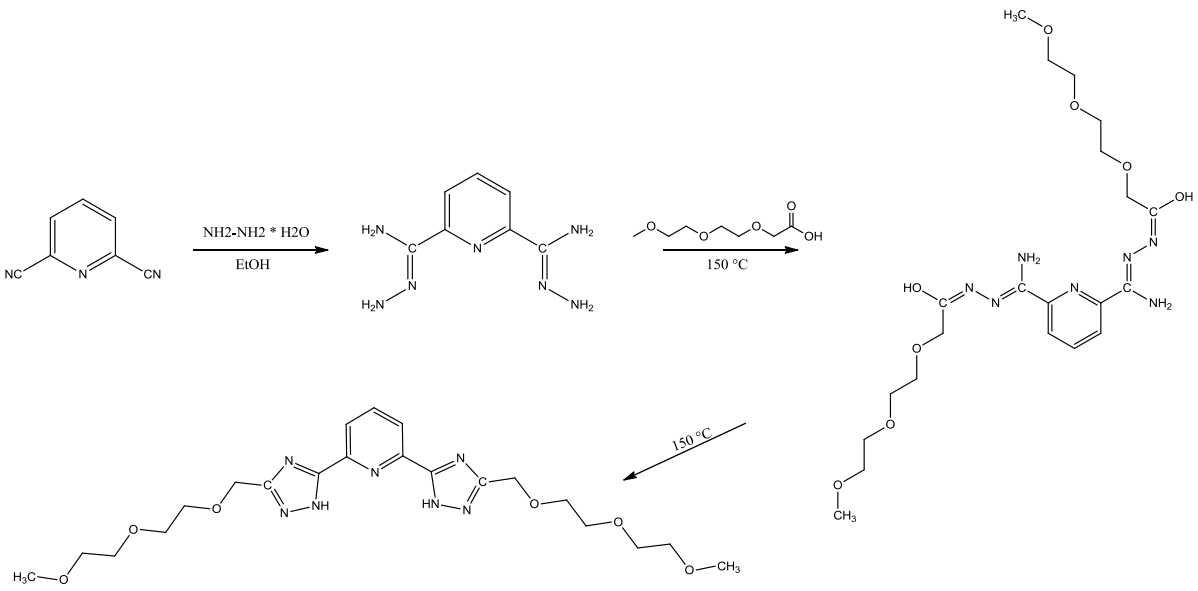

Figure 6.17 Synthetic procedure for ligand 2,6-bis(3-((2-(2-methoxyethoxy)ethoxy)methyl)-1H-1,2,4-triazol-5-yl)pyridine

The first step of the reaction is the formation of Pyridine-2,6 bis(carboximidhydrazide), which can be obtained with the procedure described in the following.

Pyridine-2,6-bis(carboximidhydrazide)**.**

To a solution of 2,6-pyridinedicarbonitrile (20 g, 0.155 mol) in ethanol (1 L), hydrazine monohydrate was added (151 mL, 3.1 mol). The reaction mixture was stirred at room temperature (rt) overnight, yielding a pale yellow precipitate in a yellow solution. The precipitate was filtered off, washed with cold ethanol, and dried (12 g, 40%).

The second and third step is the addition of PEG chain at 150°C and subsequently the dehydration at the same temperature to obtain the final tridentate ligand. The scheme of the reaction for the tridentate ligand is reported in Figure 6.17. The ligand was characterized by ^{1}H NMR in deuterated DMSO (Figure 6.18).

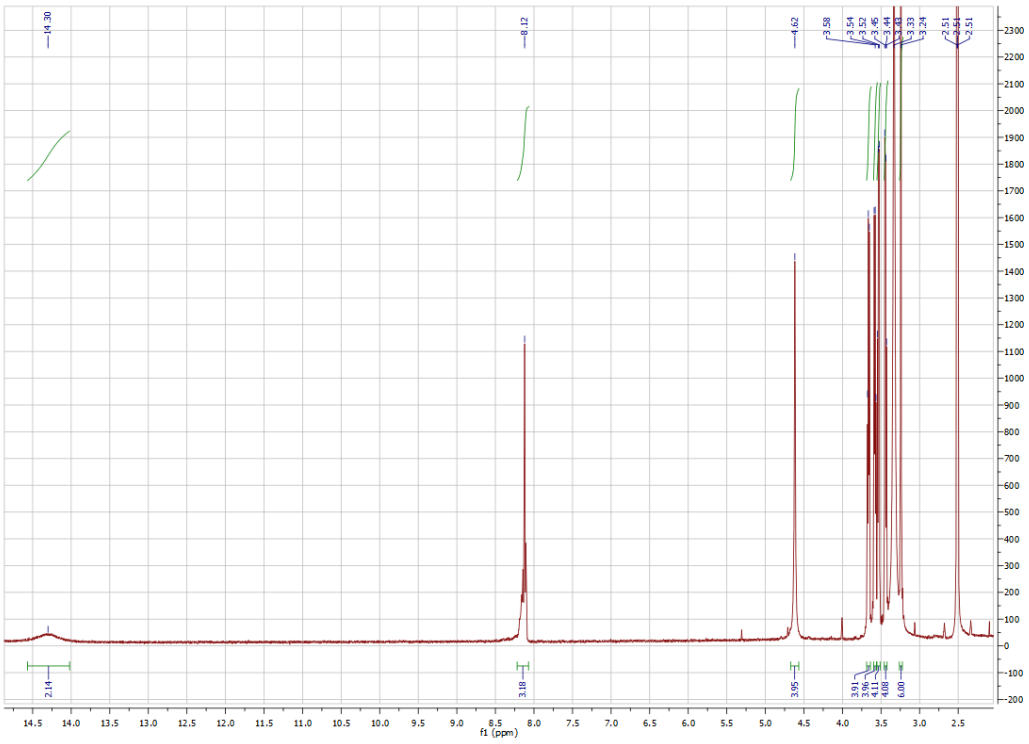

Figure 6.18 ^{1}H NMR spectrum of ligand 2,6-bis(3-((2-(2-methoxyethoxy)ethoxy)methyl)-1H-1,2,4-triazol-5-yl)pyridine in DMSO

6.5.2 Synthesis of the complex Pt N,N'-bis[4-(2-aminoethyl)pyridine]perylene 3,4:9,10-bis(dicarboximide) 2,6-bis(3-((2-(2-methoxyethoxy)ethoxy)methyl)-1H-1,2,4-triazol-5-yl)pyridine

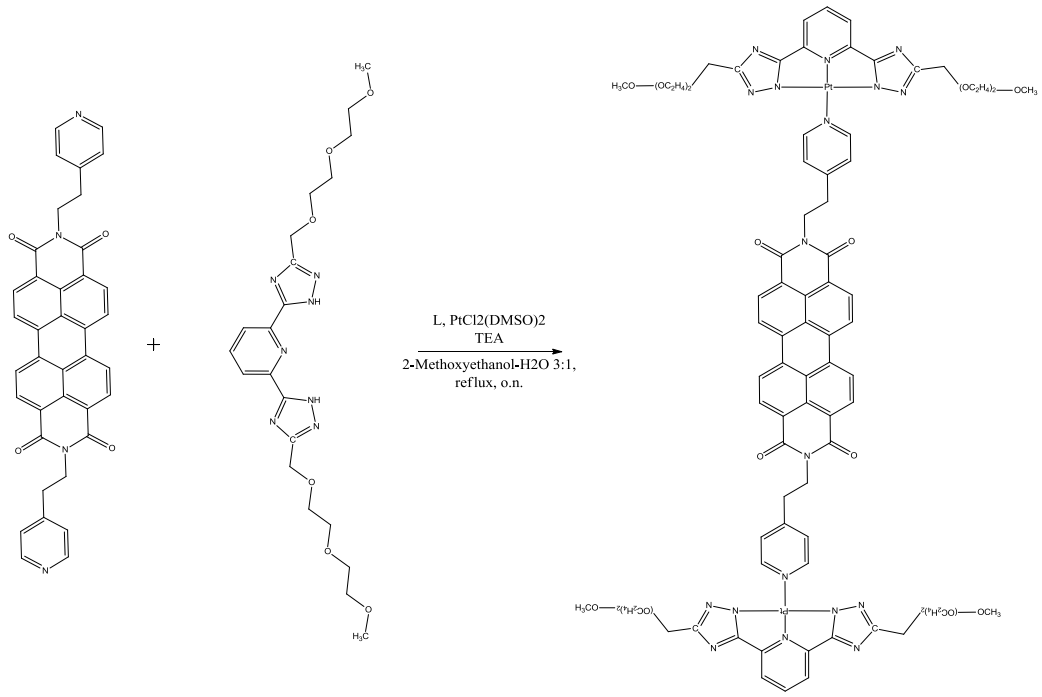

Figure 6.19 Synthetic procedure for complex Pt N,N'-bis[4-(2-aminoethyl)pyridine]perylene 3,4:9,10-bis(dicarboximide) 2,6-bis(3-((2-(2-methoxyethoxy)ethoxy)methyl)-1H-1,2,4-triazol-5-yl)pyridine

To a solution of $PtCl_2(DMSO)_2$ (2 equiv., 16.3 mg , 0.038 mmol) in methoxyethanol/water 3/1 (4 mL), the tridentate ligant AA022 (2 equiv., 18.0 mg, 0.037 mmol) and the base N,N-Diisopropylethylamine (2 equiv., 13 µl, 0.075 mmol) were added and the reaction mixture was stirred then for 20 minutes. A yellow solution was obtained and the ancillary ligand L was added (1 equiv., 12.0 mg, 0.020 mmol). The precipitation of the product started after the addition of the ancillary ligant. The mixture was then heated to 85°C under nitrogen flux for 24 hours (Figure 6.19). The mixture was cooled down and dried under vacuum overnight. 42.7 mg of a red solid were obtained.

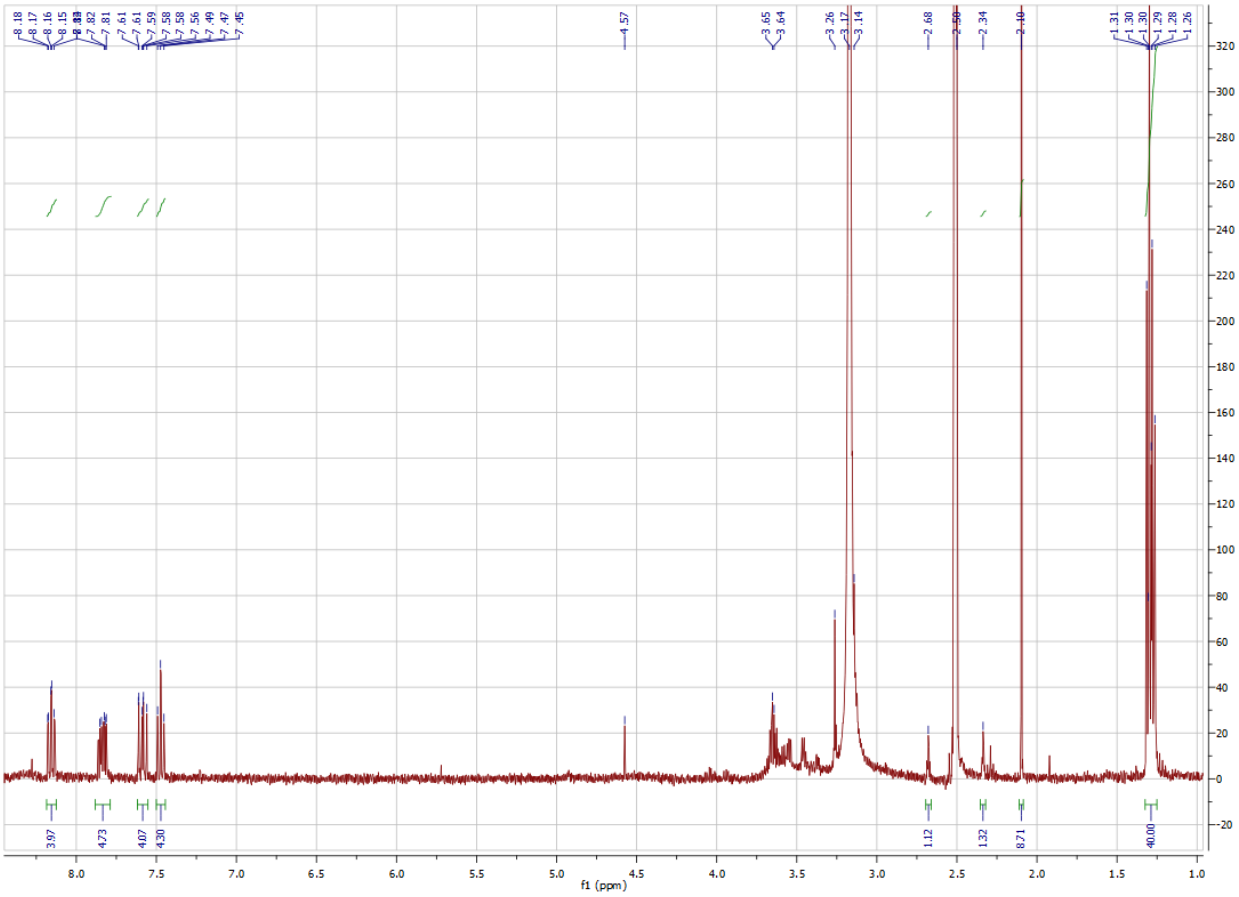

Figure 6.20 NMR spectrum of complex Pt **N,N'-bis[4-(2-aminoethyl)pyridine]perylene** 3,4:9,10-bis(dicarboximide) **2,6-bis(3-((2-(2-methoxyethoxy)ethoxy)methyl)-1H-1,2,4-triazol-5-yl)pyridine in DMSO at 60 °C**

6.6 Discussion and Conclusions

To gain further insight into the structural organization of the platinum complexes, WAXS (Wide Angle X-ray Scattering) has been employed. The WAXS spectra allow for the recognition of the intermolecular distances characterizing the π-π stacking spacings, usually found in 16-20 nm^{-1} range, i.e. corresponding to ≈ 0.34 nm [27-29].

Braggs spacings (d) are calculated calculated from the relation [30]:

$$d = 2\pi/q$$

Where q is the scattering wave vector defined as [31]:

$$q = \left(\frac{4\pi}{\lambda}\right) sin\left(\frac{2\theta}{2}\right)$$

Where 2θ is the scattering angle.

In Figure 6.21 the WAXS spectra of the perylene derivative used as ancillary ligand and of the platinum complexes functionalized with adamantly groups are compared. In the region of the π-π stacking no changes have been observed, so we can deduce that there is no influences on the packing of the perylene cores after the introduction of more steric hindered groups on the tridentate ligands.

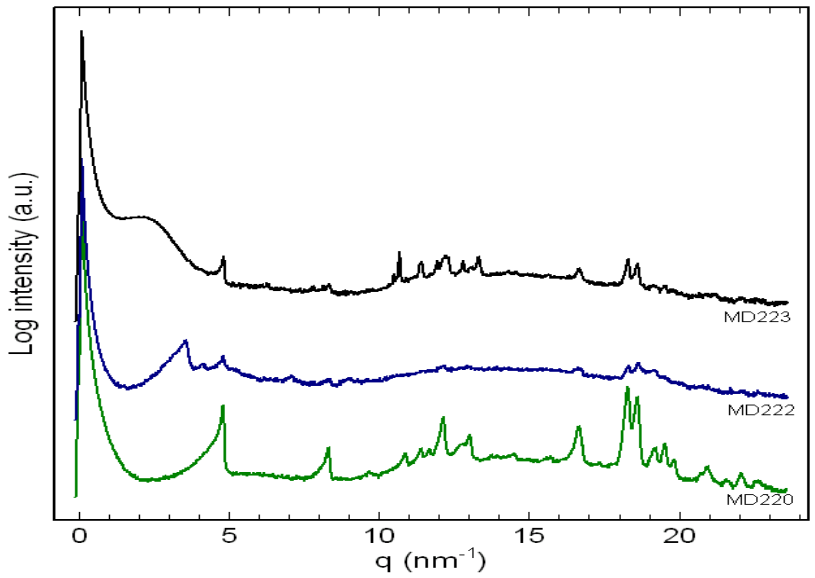

figure 6.21 WAXS spectra for ligant N,N'-bis[4-(2-aminoethyl)pyridine]perylene-3,4:9,10-bis(dicarboximide), Pt(trzpyttz)N,N'-bis[4-(2-aminoethyl)pyridine]perylene 3,4:9,10-bis(dicarboximide) and Pt(2,6-Bis(3-((3R,5R,7R)-adamantan-1-yl)-1H-1,2,4-triazol-5-yl)-pyridin

In conclusion, in this work we have demonstrated a simple and efficient way to synthesize new class of neutral platinum(II) complexes based on NˆNˆN dianionic tridentate and perylene bifunctionalized ancillary. Synthesis of asymmetric systems and the use of different functional groups on the dianionic tridentate ligands has given us the possibility to check for improved solubility and therefore for a decreased of the tendency to aggregation due the π-π and Pt-Pt interactions. In fact, only one of the obtained complexes, has displayed a good solubility and a potential for further applications.

References

[1] W. Brütting , J. Frischeisen , B. J. Scholz , T. D. Schmidt , *Europhysics News* **2011** , *42* , 20 .

[2] Duati, M.; Fanni, S.; Vos, J. G. Inorg. Chem. Commun. 2000, 3, 68.

[3] Mauro, M.; Quartapelle Procopio, E.; Sun, Y.; Chien, C.-H.; Donghi, D.; Panigati, M.; Mercandelli, P.; Mussini, P.; D'Alfonso, G.; De Cola, L. Adv. Funct. Mater. 2009, 19, 2607.

[4] Angulo, G.; Kapturkiewicz, A.; Chang, S.-Y.; Chi, Y. Inorg. Chem. Commun. 2009, 12, 378.

[5] Carlson, B.; Eichinger, B. E.; Kaminsky, W.; Bullock, J. P.; Phelan, G. D. Inorg. Chim. Acta 2009, 362, 1611.

[6] Vezzu, D. A. K.; Deaton, J. C.; Jones, J. S.; Bartolotti, L.; Harris, C. F.; Marchetti, A. P.; Kondakova, M.; Pike, R. D.; Huo, S. Inorg. Chem. 2010, 49, 5107.

[7] Wang, Z.; Turner, E.; Mahoney, V.; Madakuni, S.; Groy, T.; Li, J. Inorg. Chem. 2010, 49, 11276.

[8] Elbjeirami,O.; Rashdan,M.D.;Nesterov,V.; Rawashdeh-Omary, M. A. Dalton Trans. 2010, 39, 9465.

[9] Garg, J. A.; Blacque, O.; Fox, T.; Venkatesan, K. Inorg. Chem. 2010, 49, 11463.

[10] Armaroli, N.; Accorsi, G.; Cardinali, F.; Listorti, A. Top. Curr. Chem. 2007, 280, 69.

[11] Chowdhury, S.; Patra, G. K.; Drew, M. G. B.; Chattopadhyay, N.; Datta, D. Dalton Trans. 2000, 235.

[12] Miller, A. J. M.; Dempsey, J. L.; Peters, J. C. Inorg. Chem. 2007, 46, 7244.

[13] Williams, J. A. G. Top. Curr. Chem. 2007, 281, 205.

[14] Ma, B.; Djurovich, P. I.; Thompson, M. E. Coord. Chem. Rev. 2005, 249, 1501.

[15] Develay, S.; Williams, J. A. G. Dalton Trans. 2008, 4562.

[16] Yang, X.; Wang, Z.; Madakuni, S.; Li, J.; Jabbour, G. E. Adv. Mater. 2008, 20, 2405.

[17] Ma, B.; Djurovich, P. I.; Garon, S.; Alleyne, B.; Thompson, M. E. Adv. Funct. Mater. 2006, 16, 2438.

[18] Tang, R. P.-L.; Wong, K. M.-C.; Zhu, N.; Yam, V. W.-W. Dalton Trans. 2009, 2009, 3911.

[19] Jarosz, P.; Lotito, K.; Schneider, J.; Kumaresan, D.; Schmehl, R.; Eisenberg, R. Inorg. Chem. 2009, 48, 2420.

[20] Rochester, D.; Develay, S.; Zalis, S.; Williams, J. A. G. Dalton Trans. 2009, 2009, 1728.

[21] Schneider, J.; Du, P.; Wang, X.; Brennessel, W. W.; Eisenberg, R. Inorg. Chem. 2009, 48, 1498.

[22] Develay, S.; Blackburn, O.; Thompson, A. L.; Williams, J. A. G. Inorg. Chem. 2008, 47, 11129.

[23] Williams, J. A. G. Chem. Soc. Rev. 2009, 38, 1783.

[24] C.A. Strassert, C. H. Chien, M. D. Galvez Lopez, D. Kourkoulos, D. Hertel, K. Meerholz, L. De Cola. Angew. Chem. Int. Ed. 2011, 50, 946-950

[25] C. Cebrian, M. Mauro, D. Kourkoulos, P. Mercandelli, D. Hertel, K. Meerholz, C.A. Strassert, L. De Cola. Adv. Mater. 2012, 25, 437-442.

[26] M. Mydlak, M. Mauro, F. Polo, M. Felicetti, J. Leonhardt, G. Diener, L. De Cola, C.A. Strassert. Chem. Mater. 2011, 23, 3659-3667.

[27] Y. Liang, H. Wang, D. Wang, H. Liu, S. Feng. Dyes and Pigments 95 (2012) 260.

[28] Laschat S, Baro A, Steinke N, Giesselmann F, Hägele C, Scalia G, et al. Angew Chem Int Ed 2007;46(26), 4832.

[29] Van der Boom T, Hayes RT, Zhao Y, Bushard PJ, Weiss EA, Wasielewski MR. J Am Chem Soc 2002;124(32), 9582.

[30] C. R. Abreu, C. A. Torres, C. Solans, A. L. Quintela, G. J. T. Tiddy. ACS Appl. Mater. Interfaces 2011, 3, 4133.

[31] T. Ye, R. Singh, H. J. Butt, G. Floudas , P. E. Keivanidis. ACS Appl. Mater. Interfaces 2013, 5, 11844.

7. CONCLUSIONS

The work presented in this thesis tackles some important points on collective properties of two typical categories of molecular crystals, i.e., anthracene derivatives and charge transfer crystals. These compounds have been strategically selected as model systems for a phenomenological approach to some key properties of the solid state.

After the historical landmark of cynnamic acid, back in the sixties, anthracene derivatives have constituted the class of materials from which systematical investigations of crystal-to-crystal photodimerizations reactions started, developed and arose a renewed awakening in recent years. The present results show that, based on the structural nature of each compound, distinctive behaviors of their photo-reaction dynamics and kinetics can be identified, allowing us to define the processes as *topochemical*, *non topochemical*, *reversible* or *topophysical*. However, we showed that this classification should not be limited to the reactant structure. An elucidating example is 9MA, where, irrespective of a perfect structural fit for its photodimerization, reactions yields ranging from 20 to almost 100% were reported by the various Authors, on samples of different nature and measured with a range of techniques. We specifically mean that the variable yields found in separate experiments must be associated to different aspects of dynamical reaction mechanisms, irrespective of the paradigm that a perfect fit in the starting lattice must lead to a full conversion of the reactant. We believe that reaction rate and reaction yield are two non separable factors in solid state reactions, which both determine the outcome of the reaction. The role played by defects certainly needs to be revisited and taken into account, together with the nature and size and history of the sample.

No less important is the relationship found between incoming photons and mechanical response, that, to some extent, seems now to be a common occurrence in the solid state reactions driven by light. Probably, the most striking example we have encountered here is the reaction of DNO_2A to AQ. Although less spectacular, mechanical response was sizable also for the other systems illustrated in chapter 3. Other than this study, a vast literature is now flourishing on photomechanical effects in a variety of systems, polymers and crystals, leading to potential perspectives in the field of photomechanical actuators. The role of mechanical energy in a crystal-to-crystal reaction has not been yet fully exploited, though we believe that the considerable strain generated at the reactant/product interface requires a suitable route

to be released. The example of 9ACA, as anticipated in the literature a few years ago, is illuminating. However, in this work we cannot fully prove the previous claims concerning the formation of a stable photoproduct of this compound, for all samples and polymorphs investigated. At the moment, anyway, the possibility of employing the mechanical energy released in a reversible solid state reaction in an actual device still remains a challenge.

Finally, we would like to remark that the micro-Raman technique proved to be capable to discriminate between the molecular and the lattice transformation in the very same spot of a crystal. It was found that two distinct kinetic processes occur and in one case (9CNA) a careful kinetic analysis has been performed. Regardless of the kind of crystal-to-crystal transformation, we systematically identified the time delay between the molecular change, which obviously comes first, and the change of the original lattice into that of the product.

The problems related to polymorphism are an evergreen. Here is quite obvious that engineering the best structure of a material, likewise the morphology, is a promising route to improve its semiconductive properties. DPA and its new polymorphic forms are an example on how to try improving charge migration by changing both structure and morphology.

Related to polymorphism, the topic on pseudo-polymorphism of 9ACAD was raised with a fair amount of serendipity, giving us the chance to encounter an impressive variety of solvate structures. Once more solvents will be tried, we are confident that a record number of solvates is going to be exploited.

The final part of the thesis was focused on CT crystals formed by perylene (D) and tetracyano-quinodimethane (A), also in its fluorinated forms. This choice of materials was motivated by the semiconducting properties of the co-crystal, which are partially due to a ground state charge transfer between donor and acceptor. A number of single crystals of the binary system was prepared, and structural and spectroscopic characterizations have been performed to determine the degree of charge transfer between donor and acceptor in the co-crystals. It was found that the crystals grow in 1:1 or 3:1 ratio, for non fluorinated TCNQ, or in 3:2 ratio, for fluorinated TCNQ derivatives. The molecular ratios 1:1 adopt a monoclinic structure, but in the case of perylene-F_4TCNQ a solvate structure with toluene inclusion was obtained. One of the achievements of this work is the definition of the experimental conditions which drive the crystal growth of the binary systems either towards the low (1:1) or the high ratio (3:1 or 3:2) stoichiometries by PVT technique. We believe that the criteria

adopted for selecting the kind of end product could be applied to other co-crystals, in such a way to control the characteristics of the final material.

Acknowledgements

List of publications

1. L. Fusina, G.D. Nivellini, T. Salzillo, M. Lamarra, R. Tarroni. *Ab initio quartic force field of stannane and rotational analysis of the nu_1 infrared band of* $H^{120}SnD_3$. J. Chem. Phys. **137**, 204316/1-10 (2012)
2. T. Salzillo, I. Bilotti, R.G. Della Valle, E. Venuti, A. Brillante. *Crystal to crystal photoinduced reaction of dinitro-anthracene to anthraquinone.* J. Am. Chem. Soc. **134**, 17671-17679 (2012)
3. T. Salzillo, S. Zaccheroni, R.G. Della Valle, E. Venuti, A. Brillante. *Micro Raman investigation of the photodimerization reaction of 9-cyanoanthracene in the solid state.* J. Phys. Chem. C **118**, 9628-9635 (2014)
4. F. Burgio, P. Fabbri, G. Magnani, M. Scafè, L. Pilloni, A. Brentari, A. Brillante, T. Salzillo. *C_f/C composites: correlation between CVI process parameters and Pyrolytic Carbon microstructure.* Frattura e integrità strutturale **30**, 68-74 (2014)
5. F. Di Maria, E. Fabiano, D. Gentili, M. Biasiucci, T. Salzillo, G. Bergamini, M. Gazzano, A. Zanelli, A. Brillante, M. Cavallini, F. Della Sala, G. Gigli, G. Barbarella. *Polymorphism in crystalline microfibers of achiral octithiophene: The effect on charge transport, supramolecular chirality and optical properties.* Adv. Funct. Mater. **24**, 4943-4951 (2014)
6. F. Mazzanti, G. Magnani, S. Grilli, A. Brillante, T. Salzillo, A. Brentari, E. Burresi, C. Mingazzini, P. Fabbri. *Microstructural characterization of activated carbon obtained from waste tires.* Advances in Science and Technology **87**, 79-84 (2014)